

# **Characterization and Dynamic Studies of Drugs for Combating Multi-Drug Resistance**



**By**

**NAILA ZAMAN**

**National Centre for Bioinformatics,  
Faculty of Biological Sciences,  
Quaid-i-Azam University  
Islamabad, Pakistan,  
2023**

**Characterization and Dynamic Studies of Drugs for  
Combating Multi-Drug Resistance**



**By**

**NAILA ZAMAN**

*A thesis submitted in the partial fulfillment of the requirements for the degree of*

*DOCTOR OF PHILOSOPHY*

*in*

*BIOINFORMATICS*

**National Centre for Bioinformatics,  
Faculty of Biological Sciences,  
Quaid-i-Azam University  
Islamabad, Pakistan,  
2023**

## DECLARATION

The work reported in this thesis entitled “Characterization and Dynamic studies of Drugs for Combating Multi-Drug Resistance” was carried out by Naila Zaman under the supervision of Dr. Syed Sikander Azam. I hereby, declare that the title of the thesis and all the contents presented in the following study are the product of my effort and no part has been copied from any published source (except the references, standard mathematical or genetic models/equations/formulas/ protocols, etc). None of the work has been submitted for the award of any other degree/diploma. The University may take action if the information provided is found inaccurate at any stage.

Signature:

---

*This thesis is dedicated to the fond memory of my father*

***Khair-uz-Zaman,***

*who has given me invaluable education opportunities and had always been a source of inspiration, and courage to face the eventualities of life with zeal and enthusiasm. While writing this, I am in a roller coaster of emotions, but I am glad he saw the process through to its completion. His memory gave me the nourishment to fulfill his long-cherished dream.*

*I also dedicate this to my mother*

***Nighat Zaman,***

*For her advice, her patience, and her faith because she always understood.*

*This moment fills me with gratitude to them...*

## ACKNOWLEDGEMENTS

*The ultimate praise and gratitude to Almighty, the creator of all heavens and the earth, our sole Provider and Nourisher – without His will nothing could be done.*

*I am deeply indebted to my Ph.D supervisor, Professor Dr. Syed Sikander Azam, for believing in me and providing me an opportunity to pursue my Ph.D under his supervision. His unwavering support throughout this doctoral journey has enabled me to accomplish my research despite all odds. His advice and critical analysis of work has transformed my small efforts into big accomplishments. I will always cherish the time spent under his tutelage, especially his role in compiling this thesis.*

*Furthermore, I would like to acknowledge Dr. Sarwat Jahan, Dean of Faculty of Biological Sciences, Professor Dr. Sajid Rashid and Professor Dr. Amir Ali Abbasi for their consistent and invaluable academic support.*

*The role of Pakistan United-States Science and Technology Cooperation Program (Grant no. Pak-US/2017/360), Higher Education Commission of Pakistan (HEC), and International Foundation for Science (IFS) has been pivotal in provision of financial assistance during my research pursuit. I take this opportunity to express my deep sense of gratitude to our Pak-US collaborators Dr. Michelle Kuttel, Kushal Cuppoor, and Takunda Chikondo for expanding my learning experience. I am immensely grateful to Professor. Dr. Michele Cascella from Theoretical Chemistry department, University of Oslo, Norway who provided valuable insights to improve my understanding of theoretical concepts employed in this study.*

*All the technical and administrative staff of National center for Bioinformatics, QAU is also acknowledged for always being available for any services needed especially Mr. Naseer Ahmed (senior), Mr. Naseer Ahmed (junior), Mr. Yasir Mehmood Abbasi (computer programmer), Mr. Ali, and Yasir bhae (lab assistant).*

*Furthermore, I acknowledge the support and encouragement provided by my Ph.D fellows, who extended their helping hands at each and every step of this work; Afifa Navid, Nousheen Pervaiz, Rabia Farid, Faisal Ahmad and Ghulam Abbas. I owe thanks to M.phil members of Computational Biology Lab, especially Fouzia Gul, Kainat Gul and Rimsha*

*Yousaf who made the time spent at lab memorable by ensuring their joyful company. I would take this opportunity to express my gratitude for Dr. Saad Raza, for his guidance especially during my M.phil tenure and the academic support that has enabled me to complete my research.*

*I would like to express strongest feelings of gratitude for my beloved family. My husband Anjum Riaz for supporting me in all the possible ways and providing his perspective in my research writings. My beloved sisters Ayesha Zaman and Isra Zaman for being with me through thick and thin, for backing me with their comfort and support through their presence. Last but not the least, my kids Hareem Fatima and Muhammad Arham for comforting me and bearing with me through this journey.*

*In the end, I would again thank my parents, who I owe my deepest gratitude for their unconditional love, emotional, and moral support in every phase of my life.*

*Naila Zaman*

---

# TABLE OF CONTENTS

<b>LIST OF FIGURES .....</b>	<b>VII</b>
<b>LIST OF TABLES .....</b>	<b>XX</b>
<b>SUMMARY .....</b>	<b>1</b>
<b>1. BACKGROUND AND MOTIVATION .....</b>	<b>7</b>
<b>1.1 Drug resistance in antimicrobials .....</b>	<b>7</b>
1.1.1 Factors contributing to AMR .....	7
1.1.2 Consequences of AMR.....	8
1.1.3 Halt in drug discovery .....	8
1.1.4 Methods to control AMR .....	9
<b>1.2 Role of molecular mechanics (MM) in drug discovery .....</b>	<b>9</b>
<b>1.3 Aims and objectives .....</b>	<b>10</b>
<b>2. COMPUTATIONAL AND THEORETICAL OVERVIEW .....</b>	<b>15</b>
<b>2.1 Molecular modeling .....</b>	<b>15</b>
<b>2.2 Quantum mechanics .....</b>	<b>16</b>
2.2.1 Schrödinger equation.....	18
2.2.2 Density function theory (DFT).....	19
2.2.3 B3LYP .....	20
2.2.4 Basis set.....	20
2.2.5 Effective core potential (ECP) .....	21
<b>2.3 Molecular mechanics .....</b>	<b>22</b>
2.3.1 Statistical mechanics .....	24
2.3.1.1 Ensembles of statistical dynamics .....	24
2.3.2 Molecular dynamics simulations .....	25
2.3.2.1 Simulation integrators and thermostats .....	26
2.3.2.2 Periodic boundary conditions .....	27
2.3.2.3 Ewald summation method for long-range interactions .....	28
2.3.3 Molecular docking.....	29
<b>2.4 Hybrid QM/MM approach .....</b>	<b>31</b>
2.4.1 Umbrella sampling .....	33
2.4.2 Metal-ion modeling .....	35
<b>2.5 Evaluation of structural and dynamical parameters .....</b>	<b>36</b>

---

2.5.1	Binding free energy calculations .....	36
2.5.2	Radial distribution function.....	37
2.5.3	Axial frequency distribution.....	38
<b>2.6</b>	<b>Hardware overview.....</b>	<b>38</b>
<b>3.</b>	<b>COVALENT INHIBITION OF OXYR: A QM/MM STUDY.....</b>	<b>41</b>
<b>3.1</b>	<b>Background .....</b>	<b>41</b>
<b>3.2</b>	<b>Materials and methods .....</b>	<b>45</b>
3.2.1	Selection of covalent modifiers .....	45
3.2.2	QM-cluster calculations .....	49
3.2.3	QM/MM setup for umbrella sampling .....	51
3.2.4	Binding free energy.....	54
<b>3.3</b>	<b>Results and discussion.....</b>	<b>55</b>
3.3.1	Reaction mechanism with benzothiopyene-core inhibitor .....	57
3.3.2	Reaction mechanism with nitrile-based inhibitor .....	61
3.3.3	Reaction mechanism with Exp-1 and Exp-2 inhibitors .....	64
3.3.4	Effect of TS on binding affinities .....	68
<b>3.4</b>	<b>Concluding remarks .....</b>	<b>72</b>
<b>4</b>	<b>COMPETO-ALLOSTERIC REGULATION .....</b>	<b>75</b>
<b>4.1</b>	<b>Background .....</b>	<b>75</b>
<b>4.2</b>	<b>Materials and methods .....</b>	<b>78</b>
4.2.1	Receptor protein preparation .....	78
4.2.2	Ligand library preparation and molecular docking .....	79
4.2.3	Pocket search.....	81
4.2.4	Ligand topology and molecular dynamics simulations .....	81
4.2.5	Simulation trajectories evaluation .....	83
4.2.6	Validation of study with a positive control .....	84
<b>4.3</b>	<b>Results and discussion .....</b>	<b>84</b>
4.3.1	Docking analysis of DSPI .....	84
4.3.2	Crystal structure of DSPI .....	89
4.3.3	Druggability analysis.....	90
4.3.4	Analysis of MD simulation trajectories.....	92
4.3.5	Competo-allostery .....	97
4.3.6	Validation of competo-allostery .....	99
4.3.7	TRAPP analysis of MD simulation trajectories .....	102
4.3.8	Binding free energy analysis .....	104
<b>4.4</b>	<b>Concluding remarks .....</b>	<b>106</b>

---



---

<b>5. BI-METAL FORCE FIELD PARAMETERIZATION .....</b>	<b>109</b>
<b>5.1 Background .....</b>	<b>109</b>
<b>5.2 Materials and methods .....</b>	<b>112</b>
5.2.1 Experimentally analysis of Bi(V) metalloids .....	112
5.2.2 Novel force field parameters .....	113
5.2.3 Force field parameters validation and analysis.....	115
5.2.4 Axial frequency distribution (AFD).....	117
<b>5.3 Results and discussion .....</b>	<b>117</b>
5.3.1 Force field parameterization reveal bidentate chelating effect.....	117
5.3.2 RESP charges .....	119
5.3.3 SBKJC ECP at a glance .....	122
5.3.4 Validation of force field parameters.....	124
5.3.4.1 Modulation of trypanothione synthetase amidase by Arg.....	124
5.3.4.2 Insights into dynamics of Arg569.....	128
5.3.4.3 Molecular basis of Bi(V) with trypanothione reductase .....	136
<b>5.4 Concluding remarks .....</b>	<b>138</b>
<b>6 MYTHS AND REALITIES BEHIND COVID19 THERAPEUTIC INTERVENTIONS .....</b>	<b>142</b>
<b>6.1 Background .....</b>	<b>142</b>
<b>6.2 Materials and methods .....</b>	<b>143</b>
6.2.1 Dataset collection for pharmacophore modeling.....	144
6.2.1.1 Training set.....	144
6.2.1.2 Test set.....	145
6.2.2 Pharmacophore modeling.....	145
6.2.3 Pharmacophore validation.....	146
6.2.4 Virtual screening for lead identification.....	147
6.2.5 Molecular docking.....	148
6.2.6 Molecular dynamics simulations.....	148
6.2.7 Trajectories analysis.....	149
6.2.8 Binding free energies .....	149
6.2.9 Axial frequency distribution.....	150
6.2.10 Toxicity analysis .....	150
6.2.11 Network pharmacological analysis.....	150
<b>6.3 Results and discussion .....</b>	<b>151</b>
6.3.1 Pharmacophore modeling.....	151
6.3.2 Validation of pharmacophore models .....	153
6.3.3 Virtual screening .....	157
6.3.4 Molecular docking.....	157
6.3.4.1 Active phytochemicals.....	159
6.3.4.2 Senna compounds .....	162
6.3.5 Molecular dynamics simulations.....	163

---

6.3.5.1	Analysis of active phytochemicals.....	163
6.3.5.2	Analysis of Senna compounds.....	169
6.3.5.3	Binding free energy analysis.....	171
6.3.5.4	Axial frequency distribution.....	173
6.3.6	Pharmacokinetic profiling analysis.....	175
6.3.6.1	ADMET analysis.....	175
6.3.6.2	Toxicity analysis.....	175
6.3.7	Network pharmacological analysis.....	178
<b>6.4</b>	<b>Concluding remarks.....</b>	<b>179</b>
<b>7</b>	<b>DYNAMICS OF WATER-MEDIATED INTERACTIONS EFFECTS ON OMICRON.....</b>	<b>184</b>
<b>7.1</b>	<b>Background.....</b>	<b>184</b>
<b>7.2</b>	<b>Materials and methods.....</b>	<b>185</b>
7.2.1	Predicting the impact of multiple point mutations.....	185
7.2.2	Mutant structure modeling.....	186
7.2.3	Molecular dynamics simulations.....	187
7.2.4	Binding energy calculations.....	189
7.2.5	Principle component analysis (PCA).....	189
<b>7.3</b>	<b>Results and discussion.....</b>	<b>189</b>
7.3.1	Protein thermodynamics and mutational effects.....	189
7.3.2	Mutations-induced intra/intermolecular changes in solution.....	192
7.3.3	Molecular determinants responsible for relative binding affinities.....	194
7.3.4	Conformational rearrangements underpinning the active conformation.....	196
7.3.5	Role of EPE insertion in Omicron.....	199
7.3.6	Water-mediated interactions enhance stability.....	199
<b>7.4</b>	<b>Concluding remarks.....</b>	<b>202</b>
<b>APPENDIX.....</b>	<b>.....</b>	<b>206</b>
<b>PUBLICATIONS.....</b>	<b>.....</b>	<b>222</b>
<b>REFERENCES.....</b>	<b>.....</b>	<b>224</b>

---

## LIST OF ABBREVIATIONS

3D quantitative structure-activity relationship	3D-QSAR
Antimicrobial resistance	AMR
Artificial intelligence	AI
Assisted model building with energy refinement	AMBER
Axial frequency distribution	AFD
Becke, and Lee, Yang and Parr	B3LYP
Canonical ensemble	NVT
Centers for Disease Control and Prevention	CDC
Density Function Theory	DFT
Effective core potential	ECP
Epidermal growth factor receptor	EGFR
Extracellular signal-regulated kinases	ERK
Gaussian-type orbitals	GTO
Genetic algorithms	GA
Genetic Optimization for Ligand Docking	GOLD
Hartree-Fock	HF
High Ambiguity protein-protein docking	HADDOCK
Hydroxymethyl ketone	HMK
Isothermal-isobaric ensemble	NPT
Micro canonical ensemble	NVE
Minimum energy pathway	MEP
Molecular dynamics	MD

---

Multi-drug resistance	MDR
Normal Mode Analysis	NMA
Nuclear magnetic resonance	NMR
Particle mesh Ewald	PME
Protein data bank	PDB
Putative enoyl-coenzyme A	CoA
Quantum mechanics/molecular mechanics	QM/MM
Quorum sensing	QS
Radial distribution function	RDF
Reaction coordinate	RC
Receptor binding domain	RBD
Receptor tyrosine kinases	RTK
Restrained electrostatic potential.	RESP
Slater-type orbitals	STO
Solvent accessible surface area	SASA
Thermodynamic integration	TI
Three-dimensional	3D
Trypanothione reductase	TR
Trypanothione synthetase-amidase	TSA
Umbrella sampling	US
Van der Waal	vdW
Variants of concern	VoA

---

## LIST OF FIGURES

Figure 2.1. Schematic representation of evolution of multiple simulations methods.....	17
Figure 2.2. Approaches to treat metal ions in the framework of molecular mechanics MM. .....	23
Figure 2.3. Schematic representation of two-dimensional periodic boundary conditions.	28
Figure 2.4: Diagrammatic sketch of three main families of molecular modeling methods. .....	29
Figure 2.5: Diagrammatical sketch of QM/MM illustrating partitioning of the system into QM and MM regions. ....	31
Figure 2.6: Division of covalent bonds across the QM and MM regions. ....	32
Figure 2.7: Diagrammatic sketch of overlapping windows of Umbrella sampling illustrating algorithm behind its calculations, which are combined using WHAM.....	34
Figure 2.8: Flowchart of MCPB.py suite adopted from 142. ....	36
Figure 2.9. Multi-core GPUs available at Computational Biology Lab of National Center for Bioinformatics at Quaid-i-Azam University. ....	39
Figure 3.1: Unproductive non-covalent MD simulations of four different inhibitors. Detachment of ligands are highlighted in square.....	42
Figure 3.2. Chemical structures of the proposed covalent inhibitors A) Benzothiopene-core inhibitor B) Modified Exp-2 inhibitor with methyl oxo-enoate C) Modified Exp-1 inhibitor with hydroxymethyl ketone D) Nitrile-based inhibitor. Reaction centers are indicated with an asterisk whereas the Michael acceptor addition of two proposed experimental inhibitors is highlighted in blue.....	44
Figure 3.3. Workflow of covalent inhibition of OxyR with four proposed inhibitors.....	46

---

Figure 3.4. Comparative snapshots of proposed inhibitors in the active site of OxyR with interacting residues highlighted. A) Benzothiopene-core inhibitor B) Nitrile inhibitor C) Crystal structure of OxyR with the substrate D) Modified Exp-1 inhibitor with hydroxymethyl ketone E) Modified Exp-2 inhibitor with methyl oxo-enoate. .... 48

Figure 3.5. Simulation graphs of resulting trajectories from US simulations of thiopene-core and nitrile-based inhibitors. A) Root Mean Square Deviation (RMSD) calculated from 10 ns simulations trajectories of OxyR in complex with the thiopene-core inhibitor. B) RMSD calculated from 10 ns simulations trajectories of OxyR in complex with the nitrile-based inhibitor. Details of the atoms included in the QM region in QM/MM calculations are given on the right side. The black dots represent the hydrogen link atoms. .... 52

Figure 3.6: Simulation graphs of resulting trajectories from US simulations of Exp-1 and Exp-2 inhibitors. A) Root Mean Square Deviation (RMSD) calculated from 10 ns simulations performed on the OxyR in complex with the Exp-1 inhibitor. B) RMSD calculated from 10 ns simulations performed on the OxyR with Exp-2 inhibitor. Details of the atoms included in the QM region in QM/MM calculations are given on the right side. The black dots represent the hydrogen link atoms. .... 53

Figure 3.7. Overlapping windows of RC2 obtained from US for each compound generated with WHAM. .... 54

Figure 3.8. Non-covalent interactions between OxyR and proposed inhibitors. A) Thiopene-core inhibitor B) Nitrile-core inhibitor C) Modified Exp-1 inhibitor with hydroxymethyl ketone, and D) Modified Exp-2 inhibitor with methyl oxo-enoate. .... 56

Figure 3.9. Details of DFTB3/MM optimized structures of selected states located along the inhibition reaction of OxyR by thiopene-core inhibitor. The catalytic residues C199 and H130 are shown with key distances in Å. .... 58

Figure 3.10: DFTB3/MM free energy profile obtained from QM/MM umbrella sampling calculations for inhibition of OxyR. The inhibition mechanism of thiopene-core and nitrile-based inhibitors is illustrated in black and yellow colours respectively. The TS of thiopene-

---

core and nitrile-based inhibitors are not similar and represent individual reaction profiles. Red arrows indicate the relative Gibbs free energies ( $\Delta G$ ) for all stationary points. ....	59
Figure 3.11: Evolution of bond distances along the reaction profile of thiopene-core inhibitor, nitrile-core inhibitor, modified Exp-1 inhibitor with hydroxymethyl ketone, and modified Exp-2 inhibitor with methyl oxo-enoate.....	60
Figure 3.12. Optimized TS structures with B3LYP 6-31+G(d,p) level of theory of thiopene-core inhibitor displayed on top and nitrile-based inhibitor shown at the bottom .....	61
Figure 3.13: Details of DFTB3/MM optimized structures of selected states located along the inhibition reaction of OxyR by nitrile inhibitor. The catalytic residues C199 and H130 are shown with key distances in Å.....	63
Figure 3.14: Details of DFTB3/MM optimized structures of selected states located along the inhibition reaction of OxyR by Exp-1 inhibitor. The catalytic residues C199 and H130 are shown with key distances in Å.....	66
Figure 3.15: DFTB3/MM free energy profile obtained from QM/MM umbrella sampling calculations for inhibition of OxyR. The inhibition mechanism of Exp-1 and Exp-2 inhibitors is illustrated in green and blue colours respectively. Red arrows indicate the relative Gibbs free energies ( $\Delta G$ ) for all stationary points. ....	66
Figure 3.16: Optimized TS structures with B3LYP 6-31+G(d,p) level of theory of Exp-1 with hydroxymethyl ketone displayed on top and Exp-2 having methyl oxo-enoate is shown at the bottom.....	67
Figure 3.17: Details of DFTB3/MM optimized structures of selected states located along the inhibition reaction of OxyR by Exp-2 inhibitor. The catalytic residues C199 and H130 are shown with key distances in Å.....	68
Figure 3.18: Snapshots of four proposed covalent inhibitors from 10 ns QM/MM US simulations carried out with DFTB3 level of theory. ....	69

- 
- Figure 3.19. A) Overlap of the QM region of TS1 and TS2 of thiopene-based inhibitor optimized with 6-31+G(d,p)/MM level B) Overlap of the QM region of TS1 and TS2 of nitrile-based inhibitor. Favourable interaction free energy values (electrostatic plus Lennard-Jones) observed between binding site of OxyR and proposed inhibitors calculated at E:I and E-I states are mentioned respectively. .... 70
- Figure 3.20. A) Overlap of the QM region of TS of Exp-1 inhibitor optimized with 6-31+G(d,p)/MM B) Overlap of the QM region of TS of Exp-2 inhibitor. Favourable interaction free energy values (electrostatic plus Lennard-Jones) observed between binding site of OxyR and proposed inhibitors calculated at E:I and E-I states are mentioned respectively. .... 71
- Figure 4.1. DSPI appear as a standard crotonase fold and assembles as a homotrimer. A) Cartoon representation of the DSPI trimer where each binding site is shown in pink color. B) Cartoon style of the DSPI monomer. The secondary structure elements are highlighted and the substrate docked at normal binding site is shown in pink color..... 76
- Figure 4.2. Workflow of the current study using different computational techniques. .... 77
- Figure 4.3. 3D structure representation of DSPI protein inside the TIP3P water box..... 80
- Figure 4.4. Docked inhibitor within the normal binding pocket. A) The docked pose of compound 10195495 highlighting critical residues of the normal binding pocket. Protein is in ribbons whereas ligand is in bond style. B) 2D depiction of the docked complex highlighting hydrogen bonds and cation- $\pi$  interaction through DS Visualizer. .... 86
- Figure 4.5. Docked inhibitor within the allosteric binding pocket. A) Docked pose of compound 10252273 highlighting critical residues of the allosteric binding pocket. Protein is in ribbons whereas ligand is in bond style. B) 2D depiction of the docked complex highlighting hydrogen bonds and cation- $\pi$  interaction through DS Visualizer. .... 88
- Figure 4.6. The normal binding site and the competo-allosteric site in the same binding tunnel competing with each other for ligand binding. Electronegative atom “OE1”



---

interacted with a ligand bound at the normal binding site, whereas interactions between “O” atom of Glu118 and ligand attached at the allosteric site were observed. .... 90

Figure 4.7: Structural changes upon ligand binding at the normal and the competo-allosteric site during docking. Structural rearrangements are mentioned in red with the critical residues highlighted in each conformation. A) DSPI without ligand B) 10195495 docked at the normal site C) DSPI with substrate D) 10252273 docked at the competo- allosteric site. .... 91

Figure 4.8: Detection of druggable cavities by CavityPlus and Fpocket A) Druggable binding sites upon ligand binding at the normal site with the critical residues labeled, normal site is shown in pink and allosteric site shown in grey color B) Druggable binding sites upon ligand binding at competo-allosteric site with the critical residues labeled and allosteric site shown in grey color. The structural rearrangement of critical residues at the normal binding site is shown due to which the software failed to identify its presence... 93

Figure 4.9. Simulations analysis of resulting trajectories of a substrate, ligand bound at the normal and compete-allosteric site. A) Deviation of the backbone depicted with root means square B) deviation of individual residue depicted as root mean square fluctuation. C) disordered regions and thermal stability of protein as B-factor. D) and net volume of the DSPI depicted with a radius of gyration. Black color represents a substrate used as controls, red color represents ligand bound at the normal site, and green color is the representation of a ligand at the competo-allosteric site. .... 95

Figure 4.10. Structural analysis of a substrate at the normal binding site. A) Movement of a bottom loop as indicated with an arrow during 0 ns -10 ns. 0 ns trajectory is brown in color and 10 ns are shown in blue color. B) Movement of the substrate away from the binding pocket during 90 ns – 100 ns. 90 ns trajectory is brown in color and 100 ns are shown in blue color. .... 96

Figure 4.11. MD simulation trajectory analysis of ligand 10195495 at the normal binding site. Movement of the ligand and loop residues (71-79) during 30 ns – 40 ns are depicted A) Superimposition of 30 ns (brown color) – 40 ns (blue color) snapshots indicating the

---

structural changes. **B)** Ligplot images generated at 30 ns and 40 ns to depict the movement of ligand and residues around the active pocket. .... 97

Figure 4.12. MD simulation trajectory analysis of the competo-allosteric site at 0 ns and 100 ns. Displacement of critical residue Cys146 from original position by 8.247 Å and change of Glu138 from loop to helices is depicted, while a ligand 10252273 is bound to the allosteric site. .... 100

Figure 4.13. Comparative MD simulation trajectory analysis of the competo-allosteric site and normal site at 100 ns. The back view of the protein is presented in a hydrophobic surface style presenting the complete binding tunnel in magenta color with two pockets. Displacement of critical residues Cys146 and Glu138 at the normal binding site after 100 ns is clearly depicted in the close view. The residue Cys146 moves towards the right side and Glu138 moves to the left side away from the normal binding pocket, thus widening the normal site..... 101

Figure 4.14. Analysis of the pocket dynamics in MD trajectories using TRAPP software. A) The reference structure (PDB code: 5wyb) and representative MD snapshots of the docked normal complex and the competo-allosteric complex are shown respectively. Residues (71 – 79) are shown in red, whereas sticks represent ligand bound at the normal site. Transient/conserved regions present in 50% of the simulation are represented in mesh scheme, whereas the pocket occurrence is shown in the solid scheme. B) Graph representing the opening of transient regions during MD simulations where column 2 represents the normal pocket, and column 3 represents the competo-allosteric pocket. C) The type of contacts that residues are making with the binding site during MD simulation d) Movement of the substrate away from the normal binding site during 100 ns simulation due to the flexibility of the side loop. .... 103

Figure 5.1: Workflow and tools used in the generation and validation of [BiR3(O2CR')2] force field parameters for TSA and TR of (T(SH)2) pathway. Semianario methods SBKJC ECP level of theory was employed to determine bong angles, bong lengths, and dihedrals for Models (1-3). For validation of geometric structures defining the coordination geometry of [BiR3(O2CR')2] models, all atom MD simulations were employed. .... 111

---

---

Figure 5.2: Synthesis of eight molecular geometries comprising Bi(V). Image sourced from our previous study <sup>285</sup> .....	113
Figure 5.3: Parameterization of Bi(V) Model-1 and Model 2 alongwith Sb(V) meglumine antimonite (C <sub>7</sub> H <sub>18</sub> NO <sub>8</sub> Sb) with Seminario approach. A-C) 3D representation of optimized geometries of Model-1, Model-2, and meglumine antimonite, respectively. The geometries are optimized with SBKJC basis set coupled with ECP level of theory. Graphs represent energy potential calculated with GAMESS-US demonstrating starting point with the lowest energy level (step) mentioned in each graph. ....	118
Figure 5.4: Calculation of RESP charges for Model-1 calculated with QM DFT methods using SBKJC ECP basis set. The metal center and interacting atoms are labelled. ....	119
Figure 5.5: Calculation of RESP charges for Model-2 calculated with QM DFT methods using SBKJC ECP basis set. The metal center and interacting atoms are labelled. ....	122
Figure 5.6: Calculation of RESP charges for meglumine antimonite (C <sub>7</sub> H <sub>18</sub> NO <sub>8</sub> Sb) calculated with QM DFT methods using SBKJC ECP basis set. The metal center and interacting atoms are labelled. ....	123
Figure 5.7: Visual inspection of active site of Trypanothione Synthetase-Amidase with sub-domains labelled. The crystal structure is depicted in grey surface whereas the Bi(V) bound complex after MD simulations is represented with brown surface.....	125
Figure 5.8: Visual representation of Arg569 and ligand dynamics during MD simulations of 1 $\mu$ s in complex with Model-1. A) snapshots taken at 10 ns, 100 ns, 500 ns, and 1 $\mu$ s depict movement of Model-1 from pocket S3 to S4. B) Representation of Arg569 at 10 ns, 100 ns, 500 ns, and 1 $\mu$ s exhibiting the role of Arg569 in modulating ligand dynamics. C) Snapshot taken at 10 ns with critical residues of protein and chains of Model-1 highlighted. D) Snapshot taken at 1 $\mu$ s depicting interaction of OH present at LIG604 of Model-1 with both Arg313 and Arg569. ....	126
Figure 5.9. Replica simulations for 1 $\mu$ s of both Model-1 and Model-2 in complex with TSA. Bismuth Model-1 stayed intact till the end of simulations while making strong	

---

interactions with OH of ligand and Arg313. Bismuth Model-2 however, exhibited similar ligand dynamics and shifted to nearby pocket S4. A) Root mean square deviation B) Root mean square fluctuations C) Beta-factor D) Radius of gyration..... 127

Figure 5.10: Trajectory analysis of Model-1 and Model-2 in complex with trypanothione synthetase-amidase carried out on 1  $\mu$ s MD simulations. A) Root mean square deviation B) Root mean square fluctuations C) Beta-factor D) Radius of gyration..... 128

Figure 5.11: A) Snapshots of Model-2 overlapped to depict the movement of a ligand from position S3 to S4. B) Interactions diagram of replica simulations at 1  $\mu$ s of Model-1 in complex with trypanothione synthetase-amidase. C) Interactions diagram of replica simulations at 1  $\mu$ s of Model-2 in complex with trypanothione synthetase-amidase. .... 129

Figure 5.12: Mutated models to understand the role of Arg569 in anchoring the bismuth models (1-3). A) Mutated Model-1 at 100 ns with single mutation of residue Arg569 to Glu569. B) Mutated Model-2 with 4 mutations at S4 pocket comprising Lys546, Tyr551, Phe328, and Leu543 including Arg569 at 100 ns. C) Mutated Model-3 with 4 mutations at S4 pocket comprising Lys546, Tyr551, Phe328, and Leu543 with Arg569 non-mutated. .... 131

Figure 5.13: Trajectory analysis of mutated models (1-3) in complex with trypanothione synthetase-amidase carried out on 100 ns MD simulations. A) Root mean square deviation B) Root mean square fluctuations C) Beta-factor D) Radius of Gyration..... 132

Figure 5.14. MD simulations analysis of pentavalent antimonial; Meglumine antimoniate in complex with trypanothione synthetase-amidase. A) RMSD B) Radius of gyration (Rg) C) AFD graph generated from trajectories of 100 ns MD simulations..... 133

Figure 5.15. Native contacts established by bismuth Model-1 and Model-2 with pockets of TSA at different time intervals of 1  $\mu$ s MD simulations. A) Interacting residues of both sites (S3 and S4) of TSA in complex with bismuth Model-1 at 10 ns, 100 ns, and 1  $\mu$ s. B) Interacting residues of both sites (S3 and S4) of TSA in complex with bismuth Model-2 at 10 ns, 100 ns, and 1  $\mu$ s..... 134

---

Figure 5.16. Radial distribution functions carried out on bismuth Model-1 and Model-2 at 10 ns and 1 $\mu$ s. A) RDF calculated for bismuth Model-1 with OH group present. B) RDF calculated for bismuth Model-2. ....	135
Figure 5.17. AFD results of Model-1 and Model-2 with trypanothione synthetase-amidase calculated over 1 $\mu$ s MD simulations each indicating period of positional shifts of Arg569. A) AFD of Model-1 at 10 ns, 500 ns, and 1 $\mu$ s. B) AFD of Model-2 at 10 ns, 500 ns, and 1 $\mu$ s.....	136
Figure 6.1. Workflow of the current study to identify potential phytochemicals against Covid19 drug targets from a list of known and social media acclaimed natural products. ....	144
Figure 6.2 3D-QSAR pharmacophore model of compounds comprising alkylated chalcones, phlorotannins, tanshinones, bioflavonoids, and flavonoids. <b>A)</b> 3D-QSAR pharmacophore exhibits four common features consisting of 1 hydrogen bond acceptor (HBA), 2 hydrophobic (HYD), and 1 ring aromatic (RA) <b>B)</b> 3D-QSAR pharmacophore model with distance between chemical features. <b>C)</b> The most active medicinal compound; xanthoangelol_E from the training set mapped with the highest FitValue of 4.36 <b>D)</b> The top compound, vilazodone mapped against 3D-QSAR pharmacophore with the highest FitValue of 3.56 from the test set. <b>E)</b> The second top compound lapitinib with a FitValue of 3.54 mapped against 3D-QSAR pharmacophore from the test set. ....	152
Figure 6.3. Common feature pharmacophore of <i>Senna</i> compounds A) Results exhibit four common features consisting of 3 hydrogen bond acceptors (HBA) and 1 ring aromatic (RA) features B) Common feature pharmacophore model with distance between chemical features. C) Isoquercetin mapped the common feature pharmacophore with highest FitValue of 0.99 from the training set. <b>D)</b> Compound with lowest FitValue. ....	154
Figure 6.4. Correlation graph in logarithmic scale for experimental values vs. predicted values of training and test ligands that mapped the 3D-QSAR pharmacophore model Hypo1.....	155

- Figure 6.5. A) Heat map generated by the ligand profiler for validation of common feature pharmacophore model No. 10 with the test set **B)** ROC curves generated for the validation of common feature pharmacophore model with the test set **C)** Logarithmic graph between estimated and experimental values of the training set and test set of common feature pharmacophore..... 157
- Figure 6.6 SARS-CoV-2 virion with the four selected proteins. The structure of virion is taken from <sup>343</sup>..... 158
- Figure 6.7. Preferred binding mode of active phytochemicals in the binding site of 3CL<sup>pro</sup> depicting two-dimensional (2D) docked complex with **A)** Xanthoangelol\_E having an IC<sub>50</sub> value 11.4 ±1.4 μM **B)** Hesperetin having an IC<sub>50</sub> value 8.3 μM **C)** Beta-sitosterol with an IC<sub>50</sub> value 1210 μM. .... 160
- Figure 6.8. Preferred binding mode of active phytochemicals in the binding site of 3CL<sup>pro</sup> depicting two-dimensional (2D) docked complex with **A)** Luteolin-7-O-glucopyranoside **B)** Calceolarioside\_B **C)** Isoquercetin. .... 161
- Figure 6.9. Preferred binding modes of sennosides docked with four essential proteins of SARS-CoV-2 depicting 2D binding interactions. **A)** 3CL<sup>pro</sup> **B)** Helicase nsp13 **C)** Spike protein-ACE2 receptor complex docked at two different sites **D)** RdRp nsp12..... 164
- Figure 6.10. Insights into the MD simulations of vizimpro, hesperetin, beta-sitosterol, and xanthoangelol\_E for the time period of 200 ns each complex. **A)** RMSD in complex with 3CL<sup>pro</sup> **B)** Radius of gyration **C)** RMSF of 3CL<sup>pro</sup> residues **D)** Beta-factor. .... 165
- Figure 6.11. MD simulations of beta-sitosterol exhibited strong electrostatic interactions and stable conformational dynamics with both the chains of dimer 3CL<sup>pro</sup>. .... 166
- Figure 6.12. MD simulations analysis of Hesperetin and Xanthoangelol\_E **A)** Hesperetin detached itself from chain A due to structural dynamics in its cavity but stayed intact with chain B till 200 ns as displayed in the top-right image. **B)** Xanthoangelol\_E exhibited the same behavior with the chain while displaying strong hydrogen bond interactions and

---

ligand movement deeper in the cavity of chain B till 300 ns, as presented in the bottom-right corner image. ....	167
Figure 6.13. <b>A)</b> MD simulations analysis of luteolin-7-O-glucopyranoside for 200 ns. Snapshots from 0 ns, 60 ns, and 200 ns are superimposed depicting an increase in RMSD due to the domain movement. <b>B)</b> MD simulations analysis of calceolarioside_B depicting ligand movement attempting to completely occupy the binding site thus leading to the increase in RMSD observed as a consequence of domain movement. ....	168
Figure 6.14. Insights into MD simulations of sennosides with <b>A)</b> 3CL <sup>pro</sup> , <b>B)</b> Spike-ACE2 with ligand attached at RBD, <b>C)</b> Spike-ACE2 with ligand attached at allosteric site, <b>D)</b> RdRp nsp12, and <b>e)</b> Helicase nsp13. ....	170
.....	173
Figure 6.15. AFD plots to compare point of coordinates and geometry between the active phytochemicals <b>A)</b> Hesperetin at 10 ns, <b>B)</b> Hesperetin at 200 ns, <b>C)</b> Xanthoangelol_E at 10 ns, <b>D)</b> Xanthoangelol_E at 200 ns, <b>E)</b> Vizimpro at 10 ns, and <b>F)</b> Vizimpro at 200 ns. ....	173
Figure 6.16. AFD plots to compare point of coordinates and geometry of <b>A)</b> Calceolarioside_B at 10 ns, <b>B)</b> Calceolarioside_B at 400 ns, <b>C)</b> Luteolin-7-O-glucopyranoside at 10 ns, and <b>D)</b> Luteolin-7-O-glucopyranoside at 200 ns. ....	174
Figure 6.17. Medicinal compounds disease-target-network. Red dots represent the five-screened active phytochemicals and yellow dots represent the drug targets common between the proposed active phytochemicals and Covid19. ....	178
Figure 7.1. Normal mode analysis (NMA) of Dynamut predicted comparative thermodynamic effect of mutations on stability and flexibility of spike protein of all VoCs. Differences in free energy ( $\Delta\Delta G$ ) and variations in vibrational entropy ( $\Delta\Delta S_{Vib}$ ENCoM) between the WT and other VoCs are mentioned from lowest to highest. ....	191

Figure 7.2. **A)** Intermolecular interactions of recently emerged mutations in Omicron with neighboring residues and solvent during 100 ns MD simulations **B)** Homologous and presumably constrained interacting residues among all VoCs exhibit significant interactions with induced mutations. (+/-) signifies the charge. **C)** Recently evolved mutations from cluster II reveal multiple interactions with neighboring residues **D)** Highly diverse group of residues prone to variations in all SARS-CoV-2 sublineages exhibit the capability to dramatically affect binding affinity. **E)** Intermolecular interactions of shared mutations among all VoCs with neighboring residues and solvent during 100 ns MD simulations where (w) represents interactions with water molecules..... 195

Figure 7.3. **A)** Comparative root mean square deviation (RMSD) of all VoCs and WT are represented by box plots. **B)** Snapshot of spike protein (green ribbon) exhibiting position of mutated residues at RBD (mutations belonging to different clusters are color coded) directly involved in making interactions with ACE2 receptor (grey surface) **C)** Comparative free binding energy profile of reported mutations at RBD **D)** Comparative PCA of Delta and Omicron mutation T478K exhibit opposite conformer distribution along the subspace **E)** Comparative PCA of Gamma, Delta and Omicron mutation E484/A/K exhibit varying conformer distribution along the subspace depending on the variant. .. 197

Figure 7.4. **A)** Comparative RMSD box plots of RBM of Delta, Omicron, and WT monomers **B)** Snapshot of spike protein (green ribbon) exhibit position of mutated residues at RBM critical for compact conformation of Omicron **C)** Comparative free binding energy profile of reported mutations at RBM **D)** Comparative RMSD box plots of mutated residues at fusion peptide site and HR1 along with insertion EPE lying at position 214 **E)** PCA of monomer Delta exploit different energy minima while sampling trajectories **F)** PCA of monomer Omicron sampling in completely opposite direction compared to Delta monomer. **G)** Comparative free binding energy profile of reported mutations at N-terminal, fusion peptide site and HR1..... 198

Figure 7.5. Conformational changes observed in different variants of spike protein during simulation run. **A)** WT trimer and **B)** Omicron trimer, highlighting receptor in green and the three RBD domains in orange, red and yellow. The ‘Up’ and ‘Down’ conformation of



---

RBD is visible while interacting with the receptor and during no interaction, respectively. **C)** WT trimer **D)** Omicron trimer zoomed in view to show the difference in structural compactness and stability. **E)** Comparison of structural and conformational changes that occur during the binding of Delta and Omicron variants to ACE2 receptor. Zoomed in view of superimposed RBD domain and HR1 peptide where purple surface depicts L452R. 200

Figure 7.6. Monomers at 100 ns simulation run each. Insets representing the diverse structural shifts and altered angles formed (RBD-HR1-NTD) in the variants that were triggered by ACE2 binding. Orange ribbon displays the receptor..... 201

Figure 7.7. Intermolecular interactions surrounding the ins214EPE in the WT spike protein after 100 ns of simulation run. **A)** ACE2 receptor is in surf representation in green whereas the rest of the monomer is in ribbon representation **B)** Zoomed in view of ins214EPE and interacting protein residues forming salt bridge and hydrogen bond interactions..... 202

Figure 7.8. Intermolecular interactions surrounding the ins214EPE in the Omicron spike protein after 100 ns of simulation run. **A)** ACE2 receptor is in surf representation in green whereas the rest of the monomer is in ribbon representation **B)** Zoomed in view of ins214EPE and interacting protein residues forming salt bridge and hydrogen bond interactions..... 203

---

## LIST OF TABLES

Table 2.1. Widely used consistent basis set developed by dunning and coworkers. ....	21
Table 2.2. Commonly used examples of split valence double zeta and minimal basis set. .....	22
Table 3.1: virtually screened non-covalent docking results from chembridge, zinc, and asinex library.....	47
Table 3.2: pka of all titratable residues computed with propka alongwith their residue name and number. Protonated and deprotonated his residues are mentioned accordingly. ....	50
Table 4.1. Admet and drug-related properties of top two ligand molecules of the normal and the predicted allosteric sites. ....	79
Table 4.2. Cavityplus scores representing the druggable binding sites of dsp. ....	82
Table 4.3. Differences in volume in the absence and presence of inhibitor at normal and competo-allosteric sites.....	82
Table 4.4. Interaction details of hydrogen bonding of docked complexes. ....	87
Table 4.5: mm/gbsa and mm/pbsa value for the docked trajectories of dsp at the normal site, the competo-allosteric site, and the substrate that has been used as a control. ....	104
Table 5.1: anti-leishmanial activity of bi(v) model-1 and model-2 with respective free binding energies. ....	112
Table 5.2. The lj parameters for three models (1-3) computed using mcpb.py with gamess- us. ....	116
Table 5.3: average bond length (Å) and average internal angles (°) calculated with <sup>1</sup> qm <sup>2</sup> dft methods using sbkjc <sup>3</sup> ecp basis set for the molecular models [biar3(o2cr)2] and meglumine antimonite (c <sub>7</sub> h <sub>18</sub> no <sub>8</sub> sb). ....	120
Table 6.1: statistical parameters of top 10 3d-qsar pharmacophore hypotheses generated using hypogen algorithm.....	151
Table 6.2: predicted and experimental ic <sub>50</sub> values of the training set compounds based on the 3d-qsar hypothesis 1 pharmacophore model.....	153

Table 6.3 statistical variations of common feature pharmacophore models.....	156
Table 6.4. Binding free energy and its components in mm/gbsa and mm/pbsa for the active phytochemicals, senna compounds, and vizimpro in complex with 3clpro, rdrp, and spike-ace2 proteins in kcal/mol. ....	172
Table 6.5. Admet properties of chemical compounds present in senna in comparison with the active phytochemicals and fda-approved drugs.....	176
Table 6.6 toxicity properties of chemical compounds present in senna in comparison with the active phytochemicals and fda-approved drugs calculated with topkat.....	177
Table 7.1: mutations in alpha, beta, gamma, delta, and omicron. ....	188

---

## SUMMARY

Drug resistance within a wide range of infectious agents has become a global menace, handling of which through the application of computational chemistry and molecular mechanics techniques is one of the possible solutions. Advancements in multidisciplinary field of computational chemistry have paved the way for computational scientists to take lead in exploring structural and dynamical attributes of various biological systems that play a significant role in addressing drug resistance. Furthermore, the contemporary headway in computational biology is primarily attributed to massive growth in data, power and its mammoth ability to predict multiscale modeling of complex biological phenomena. Subsequently, the improvement in computer speed and performance has permitted integration of advanced computational techniques such as hybrid quantum mechanical and molecular mechanical (QM/MM) simulations to elucidate intricate details of complex biological processes such as enzyme catalysis, protein ligand interactions, and binding and unbinding dynamics of a protein.

In line with the aim to materialize classical molecular dynamics and QM/MM simulations in response to drug resistance, this dissertation outlines the enormous potential of these methods particularly in connection with nosocomial infections. The first section of thesis is focused on the infections controlled by quorum sensing (QS), biofilm dispersion and transcription factors within *Pseudomonas aeruginosa*. The state-of-the-art QM/MM methods are employed to investigate the intricate details of covalent inhibition of target proteins that interfere with the defense mechanism of *P. aeruginosa*. Umbrella sampling (US) simulations at the DFTB3/MM level of theory are employed to propose a reaction mechanism with four potential covalent inhibitors. The potential of mean force reveals the direct role of intrinsic reactivity of inhibitors, for example inhibitors with methyl oxo-enoate warhead activate carbonyl samples in the first step of a reaction, which shed light on the significance of proton transfer indispensable for full inhibition. Whereas the nitrile inhibitor undergoes a stepwise mechanism with a small proton-transfer energy barrier and

lower imaginary frequencies that materialize instantly after nucleophilic attack. Furthermore, to unveil the molecular determinants of respective binding affinities, transition states along the reaction path are optimized and characterized with B3LYP6-31+G(d,p). This study serves as a preamble to add variation in the proposed structures and unveils the impact of functional groups lying in warheads that modulate the kinetics of proton transfer, which will certainly aid to design more selective and efficient irreversible inhibitors for bacterial transcription factors.

Under the same domain of addressing MDR through *P. aeruginosa*, a quorum sensing (QS) signal molecule is targeted with the primary objective to identify and propose competitive inhibitors for multiple sites within the same binding tunnel. This study not only adapts a broad-spectrum strategy for the lucid design of small molecule modulators but also provides novel allosteric inhibitors of the enzyme in hand. The term “competo-allosteric” is coined for the first time in this study, which entails the presence of competo-allosteric site in the same binding tunnel as the normal site competing for binding to similar residues.

Another contemplating resistance emerging nowadays is parasitic resistance which is another main focus of this work. This domain enlightens rapidly emerging drug resistance in leishmaniasis particularly to available treatment of antimonial (Sb) drugs and propose the computational design of alternate formulations encompassing relatively less explored functional metalloids. Large-scale atomistic simulations particularly with Au(I), Ag, Bi(V), and Sb(V) metalloids pose a major challenge to elucidate their molecular mechanism due to the absence of force field parameters. This study quantum mechanically (QM) derives force field parameterization of heteroleptic triorganobismuth(V) biscarboxylates. Findings from force field parameterization are simultaneously supported by the antileishmanial experimental study, results of which prove to be a preamble for successive QM treatment. Two organo-bismuth(V) carboxylates are modeled, which are optimized and parametrized along the famous pentavalent antimonial drug: meglumine antimoniate using QM original Seminario methods with SBKJC basis set coupled with effective core potential (ECP) level of theory. Findings underpin the role of bidentate chelating

behavior acquired by Bi(V) models on bond length that highlight the significance of OH group present at ortho position of sub-structure subsalicylate. This is preceded by atomistic simulations of bismuth and antimony containing compounds in complex with two enzymes, trypanothione synthetase-amidase (TSA) and trypanothione reductase (TR) to target the (T(SH)<sub>2</sub>) pathway at multiple points. MD simulations provide novel insights into the binding mechanism of both enzymes and highlight the role of active site residues in modulating ligand dynamics. Moreover, the presence of an ortho group in ligand is emphasized to facilitate interactions for higher inhibitory activity of enzymes. This preliminary generation of parameters specific to bismuth validated by simulations in replica will become a source of further in future computational and experimental research work to open avenues for newer and suitable drug targets.

The final section of this work is categorically focused on Covid19 pandemic with the aim to identify appropriate choice of inhibitors to curb this deadly viral infection and bring to light alternative methods that would address the existing problem of drug resistance. In this respect, with the aim to contribute to scientific research community in the challenging times of Covid19 pandemic, this study pulled efforts to bring awareness to public as a matter of global dissemination that resorted to excessive use of herbal tea “*Senna Makki*” in treatment of Covid19. There has been a myth regarding the use of famous *Senna* Tea in treatment of Covid19, overdose of which led to diuresis and death of many patients unknowingly within the paraphernalia of this pandemic. Under this domain, the binding potential of chemical compounds of *Senna* in comparison with the experimentally tested active phytochemicals against SARS-CoV-2 protein targets are investigated. The entire set of phytochemicals from both the groups are subjected to 3D-QSAR modeling followed by MD simulations with multiple SARS-CoV-2 target proteins namely; the spike protein, helicase nsp13, RdRp nsp12, and 3-Chymotrypsin-Like Protease (3CL<sup>Pro</sup>). Findings manifest the importance of hydrophobic substituents in chemical structures of potential inhibitors through cross-validation with the FDA-approved anti-3CL<sup>Pro</sup> drugs. Noteworthy improvement in end-point binding free energies and pharmacokinetic profiles of active phytochemicals is perceived in comparison to the

control drug, Vizimpro. However, *Senna* metabolites in comparison exhibit weak binding affinity, instability and toxicity against all drug targets. Findings contravene fallacious efficacy claims of *Senna* tea interventions circulating on electronic/social media as Covid19 cure and discredit the use of *Senna* tea as whole with all its chemical constituents in Covid19 treatment. This emphasizes the importance of well-examined standardized data of the natural products in hand; thereby preventing unnecessary deaths under pandemic hit situations worldwide.

Additionally, the comparative MD simulations analysis is carried out on SARS-Cov-2 Omicron variant and its highly transmissible sublineages that undergo mutations to mitigate antimicrobial resistance. This work is in connection with the viral architecture or changes in viral structural attributes due to mutations and propose their potential effects on stability and transmission of the virus. A thorough investigation on Omicron and other variants of concern (VoC) namely Alpha, Beta, Gamma, Delta, and Omicron reveal the role of hydration forces in mediating function and dynamics based on a stronger interplay between protein and solvent. Mutations of multiple hydrophobic residues into hydrophilic residues trigger concerted interactions with water leading to variations in charge distribution during MD simulations. Moreover, comparative analysis of interacting moieties characterize a large number of mutations lying at RBD into constrained, homologous and low-affinity groups referred to as mutational drivers inferring that the probability of future mutations relies on the function of these residues. Furthermore, the computational findings reveal a significant difference in angular distances among variants of concern due 3 amino acid insertion (EPE) in Omicron variant that not only facilitates tight domain organization but also seems requisite for characterization of mutational processes. The outcome of this work signifies the possible relation between hydration forces, their impact on conformation and binding affinities, and viral fitness that will significantly aid in understanding dynamics of drug targets for Covid-19 countermeasures.

The overall concurred outcome of this dissertation in reference to integration of QM/MM methods reaffirm role of computational modeling in yielding intricate

details about processes like proton transfer, role of well-optimized coordination geometry of metal ions, and other important structural and dynamical attributes of biomolecules. These instrumental phenomena are of utmost medicinal importance that can impact ARM/drug resistance if applied in the context of biologically relevant enzymes.



---

# **CHAPTER 1**

---

## **BACKGROUND AND MOTIVATION**

## 1. BACKGROUND AND MOTIVATION

### 1.1 Drug resistance in antimicrobials

Drug resistance in a broader perspective directly impacts the ability of antimicrobial agents to treat fatal diseases, post-surgical infections multiple cancer treatments alongwith other debilitating diseases<sup>1</sup>. Drug resistance drastically undermines the effectiveness of antimicrobial agents and pose a serious threat to public health globally that prompts uncontrolled resistance in micro-organisms. According to the definition of antimicrobial resistance (AMR) by World health organization (WHO), it is the inability of antimicrobial drugs to respond to bacterial, fungal, or viral infections due to acquired or intrinsic resistance. Multiple breakthrough antimicrobial agents encompassing antibiotics, antifungals, and antivirals are experiencing multi-drug resistance (MDR) to high priority infections that created havoc worldwide<sup>2</sup>. MDR infections surface when resistance to more than one antimicrobial drug is exhibited by an organism, which is alarming to greater extent since majority of third and fourth generation antibiotics are experiencing MDR<sup>3-6</sup>. According to WHO, antimicrobial treatment is inconceivable in the absence of effective antimicrobial agents that could lead to more than 10 million deaths annually by 2050 if left unaddressed<sup>7,8</sup>.

#### 1.1.1 Factors contributing to AMR

There are various factors that intensively contribute to AMR. Acquisition of AMR genes are commonly associated with multiple factors such as (i) drug transport through horizontal gene transfer, (ii) target modification as a result of mutations, and (iii) drug inactivation by enzymatic activity of microbes<sup>9,10</sup>. Microbes encompassing bacteria, fungi, and viruses have multiple ways to build up intrinsic resistance; mostly evolutionary processes, to protect themselves whenever they encounter threat or stress, thus modulating their mechanism in response to environmental conditions<sup>11</sup>. Mutagenesis is one of multiple competing factors of intrinsic resistance that incorporates changes in genetic makeup leading to enhanced virulence in microbes<sup>12-15</sup>. Another reason in rapid spread and evolution of drug resistance is reticulated dynamics of human and healthcare systems that

leads to acquired AMR due to poor waste management, overuse, and misuse of antibiotics<sup>16-19</sup>.

### 1.1.2 Consequences of AMR

Consequently, organizations like WHO and Centers for Disease Control and Prevention (CDC) have been concerted raising awareness by monitoring and reporting emergence of AMR worldwide<sup>20-22</sup>. Multiple reports on clinically resistant strains that encompass *Escherichia coli*<sup>23,24</sup>, *Klebsiella pneumoniae*<sup>25,26</sup>, *Staphylococcus aureus*<sup>27</sup>, and *Mycobacterium tuberculosis*<sup>28</sup> estimate that more than 50% strains are resistant to first generation antibiotics. Furthermore, resistance to second-line drugs in strains of *M. tuberculosis* are also witnessed in India and South Africa, which depicted lesser efficacy and resistance to broad spectrum antibiotics to treat tuberculosis related infections<sup>29,30</sup>.

Furthermore, antibiotic stewardship has predicted AMR to coincide with Covid19 pandemic mortality rate presenting itself as an unprecedented challenge for health care systems globally, which have already laid out hefty investments in vaccine development, drugs repurposing and discovery of novel antivirals<sup>31-33</sup>. Noticeably, Covid19 has radically hampered the use of antibiotics and contributed to ongoing rise of AMR due to cotreatment of secondary infections acquired from hospital settings that largely affected immunocompromised patients<sup>34,39</sup>. Similarly, resistance to antifungals that cause an estimated 700,000 or more cases annually threatens the prevention and treatment of antifungal infections, which needs to be counteracted to lift the economic burden and adverse societal consequences<sup>40-42</sup>.

### 1.1.3 Halt in drug discovery

In that respect, concerted efforts in design and development of effective drugs are required to overcome the emergence of AMR that has outpaced drug discovery due to limitations of investment in research and pharmaceutical industry. Unfortunately, due to dearth in development of antimicrobial drugs despite the availability of around 4,000 therapeutic agents, only 30 - 40 % have made it to the clinical trials, which cannot counteract rise of AMR<sup>43-45</sup>. The overlooked aspect of concern is that only 25% of these drugs target a novel mechanism or offer a novel class<sup>45,46</sup>. In these challenging times, fastest way to curb AMR

and revolutionize drug development is to bring researchers or skilled practitioners from research/academia and medicinal chemistry together. They can collectively design, assemble, and curate large libraries of compounds and aid in devising new strategies and fabricated therapies.

### **1.1.4 Methods to control AMR**

Prerequisite to development of modern medicine amidst AMR directs to materialize methods that not only cater resistance in response to drugs but also target novel mechanism of action to avoid cross-resistance with drugs already in use. Generally, the convergent approach to classify antimicrobial compounds is: (i) to target essential enzymes that are significant for bacterial life cycle, or (ii) target non-essential enzymes crucial for regulating virulence or defense mechanisms of organisms<sup>47-49</sup>. Aiming at antivirulent targets is a new strategy that rather interferes with virulent pathways and defense mechanisms and deactivate the pathogen instead of effecting its growth and sustainability, thus providing milder possibility of evolutionary resistance. Thus, compounds designed for non-essential pathways with existing knowledge about molecular pathogenesis of microbes target different classes of enzymes and are referred as: (i) virulence factor inhibitors or pathway blockers that are specifically designed to target quorum sensing systems, and biofilm formation, (ii) pathway inhibitors involved in regulation of stress modulation as a mechanism of host defense mechanism, and (iii) modulators/inhibitors of metabolic pathways<sup>49-51</sup>. Most of these targets while expending non-traditional approaches in disarming MDR pathogens have exhibited their capability to reverse resistance to some antimicrobials<sup>52</sup>. Similarly, pathway inhibitors have proven less susceptibility to resistance in high priority MDR pathogens particularly Gram-negative bacteria *Pseudomonas aeruginosa*, thus acting as valuable therapeutic targets with less potential to either intrinsic or evolved resistance<sup>53</sup>.

## **1.2 Role of molecular mechanics (MM) in drug discovery**

Application of computational techniques in the field of medicinal chemistry has been validated by numerous recent accomplishments. In microbiology, the availability of crystallographic structures of many pharmacologically relevant proteins makes the use

of *in silico* simulations, an increasingly powerful methodology to fight MDR pathogens. This is a multidisciplinary perspective that includes approaches from computational biology, chemistry, and biophysics. Classical molecular dynamics (MD) simulations, pioneered by Warshel and Levitt and Karplus and McCammon are well-known for analyzing motion of atoms/molecules of biological systems with respect to Newton's law of motion. Starting from drug discovery as early as 1994, it has been implemented in several successful studies including G-protein-coupled receptors, and protein kinases. One of the recent example is the implementation of artificial intelligence (AI) in prediction of three-dimensional (3D) protein structures using AlphaFold that will accelerate research in nearly every field of biology<sup>54</sup>

Moving beyond the classical MD simulations, past two decades have presented multiple powerful methods such as quantum mechanics (QM) combined with molecular mechanics (MM) with the ability to predict discrete mechanisms such as binding and unbinding of drugs and allosteric modulation through evaluation of their kinetic and thermodynamic properties. QM/MM combined with enhanced sampling techniques such as steered molecular dynamics, meta dynamics, replica exchange, thermodynamic integration (TI), and umbrella sampling (US) have drastically fast-paced drug discovery programs in terms of time and accuracy. Outcome of these approaches were apparent in pandemic-hit situation when multiple studies surfaced with productive results to refine drug discovery such as researchers of Oak Ridge National laboratory used Schrodinger equation to predict key binding site of S-protein<sup>55</sup>.

### **1.3 Aims and objectives**

Within the paradigm of current work, we outline the enormous potential of classical MD simulations in understanding complex allosteric mechanism in drug discovery and QM/MM methods to decipher kinetics of drugs and metalloids. This work thus demonstrates multiple strategies and novel therapeutic options expended in the consortium to ensure a sustainable flow to target antimicrobial drug candidates. Topics which lay the foundation of this thesis are listed below which are discussed in detail in forthcoming chapters:

- i. allosteric inhibition of bacterial quorum-sensing (QS) signaling systems

- ii. covalent inhibition to unveil molecular mechanisms of bacterial defense mechanisms using QM/MM
- iii. QM optimization of metalloids with novel geometries to address drug resistance in leishmaniasis
- iv. screening of active phytochemicals against SARS-CoV-2, and
- v. comparative mutational analysis of Covid19 Omicron and other variants.

Chapter 3 and 4, investigate bacterial proteins within *P. aeruginosa* that control bacterial defense mechanism and bacterial quorum sensing. Given the significance of aforementioned bacterial processes in antibiotic resistance, production of biofilm and instigating resistance in *P. aeruginosa*, interference in these system is therefore, an attractive strategy to repress AMR<sup>56,57</sup>. Chapter 3 emphasizes on combinatorial approach targeting transcription factor enzymes with covalent inhibition approach. Example of highly sensitive and selective transcription factor sensor, which holds cysteine in its active site is KatA, responsible for acute intrinsic resistance in *P. aeruginosa*<sup>58,59</sup>. In this connection, bacterial transcriptional factor OxyR that is a sensor of hydrogen peroxide is targeted for inhibition studies under the umbrella of QM/MM simulations. QM/MM coupled with US approach propose irreversible covalent inhibitors with varying chemical environments and assess the impact of warhead modulation on binding catalysis of OxyR.

The primary objective of the subsequent study in chapter 4 however, is to identify competitive allosteric inhibitors against QS signaling molecule; DSPI of *P. aeruginosa*. In addition to targeting the noxious mechanism of bacterial resistance, an alternative inhibition strategy; allosteric inhibition provides an effective avenue for selective and potent inhibition. Allosteric inhibitors when combined with orthosteric drugs in literature revealed suppressed mutation resistance and exhibited the capability to synergistically overcome emergence of drug resistance in multiple MDR pathogens<sup>60,61,62</sup>. This work thus; employs allosteric inhibition, which has allowed us to classify both normal binding site and allosteric inhibitors using techniques of molecular mechanics (MM). It concurs that widening phenomenon and disruption of the normal binding site and inhibition of allosteric site at the cost of the normal binding site are significant and noticeable outcomes.

Chapter 5 addresses the investigation into rapidly emerging drug resistance among parasites that has drastically limited the treatment options resulting in more than 500,000 cases annually<sup>63-65</sup>. According to WHO, protozoan parasitic diseases from the genus *Trypanosoma* and *Leishmania* particularly visceral leishmaniasis VL, has reportedly caused more than 90% new cases in 2020<sup>42,65</sup>. However, frequently available treatment to leishmaniasis comprise antimonial drugs that target precarious metabolic pathways involved in AMR. Substantial role of metabolic pathways in myriad of reactions comprise defense against oxidative damage, redox, homeostasis and replication<sup>66</sup>. Despite the growing demand of molecular investigations with metalloids, particularly antimonial drugs, these compounds are not fully characterized in computational analysis due to the absence of force field parameters. In the midst of emerging resistance to antimonial drugs, the intention of this work is to investigate metalloids lying right below Sb according to the periodic table. This work therefore quantum mechanically generates force field parameters of both bismuth and antimony metalloids and provide optimized geometries and topology files for classical MD simulations. Parameterization at the hub of an inorganic metal centers and specifically bi-inorganic complex will give rise to further parameterization of new metals of biological relevance and can be considered as baseline importance of this work. In a broader context, this work will aid in inhibiting parasitic redox metabolism and the infectious period of pathogenic trypanosomatids, with lesser chances to develop AMR.

Last two chapters; chapter 6 and 7 are categorically focused on Covid19 with the aim to identify appropriate choice of inhibitors to curb this deadly viral infection and bring to light alternative methods that would not aggravate the existing problem of drug resistance. In the desperate times of Covid19 pandemic, excessive use of antibiotics to treat secondary infections hampered the regulation of AMR alongwith the uncontrolled rise in alternative treatment options. Role of natural products was therefore endorsed by WHO and several other studies, which emphasized on incorporating natural products as an alternative treatment in Covid19 with lesser probability to resistance<sup>67-69</sup>. Natural products that comprise antimicrobial properties can significantly contribute to reversing antibiotic resistance by interfering with multiple molecular processes such as cell signaling. Chapter six on Covid19 however, after thorough investigations carefully distinguish the scientifically proven active phytochemicals from harmful medicinal plants that can rather

aggravate the already frightful situation. Whereas, the last chapter 7 provides structural and dynamical insights of evolving mutations of SARS-Cov-2 Omicron variant and its highly transmissible sublineages.

The more in-depth explanation and methodological protocols of topics discussed above are included in their respective chapters. However, the background and theoretical overview of QM/MM and MD simulations are expended in second chapter of this thesis.



---

## **CHAPTER 2**

---

# **COMPUTATIONAL AND THEORETICAL OVERVIEW**

## 2. COMPUTATIONAL AND THEORETICAL OVERVIEW

### 2.1 Molecular modeling

To elucidate relationship between any molecule with its biological activity, it is imperative to accurately identify and understand the basis of interactions established between molecule and its site of action. Molecular modeling at any given time relies largely on conformational geometries and its ability to acquire specific attractive or repulsive interactions or both to successfully predict approximate binding affinity between two molecules<sup>70,71</sup>. Molecular modeling methods and tools rely on small atomic molecular level properties to govern microscopic and macroscopic behaviour of physical systems such as hydrogen bonding, electrostatic interactions, bond-lengths, dihedrals, van der Waal (vdW), and hydrophobic interactions<sup>72,73</sup>. Last two decades have witnessed enormous growth of coherent computational methods in the field of drug design that are aimed at designing and optimizing specific lead molecules for a given 3D structure of a protein. For instance, 3D quantitative structure-activity relationship (QSAR) encompassing necessary ensembles of structures and molecular descriptors is capable of drawing a biological response between a given set of molecules<sup>74,75</sup>. Similarly, articulated methods like allosteric and covalent modification of proteins are integral phenomena that grant complete control of biological function by modifying structural properties in a way that respective thermodynamic ensembles of systems are completely altered<sup>76-78</sup>.

Despite enormous progress in this field, it is still difficult to exactly elucidate binding mechanism of two molecules especially when dealing with metal moieties. However, in an attempt to provide complementary approaches to experiment, recent breakthroughs in development of multiple mathematical models based on molecular physics and biophysics such as X-ray crystallography and nuclear magnetic resonance (NMR) has enabled dynamic studies between macromolecules. Such analysis cannot only predict multiple ensembles of structures but can also model impact of interactions that have established between molecular partners in solution by allowing complete degree of freedom. Computational methods like MM and QM can efficiently relate biological activity to structure by optimizing relevant geometries and parameterizing the molecule by

computing potential energy of constituent atoms<sup>79,80</sup>. Current resources of high-speed computer processors have enabled micro to milli nanoseconds simulations of ionic solution, proteins, and other macromolecules to probe into distribution of multiple conformational states and provide relevant information about thermodynamics and kinetics of any given system. In this context, multiscale simulations independent of time evolution first proposed by Metropolis and coworkers, characterized statistical ensembles of a given state; known as Monte Carlo (MC) simulations<sup>81,82</sup>. Whereas, groundbreaking approaches proposed by a Noble Prize winner, Michael Levitt, and coworkers, estimated dynamics of a system over a period while employing Newton's second law of motion<sup>83</sup>. However, to achieve higher accuracy for description of chemical and physical phenomena, the use of QM approaches is pursued. QM methods take into account the polarization effects, proton transfer, and most importantly, model chemical reactions capable of depicting effect of charge transfer that is otherwise typical to explain using other methods like MM<sup>79,84,85</sup>. The schematic representation of evolution of multiple simulations methods is presented in **Figure 2.1**

Nevertheless, the basic theme of this chapter is to provide a brief overview of computational techniques employed to investigate the structure and dynamics of multiple systems and introduce theoretical principles working behind them. Various methods encompassing metal ion modeling, protein modeling to examine the effect of mutations, MD simulations and QM methods are explained in forthcoming sections alongwith tools used to obtain valuable results.

## 2.2 Quantum mechanics

Quantum mechanics is a pillar of theoretical chemistry that has significantly aided in exploration of small objects of nanometer of size. These methods have the ability to supersede experimental techniques in delivering intricate information about molecular geometries, compounds with transition metal ions, vibrational frequencies, ionization potential, electronic structure configuration including sensitivities of electron correlation energies. Whereas, classical mechanics is preferred for large objects to act according to the Newtonian mechanics best suited for exploring conformational space. Though, quantum chemical methods are computationally expensive while at the same time hybrid QM/MM

approaches utilizing the affordability of MM along with accuracy of QM has revolutionized the subjective exploration of biomolecules. Density function theory (DFT) both as extension and semi-empirical method have exhibited capabilities generally in addressing proteins and specifically in complicated arena of force field parameterization<sup>79,84</sup>. Under this era, commonly utilized software packages that employ QM are GAMESS-US, Gaussian, GROMACS, ORCA, Avogadro etc.

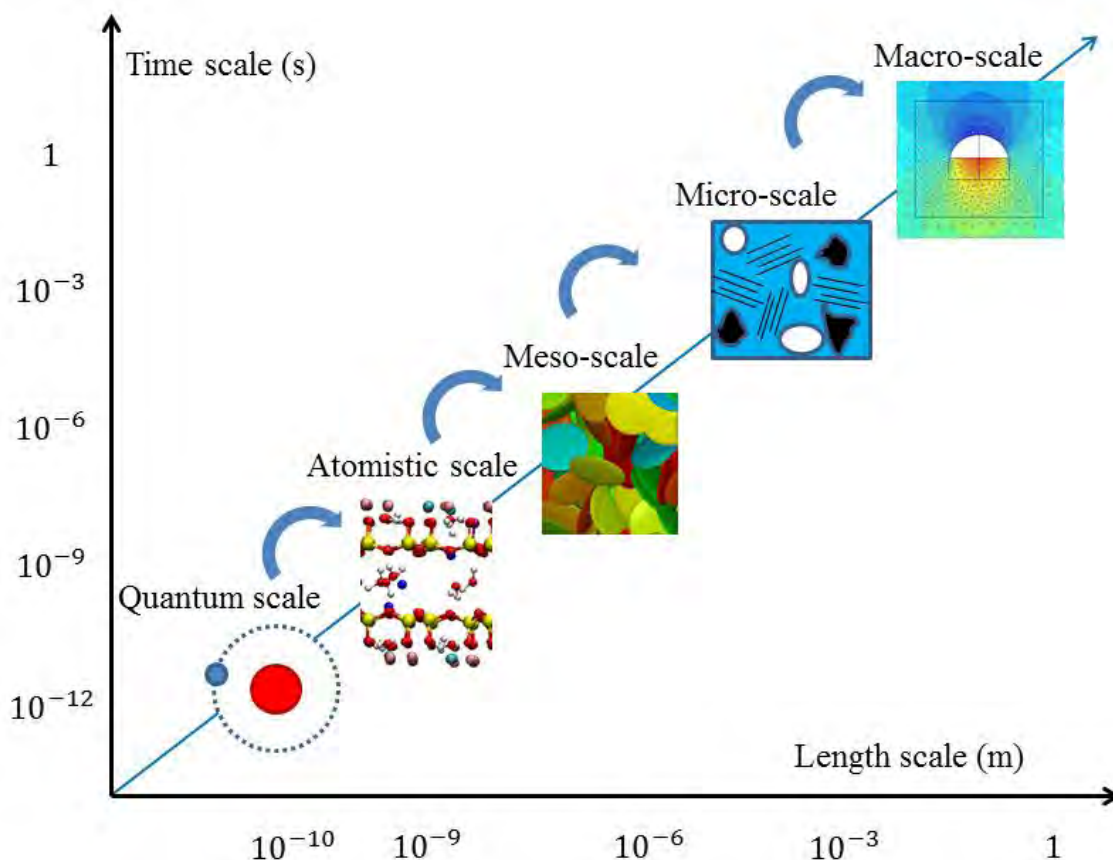


Figure 2.1. Schematic representation of evolution of multiple simulations methods.

Unlike classical mechanics that was unable to explain certain experimental properties like hydrogen spectrum emission and levels of quantized electrons with Newton's law of motions, an improved way for explaining movement of electrons emerged in 20<sup>th</sup> century. Concept of wave mechanics surfaced that rather dealt with particle travelling as a wave than a finite particle moving across the definitive path in a straight

line<sup>86,87</sup>. QM describes these dynamical properties based on probability functions to describe the position of a particle in space using Schrödinger equation.

### 2.2.1 Schrödinger equation

The conceptual understanding of QM is based on the postulates of Max Planck dated back to 1900 that proved that energy levels of electrons are quantized, which occurs in discrete unit called “quanta”<sup>8889</sup>.

$$E = h.v \quad (2.1)$$

where h is referred as Planck’s constant based on his contributions. However, Schrodinger equation derived from this model by an Austrian Physicist Erwin Schrödinger was a breakthrough in the field of QM and theoretical chemistry<sup>90</sup>. All the properties of the system were determined using time-independent function called “probability function” or wavefunction denoted as ‘ $\Psi$ ’, where  $\hat{H}$  is the Hamiltonian operator, and E is the energy.

$$\hat{H}\psi = E\psi \quad (2.2)$$

When dealing with N number of particles, both kinetic (T) and potential (V) energy constitute the Hamiltonian operator with respect to variables (r). The expanded form of Hamiltonian term is then calculated using approximate values of all particle coordinates while employing second-order fractional derivative equation, illustrated in equation given below:

$$\hat{H} = - \sum_{i=1}^N \frac{\hbar^2}{2m_i} \nabla_i^2 + \sum_{i \neq j}^N V_{ij} \quad (2.3)$$

where m is the mass of a particle (e.g. electron),  $V_{i,j}$  is the potential energy between two particles, and  $\nabla_i^2$  is Laplacian operator acting on particle i. The Laplacian operator is a scalar differential operator expressed as:

$$\nabla_i^2 = \frac{\partial^2}{\partial x} + \frac{\partial^2}{\partial y} + \frac{\partial^2}{\partial z} \quad (2.4)$$

Noticeably, Schrödinger solution exists for one-electron system such as hydrogen atom where the electromagnetic interactions between two particles (nuclei-electron and electron-electron) are calculated. However, for molecular systems, it can be numerally solved using methods like *ab initio* and/or semiempirical. Numerous approximation

methods have been solved using Schrödinger equation so far such as Born-Oppenheimer approximation, Hartee-Fock (HF) theory, and DFT. The forthcoming section, however, will discuss DFT in detail, which is employed in the current study.

### 2.2.2 Density function theory (DFT)

DFT method is preferred over HF while dealing with larger systems like proteins and systems containing metal ion transition states. DFT obtains ground-state energy and relate properties using molecular density  $\rho$ . It was first conceptualized by Thomas and Fermi who demonstrated compliance between molecular electron density and the wavefunction<sup>91</sup>. However, this theory was later upgraded in 1964 by Hohenburg and Kohn<sup>92</sup>, who proposed two theorems to overcome poor representation of properties like molecular bonding and kinetic energy defined previously and rather treated the electron energy as a function of electron density defined as:

$$E[\rho(r)] = \int V_{ext}(r) \rho(r) dr + F[\rho(r)] \quad (2.5)$$

In the above equation, external potential  $V_{ext}$  defines the interactions of the electrons whereas the right-hand-side illustrates the sum of the kinetic energy of the system combined with interatomic interactions<sup>93</sup>. However, F in this equation represents Kohn and Sham theory expanded below:

$$E[\rho(r)] = E_{KE}[\rho(r)] + E_H[\rho(r)] + E_{XC}[\rho(r)] \quad (2.6)$$

$E_{KE}$  and  $E_H$  are described in equation 2.7 and 2.8, where density is defined according to Kohn-Sham orbitals, thus defining the kinetic energy  $E_{KE}$  and the coulomb energy  $E_H$  of orbitals.

$$E_{KE}[\rho(r)] = \sum_{i=1}^N \int \Psi_i \left(-\frac{1}{2} \hat{\nabla}^2\right) \Psi_i(r) dr \quad (2.7)$$

$$E_H[\rho(r)] = \frac{1}{2} \int \int \frac{\rho(r_1)\rho(r_2)}{|r_1 - r_2|} dr_1 dr_2 \quad (2.8)$$

The last term  $E_{XC}$  component given in equation 2.6, however, is not categorically defined and therefore is the source of problems encountered while approximating calculations. There are several approximation operators to address the this problem who can efficiently integrate inter-electronic contribution to the kinetic energy namely, local

density approximations (LDA)<sup>94</sup>, Generalised gradient approximation (GGA)<sup>95</sup>, and *hybrid functionals*.

### 2.2.3 B3LYP

Commonly used hybrid functionals are B3LYP that works by combining exchange energies such as  $E^{\text{LSDA}}$ ,  $E^{\text{HF}}$  and Delta  $E^{\text{B88}}$  with the correlation energies  $E^{\text{LYP}}$  and  $E^{\text{VWN}}$  given below:

$$E_{rc}^{\text{B3-LYP}} = (1 - a_0)E_x^{\text{LSDA}} + a_0E_x^{\text{HF}} + a_x \Delta E_x^{\text{B88}} + a_cE_c^{\text{LYP}} + (1 - a_c)E_c^{\text{VWN}} \quad (2.9)$$

A hybrid function illustrated by Becke<sup>96</sup>, and Lee, Yang and Parr<sup>97</sup> is a standard model used in multiple application of chemistry. B3LYP incorporates various approximations where parameters ( $a_0$ ,  $a_x$  and  $a_c$ ) have been determined by least-squares fitting mapped to the test set comprising multiple small molecules. However, key problem arises while selecting an appropriate method for optimization whereas another debate originates when semiempirical approaches are applied for parameterization, which yield unknown amount of electron calculations. The B3LYP extension was utilized for better results specifically in averaging densities under the domain of biomolecules and explaining metal transitions states to define quantum mechanical region.

### 2.2.4 Basis set

Presentation of a basis set in approximation of Schrödinger equation is fundamental, which represents a set of one electron functions composed of finite number of atomic orbitals that lie in the atomic nuclei within the molecule. Commonly used basis set to treat atomic orbitals are Gaussian-type orbitals (GTOs) and Slater-type orbitals (STOs). STOs is the most natural way to describe atomic orbitals that relies on solution to Schrödinger equation and corresponds to set of functions that decay exponentially with distance from nuclei<sup>98</sup>. STOs gives optimal results if used on atomic orbitals located on the same atom. Whereas GTOs are comparatively less accurate but work well if atomic orbitals are based on different atoms. GTOs accuracy can be achieved by employing extended number of functions to the orbitals in each atom, known as minimal basis set. Notation originating from John Pople is **X-YZg** where **Y and Z** represent valence orbitals based on two functions and **X** indicates the number of Gaussian comprising basis set to implement higher

momentum functions. Both these basis sets are extended forms of most widely used basis sets developed by Dunning and coworkers called correlation consistent basis set.<sup>99,100</sup> Some of the examples are given in Table 2.1.

Table 2.1. Widely used consistent basis set developed by Dunning and coworkers.

Basis set	Explanation
<b>cc-pVDZ</b>	cc-p refers to correlation consistent polarized, V means Valence and DZ stands for double-zeta
<b>cc-pVTZ</b>	cc-p refers to correlation consistent polarized, V means Valence and TZ stands for triple-zeta
<b>cc-pVQZ</b>	cc-p refers to correlation consistent polarized, V means Valence and QZ stands for Quadruple-zeta
<b>aug-cc-pVDZ</b>	Augmented basis sets with added diffuse functions

Whereas, minimal basis set is represented as **STO-XG** where **X** refers to an integer. Despite computationally cheaper than its counterparts, minimal basis set provides insufficient results lacking research-quality publication<sup>101</sup>. On the contrary, split valence basis set implements polarization function that treats valence electrons of inner shell separately with single functions, hence the reason they are called split valence basis set, which are constantly evolving<sup>102,103</sup>. Commonly used examples of split valence double zeta and minimal basis set are illustrated in Table 2.2. If a basis set doubles the number of functions in minimal basis set, they acquire the form of double zeta basis. Increasing the number of functions to doubles or triples clearly indicate much better description of varying electron distribution in a certain direction.

### 2.2.5 Effective core potential (ECP)

Furthermore, the systems with higher period number such as transition metals from third and fourth row according to the periodic table are treated with an effective core potential (ECP). ECP provides an alternative solution to otherwise poorly characterized basis set due to realistic effects. Because inner electrons do not directly contribute to predicting chemical properties of heavy atoms, the basis set is required for valence electrons alone. These inner electrons are replaced by ECP thus disregarding the need for core basis function that needs larger sets of Gaussian. The best results in terms of accuracy and period, however, can be



acquired by the inclusion and combination of ECP and standard zeta, or polarization basis sets<sup>103,104</sup>.

Table 2.2. Commonly used examples of split valence double zeta and minimal basis set.

<b>Minimal basis set</b>
<b>STO-2G</b>
<b>STO-3G</b>
<b>STO-6G</b>
<b>Split valence basis set</b>
<b>3-21g</b>
<b>3-21+g</b>
<b>3-21+g*</b>
<b>6-31g*</b>
<b>6-31g*</b>
<b>6-311G(d,p)</b>

In this work, a split valence basis set 6-31+G(d,p) and SBKJC basis set derived by Stevens and coworkers encompassing the valence double-zeta potential set coupled with ECP has been employed<sup>105</sup>. SBKJC particularly deals with large sets of systems comprising elements of higher period number covering atoms from mostly group 14-17 (C-Sn, N-Sb, O-Te, and F-I). Whereas, 6-31+G(d,p) is a higher order basis set capable of yielding better results with polarization functions included to treat chemical bonds and long-range interactions efficiently in the presence of diffuse functions (+). This basis set with (d,p) indicates that it will treat heavy atoms with first function and hydrogen atoms exclusively with second function. Additionally, DFT method DFTB3 is employed in QM/MM US study of covalent inhibition. However, to address a large part of our molecule in production run especially out of the active site is usually treated by molecular mechanics approaches.

## 2.3 Molecular mechanics

It is apparent from the aforementioned discussion and theories that to determine any model using either MM or QM methods, accurate force field (FF) parameters are necessary to define interatomic forces acting upon a particle at any given time. MM approaches are

preferably used to elucidate structural properties of large systems including metalloproteins, which employ classical mechanics to calculate potential energy of the system. Energy of the system is derived from a series of empirical parameters defined as a function of nuclear positions typically described as FF parameters. FF parameters are usually generated for two well-known interactions namely, bonded, and non-bonded interactions<sup>106,107</sup>. Commonly used FF parameters include bond, angles, torsion angles, dihedrals etc. calculated for bonded interactions, which are available in software packages like AMBER and CHARMM. Non-bonded interactions however constitute vdW and electrostatic interactions that are calculated using 12-6 Lennard Jones or a combination of Coulomb equation and 12-6 Lennard-Jones potential<sup>108-110</sup>. Despite the presence of these widely used methods, their accuracy and applicability are questionable while implying metals in bioinorganic. However, there are several approaches now available to overcome these limitations illustrated in **Figure 2.2** such as representation of the metal ion as soft-sphere that employs Lennard-Jones potential, treat non-bonded model as dummy atoms, or use harmonic function for bonded models. While bonded models can be efficiently treated with QM approaches, MD simulations provide finest structural and dynamical insights of large molecular system, by calculating potential energy of all forces acting on non-bonded models. Theoretical background of principles of MD simulations that shed light on various ensembles, algorithms used for integration and vice versa are described in detail.

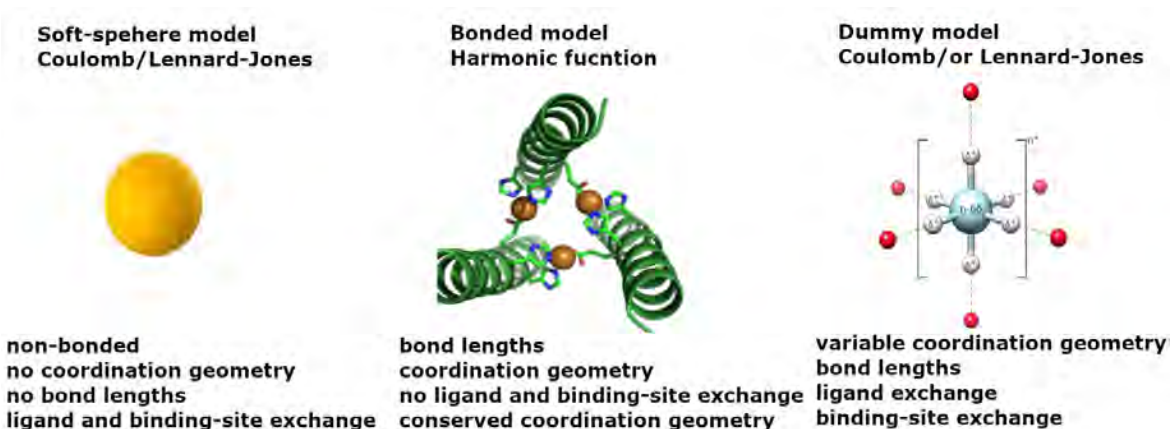


Figure 2.2. Approaches to treat metal ions in the framework of molecular mechanics MM.

### 2.3.1 Statistical mechanics

Statistical mechanics or statistical thermodynamics is a discipline that provides framework to connect properties from microscopic to macroscopic states. Microscopic properties generally refer to molecular properties such as atomic configurations, molecular geometries, their inter and intramolecular interactions, velocities, and positions<sup>111,112</sup>. It determines relative information about molecular distribution of given states and relate that information to retrieve macroscopic average properties like volume  $V$ , energy  $E$ , temperature  $T$ , and  $N$  number of particles. Statistical mechanics generally revolve around the equation of entropy that differs depending on ensembles, thus act as a preamble for all other thermodynamics quantities that follows  $S$ .

$$S = \kappa_B \ln \Omega \quad (2.10)$$

#### 2.3.1.1 Ensembles of statistical dynamics

Statistical dynamics provides means to calculate thermodynamics of different ensembles for our system<sup>113</sup>. These ensembles refer to different parameters or physical properties that are monitored while these particles are allowed to interact with each other. Particularly MD simulations and MC simulations that encompass  $N$  number of atoms or molecules can acquire any of these ensembles for predefined period<sup>114</sup>. Ensembles commonly used to calculate possible states of thermodynamics are explained herein:

##### **Canonical ensemble (NVT)**

It is a statistical mechanics ensemble that incorporates all possible states maintained at constant temperature and acquire thermal equilibrium with heat bath for exchange of energy. System of any size can be treated with this ensemble given the relative size of heat bath is large enough. There are three parameters that are fixed in canonical ensemble: the volume  $V$ , the absolute temperature  $T$ , and the number of atoms  $N$ .

##### **Micro canonical ensemble (NVE)**

In the absence of absolute transfer of energy between the system and its surroundings, micro canonical ensemble which works with fixed number of atoms  $N$ , the total volume  $V$ , and

the total energy  $E$  is expended. Since there is no interaction with surroundings, this ensemble does not cater the temperature  $T$  and represent an isolated system.

### **Isothermal-isobaric ensemble (NPT)**

It is one of the significant ensembles that maintains the total number of particles  $N$ , the constant temperature  $T$ , and the pressure  $P$ , while allowing flow of energy in and out of the system boundaries in the presence of heat bath. Isothermal-isobaric system as the name indicates holds a critical position in chemistry and especially when describing Gibbs free energy or any other system that requires to function at constant pressure  $P$  and temperature  $T$ .

### **2.3.2 Molecular dynamics simulations**

Two frequently used methods to control properties and interactions of atoms or molecules based on selected ensembles are MC and MD simulations. MC methods preferably exploit canonical ensemble (NVT) while searching for conformational phase space of any molecular system. MC simulations introduced by Metropolis in 1950 is preferred to sample the configuration phase space of the system to efficiently represent its thermodynamic behaviour, as it does not calculate time dependent kinetics of the given system<sup>81</sup>. Various algorithms are expended in MC to locate potential energy surface of the system as a function of all coordinates are granted complete degree of freedom<sup>115</sup>. Whereas MD simulations provide evolution of both kinetics and thermodynamic behaviour of the system while employing Newton's equation of motion ( $F=ma$ ), most commonly under NVT or NPT ensembles<sup>114</sup>. Key difference between MC and MD simulations, however, is the enclosure of time variable that takes into account  $N$  body simulations of system that are allowed to interact for predefined period using either of the statistical ensembles. All MD simulations employ certain integrators to determine relative position of a particle, which is calculated by assuming relative position of atoms or molecules ( $r$ ), velocity ( $v$ ), and acceleration ( $a$ ) that will be acted upon by another atom/molecule. The Taylor's expansion<sup>116</sup> of these approximations that commonly use Verlet/Velocity-Verlet algorithm are:

$$r(t + \delta t) = r(t) + v(t)\delta t + \frac{1}{2}a(t)\delta t^2 + .. \quad (2.11)$$

$$v(t + \delta t) = v(t) + a(t)\delta t + \frac{1}{2}b(t)\delta t^2 + \dots \quad (2.12)$$

$$a(t + \delta t) = a(t) + b(t)\delta t + \dots \quad (2.13)$$

### 2.3.2.1 Simulation integrators and thermostats

Verlet algorithm was first coined by a French physicist Loup Verlet in 1967, which deems the position  $r$  and acceleration  $a$  at a given time  $t$  to calculate one time-step forward positions  $r(t + \delta t)$  at  $r(t + \delta t)$  starting from the previous position  $r(t + \delta t)$ . This scheme, however, does not compute the velocities rather integrates to compute kinetic energy, eventually leading to the total energy. The total energy of a system indicates the sum of kinetic and potential energy. While kinetic energy is retrieved from the velocities of atoms/particles, the potential energy is extracted from relative positions from all three directions, denoted as  $3N$  where  $N$  is the number of atoms that needs second order differential equations integrated in several algorithms including the Verlet predictor.

Furthermore, to elucidate the dynamics or behaviour of a system with specific thermodynamic constraints, it is required to incorporate thermostat or barostat in your simulations. The accurate way of maintaining temperature according to *Berendsen et al.* is to add an external heat bath with constant value of  $T$  coupled with temperature of the system to administer fluctuations at each time step<sup>117,118</sup>. The resulting velocities that are scaled at each time step will produce difference in temperature that is proportional to the rate of change in temperature to avoid numerical error during MD simulations. Similarly, barostat is employed to maintain constant pressure of the system while volume is scaled in spite of velocities in this case. Berendsen algorithm is one of the efficient algorithms to relax the system in order to acquire equilibrium state. However, another method employed in this study is the Langevin thermostat that also considers each atom coupled with heat bath while employing Langevin equation as an integrator<sup>119</sup>.

$$m\ddot{r} = -\frac{\partial E}{\partial r} - m\eta_{el}\dot{r} + F_L(t) \quad (2.14)$$

where  $E$  refers to the potential energy,  $m$  is the mass,  $\eta_{el}$  is the friction constant, and  $F_L(t)$  is the random force acting on the system.

### 2.3.2.2 Periodic boundary conditions

Another very important parameter in MD simulations is the integration of solvent since macromolecules cannot exist in isolation and need water molecules and ions to obtain realistic simulation results. Computer programs designed to study the properties in bulk cannot handle extremely large number of atoms covered in water, which will compromise efficiency of the system. It is pertinent to calculate precise and accurate macroscopic properties for reliable simulation results; therefore, treatment of boundaries and boundary effects is crucial. In this connection, two methods are commonly used for solvation: either implicit or explicit<sup>120</sup>. While explicitly defining a periodic water box around macromolecules, appropriate representation of the system is necessary that can hold enough atoms at an appropriate density<sup>121</sup>. A cubic box used for simulating a typical system is mentioned in **Figure 2.3**. However, incorporation of periodic box must be carefully monitored to avoid unphysical artefacts and unrealistic interactions due to charged system.

Furthermore, it is advised to calculate properties based on interactions according to the minimal image convention to avoid duplicate interactions or self-interactions of molecules. Concept of minimal image convention was first introduced by Metropolis et al. in 1953<sup>81</sup>, which is based on the equation that corresponds to movement of non-Coulomb or long-range interactions during simulations for each molecular motion which will consequently avoid the surface effects.

$$\text{If } r_{x,y,z}(i) \geq -\frac{BL}{2} \Rightarrow r_{x,y,z}(i) = r_{x,y,z}(i) - BL \quad (2.15)$$

$$\text{If } r_{x,y,z}(i) \leq -\frac{BL}{2} \Rightarrow r_{x,y,z}(i) = r_{x,y,z}(i) + BL \quad (2.16)$$

where  $r_{x,y,z}(i)$  demonstrates Cartesian coordinates of corresponding  $i^{\text{th}}$  particle whereas BL represent length of the elementary box. However, it is obvious that short-range order needs to be composed of few hundred particles to constitute a system to avoid artificial symmetry effects. Whereas the description of long-range order must exceed number of particles accordingly.

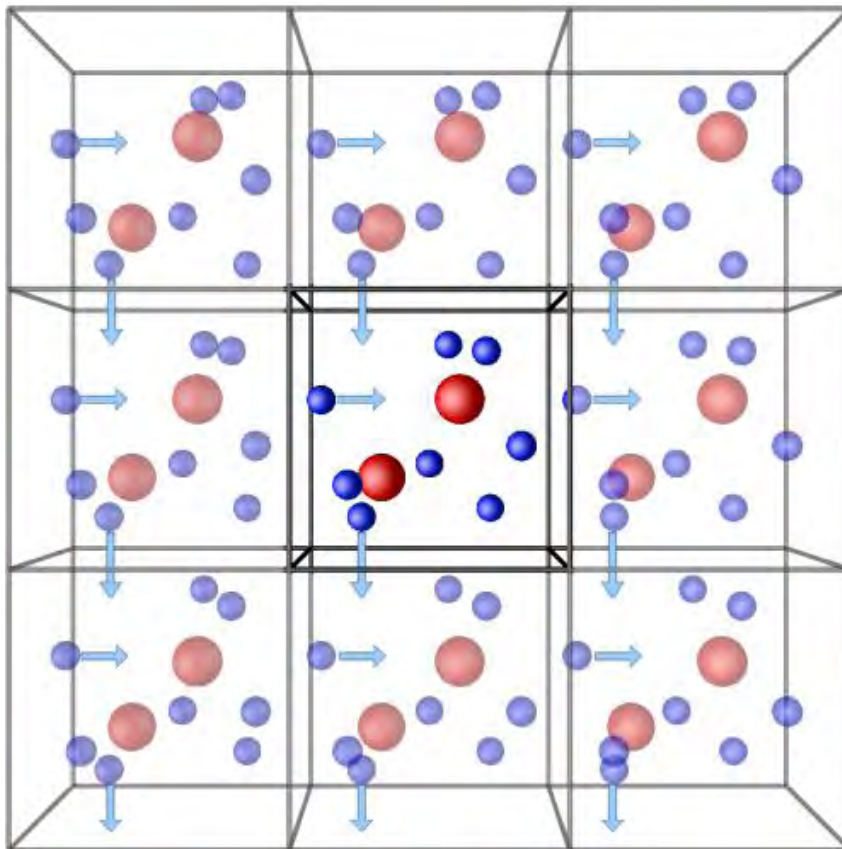


Figure 2.3. Schematic representation of two-dimensional periodic boundary conditions.

### 2.3.2.3 Ewald summation method for long-range interactions

Handling of electrostatic interactions constituting long-range forces of order  $r^{-n}$  with  $n \leq 3$  needs proper treatment especially while working with charged species to calculate properties like dielectric constant<sup>122</sup>. There's tendency in the above explained methods to define box length for long-range simulations, which is usually greater than half of the box length. However, to address proper handling of such interactions, variety of methods have been proposed, out of which Ewald summation method is employed in the current study to perform MD simulations.

Ewald summation method employed in particle mesh method (PME) was devised by Ewald in 1921 that efficiently calculated all the electrostatic interactions occurring inside of the periodic box with all their periodic images<sup>123</sup>. It is so far the most widely used

method of periodic systems that was originally built for ionic crystals' energy calculation. It calculates total Coulomb interactions/Lennard-Jones potential alongwith periodic boundary condition and charge neutrality of any molecular system<sup>110</sup>. PME method is recommended while considering larger systems containing lipid bilayers, proteins and DNA that can be implemented on a supercomputer for increased computer performance.

### 2.3.3 Molecular docking

Last but not the least, one of the most important binding site predictions and the foremost step to explore ligand-receptor binding potential is molecular docking defining the preliminary stage of molecular modeling. Based on concepts proposed by Warshel, Karplus, and Levitt, the best strategy to study molecular interactions is to combine docking protocols with MM and QM methodologies<sup>124–126</sup> indicated in **Figure 2.4**. Docking packages run on two basic steps: 1) first step focuses on finding the best docking pose through sampling and prediction of multiple conformations, and 2) the second step assesses the bound ligands to their proteins based on binding affinities, which are calculated using different scoring functions.

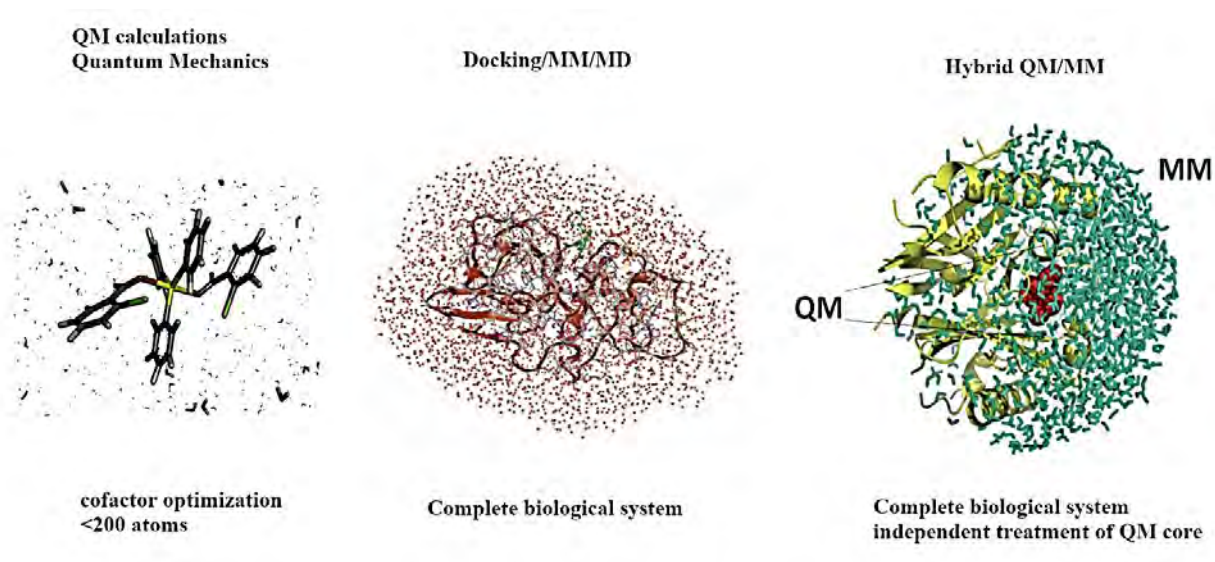


Figure 2.4: Diagrammatic sketch of three main families of molecular modeling methods.

These scoring functions incorporate exhaustive search algorithms, algorithms based on heuristic approaches like genetic algorithms (GA) and simulated annealing.



Docking protocols generally imply two docking approaches: rigid and flexible docking. The latter is frequently used in performing virtual screening of large libraries efficiently, which are based on fast and inexpensive conformational and stochastic algorithms. Current study has employed three different docking software's for multiple studies namely, Autodock and Genetic Optimization for Ligand Docking (GOLD) for non-bonded docking, and High Ambiguity protein-protein docking (HADDOCK) for covalent docking.

Both GOLD and Autodock employ genetic algorithm GA that emphasizes on sampling each pose based on energetics of previous one through individual physics and machine learning scoring functions<sup>127,128</sup>. GA provides a ligand pose with highest fitness and lowest energy conformation<sup>129</sup>. However, GOLD and HADDOCK both keep the protein flexible while performing molecular docking whereas GOLD implements two scoring functions: Goldscore and Chemscore expanded in equations 2.17.

$$\nabla G_{Bind} = \nabla G^0 + \nabla G_{HB} \sum_{HB} f(\Delta r) f(\Delta \mathbf{1}\alpha) + \Delta G_{met} \sum_{met} f(\Delta r) + \Delta G_{lipo} \sum_{lipo} f(\Delta r) + \Delta G_{rot} N'_{rot} \quad (2.17)$$

Equation 2.17 sums up the binding energy of translational and rotational entropy, energy from hydrophobic to hydrogen bonds, and metal ligation. Furthermore, the penalty function  $f(\Delta r)f(\Delta \mathbf{1}\alpha)$ , and the loss of entropy  $\Delta G_{rot}$  at the time of binding are all fitted to experimental affinities by plotting regression. GOLD also characterized the energy in result of clash penalties, close contacts, and poor conformations pose that give rise to the final Chemscore:

$$ChemScore\ Fitness = \Delta G_{bind} + E_{clash} + E_{int} \quad (2.18)$$

Noticeably, both these software's rely on scoring functions based on FF to cater vdW, and electrostatic interactions between the interacting partners. FF parameters expended in these software's are listed in equation 2.19, where  $A_{ij}$  and  $B_{ij}$  signify potential of mean forces between  $i$  and  $j$  and yield sum of all the forces acting on the two molecules.

$$\Delta G_{bind} = \sum_i^{lig} \sum_j^{rec} \left[ \frac{A_{ij}}{r_{ij}^{12}} - \frac{B_{ij}}{r_{ij}^6} + \frac{q_i q_j}{\epsilon r_{ij}} \right] \quad (2.19)$$

Furthermore, we incorporated HADDOCK particularly for its ability to carry out covalent docking efficiently. HADDOCK generally carries out docking in three stages: 1)

First, it undergoes rigid body minimization till the local energy minima is found, 2) followed by semi-flexible simulated annealing by imparting flexibility to side chains of protein, and 3) to render refined complexes submerged in explicit solvent<sup>130</sup>. The software predicts total 200 conformations after the first stage, which are later clustered on the basis of structural similarities and can be differentiated from respective scores.

## 2.4 Hybrid QM/MM approach

Combined QM/MM methods have obtained a place while dealing with large systems in need of pure QM methods that needs solvation alongwith the simulations of proteins and nucleic acids. This approach was first introduced by Warshel and Levitt in 1976 but it gained pace in 1986 in the form of a practical QM/MM protocol successfully developed by Singh and Kollman<sup>83,131</sup>. The idea of QM/MM surfaced to provide an affordable method of molecular mechanics coupled logically between both systems when applied. Diagrammatical sketch of QM/MM is illustrated in **Figure 2.5** that indicates partitioning of the system into two regions; QM and MM whereby quantum mechanical electronic structure calculations partially determine molecular potential of the system whereas the other half is treated by force field generated by molecular mechanics.

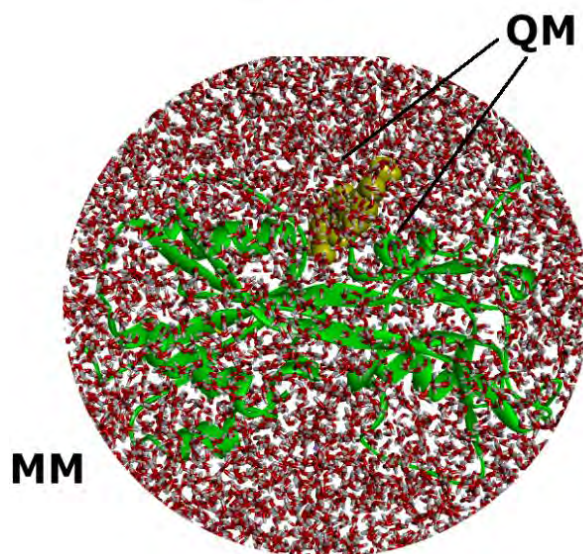


Figure 2.5: Diagrammatical sketch of QM/MM illustrating partitioning of the system into QM and MM regions.

QM approaches provide for calculations of electronic structures to retrieve ground and excited state properties like atomic charges, thermodynamic statistics, energies etc. Whereas MM depends on careful calibration of force field parameters of larger number of atoms. However, forces acting on QM/MM system are calculated according to equation 2.20.

$$F_{tot} = F_{sys}^{MM} + (F_{QM}^{QM} - F_{QM}^{MM}).S(r) \quad (2.20)$$

where  $F_{tot}$  and  $F_{sys}^{MM}$  are the forces acting on single particle and whole system.  $F_{QM}^{QM}$  and  $F_{QM}^{MM}$  in the equation 2.20 represent MM and QM regions, which provide smooth transition of particles from one region to another with the implementation of  $S(r)$  with cutoff 0.2 Å. Another important phenomenon that is implemented in the current study is to carefully divide the covalent bonds while defining QM and MM regions. Various covalent embedding schemes are in use such as the one introduced by Singh and Kollman in 1986 that cuts across the covalent bonds while incorporating a link atom that needs to be connected to MM region illustrated in **Figure 2.6**<sup>132,133</sup>. However, it must be done very carefully to cater the electronegative atoms lying at the surface of electronic structure. Furthermore, to fully understand and analyse the dynamics of QM/MM potential, we have employed US in the current study.

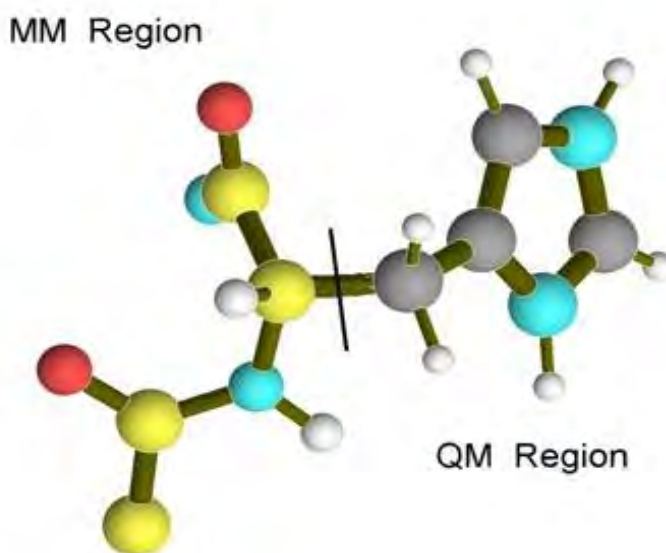


Figure 2.6: Division of covalent bonds across the QM and MM regions.

### 2.4.1 Umbrella sampling

QM/MM approach, Umbrella sampling (US), generates reaction free energy profiles of reaction pathways explored using DFT methods. US is preferred when dealing with electron transfer chemical reactions involving transfer of proton from one atom to another donor or acceptor atoms or processes like protein folding and unfolding<sup>134–136</sup>. In a broader perspective, it provides changes in free energy that reveal valuable information about kinetics and thermodynamics of processes like ligand-receptor binding. US approach applies harmonic constraints to move along the reaction path to run parallel simulations. Diagrammatic sketch of US algorithm is illustrated in **Figure 2.7**. It is run in separate windows representing individual simulations, which are then combined to generate free energy landscape of the system. The method developed by Torrie and Valleau<sup>109,137</sup> introduced biasing potential that directs the path of simulations in a certain direction to keep the reaction coordinate  $\mathbf{q}(\mathbf{r})$  along successive positions expanded below:

$$U_{bias} = \sum_i k_i (q^{(i)}(r) - q_0^{(i)}(r))^2 \quad (2.21)$$

Biasing potential  $q_0(r)$  carried out simulations on equally placed multiple windows in reaction coordinate space that provide histograms. Histograms are generated such that they are overlapped by defining correct force constants  $k_i$  and spacing between the centers. This equation is sufficient to study the unbiased simulation of one window that chooses force constants arbitrarily. Whereas, if one wishes to combine the energy curves of multiple windows, then force applied needs to be calculated by introducing the bias potential and by combining the free energy curves<sup>138,139</sup>. This process is termed as adaptive umbrella sampling that used the following equation:

$$U_{bais}(q) = -G(q) = k_B T \ln p(q) \quad (2.22)$$

To combine the data from unbiased sampling of US, the weighted histogram analysis method (WHAM) is expended. Successful implementation of WHAM depends on number of factors including the strength of biasing potential applied on the reaction coordinate, number of windows to allow sufficient overlap, and the section of correct method for slow and accurate convergence<sup>140,141</sup>. WHAM is one of the most promising

methods to estimate calculate weighted average of individual window by minimizing the statistical error and functions on the following equation:

$$L = \ln \prod_{k=1}^{NSim} \prod_{i=1}^{bin} \left( f^{(k)} e^{-\beta U_i^{(k)}} p_i \right)^{n_i^{(k)}} + \sum_{k=1}^{NSim} \lambda^{(k)} \left( 1 - \sum_{i=1}^{Nbin} f^{(k)} e^{-\beta U_i^{(k)}} p_i \right) \quad (2.23)$$

where  $p_i$  is the equilibrium probability for bin  $i$  and  $n_i^{(k)}$  is the histogram count in bin  $i$ .

However,  $f^{(k)} = \frac{1}{\sum_{j=1}^{Nbin} e^{-\beta U_j^{(k)}} p_j}$  is the Boltzmann factor biasing energy, and  $\frac{-U_i^{(k)}}{e^{k_B T}}$  is the

normalizing factor for equilibrium probability used to generate the equation 2.23.

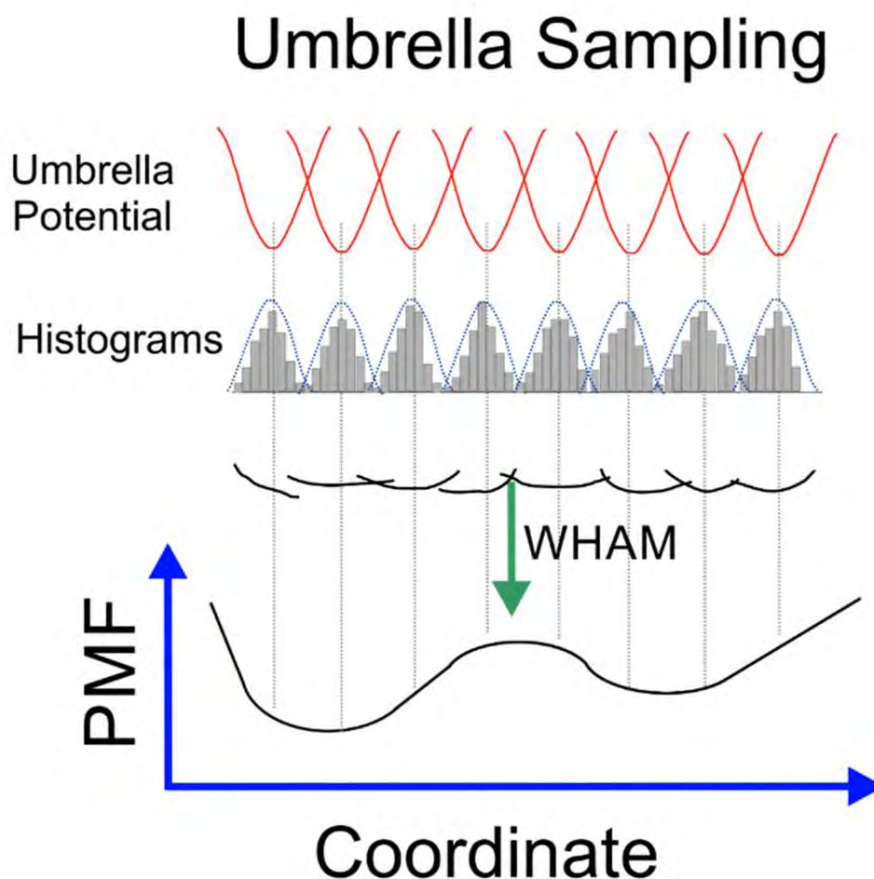


Figure 2.7: Diagrammatic sketch of overlapping windows of Umbrella sampling illustrating algorithm behind its calculations, which are combined using WHAM.

### 2.4.2 Metal-ion modeling

Metal center parameters of novel metals or residues can be derived using QM or hybrid QM/MM approaches, which typically deal with metalloprotein region from QM perspective whereas MM region is dealt using MD simulations for having insights into dynamics of the system. One of the prominent tools employed in this study to model metal sites using bonded models is the metal center parameter builder (MCPB) developed by Martin Peters in 2010<sup>142,143</sup>. The complete workflow adopted from MCPB is given in **Figure 2.8**.

First step of model builder focuses on optimizing the geometry of bismuth metalloids with SBKJC ECP using DFT level of theory. The basis and role of SABKJC in parametrizing metalloids have been discussed in section 2.2.5. MCPB currently supports more than 80 metal ions, which are parametrized using vdW parameters comprising RESP fits from vdW radii and Lennard-Jones potential adopted from *Li et al.* and UFF<sup>144</sup>. The second corresponds to generation of FRCMOD that can use any of the predefined methods such as Seminario methods, Z-matrix method, or an empirical method. The third step however encompass RESP charge fitting leading to respective mol2 files containing fitted RESP charges. This step also provides multiple options to choose from i-e ChgModA for treating all charges with flexibility, ChgModB that treats only heavy atoms, ChgModC for keeping charges of backbone atoms fixed, and ChgModD, which keeps charges of both backbone and CB atoms fixed. However, all these charges are assigned using AMBER FF. Finally, the last step is to constitute PDB file with their respective metal residues that can be implemented in any MD simulations package including AMBER, CHARM, ParmEd, GROMACS etc. All these parameterizations have been carried out on GAMESS\_US whereas MD simulations have been performed with AMBER suite.

Despite the challenges, the molecular and electronic level insights provided by classical mechanics and QM approaches are unmatched and hard to attain using experimental procedures. This study has pulled efforts in parametrizing novel bismuth compounds and explore the kinetic and thermodynamics effect of covalent bond on an enzyme binding site using the above-mentioned methods. However, methods defined in forthcoming sections constitute the pillar of this study in expanding the applicability of

molecular modeling to unveil ligand-receptor interactions and interactions established by metallo-ligands with neighboring residues.

## 2.5 Evaluation of structural and dynamical parameters

Various tools have been employed to analyse the structural and dynamical properties from molecular docking to MD and QM/MM simulations. A few of these methods and tools are listed here that include binding free energy calculations, radial distribution function (RDF), and axial frequency distribution (AFD).

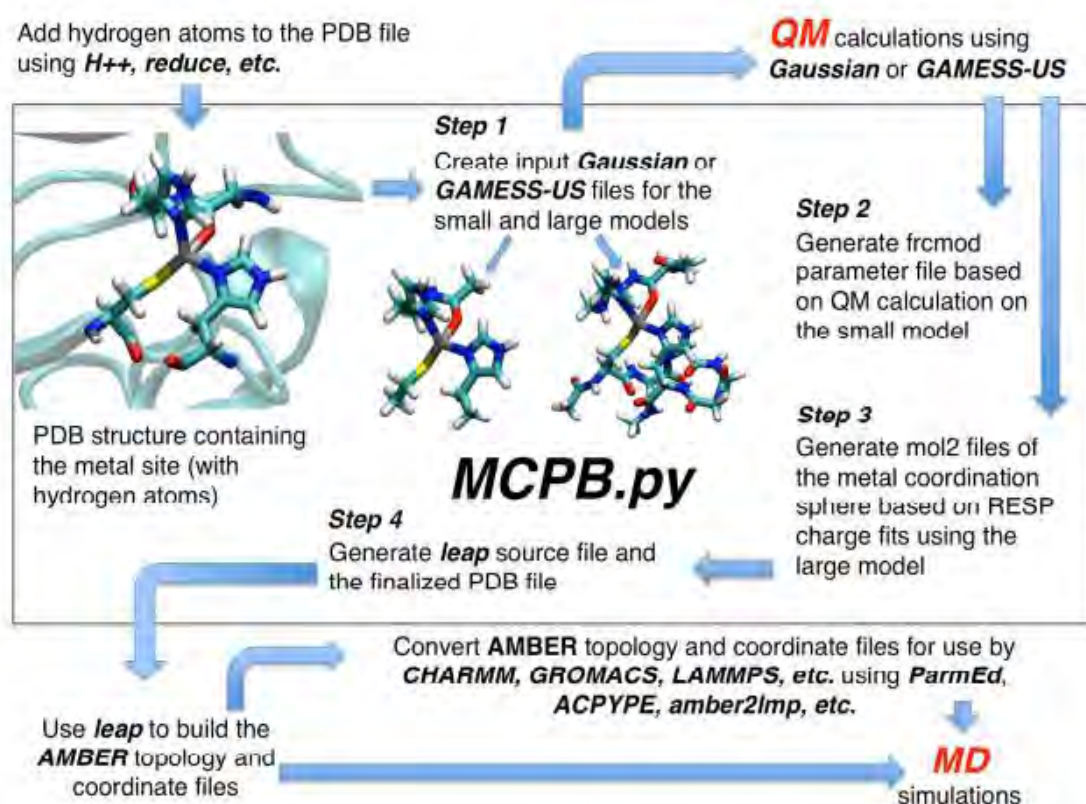


Figure 2.8: Flowchart of MCPB.py suite adopted from 142.

### 2.5.1 Binding free energy calculations

A popular method to calculate absolute binding affinities generally between ligand and its receptor while analysing biomolecules is Molecular Mechanics Generalized Born/Poisson Boltzman Surface Area MM(PB/GB)SA method implemented in AMBER package<sup>145</sup>. This method provides results in correlation with experimental values with  $r^2$  ranging from

0.0 to 0.8 for individual proteins unless the difference between ligand affinities remain below 12 kJ/mol<sup>146</sup>. These theoretical methods are capable of drawing correlation between their equivalents while making definitive predictions. In this context, this method has been employed in this thesis to evaluate interaction energy between the enzymes and their mutant counterparts on simulated trajectories retrieved from MD and QM/MM ensemble averages. The Eq used to calculate the binding free energy contains multiple energy terms that can be individually executed and improved.

$$\Delta G_{binding} = E_{bind} + E_{el} + E_{vdW} + G_{pol} + G_{np} - TS \quad (2.24)$$

Electrostatic, vdW interactions, and information from bonded terms account for the first three MM energy terms. Whereas  $G_{pol}$  and  $G_{np}$  are the polar and non-polar energy solvation terms calculated from PB equations and linear equations drawn from solvent accessible surface area (SASA)<sup>145</sup>. However, the last term takes into account the temperature T and entropy S using normal-mode analysis, which employs harmonic-oscillator in ideal-gas approximations<sup>147</sup>. Apart from discrepancies in this method that strongly rely on continuum solvation method employed and thermodynamic approximations, it has been popular in evaluating post-processing trajectories of simulations. Furthermore, it highlights functional significance of critical residues by employing alanine scanning, which has revealed useful information to screen and propose a handful of inhibitors for respective enzymes.

## 2.5.2 Radial distribution function

RDF provides distribution of atoms that lays basis on either the center of mass of molecule or pair distribution functions. RDF is capable to shed light on structural properties of the solvated system and can efficiently predict the orientation of molecules lying at the interaction center<sup>148</sup>. One of the significant advantages of this method is that results are comparable to the data received from experiment diffraction assays. RDF is mathematically represented as:

$$g(r) = \frac{pl(r)}{\langle pj \rangle} = \frac{nij(r)}{\langle pj \rangle 4\pi r \delta r} \quad (2.25)$$



which gives the probability of finding one particle  $i$  from another particle  $j$  lying at a distance  $r$  from each other. Furthermore,  $n(r)$  denotes number of atomic shells of certain width  $\Delta r$ , leading to the mean atomic density presented as peaks in resulting graphs.

### 2.5.3 Axial frequency distribution

However, another method to estimate structural properties of a system is AFD indigenously developed and implemented in our lab<sup>149</sup>. AFD hold the capability to estimate the coordination geometry of ligands with respect to proteins while averaging the density form all the directions based on initial atom masks. Exact details pertinent to the orientation and movement of protein-ligand complex over the simulation trajectories are revealed. It not just provides the coordination geometry but also ascertain their stability by estimating the distribution of relative coordinate axis defined using the atomic masks. The equation to represent AFD is defined as:

$$AFD = \sum_{i=1, j=1}^{kl} m_{i,j} \quad (2.26)$$

where  $m_{i,j}$  correspond to the distance between two particles  $i$  and  $j$ . AFD in principle provide local movements and structural changes unlike RDF based on two-particle correlation, which is not responsive to local structural reorganization events.

## 2.6 Hardware overview

To implement the methods discussed above, comprising classical MD simulations and QM to elucidate protein-ligand complex, or metalloids solvated in hundreds of water molecules can take up to days or several hours on an ordinary desktop computer. Computational efforts required to perform QM jobs largely depend on number of atoms included in the QM region and the timestep, which requires supercomputers. To perform simulations implemented in this thesis, Intel ® Core™ 2 Duo e8600@3.33 GHz and Intel ® Core™ i7-5930k CPU@3.50GHz with 12 processors was employed with Centos 7 as an operating system. Computational Biology Lab of National Center for Bioinformatics at Quaid-i-Azam University ensures provision of high-performance cluster GPUs given in **Figure 2.9** to conduct these computational analyses.



Figure 2.9. Multi-core GPUs available at Computational Biology Lab of National Center for Bioinformatics at Quaid-i-Azam University.

---

## CHAPTER 3

---

# Discrete Dynamics of Warhead Modulation on Covalent Inhibition of Oxyr:

## A QM/MM Study

## 3. COVALENT INHIBITION OF OXYR: A QM/MM STUDY

### 3.1 Background

Rapid evolution and dissemination of AMR drastically undermines the effectiveness of antimicrobial agents; thus, posing a serious threat to public health globally that prompts uncontrolled resistance in microorganisms<sup>1,9,19,52</sup>. According to the WHO, antimicrobial treatment is inconceivable in the absence of effective antimicrobial agents that could lead to more than 10 million deaths annually by 2050 if left unaddressed<sup>3,13,150,151</sup>. In that respect, concerted efforts in design and development of effective drugs are required to overcome the emergence of MDR that has outpaced drug discovery due to limitations of investment in research and pharmaceutical industry<sup>44-46</sup>. Generally, the convergent approach to classify antipathogenic compounds is to target virulent pathways that interfere with regular defense mechanisms of organisms; thus, limiting the possibility of acquired resistance due to milder evolutionary pressure<sup>50,53,152-154</sup>.

In this context, Gram negative bacteria exhibit a reactive oxidative specie; H<sub>2</sub>O<sub>2</sub>, that is produced in response to higher stress levels, which in turn triggers expression of multiple genes involved in maintenance of homeostasis, or repair especially the transcription factors that regulate bacterial defense mechanisms<sup>155</sup>. H<sub>2</sub>O<sub>2</sub> mainly targets protein thiol groups or metal centers present in transcription factors especially those that have relatively higher reactivity towards oxygen/nitrogen species<sup>156,157</sup>. One such transcription sensor OxyR that responds to enhanced levels of H<sub>2</sub>O<sub>2</sub> is necessary for full virulence of *P. aeruginosa*<sup>158-160</sup> and is thus the protein of interest in this study. OxyR is highly sensitive and selective transcription factor sensor of H<sub>2</sub>O<sub>2</sub>, which is reduced by cysteines present in the active site leading to increased transcription of antioxidant genes such as KatA, responsible for acute intrinsic resistance in *P. aeruginosa*<sup>58</sup>. To date, multiple crystal structures of OxyR regulatory domain (RD) have been solved from *Escherichia coli*, *Pseudomonas aeruginosa*, *Vibrio vulnificus*, *Neisseria meningitidis*, and *Porphyromonas gingivalis*. However, the molecular evidence of involvement of H<sub>2</sub>O<sub>2</sub> in catalysis and binding at catalytic triad of OxyR is published in biochemical studies of full-length *P. aeruginosa* OxyR (Pa-OxyR)<sup>161</sup>. OxyR monomer encompasses six cysteine

residues, out of which Cys199 and Cys208 are involved in gene activation by disulfide bond formation that participates in sensing  $\text{H}_2\text{O}_2$  in its environment<sup>159,160,162,163</sup>. The reported crystal structure of Pa-OxyR concluded the role of particularly one cysteine residue; Cys199 by mutating it to Asp, which resulted in drastic reduction of  $\text{H}_2\text{O}_2$ <sup>160,162-164</sup>. Thus, in this study, we elucidated molecular mechanism of OxyR active site by modifying the catalytic Cys199 with the addition of covalent adducts comprising different chemical warheads. These lines of work provide insights into inhibition of unexplored antipathogenic virulence factor OxyR and shed light on design of such molecules that impair the ability of bacterial response to oxidative stress.

Prior to covalent modeling of OxyR, we performed non-covalent MD simulations with multiple virtually screened ligands of varying scaffolds to have insights into the binding dynamics of OxyR and its neighboring residues. Interestingly, results yielded unproductive and highly unstable enzyme:inhibitor complexes after multiple attempts with different chemical scaffolds demonstrated in **Figure 3.1**.

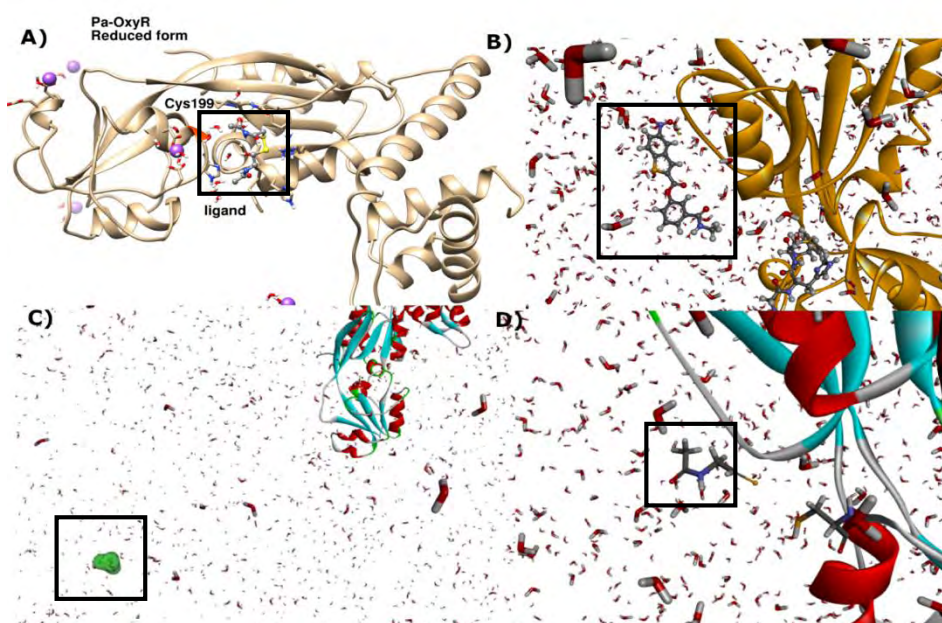


Figure 3.1: Unproductive non-covalent MD simulations of four different inhibitors. Detachment of ligands are highlighted in square.

These findings signify detachment of non-covalent inhibitors lying at the surface of OxyR due to its flexible binding site that reinforce the significance of irreversible

covalent inhibition of stress modulator protein in hand with underlying structural aspects. Multiple studies have previously reported ligand-induced modifications especially one of the most studied Receptor tyrosine kinases (RTK), laid basis in understanding modulations of signaling pathways by targeting cysteine containing proteins<sup>165,166</sup>. Several FDA drugs covalently modify Epidermal growth factor receptor (EGFR) and prevent its activation by H<sub>2</sub>O<sub>2</sub> for example afatinib, neratinib, dacomitinib, and rociletinib that incorporate a Michael acceptor in their structure as an electrophilic warhead<sup>166,167</sup>. Furthermore, inhibitors with reported biological activity encompass warheads like  $\alpha$ -ketoamides, pyrazoles, aldehydes, and hydroxymethyl ketone (HMK). These warheads are famous in forming covalent adducts with extracellular signal-regulated kinases (ERK), akin to peroxide stress response sensor OxyR<sup>168-172</sup>. However, apart from the mutational analysis of OxyR catalytic site that effectively resulted in reduction of H<sub>2</sub>O<sub>2</sub><sup>173-175</sup>, recently published experimental inhibitor of OxyR; an antipathogenic compound significantly decreased the activity of H<sub>2</sub>O<sub>2</sub><sup>176</sup>. This sheds light on strategic development of small molecules or fragments through which the adaptive stress response can be regulated. Nevertheless, covalent modifications, mutational and inhibition studies discussed so far have laid basis in design of the current study.

Thus, to elucidate the function-regulated effect of cysteine modification and to understand the impact of warhead modulation on reactive center and chemical stability of OxyR, we expended QM/MM methods in this study. The second aspect is fundamental in designing reversible or irreversible inhibitors since irreversible inhibitor designing is the most sustained strategy due to slow dissociation rates unless resynthesis of particular drug target takes place<sup>177-179</sup>. Perhaps, while designing specific covalent modifiers, choice of suitable warhead in systematic design is significant since it directly impacts binding affinities of non-covalent interactions ( $K_i$ ) and electrophilic warheads in particular reactions ( $K_{inact}$ )<sup>180,181</sup>. Michael acceptors, which are widely accepted covalent inhibitors containing  $\alpha,\beta$ -unsaturated carbonyl moieties in their substructures therefore directed our efforts in design of covalent inhibitors comprising Michael acceptors as an electrophilic specie<sup>182,183</sup>. However, our efforts were not limited to Michael acceptors rather we incorporated the famous nitrile and thiopene-based inhibitors<sup>184,185</sup> to expand our inhibitor library. Furthermore, *Hyo-Young et al.* recently reported first experimental study on OxyR

inhibition, which compelled us to incorporate that chemical structure in this study. We thus modified the experimental inhibitor with the addition of Michael acceptor warheads methyl oxo-enoate and HMK inspired from dimethyl fumarate structure<sup>186,187</sup>. Chemical structures of all four inhibitors are exhibited in **Figure 3.2**.

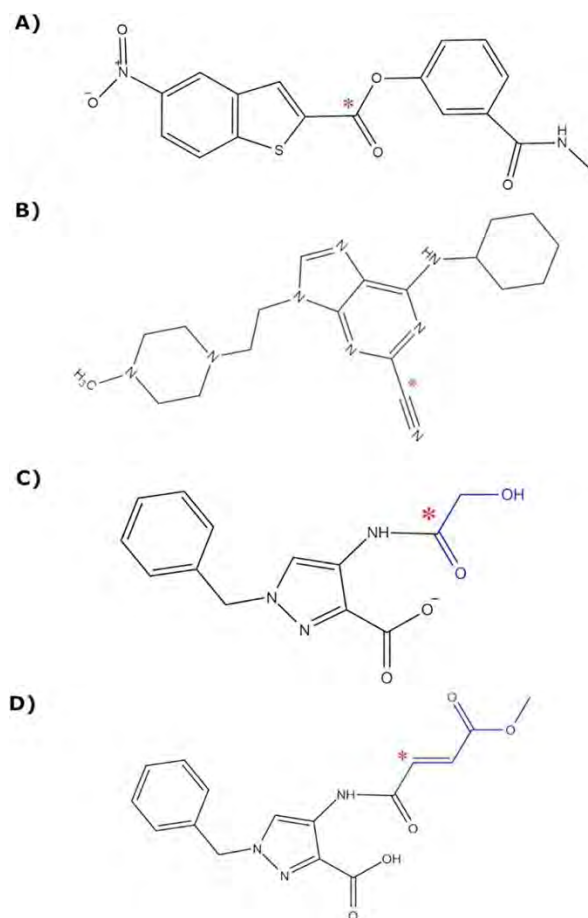


Figure 3.2. Chemical structures of the proposed covalent inhibitors A) Benzothiophene-core inhibitor B) Modified Exp-2 inhibitor with methyl oxo-enoate C) Modified Exp-1 inhibitor with hydroxymethyl ketone D) Nitrile-based inhibitor. Reaction centers are indicated with an asterisk whereas the Michael acceptor addition of two proposed experimental inhibitors is highlighted in blue.

Current study, thus, expands its efforts to propose QM/MM inhibition study of OxyR and investigate its biochemical process with warheads of varying chemistry, which unveil origin of different kinetic rate-constants. Noticeably, considering the importance of transient proton transfer from specificity in ribozymes till the shuttling in carbonic anhydrase<sup>188,189</sup>; the phenomenon of proton transfer in current work is observed to differ

greatly depending on the nature of warheads that directly impacts the reaction profile. Involvement of nearby water molecules and residues forming catalytic triad significantly impact the modulation of proton transfer which holds critical standing when dealing with extracellular signal-regulated enzymes with flexible binding sites and underlying structural aspects.

## 3.2 Materials and methods

The workflow of current study is mentioned in **Figure 3.3**.

### 3.2.1 Selection of covalent modifiers

The atomic coordinates of three-dimensional structure of OxyR were retrieved from X-ray crystal structure available with PDB ID 1I69 in reduced form. To unveil the mechanistic of OxyR active site, we chose compounds in a manner that could potentially react in different routine due to variations in electrophilic reaction centers, which possess capability to exhibit different chemical and topological environment.

Thus, the first step in selection of inhibitors started from virtual screening that established its basis on the presence of electrophilic Michael acceptor in their core structure. For this purpose, thiophene-2-one or pyrrol-2-one fragment present in most of the biological active compounds was used as starting structure (given in **Figure 3.4**) for similarity searching with BIOVIA Discovery studio<sup>190</sup>. Three different libraries commonly used for inhibitor screening were employed; namely ZINC database, Asinex and Chembridge database with >80% threshold for ligand selection<sup>191–193</sup>. The resulting library constituted 1,500 compounds that underwent non-covalent docking with GOLD suite<sup>194</sup> to further screen compounds exhibiting higher binding potential for OxyR active site. The top ranked 50 non-covalent complexes mentioned in **Table 3.1** were finally selected for covalent docking with HADDOCK server<sup>195</sup>, which screened single compound comprising benzothiopeptide moiety in its structure presented in **Figure 3.2a**.

Secondly, recently reported experimental inhibitor of OxyR that underwent physiochemical characterization for Gram-negative pathogens namely; *P. aeruginosa* and *E. coli* was modified<sup>176</sup>. Addition of Michael acceptor warheads namely, methyl oxo-enoate and HMK inspired from dimethyl fumarate structure was carried out resulting in



two inhibitors namely Exp-1 and Exp-2. Since this is the first experimental inhibitor of OxyR that can serve as a template to verify our results, these modified inhibitors remained of particular importance.

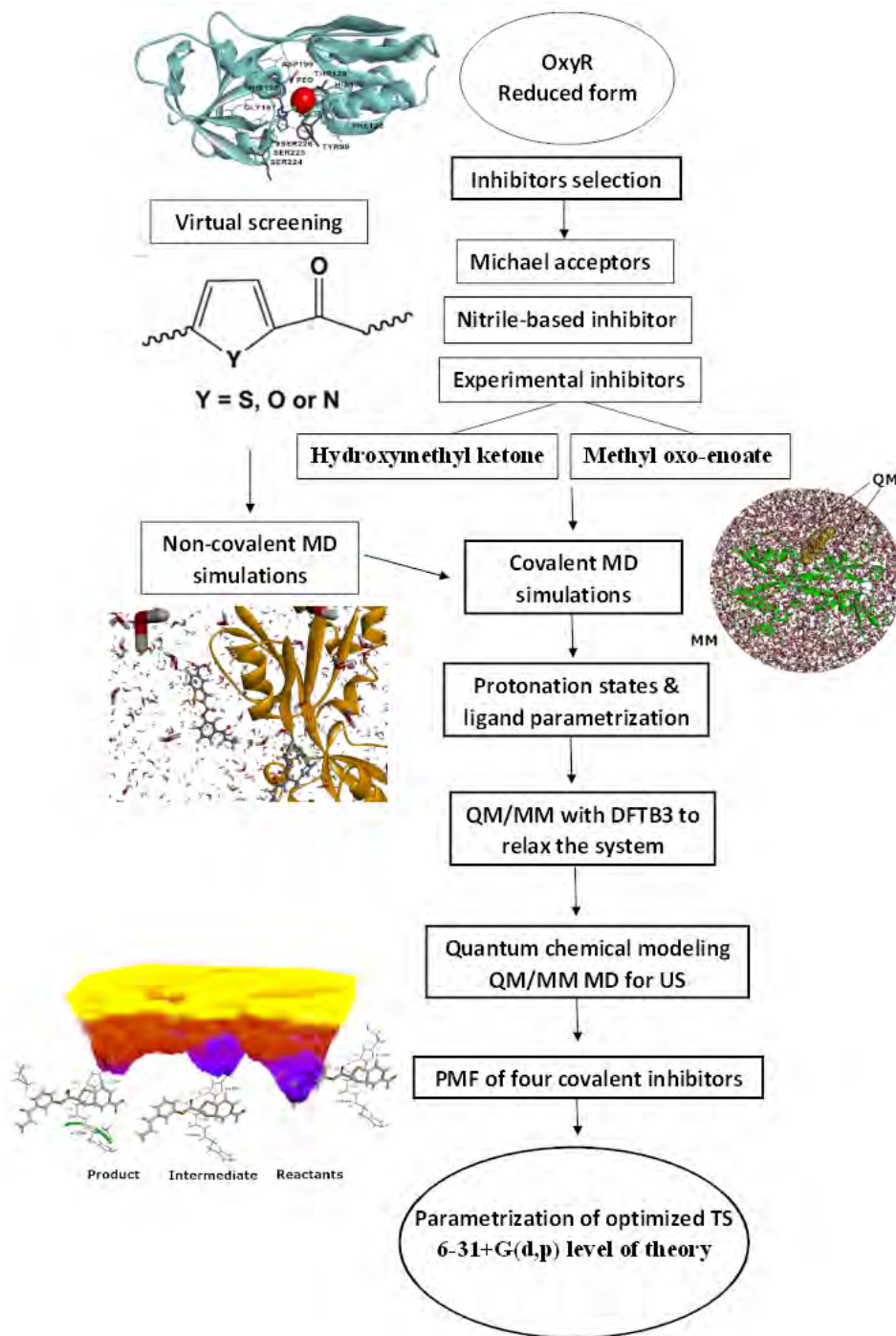


Figure 3.3. Workflow of covalent inhibition of OxyR with four proposed inhibitors.

Table 3.1: Virtually screened non-covalent docking results from chembridge, zinc, and

Sr. No	ID	Gold score	Sr. No	ID	Gold score
1	19796635	62	36	77322699	66
2	09430801	63	37	09430801	66
3	09430814	63	38	12585013	67
4	13129114	63	39	13139114	67
5	14550325	63	40	19796635	67
6	19531534	63	41	26095673	67
7	19796635	63	42	71858580	67
8	19796636	63	43	11665126	67
9	35375917	63	44	15946975	68
10	36389700	63	45	55384989	68
11	77322699	63	46	13129114	69
12	02810635	63	47	17301146	69
13	10337584	63	48	65061768	69
14	19501458	63	49	5714545	71
15	64999848	63	50	ZINC41251450	71
16	65051769	63	51	ZINC41283974	71
17	13644802	64	52	ZINC41850812	73
18	65061769	64			
19	02111689	64			
20	04968733	64			
21	14550325	64			
22	15946975	64			
23	17051075	64			
24	19796636	64			
25	55384989	64			
26	63147075	64			
27	06181065	65			
28	14550344	65			
29	14550325	65			
30	17301146	65			
31	19796636	65			
32	32537610	65			
33	40056811	66			
34	65061768	66			
35	71858580	66			

asinex library.

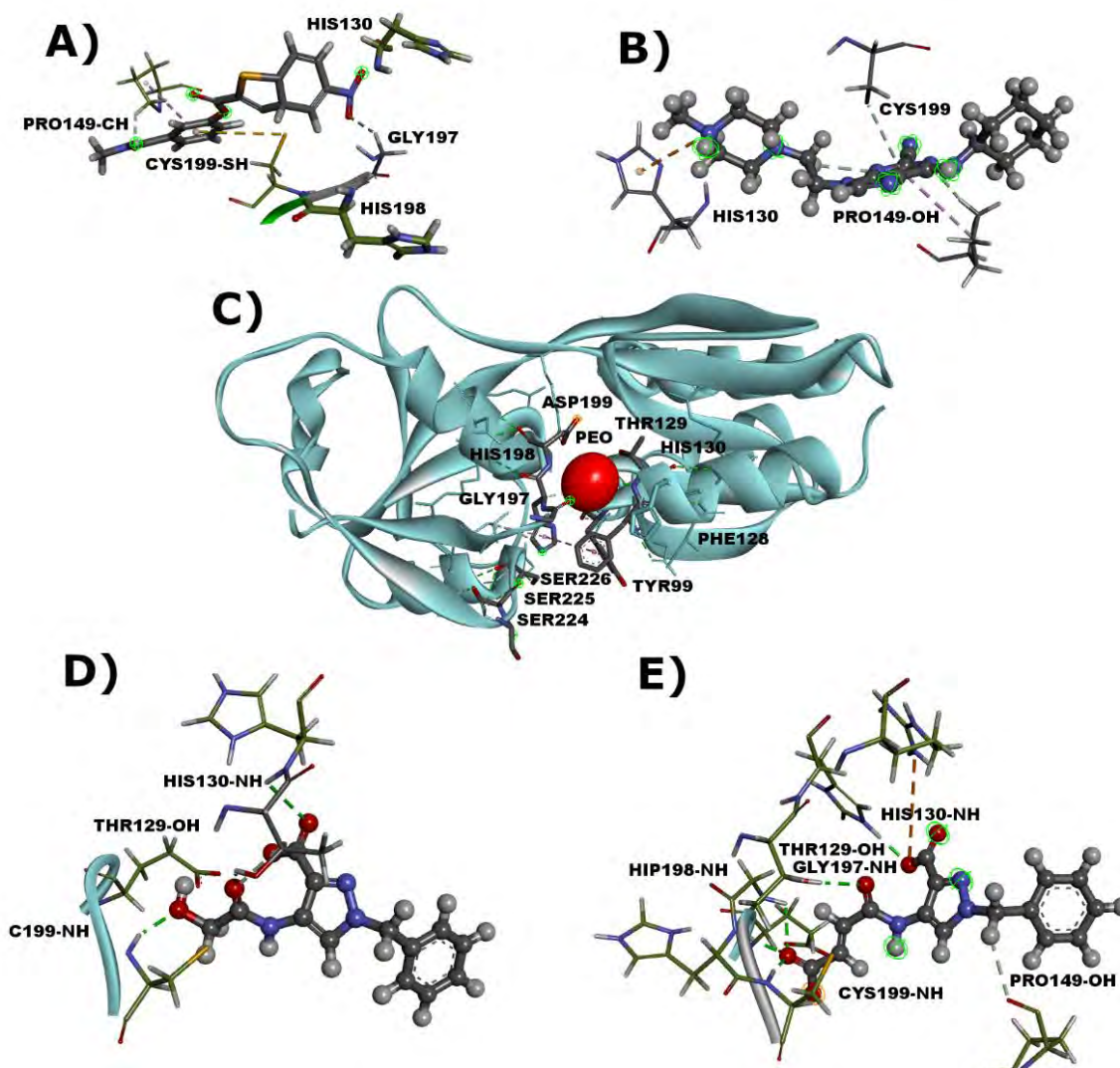


Figure 3.4. Comparative snapshots of proposed inhibitors in the active site of OxyR with interacting residues highlighted. A) Benzothiopene-core inhibitor B) Nitrile inhibitor C) Crystal structure of OxyR with the substrate D) Modified Exp-1 inhibitor with hydroxymethyl ketone E) Modified Exp-2 inhibitor with methyl oxo-enoate.

Lastly, the core structure of highly potent heterocyclic inhibitors of cathepsin-K<sup>196</sup> based on purine template was included in the study to form a covalent adduct with critical regulatory cysteine of OxyR, Cys199. So far, a fewer studies have undergone covalent inhibition of cysteine proteases with nitrile-based inhibitors, particularly limited computational analysis is available. However, the experimentally available information suggest that these inhibitors react in an irreversible manner and bind tightly to the active

site can thus serve as valuable template<sup>196</sup>. We, therefore, included this warhead in our study to elucidate kinetics of Oxyr under different chemical environment.

### 3.2.2 QM-cluster calculations

DFT calculations that are mainly based on key interactions established between the active site of OxyR and proposed inhibitors is exhibited in **Figure 3.4**. Notably, the location of active site of OxyR like many cysteine proteases lies on the surface of protein and hold the capability to establish number of interactions including hydrogen bonding demonstrated in **Figure 3.4**. Involvement of interacting residues and conformational information was overlaid with the available crystal structure of OxyR with bound substrate that laid basis in selection of QM region of each inhibitor. Thus, the selection of QM region included Cys199, His198, and His130 along with the inhibitors except for nitrile-based inhibitor that lacked His198 in its interaction site. To obtain natural and unbiased results, QM regions were kept smaller where Exp-1 inhibitor has 79 atoms and 4H link atoms with overall charge -1 whereas the Exp-2 inhibitor has 77 atoms with overall charge -1 including 3H link atoms. Furthermore, the QM region of nitrile-based inhibitor has 85 atoms and overall charge +2 after 2H link atoms and lastly, the benzothiopene-core inhibitor from zinc database contains 83 atoms and +0 charge including 2H link atoms. However, inhibitors that used only one His residue while carrying out the reaction, enclosed one doubly protonated His residue and the other as singly protonated to keep the charge of the overall system neutral. Before undergoing the QM/MM simulations, the protonation states of the protein were determined using PropKa server v3.3 given in **Table 3.2**.

All four systems were minimized and equilibrated before undergoing US with AMBER suite using QM/MM simulations at DFTB3 level of theory that implemented theoretical context of QM/MM explained in Section 2.3 and 2.5.1. However, to calculate more difficult interaction term  $H_{QM/MM}$ , an electronic bedding scheme given in equation 3.1 is expended in *sander*, which undergoes MM point charges calculations with electrons of the QM system and considers the interactions between MM point charges and QM nuclei explicitly.

$$H_{QM/MM} = H_{QM/MM}^{mechanical} + \sum_{i \in MM} q_i \int \frac{\rho_{QM}(r)}{|r-r_i|} dr \quad (3.1)$$

Table 3.2: pKa of all titratable residues computed with PropKa alongwith their residue name and number. Protonated and deprotonated His residues are mentioned accordingly.

<b>RESIDUE</b>	<b>pKa</b>	<b>RESIDUE</b>	<b>pKa</b>
<b>ASP 51</b>	3.87	<b>TYR 18</b>	10.01
<b>ASP 56</b>	3.10	<b>TYR 37</b>	10.01
<b>ASP 76</b>	3.42	<b>TYR 84</b>	12.41
<b>ASP 86</b>	3.80	<b>TYR 164</b>	10.07
<b>ASP 99</b>	3.14	<b>TYR 180</b>	11.01
<b>ASP 110</b>	4.00	<b>TYR 190</b>	10.32
<b>ASP 116</b>	1.59	<b>LYS 54</b>	10.50
<b>ASP 124</b>	3.65	<b>LYS 64</b>	10.50
<b>ASP 160</b>	2.82	<b>LYS 104</b>	10.36
<b>ASP 202</b>	4.01	<b>LYS 158</b>	10.50
<b>ASP 206</b>	3.80	<b>LYS 169</b>	10.50
<b>GLU 1</b>	3.13	<b>ARG 92</b>	11.38
<b>GLU 35</b>	4.64	<b>ARG 115</b>	12.29
<b>GLU 40</b>	4.64	<b>ARG 128</b>	11.66
<b>GLU 65</b>	4.50	<b>ARG 136</b>	11.38
<b>GLU 67</b>	4.50	<b>ARG 157</b>	11.80
<b>GLU 71</b>	3.98	<b>ARG 159</b>	11.94
<b>GLU 77</b>	2.33	<b>ARG 173</b>	11.66
<b>GLU 85</b>	4.71	<b>ARG 174</b>	12.59
<b>GLU 93</b>	2.56	<b>ARG 181</b>	11.80
<b>GLU 103</b>	4.64	<b>ARG 187</b>	12.08
<b>GLU 109</b>	4.75	<b>ARG 189</b>	12.36
<b>GLU 133</b>	1.61	<b>ARG 198</b>	11.94
<b>GLU 156</b>	3.48	<b>ARG 200</b>	11.80
<b>GLU 171</b>	3.88		
<b>GLU 191</b>	3.91		
<b>GLU 195</b>	3.91		
<b>CYS 199</b>	7.94		
<b>CYS 208</b>	6.79		
<b>HIE 21</b>	6.34		
<b>HIE 27</b>	3.94		
<b>HIE 86</b>	4.60		
<b>HID 130</b>	5.72		
<b>HIE 132</b>	3.71		
<b>HIE 145</b>	4.80		
<b>HIE 164</b>	1.53		
<b>HID 198</b>	5.71		

Methods and parameters used to generate the topology of all four models are enclosed herein. All systems were neutralized with the addition of Na<sup>+</sup> counter-ions and submerged in TIP3P water box of 15 Å periodic boundary. Equilibration of these systems was carried out in a consecutive manner starting from a restrained to completely unrestrained system. In a first step, classical minimization was performed with restraints set for protein and ligand to allow free movement of water molecules around the system for 10<sup>3</sup> steps with constant volume and non-bounded cutoff set to 10 Å. Minimization without restraints at T=0 was carried out to obtain a stable configurational state for additional 10<sup>3</sup> steps under similar NVT and cut-off. Following that, the NVT molecular dynamics simulations preceded with thermostat T=300 K with barostat set to 1 for 2 ns. In this step, positional restraints were activated by applying weight of 5 kcal/mol/Å<sup>2</sup> that was followed by density equilibration with positional restraints, using Langevin dynamics in NPT ensemble and non-bounded cutoff set to 10 Å for 4 ns. Whereas production run on each inhibitor was carried out for 10 ns on E-I complexes, which employed PME algorithm to regulate electrostatic interactions. Simulation graphs (RMSD) of resulting trajectories are depicted in **Figure 3.5 and 3.6** generated by CPPTRAJ of AMBER suite exhibiting well-equilibrated systems.

### 3.2.3 QM/MM setup for umbrella sampling

However, the purpose of QM modeling of four models was to examine reaction mechanism of covalently modified OxyR inhibitors with different warheads and to determine the mechanistic of active site of OxyR. Thus, the US approach was employed to generate PMF using DFTB3 QM method with 1 fs of MD sampling per reaction coordinate (RC). Theoretical background of US is illustrated in Section 2.4.1 whereas, the complete protocol is explained here. QM/MM MD for US was run with ibelly restraint set outside 20.0 sphere, cutoff 10 Å, and force constants 50-200 kJ mol<sup>-1</sup> Å<sup>-2</sup> using QM/MM MD-NVT simulations. General approximations to explore the reaction coordinate carried out sequential steps of nucleophilic attack followed by proton transfer in each system. First step of inhibition started with attack from thiolate group of Cys199 represented as RC2 that was defined from

1.8 to 3.5 Å. Whereas the proton transfer step RC1 was defined from -0.5 to 1.5 Å for each inhibitor respectively.

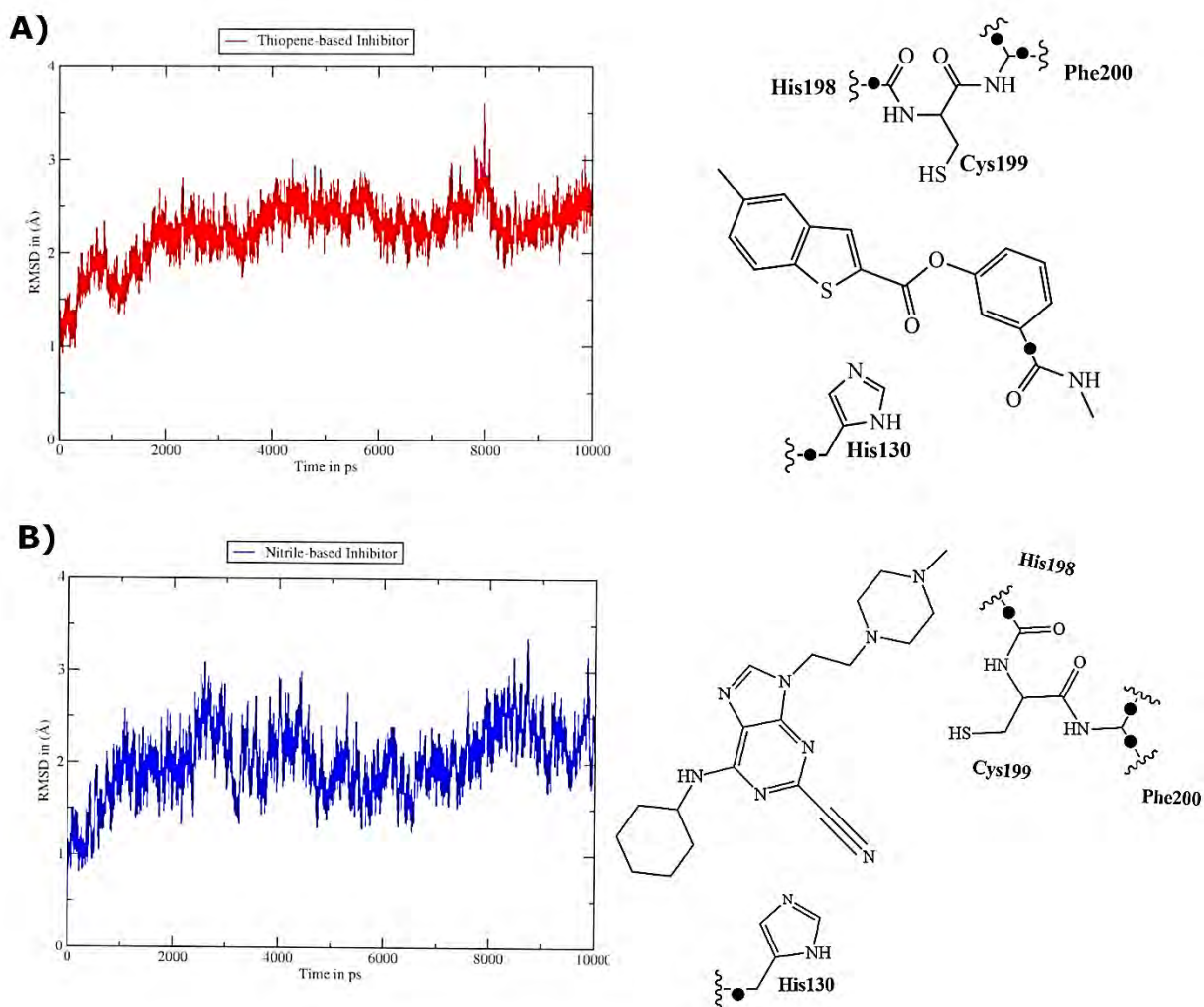


Figure 3.5. Simulation graphs of resulting trajectories from US simulations of thiopene-core and nitrile-based inhibitors. A) Root Mean Square Deviation (RMSD) calculated from 10 ns simulations trajectories of OxyR in complex with the thiopene-core inhibitor. B) RMSD calculated from 10 ns simulations trajectories of OxyR in complex with the nitrile-based inhibitor. Details of the atoms included in the QM region in QM/MM calculations are given on the right side. The black dots represent the hydrogen link atoms.

QM method for each step involved in a chemical reaction was analysed by WHAM to acquire an approximate minimum energy pathway (MEP) of the reaction. Output

generated by WHAM for US is demonstrated in **Figure 3.7** of four proposed compounds for covalent inhibition. Furthermore, based on multiple studies<sup>197–199</sup> that have employed hybrid DFT with B3LYP while analyzing nucleophilic addition reactions, we have used split-valence 6-31+G(d,p) calculations with RED server for both geometry optimization and RESP charge derivation of missing parameters. Whereas, known parameters from AMBER were retrieved with Antechamber program of AmberTools package. Complete parameter files of all four optimized models at E-I state are mentioned in their respective sections.

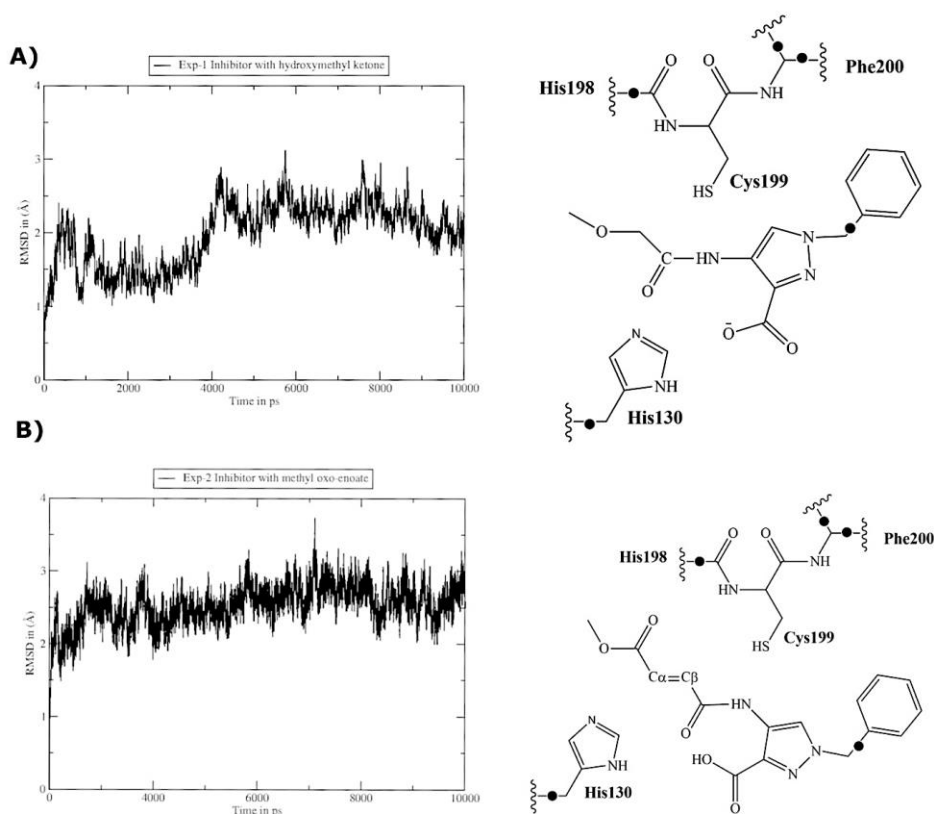


Figure 3.6: Simulation graphs of resulting trajectories from US simulations of Exp-1 and Exp-2 inhibitors. A) Root Mean Square Deviation (RMSD) calculated from 10 ns simulations performed on the OxyR in complex with the Exp-1 inhibitor. B) RMSD calculated from 10 ns simulations performed on the OxyR with Exp-2 inhibitor. Details of the atoms included in the QM region in QM/MM calculations are given on the right side. The black dots represent the hydrogen link atoms.



### 3.2.4 Binding free energy

To conclude, the absolute binding free energies of all four inhibitors were calculated for non-covalent bound state with MMPBSA/MMGBSA with ABMER whereas the decomposition of free energies of catalytic residues was evaluated using MMPBSA.py module that based on equation 3.2 leads to difference between the free energy of complex, receptor, and ligand.

$$\Delta G_{bind} = G_{complex} - [G_{receptor} + G_{ligand}] \quad (3.2)$$

However, the QM/MM interaction energies were calculated with equation 3.3 as a sum of energy contribution of decomposed residues to the total interaction energy. It decomposes the interaction of residues while employing polarized wave function ( $\Psi$ ) applied on subset of QM atoms used.

$$E_{QM/MM}^{Int} = \sum \langle \Psi | \frac{q_{MM}}{r_{e,MM}} | \Psi \rangle + \sum \sum \frac{Z_{QM} q_{MM}}{r_{QM,MM}} + E_{QM/MM}^{vdW} \quad (3.3)$$

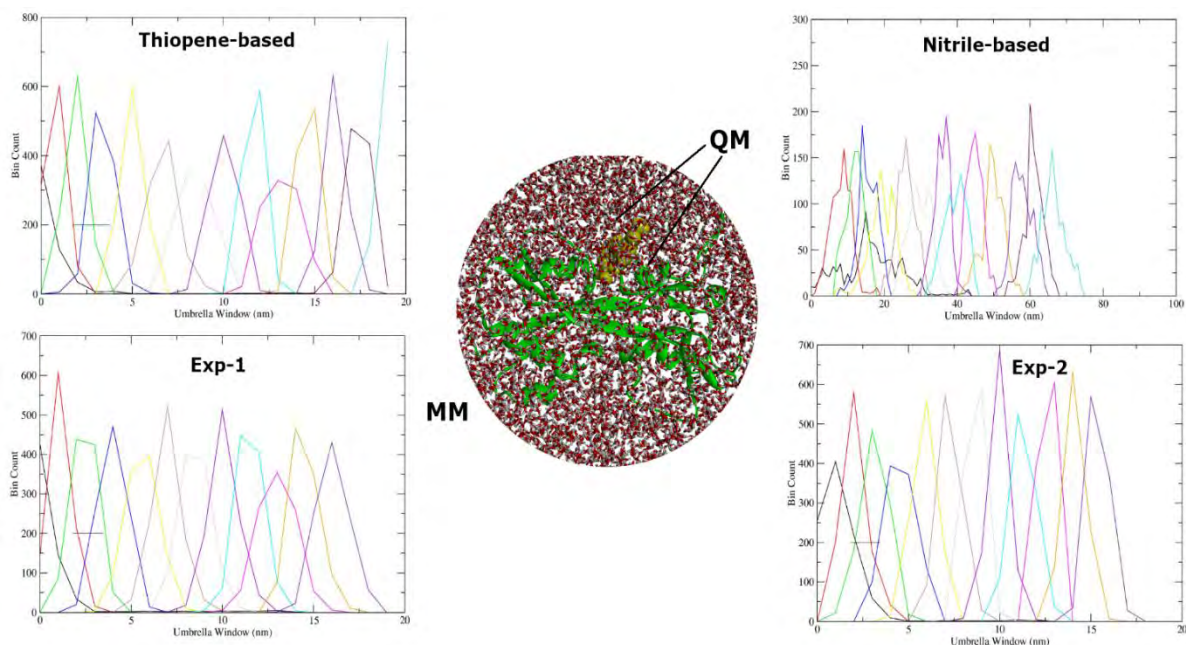


Figure 3.7. Overlapping windows of RC2 obtained from US for each compound generated with WHAM.

### 3.3 Results and discussion

Before indulging in deep analysis to understand the reaction mechanism, first step included systematic analysis of interactions established by all four ligands with the active site of OxyR that is located on the surface of protein demonstrated in **Figure 3.8**. It has been reported in multiple studies that the role of basic residues present around the active site is critical in defining the catalytic process of OxyR<sup>173,200</sup>. Two or more basic residues namely His130, His198, Arg201, and Arg226 were observed in the vicinity of all four complexes, which are conserved in OxyR homologs<sup>173,201–203</sup>. In the current study, side chains of His130 and His198 were frequently observed located near the sulfur atom of Cys199 exhibiting average distance of 5 to 3Å° between Cys199-Sy...Ne-His198 and Ne-His130. Frequent occurrence of short distances with His residues indicated their capability to act as general acid-base catalyst and assist in the nucleophilic attack by Cys199. Similar findings have been reported by *Jurajet al.* that reaffirms the role of nearby His residues, which are likely to facilitate the catalytic process of OxyR<sup>200</sup>.

All four complexes were then subjected to US and overlaid with the crystal structure of OxyR with PEO present in its active site to identify any conformational modifications, which is mentioned in **Figure 3.4**. Noticeable key differences between proposed inhibitors namely; thiopene-core, Exp-1, Exp-2, and nitrile-based inhibitor, is the presence of different warheads in their chemical structures. Thiopene-core, Exp-1, and Exp-2 demonstrated both His130 and His198 in proximity with cutoff value of 5Å°, which exhibited hydrogen bonds and pi-alkyl interactions. Thiopene-core inhibitor carries pyrrol-2-one fragment as Michael acceptor in its structure whereas the difference between Exp-1 and Exp-2 is restricted to their warheads. Nitrile-based inhibitor, however, holds pyrrolopyrazine substructure that exhibited comparatively decreased interactions with neighboring moieties. However, to select starting structures to undergo cysteine modifications and proton transfer, all ligands were first carefully optimized and subjected to initial QM/MM simulations with distance restraints. Stabilized reactant complexes were further used to study the inhibition reaction mechanism proposed in **Scheme 1-4**. Transition states (TS1 and TS2) are separated by the intermediate which is not shown in

scheme 1 and 2 separately however their representative structures are depicted in their respective structural displays.

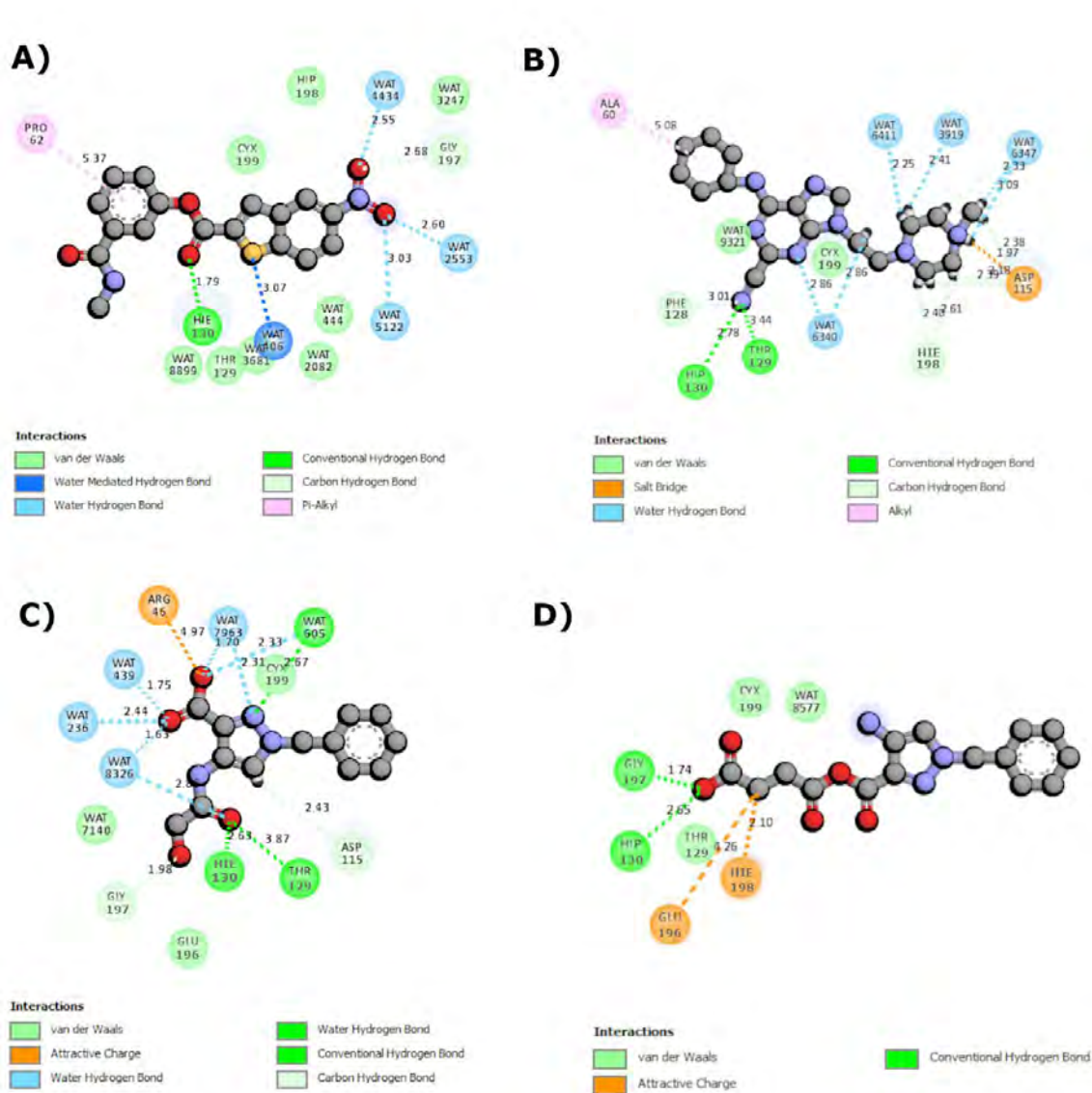
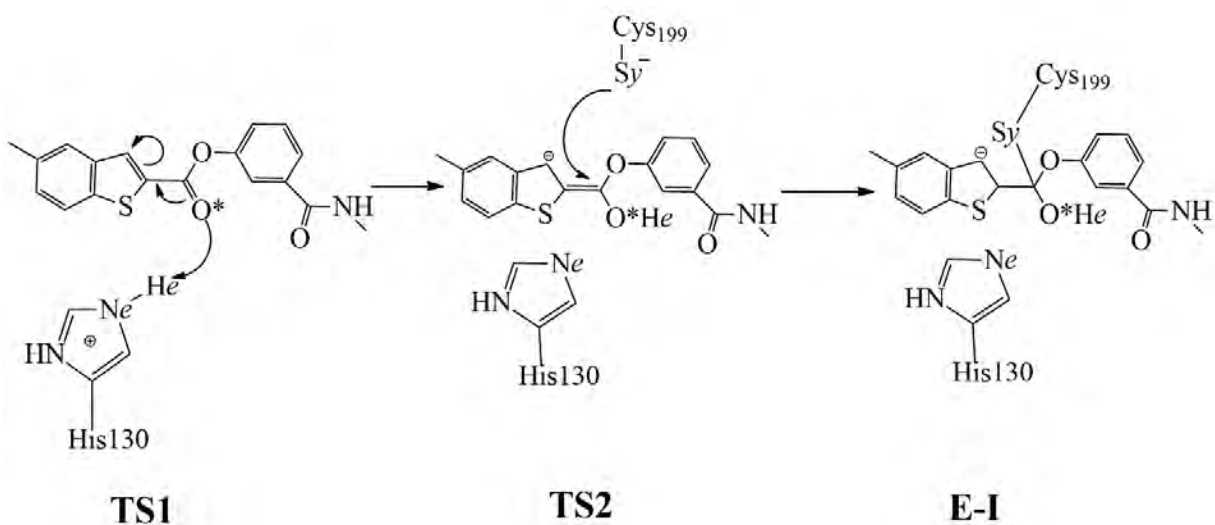


Figure 3.8. Non-covalent interactions between OxyR and proposed inhibitors. A) Thiopene-core inhibitor B) Nitrile-core inhibitor C) Modified Exp-1 inhibitor with hydroxymethyl ketone, and D) Modified Exp-2 inhibitor with methyl oxo-enoate.

### 3.3.1 Reaction mechanism with benzothiophene-core inhibitor

Previous studies conducted by *Kummari et al* reported nucleophilic attack on benzo[*b*]thiophene scaffold at C3 position, which underwent *in vitro* and mass spectrometry assays on benzo[*b*]thiophene 1,1-dioxide compounds, predicting irreversible covalent binding of cysteine proteases. This study thus targeted the C3 position on benzothiophene scaffold for nucleophilic attack mentioned in **Scheme 1**. MD simulations accommodated the ligand in active site of OxyR by supplying a salt bridge hydrogen bond between He of His130 and O\* of ligand and another salt bridge hydrogen bond between O\* and sulfur S of Cys199. However, the difference in distances between two salt bridges 2.410 and 2.961 prioritized proton transfer from His130, which drifted Cys199 at optimal position and distance to accompany nucleophilic attack at position C3. According to Scheme 1, the proton transfer from He of His130 to O\* initiates the reaction without any reorganization and rehybridization. The reaction proceeded from the proton transfer via TS1 leading to the intermediate state (I-E). The product (E-I) was formed in a subsequent step by the nucleophilic attack of S $\gamma$ -Cys199 on C $\beta$  of the ligand via TS2. Optimized geometries of each transition state observed during QM/MM US calculations of this reaction are illustrated in **Figure 3.9**.

**Scheme 1:** Proposed mechanism of OxyR inhibition by thiopene-core inhibitor.



The reaction is characterized in a stepwise mechanism with two barriers TS1 and TS2 separated by an intermediate state. The TS1 and TS2 were verified and characterized with B3LYP/6-31+G(d,p) in gas phase resulting in imaginary frequencies  $i270.08\text{ cm}^{-1}$  and  $i543.40\text{ cm}^{-1}$ , respectively.

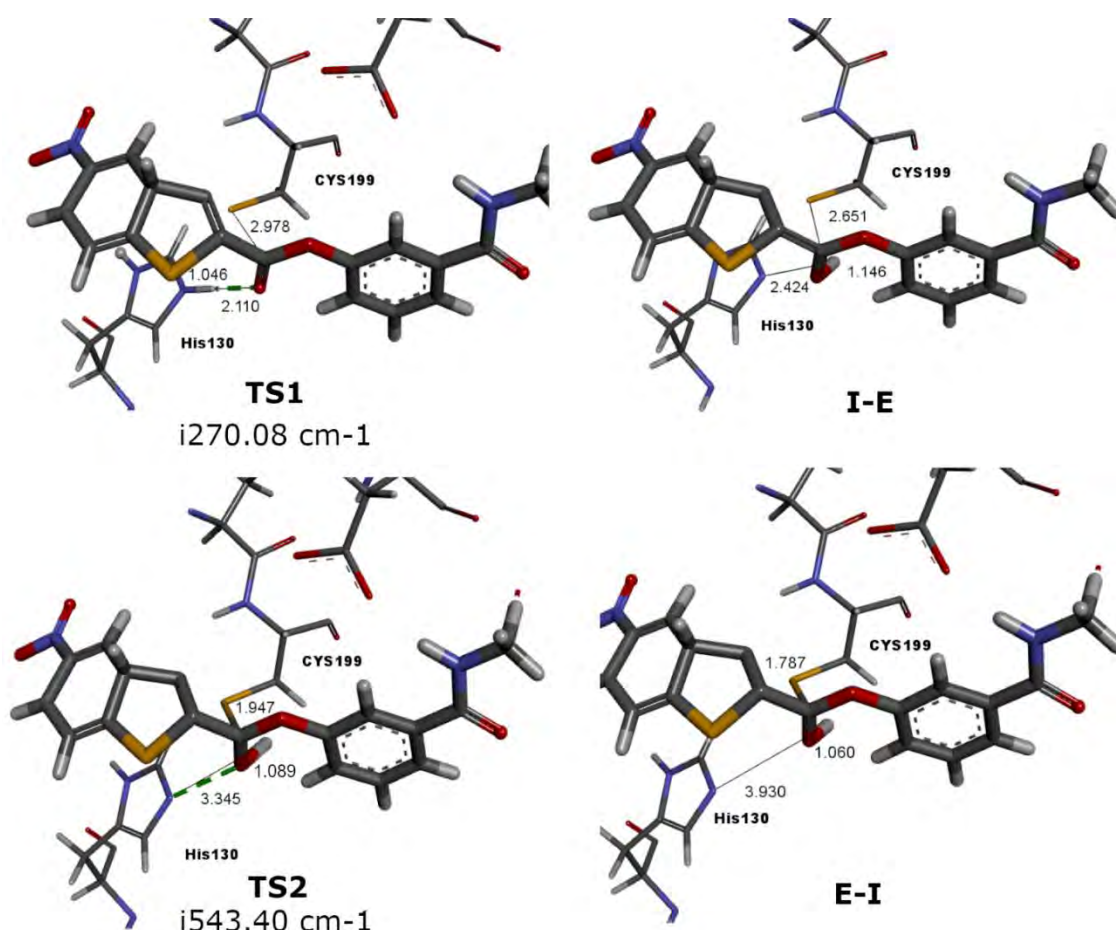


Figure 3.9. Details of DFTB3/MM optimized structures of selected states located along the inhibition reaction of OxyR by thiopene-core inhibitor. The catalytic residues C199 and H130 are shown with key distances in Å.

The reaction energy  $-5.5\text{ kcal mol}^{-1}$  was released upon product formation while demonstrating energy barriers  $3.1\text{ kcal mol}^{-1}$  in TS1 and  $13.6\text{ kcal mol}^{-1}$  in TS2. Rate-limiting step; however, is the covalent bond formation with energy barrier  $13.6\text{ kcal mol}^{-1}$  depicted as TS2 in **Figure 3.10**. Furthermore, differences observed in distances between  $d(S\gamma, C\beta)$  and  $d(O^*, H\epsilon)$  throughout the reactions are mentioned in **Figure 3.11**. Notably,

the distance  $d(\text{H}\epsilon, \text{N}\epsilon)$  changed from 1.046 Å to 3.930 Å while  $d(\text{O}^*, \text{H}\epsilon)$  decreased from 2.110 Å to 1.060 Å whereas  $d(\text{S}\gamma\text{Cys199}, \text{C}\beta)$  changed from 2.978 Å to 1.787 Å.



Figure 3.10: DFTB3/MM free energy profile obtained from QM/MM umbrella sampling calculations for inhibition of OxyR. The inhibition mechanism of thiopene-core and nitrile-based inhibitors is illustrated in black and yellow colours respectively. The TS of thiopene-core and nitrile-based inhibitors are not similar and represent individual reaction profiles. Red arrows indicate the relative Gibbs free energies ( $\Delta G$ ) for all stationary points.

These findings comprehend that the reaction is exergonic where the proton transfer takes place prior to the nucleophilic attack. Furthermore, the post simulations analysis carried out on covalently bonded (E-I) complexes (**Figure 3.18**) depict deprotonated His130, which is stabilized by the formation of two hydrogen bonds with  $\text{O}^*$  of the ligand thus restricting the protonation of His130 by water molecules again. These findings signify the irreversible reaction with thiopene-core inhibitor, which is concurrent with the previous study conducted by *Kummari et al.*<sup>34</sup>. The study comprised similar scaffold as thiopene-inhibitor which predicted irreversible covalent binding via *in vitro* and mass spectrometry assays with benzo[b]thiophene 1,1-dioxide compounds<sup>34</sup>.

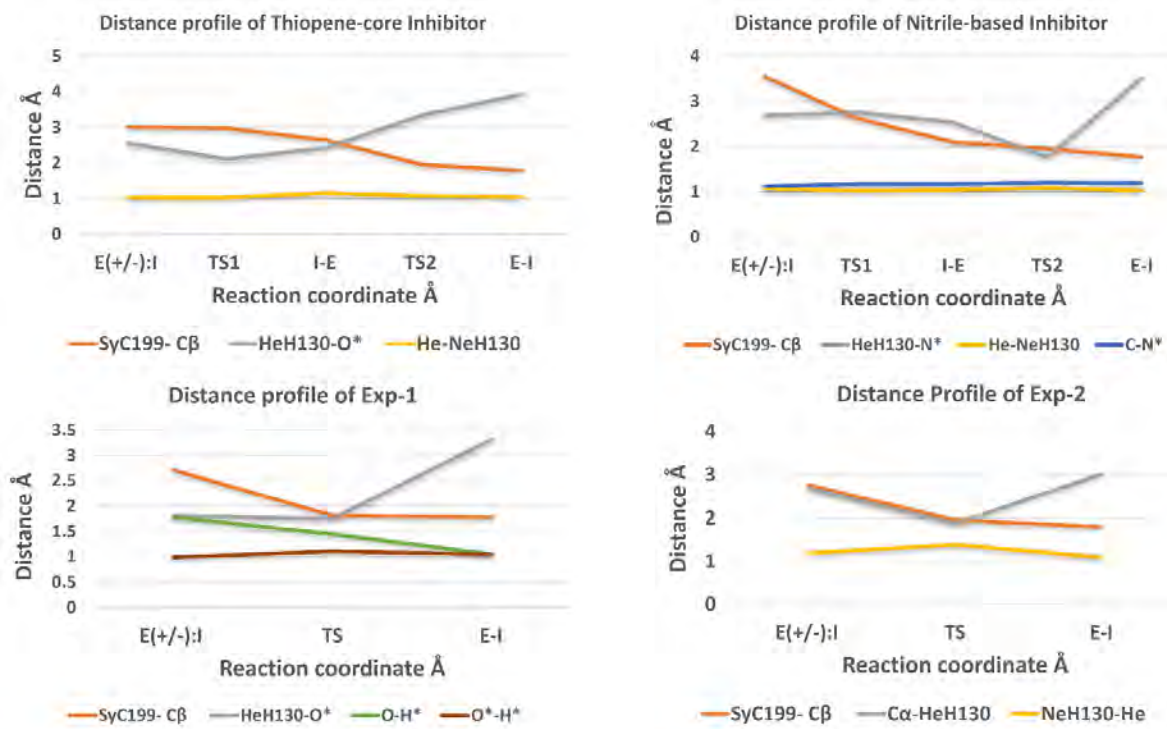


Figure 3.11: Evolution of bond distances along the reaction profile of thiopene-core inhibitor, nitrile-core inhibitor, modified Exp-1 inhibitor with hydroxymethyl ketone, and modified Exp-2 inhibitor with methyl oxo-enoate.

Furthermore, to have insights into significant interactions with neighboring residues at E-I, we optimized TS structures at this state and parametrized it for MD simulations, which revealed significant differences in binding affinities discussed in forthcoming sections. However, ready-to-use parameters are given in **Figure 3.12**. The resulting trajectories exhibited deprotonated His130 in TS1 and a dominant hydrogen bond with O\* stabilized by the formation of two hydrogen bonds, which restrict the protonation of His130 by water molecules is depicted in **Figure 3.18**. Our findings comprehend that the reaction is exergonic where the proton transfer takes place prior to the nucleophilic attack. The same mechanism highlighted by *Marti et al.* revealed proton transfer as low energy barrier step that led to rapid inhibition process<sup>169</sup> thus presenting overall process spontaneous with undetectable inactivation rate-constant. Moreover, similar reaction kinetics are predicted if starting structure is a neutral catalytic dyad than the metastable ion pair E( $\pm$ ):I where

His130 will rather contribute in proton transfer to Cys199, due to surrounding water molecules and highly electronegative O\*.

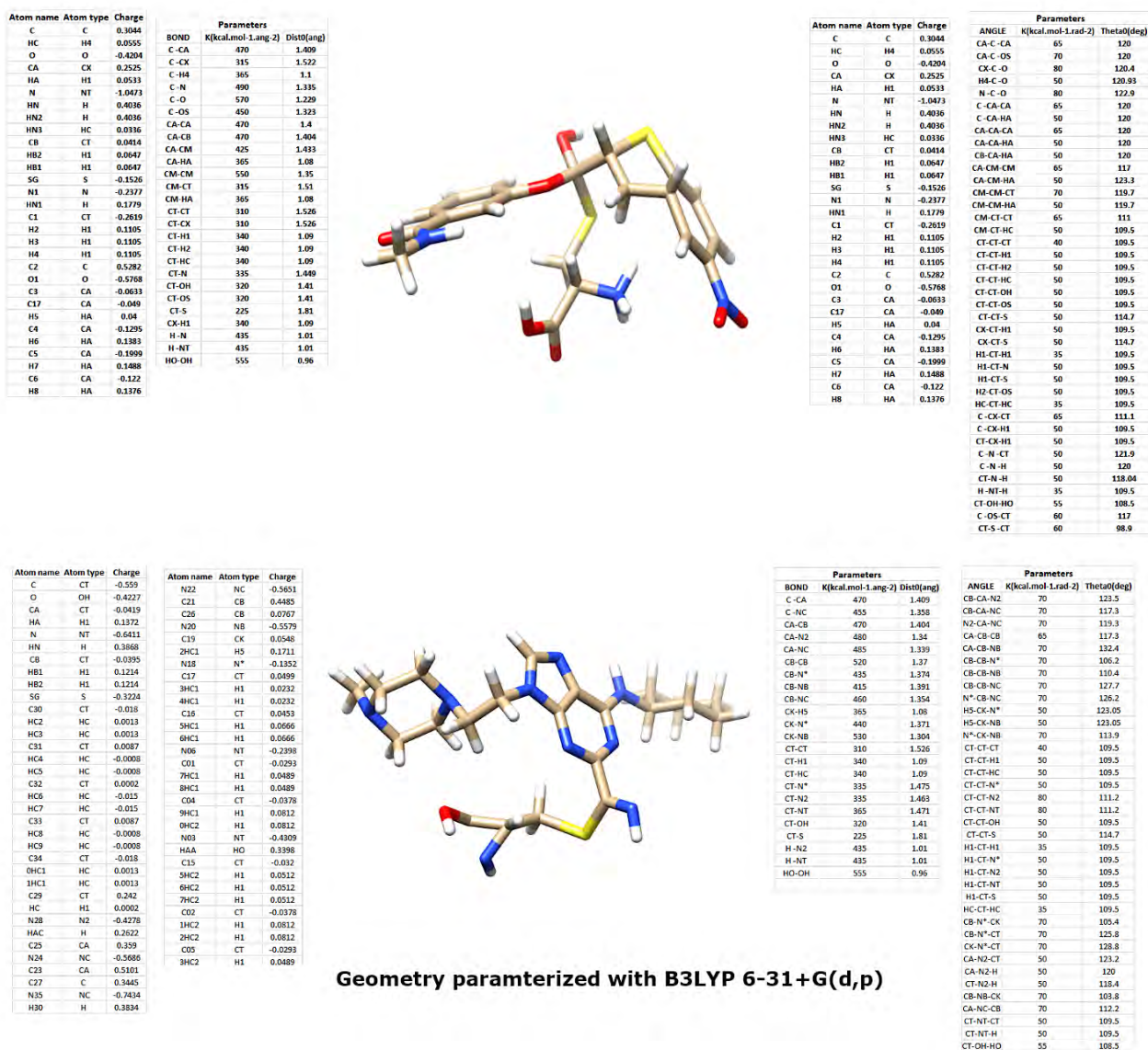


Figure 3.12. Optimized TS structures with B3LYP 6-31+G(d,p) level of theory of thiophene-core inhibitor displayed on top and nitrile-based inhibitor shown at the bottom

### 3.3.2 Reaction mechanism with nitrile-based inhibitor

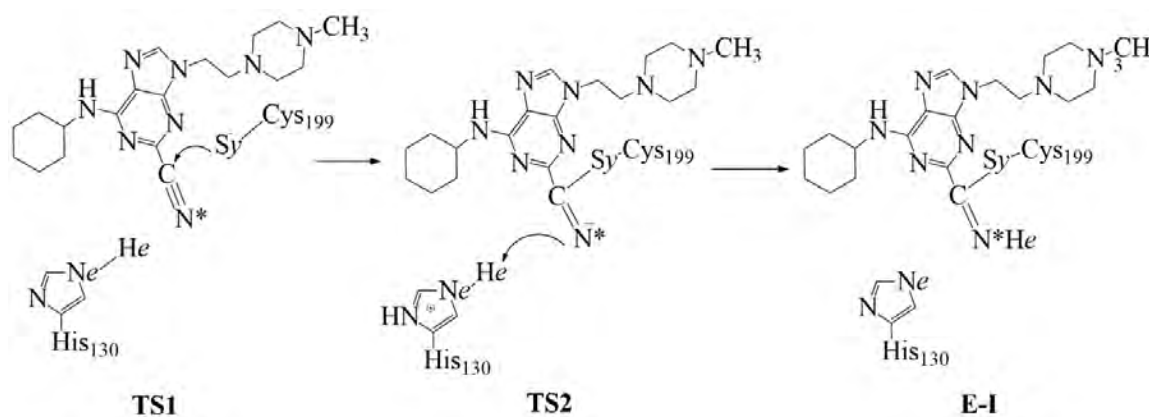
**Scheme 2** represents nitrile-based inhibitor, which unlike thiophene inhibitor exhibited only His130 as its interacting partner in binding groove located at the surface of OxyR (**Figure**



3.4) thus; we kept His130 as doubly protonated and His198 as singly protonated to keep our system neutral.

The PMF of QM/MM US calculations presented in **Figure 3.10** demonstrates the reaction proceedings that is initiated by the electrophilic attack of S $\gamma$ -Cys199 thiolate on the nitrile via TS1 leading to an intermediate (I-E). TS2 however, completed the reaction by proton transfer from H $\epsilon$ -His130 to the substrate and rendered the product complex (E-I). Representative structures of transition states are characterized with B3LYP 6-31+G(d,p) which are illustrated in **Figure 3.13** alongwith their imaginary frequencies.

**Scheme 2:** Proposed mechanism of OxyR inhibition by nitrile-based inhibitor.



A stepwise mechanism with a substrate having imidazolium group deprotonated at the position N $_d$  was observed, which established C-S bond at 1.820 to 1.74 Å and proton transfer originating at a relatively longer distance of 1.89 to 2.6 Å illustrated in **Figure 3.11**. The imaginary frequencies of two transition states TS1 and TS2 separated by the intermediate are  $i592.13\text{ cm}^{-1}$  and  $i428.83\text{ cm}^{-1}$  respectively. Noticeably, the two inhibitors; thiopene-core inhibitor and the nitrile inhibitor have exhibited distinct imaginary frequencies for a proton transfer step *i-e*  $i270.08\text{ cm}^{-1}$  and  $i428.83\text{ cm}^{-1}$  respectively. The characterization of proton transfer is in accord with the study conducted by *Matthew et al.* on nitrile-based inhibitors that displayed longer distances for step-wise reaction mechanisms with comparatively higher imaginary frequencies<sup>74</sup>. Moreover, the covalent bond formation revealed higher energy barrier of  $14.0\text{ kcal mol}^{-1}$  which originated from the initial state E( $\pm$ ):I. Whereas, for the proton transfer, a single route was explored with N\*

due to the limited possibility of proton transfer from neighboring atoms. The energy profile revealed that He-His130 participated in proton transfer with energy barrier of 5.9 kcal mol<sup>-1</sup>

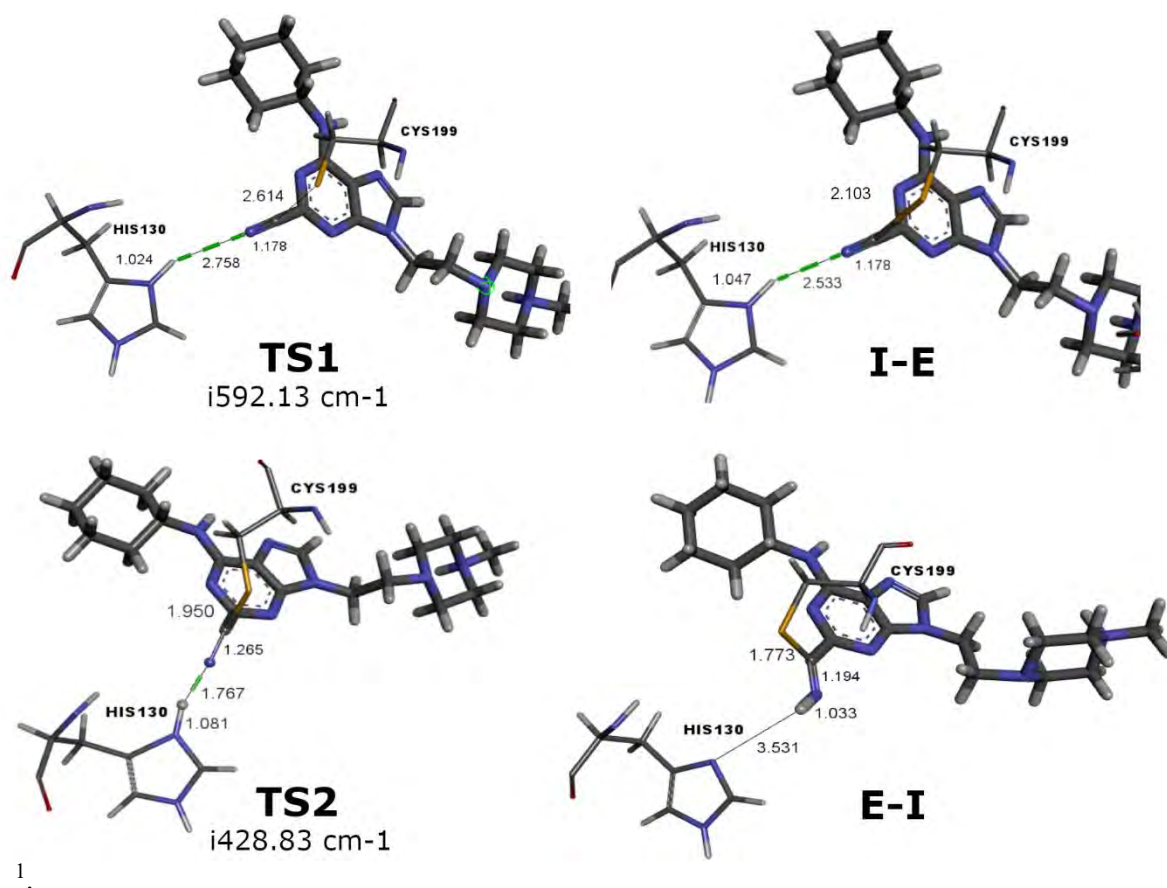


Figure 3.13: Details of DFTB3/MM optimized structures of selected states located along the inhibition reaction of OxyR by nitrile inhibitor. The catalytic residues C199 and H130 are shown with key distances in Å.

The final product E-I rendered an exergonic reaction with -6.1 kcal mol<sup>-1</sup> revealing TS1 as a rate limiting step. Furthermore, the post simulations analysis of covalent complexes demonstrates that unlike thiopene-core inhibitor, contribution of catalytic triad (His130, Cys199, Thr129) was observed instead of a dyad (Cys199, His130) depicted in **Figure 3.18**. His130 after deprotonation drifted away from the catalytic position and was replaced by Thr129, which established strong hydrogen bonding with N\* along with two additional hydrogen bonds between water and HN\* that stabilized the covalent complex.

These findings reinforce the significance of catalytic residues His130 and Thr129 during and after the covalent bond formation.

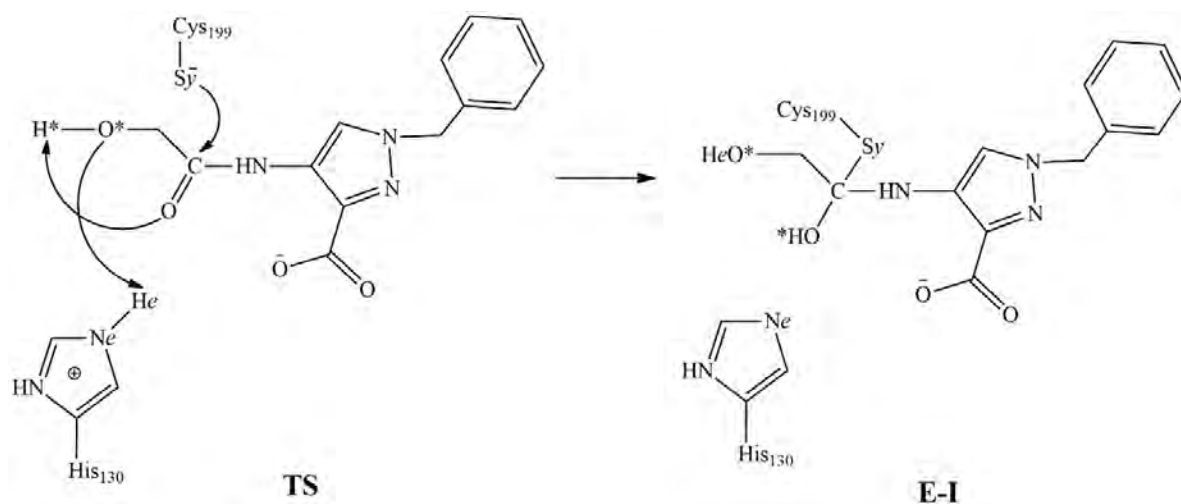
Furthermore, MD simulations of fully optimized E-I structures (**Figure 3.12** for parameters) demonstrate that unlike thiopene-core inhibitor, contribution of catalytic triad (His130, Cys199, Thr129) was observed instead of a dyad (Cys199, His130). His130 after deprotonation drifted away from the catalytic position replaced by Thr129, which established hydrogen bond with N\* alongwith an additional hydrogen bond between water and HN\* that stabilized the covalent complex mentioned in **Figure 3.18**. These findings thus reinforce the significance of proton transfer step that controls the activity of catalytic residues His130 followed by Thr129 during and after covalent complex formation. Nevertheless, TS2 in purine-based nitrile inhibitors are energetically more favorable with higher reactivity, which is concurrent with experimental findings thus leading to a more stable reactant product complex<sup>205</sup>.

### 3.3.3 Reaction mechanism with Exp-1 and Exp-2 inhibitors

The experimental inhibitor of OxyR that was reported in 2021 by *Hyo-Young Oh et al.* presented the first OxyR inhibition study that revealed selective antibacterial efficacy against *P. aeruginosa*<sup>51</sup>. We modified this inhibitor (**Figure 3.2**) with the addition of methyl oxo-enoate and HMK. Multiple possibilities of proton transfer were observed in this case for instance the hydroxyl group was indirectly involved in proton transfer of C $\beta$  carbonyl oxygen, similarly the presence of oxygen on pyrimidine ring anticipated to actively participate in proton transfer. Presence of terminal OH group discussed by Hoffman and co-workers clearly demonstrate the decrease in HMKs potency on its removal<sup>172</sup>. Thus, we particularly focused on terminal hydroxyl group, which rather interacted more actively with the oxygen of pyrimidine compared to He-His130. The distance profile (**Figure 3.11**) demonstrated Sy-C199...C $\beta$  changing from 3.06 to 1.83 Å whereas He-His130...O changed from 3.5 to 2.01 Å. As shown in **Scheme 3**, Exp-1 inhibitor reacts in a concerted fashion comprising single TS leading to the product formation E-I. Initial assessment of binding site revealed active participation between Exp-1 side chain comprising OH and the protein illustrated in **Figure 3.4**. Therefore, it is kept in the loop while investigating the reaction mechanism and was incorporated in QM/MM

calculations. The reaction comprised nucleophilic attack by  $S\gamma$ -Cys199 on  $C_{\beta}$  atom of Exp-1 leading to Cys199-Sc bond formation and simultaneous proton transfer from adjacent He-His130 to the  $O^*$  atom of  $C_{\beta}$  rendering a product complex E-I. The representative snapshots along the reaction path are demonstrated in **Figure 3.14** whereas the energy barrier of reaction is  $14.1 \text{ kcal mol}^{-1}$  demonstrated in **Figure 3.15**.

**Scheme 3:** Proposed mechanism of OxyR inhibition by Exp-1 hydroxymethyl ketone inhibitor.



Consequently, a single transition state is characterized with imaginary frequency  $i912.47 \text{ cm}^{-1}$  depicting simultaneous process comprising both the nucleophilic attack and the proton transfer. The transition state TS identified as maximum of PMF has been optimized and characterized using the B3LYP/6-31+G(d,p). The proton transfer from He-His130 originated from a slightly shorter distance of  $1.746 - 1.815 \text{ \AA}$  compared to the C-S bond formation at a distance  $2.312 - 1.785 \text{ \AA}$ .

Furthermore, the distance evolution profile depicts that proton transfer takes place indirectly via the OH group of the substrate, which transfers H\* to the O\* atom of C $\beta$  and simultaneously accepts a proton from Ne-His130. Thus, the rate limiting step of the full inhibition involves protein acylation along with the proton transfer from His130 to the carbonyl oxygen of the inhibitor. The activation energy of Exp-1 is slightly higher than thiophene-core inhibitor, which makes it kinetically less favorable. The E-I complex of Exp-1 inhibitor with  $4.7 \text{ kcal mol}^{-1}$  is, however, indeed slightly favored over the thiophene-core

inhibitor with  $5.5 \text{ kcal mol}^{-1}$ . Parameters of fully optimized Exp-1 QM system are readily available and presented in **Figure 3.16**.

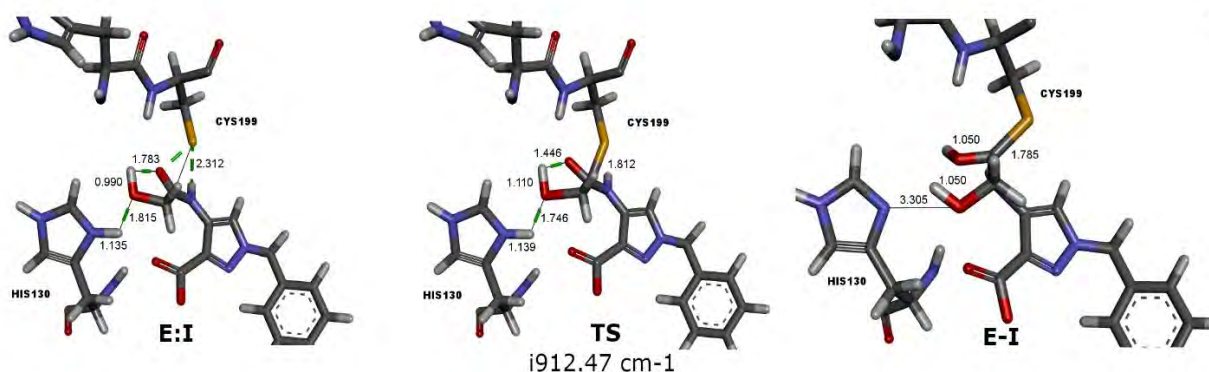


Figure 3.14: Details of DFTB3/MM optimized structures of selected states located along the inhibition reaction of OxyR by Exp-1 inhibitor. The catalytic residues C199 and H130 are shown with key distances in Å.

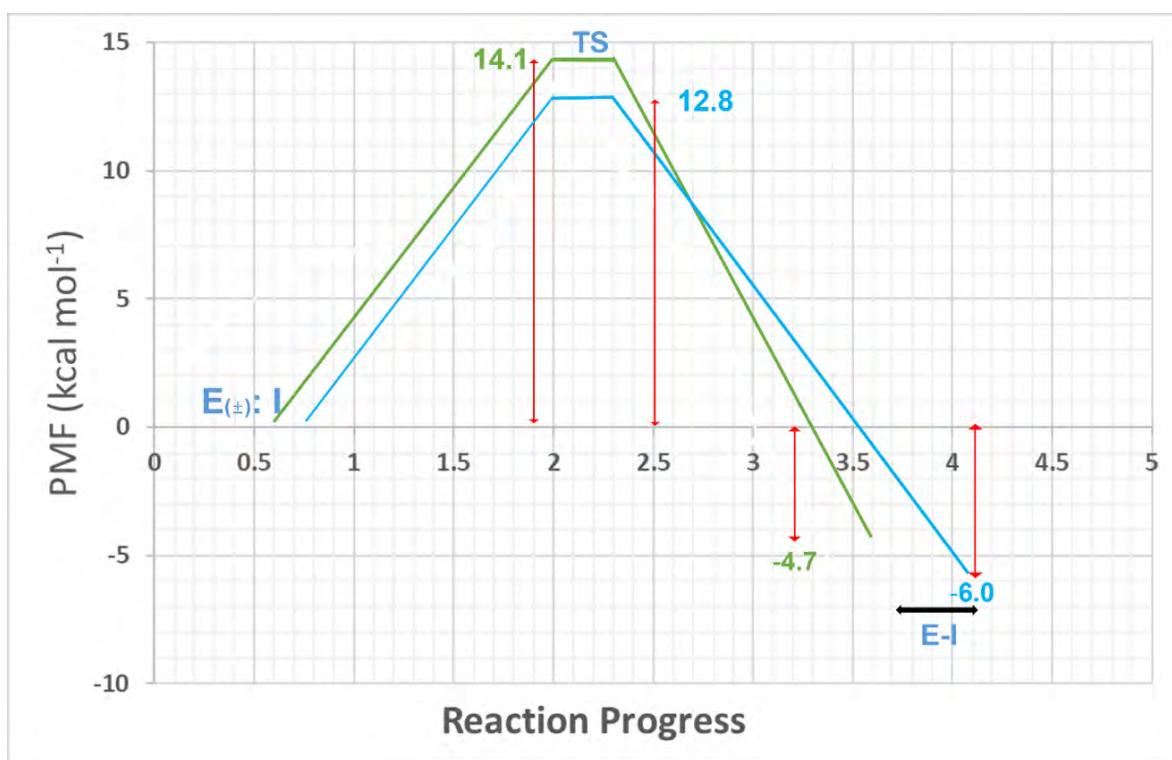


Figure 3.15: DFTB3/MM free energy profile obtained from QM/MM umbrella sampling calculations for inhibition of OxyR. The inhibition mechanism of Exp-1 and Exp-2 inhibitors is illustrated in green and blue colours respectively. Red arrows indicate the relative Gibbs free energies ( $\Delta G$ ) for all stationary points.

Furthermore, the inhibition mechanism proposed by the second modified experimental inhibitor referred as Exp-2 encompasses methyl oxo-enoate is depicted in **Scheme 4**. The active site of Exp-2 exhibits the catalytic triad (Cys199, His198, His130), actively engaged in making interactions with  $C\alpha$  of the Exp-2 lying at a distance less than 3 Å (**Figure 3.8**).

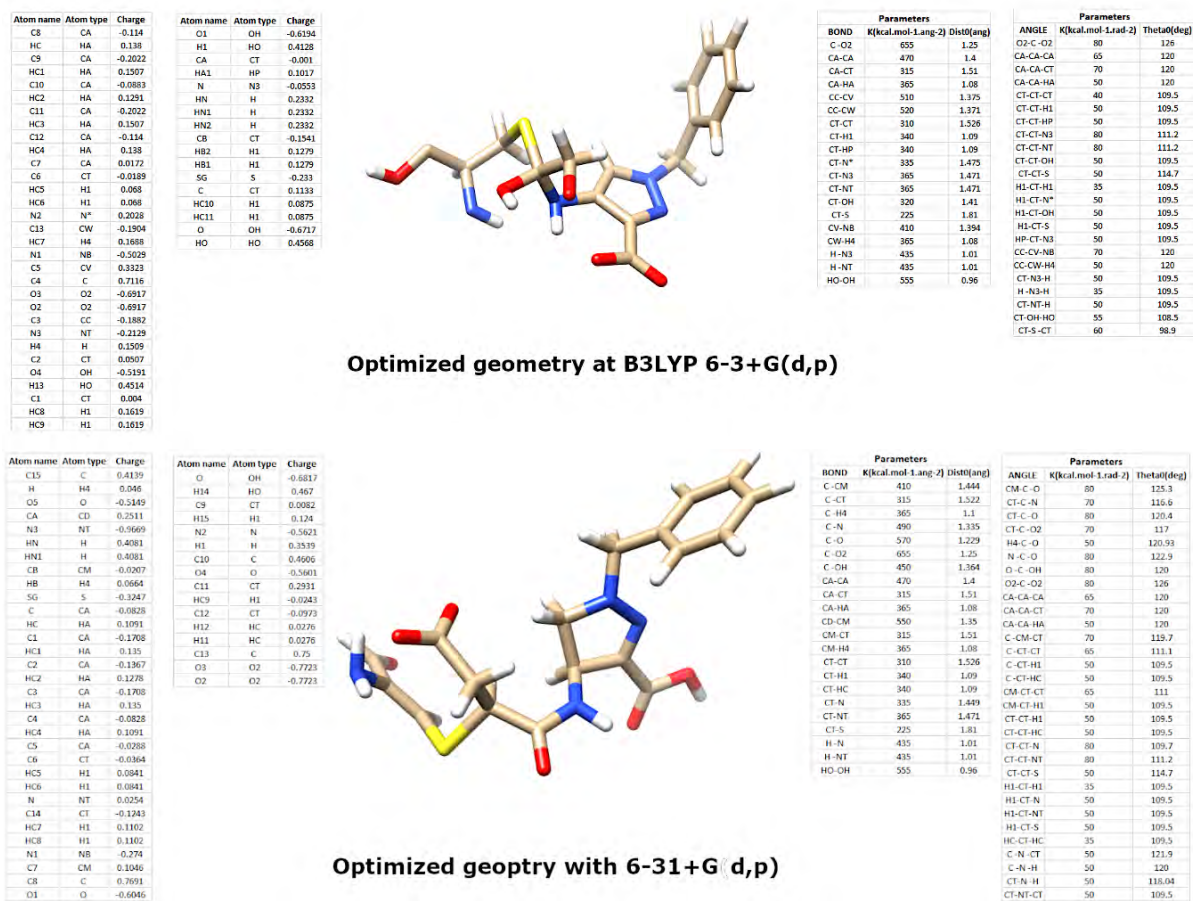
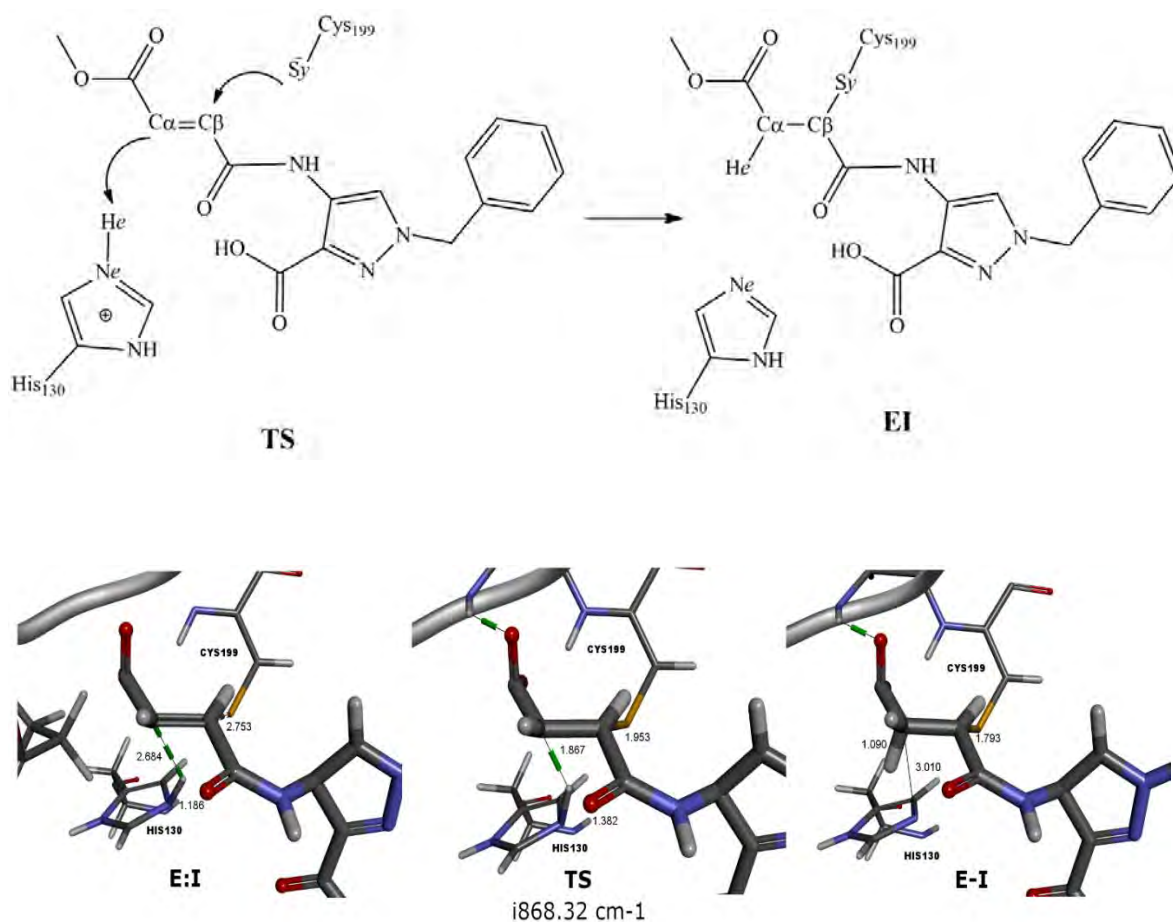


Figure 3.16: Optimized TS structures with B3LYP 6-31+G(d,p) level of theory of Exp-1 with hydroxymethyl ketone displayed on top and Exp-2 having methyl oxo-enoate is shown at the bottom.

Multiple routes with similar warhead were proposed by *Sergio et al.* that characterized proton transfer at  $C\alpha$  to be more favorable both kinetically and thermodynamically while employing M06-2X/6-31+G(d,p)/MM<sup>36</sup>. Therefore, a single route was observed to examine proton transfer from  $C\alpha$  atom. The PMF (**Figure 3.15**) and QM/MM US snapshots displayed in **Figure 3.17** determine that the reaction underwent

nucleophilic attack from  $S_{\gamma}$ -Cys199 on  $C_{\beta}$  atom of Exp-2 and simultaneous proton transfer from neighboring residue His130 to  $C_{\alpha}$  atom.

**Scheme 4:** Proposed mechanism of OxyR inhibition by Exp-2 inhibitor with methyl oxo-enoate.



31+G(d,p)/MM level with Red server and used as representative snapshots for Gibbs free energy calculations. Starting from thiophene-core compound, it was observed that  $\text{NO}_2$  extended its interactions with Gly197 in TS2 whereas [3-(Methylcarbamoyl)phenyl] acetate exhibited interactions with Ala60 and Pro62 by the end of simulations, which has forced the ligand to move inside the cavity of OxyR demonstrated in **Figure 3.19**. Moreover, slight structural shift in thiophene-based compound was observed in TS1 to interact with His130 that was favored despite the presence of water molecules.

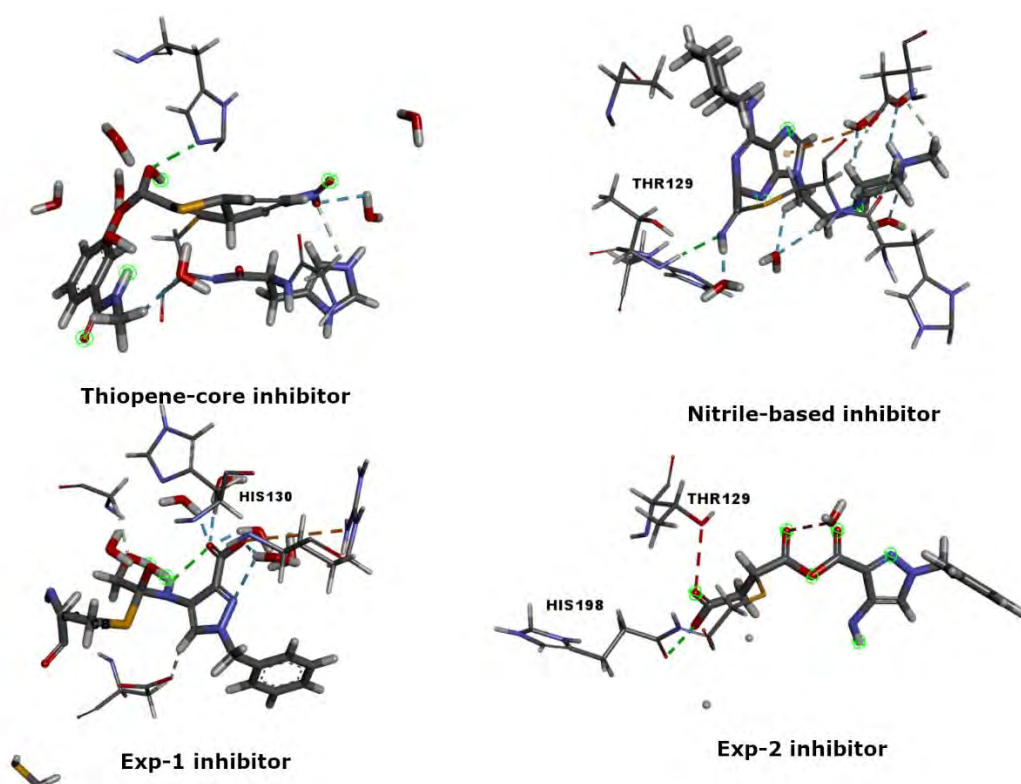


Figure 3.18: Snapshots of four proposed covalent inhibitors from 10 ns QM/MM US simulations carried out with DFTB3 level of theory.

Whereas the second nitrile-based inhibitor did not demonstrate any significant changes in the binding site of OxyR except the possibility of electron sharing with neighboring water residue lying at  $2.5\text{\AA}$ , which is greater than O-Ne-His130  $1.29\text{\AA}$  depicted in **Figure 3.19**. Increase in contribution of interacting residues particularly Thr, Arg and His that comprise catalytic triad of OxyR, thus has direct role in enhanced binding affinity at E-I state displayed in **Figure 3.19**. Furthermore, two experimental compounds



especially Exp-2 exhibited extensive hydrogen bonding using its negatively charged oxygen atom of the enolate moiety with residues His198 and Gly197 of OxyR.

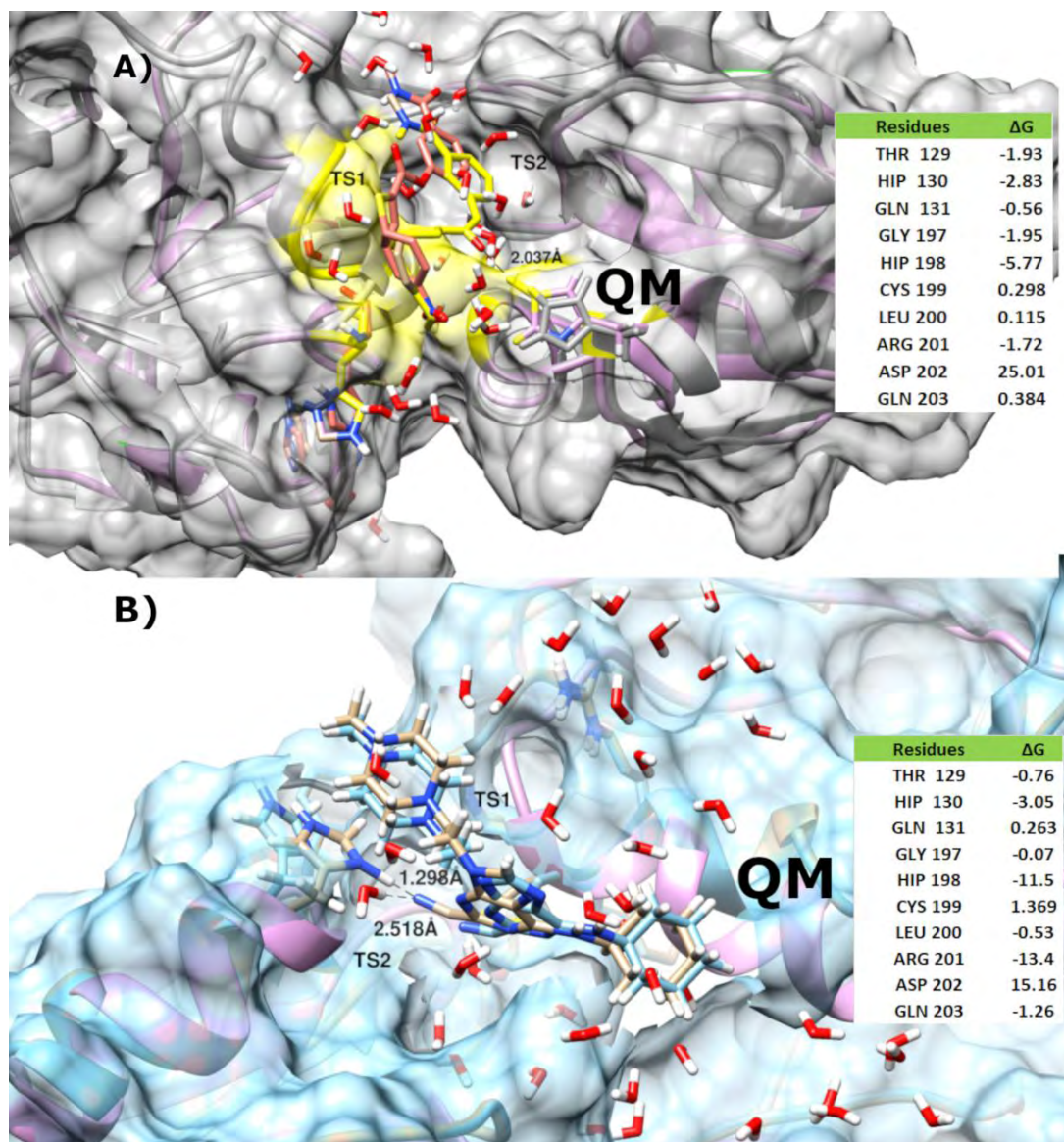


Figure 3.19. A) Overlap of the QM region of TS1 and TS2 of thiopene-based inhibitor optimized with 6-31+G(d,p)/MM level B) Overlap of the QM region of TS1 and TS2 of nitrile-based inhibitor. Favourable interaction free energy values (electrostatic plus Lennard-Jones) observed between binding site of OxyR and proposed inhibitors calculated at E:I and E-I states are mentioned respectively.

Similarly, activity of compound Exp-1 is concurrent with the activity of final step in QM results where the OH groups involve Thr129 in making interactions. Role of

catalytic triad and Arg133 is obvious in stabilization of two modified experimental inhibitors, which is demonstrated in **Figure 3.20**.

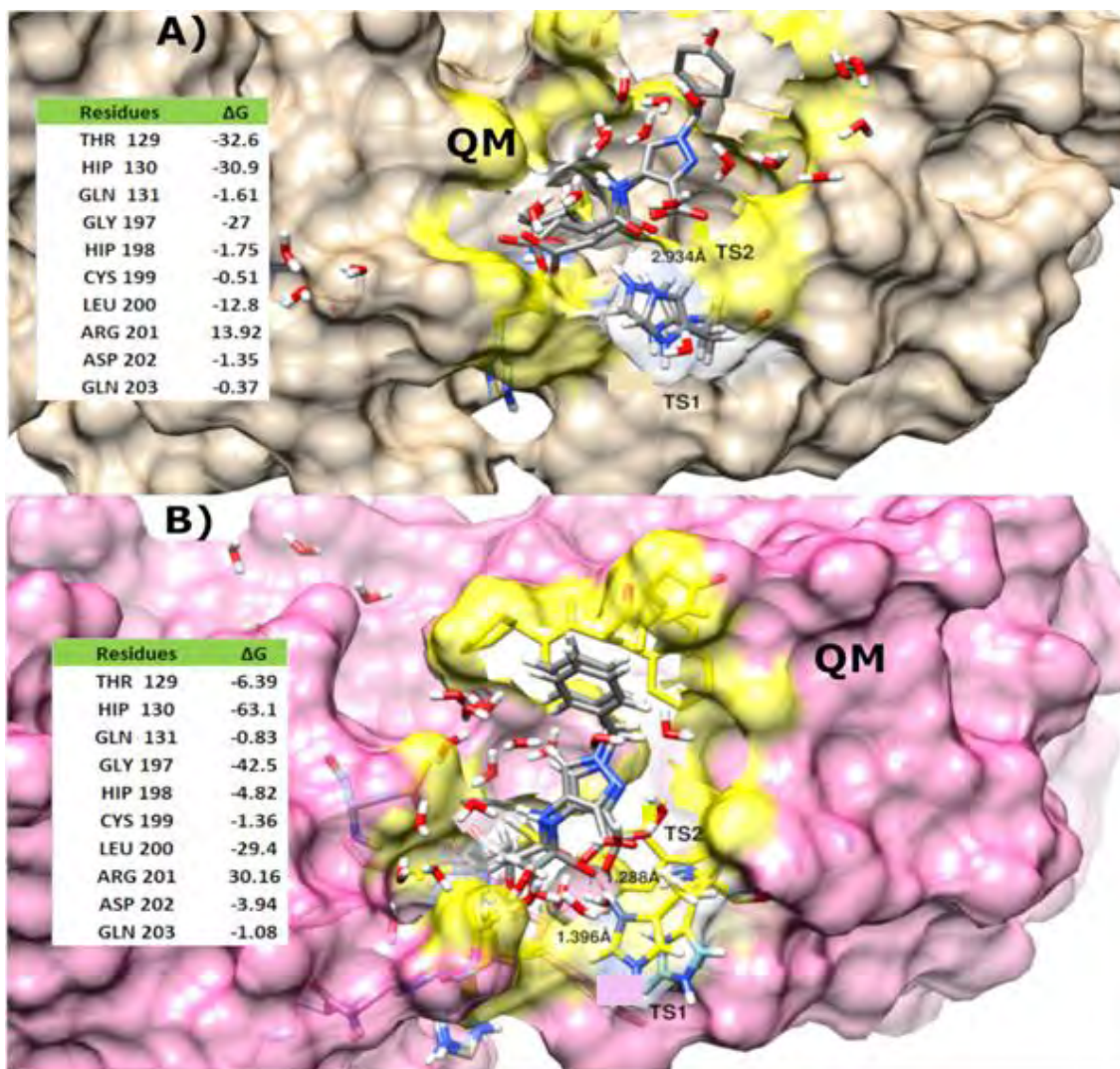


Figure 3.20. A) Overlap of the QM region of TS of Exp-1 inhibitor optimized with 6-31+G(d,p)/MM B) Overlap of the QM region of TS of Exp-2 inhibitor. Favourable interaction free energy values (electrostatic plus Lennard-Jones) observed between binding site of OxyR and proposed inhibitors calculated at E:I and E-I states are mentioned respectively.

Notably, oxygen atoms present in the core of compounds Exp-2 and the side chains extend its interactions with Arg133 and Thr129; residues critical for the function of OxyR<sup>161,173</sup>. These findings are concurrent with the experimental mutational studies that reported the loss/decrease of catalytic activity due to mutation of these residues<sup>162,206</sup>. Thus,

direct role of these residues in enhanced binding energies at E-I state reaffirms the conformation of ligands in the active site of OxyR suitable for its activity. Lastly, the participation of catalytic triad as acid base catalysts is apparent in the active site of OxyR that facilitates protonation and deprotonation of residues during covalent bond formation.

### 3.4 Concluding remarks

This study provides insights into the detailed QM/MM analysis of OxyR inhibition with four proposed covalent inhibitors encompassing different chemical warheads. We particularly focused on incorporating compounds capable of interacting differently in their chemical environment and exhibit respective reaction mechanisms with OxyR active site. The proposed compounds include nitrile-based inhibitors, thiopenes, and a recently reported experimental inhibitor of OxyR.

In a first step, a known covalent inhibitor (nitrile-based) was explored to provide detailed information on the formation of covalent adduct and proton transfer to lay strong basis of reaction mechanism and opportunistic interactive residues of OxyR such as Cys199, His198, and His130. Together with these results and the literature reported on other cysteine protease inhibitors, we modified the experimental inhibitor by the addition of methyl oxo-enoate and HMK. The calculated FEP of US revealed that out of the four studied inhibitors, two proceed in a concerted fashion undergoing simultaneous nucleophilic attack and proton transfer leading to the covalent bond formation and the two react in a stepwise mechanism. The thiophene-core and nitrile-based inhibitors underwent nucleophilic attack and proton transfer in a stepwise mechanism with two transition states separated by the intermediate. The energy profiles of these two inhibitors illustrate the nucleophilic attack as the rate-limiting step with free energy values of 14.0 and 13.6 kcal mol<sup>-1</sup>, respectively.

Nevertheless, impact of warhead modulation was apparently more valuable in terms of both kinetics and thermodynamics involved in the proton transfer step. Proton transfer is a crucial rate limiting step whose significance in different biological processes especially between organic molecules is evident through various substantial work conducted under the domain of both experimental and computational frameworks<sup>207</sup>. For instance, in the current study, the thiophene-core inhibitor exhibited a stepwise mechanism

where the enol formation via proton transfer occurred before the nucleophilic attack. Similarly, the mechanism of proton transfers for Exp-1 and Exp-2 inhibitors differ largely due to the terminal hydroxyl group lying in the side chain, which modulates the proton transfer and exhibit significant interactions, particularly in the presence of water molecules in the surroundings. The transition states characterized with imaginary frequencies are in line with the energy profiles which demonstrate the effect of warhead modulation on the kinetics and thermodynamics of the process.

Furthermore, the comparative analysis of interactions energies of the active site residues supports the binding potential of the proposed inhibitors in the reactive conformations. The role of the catalytic triad (Cys199, His130, and Thr129) in imparting stability to covalent complexes is apparent in all reactions, which is concurrent with the experimental mutational studies of OxyR<sup>173</sup>. List of updated parameters and Cartesian coordinates of all states are given in Appendix Table A1-A8.

In summary, this study serves as a foreword to characterize the chemical inhibitors of OxyR that explored its binding environment and exhibited the effect of multiple warheads and their modulation on the reaction mechanism of this enzyme. Thiophenes and nitrile-based inhibitors that have been frequently used in the formation of covalent inhibitors have provided powerful insights. Furthermore, with further biochemical evidence of the experimental inhibitor, it would serve as a valuable template in the design of selective covalent modulators of OxyR in future.

This research work has been published in *Journal of Physical chemistry B* by the ACS publishers and can be found in the publication section of this thesis.

---

## CHAPTER 4

---

### Competo-Allosteric Regulation and Binding Pattern Dynamics of DSPI Protein of *Pseudomonas aeruginosa*

## 4 COMPETO-ALLOSTERIC REGULATION

### 4.1 Background

Bacterial virulence mechanisms have emerged as new potential targets for the progression of antibacterial mediators. These mechanisms include pervasive signaling pathways that are of vital importance in many of these processes, such as the quorum-sensing (QS) signaling system<sup>211</sup>. In many pathogenic bacteria, QS signaling is a significant controlling factor that contributes to bacterial virulence and persistence<sup>212</sup>. *Pseudomonas aeruginosa*, one of the foremost causes of nosocomial infections, is primarily controlled by QS<sup>213</sup>. Therefore, inhibiting these signaling pathways represents attractive strategies for developing novel therapeutics against *P. aeruginosa* infection<sup>214 215</sup>. So far, the frequently studied QS system in *P. aeruginosa* is the one established on the DSF fatty acid (FA) signal *cis*-11-methyl-2-dodecenoic acid (CDA), formerly justified in *Xanthomonas campestris* (*Xcc*)<sup>216</sup>. The diffusible signaling factor (DSF)-based QS system has been recognized as an extensively preserved cell-cell communication mechanism in Gram-negative bacteria<sup>217</sup>. Lately, a small messenger fatty acid molecule *cis*-2-decenoic acid (CDA), produced by *P. aeruginosa*, is reported to work as the autoinducer of biofilm dispersion. The role of this molecule has also been observed in multiple Gram-negative and Gram-positive bacteria to enhance the biofilm dispersal<sup>218</sup>.

Recently reported protein DSPI has been identified as a significant virulence factor in *P. aeruginosa* and further characterized as an essential enzyme for CDA biosynthesis<sup>219</sup>. Significant homology to RpfF in *Xcc* has been observed in the gene sequence for this protein. DSPI is a member of the crotonase superfamily (CS), demonstrating a common crotonase motif and assembles as a homotrimer<sup>220</sup>. The structural representation of DSPI in biological assembly and as a monomer is depicted in **Figure 4.1**. CS members catalyze diverse metabolic reactions with CoA-ester substrates. Approximately 20 CS reactions, including alkene hydration/isomerization, aryl-halide dehalogenation, carboxylation, CoA ester, and peptide hydrolysis, have been classified in previous studies<sup>221</sup>. As a critical enzyme responsible for the 2,3 double bond formation during CDA biosynthesis, DSPI has been predicted as an Enoyl-CoA hydratase (ECH) according to its sequence alignment with

the rat mitochondrial ECH<sup>222</sup>. To eradicate biofilm dispersion autoinduction in recurrent cultures of *P. aeruginosa*, DSPI was inactivated, suggesting the need to develop a specific inhibitor for the enzyme<sup>219</sup>.

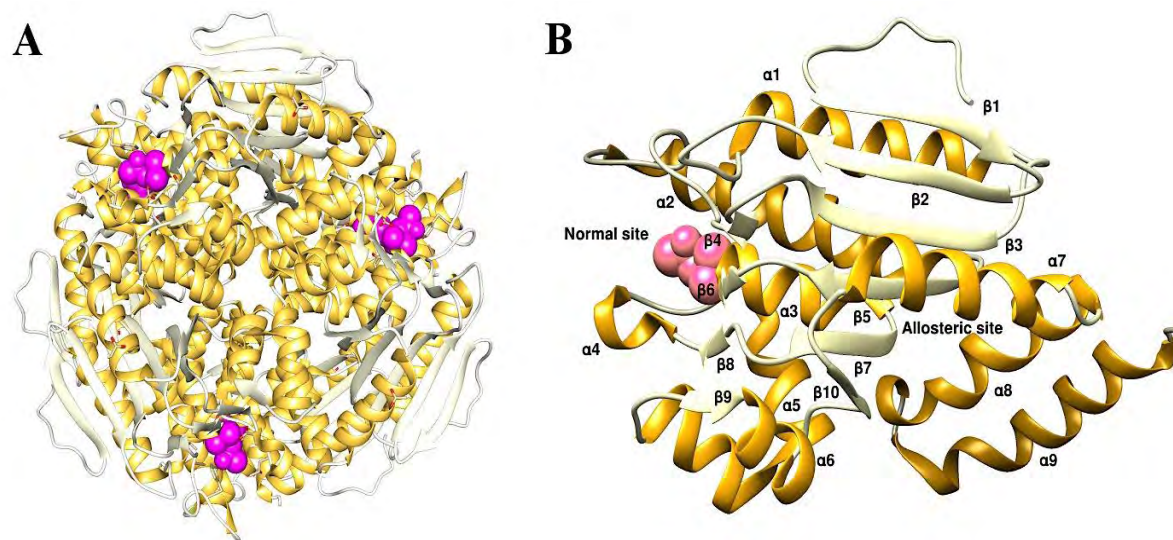


Figure 4.1. DSPI appear as a standard crotonase fold and assembles as a homotrimer. A) Cartoon representation of the DSPI trimer where each binding site is shown in pink color. B) Cartoon style of the DSPI monomer. The secondary structure elements are highlighted and the substrate docked at normal binding site is shown in pink color.

Due to the influx of drug resistant strains in *P. aeruginosa*, the mortality rate is increasing drastically. Therefore, an immense number of approaches is perused, which are directed at developing novel therapeutic drugs. Considering the need for developing new antibiotics against MDR bacteria *P. aeruginosa*, this study unravels the binding mechanism of DSPI bound with CoA substrate and the predicted inhibitors. The current work employs two structure-based drug development approaches to inhibit a potential therapeutic target protein; DSPI. First and foremost, the catalytic binding pocket of DSPI was analyzed to identify the potential inhibitors. The presence of the binding tunnel that passes through the active site of DSPI has been reported recently. The catalytic characteristics of the DSPI active binding site, therefore provide a valuable template for structure-based drug development<sup>223</sup>. The complete workflow of the current study is presented in **Figure 4.2**.

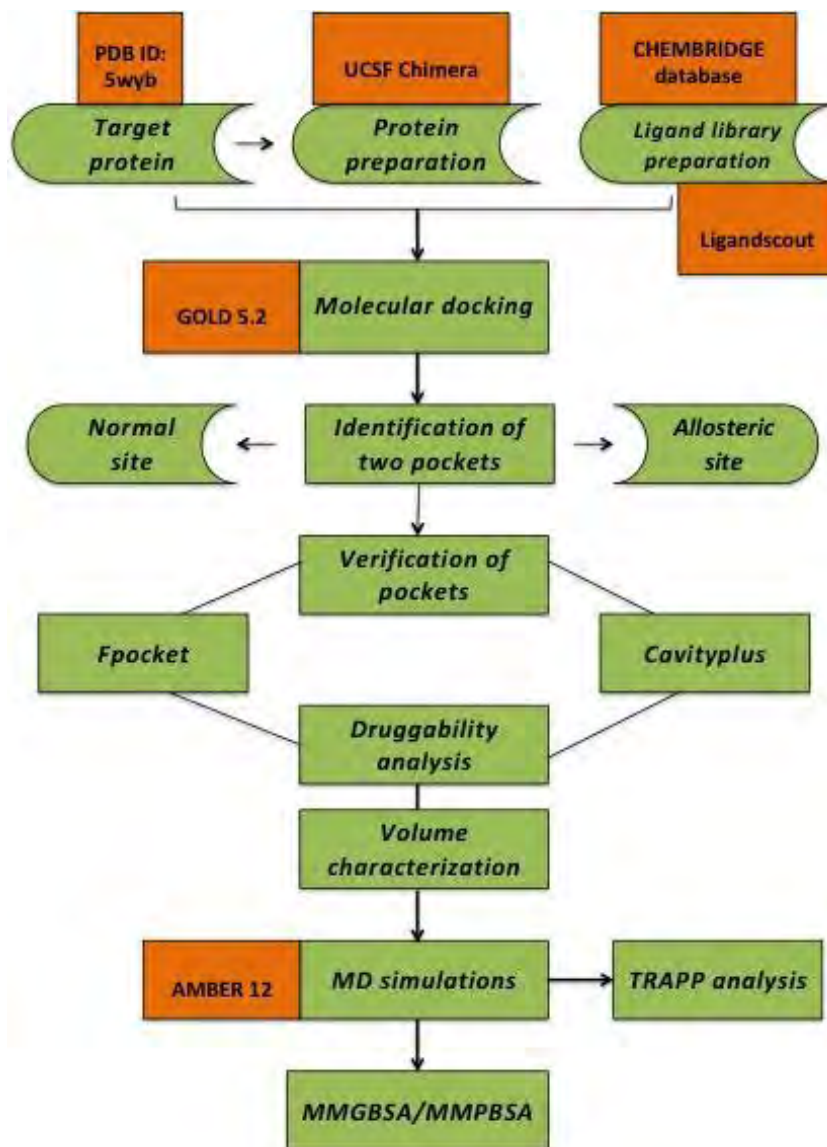


Figure 4.2. Workflow of the current study using different computational techniques.

Secondly, the synergistic or complete antimicrobial activity is attained by focusing on the research studies, which are currently aiming at the salvaging of prevailing drugs by exploring the allosteric mechanism. Typically allosteric sites are targeted to design selective inhibitors to control the enzyme activity and to determine novel functions<sup>224</sup>. Discovering and characterizing new allosteric sites by experimental approaches cannot be regarded as trivial. Alternatively, computational advances are valuable in facilitating researchers to explore potential allosteric sites for drug discovery<sup>225</sup>. For instance, inhibition studies have been carried out on farnesyl diphosphate synthase (Fds) of



*Staphylococcus lugdunensis* using allosteric modulation<sup>226</sup>. Furthermore, the allosteric binding sites of drug-resistant bacteria *Staphylococcus aureus* were exploited, which resulted in the discovery of quinazolinones<sup>227</sup>.

In the present study, we observed the presence of another site in the same binding tunnel as the active site using multiple computational techniques, which was stabilized by strong hydrophobic interactions. Therefore, the current study is also intended to analyze the potential allosteric site in DSPI, which has allowed us to classify both normal binding site inhibitors and allosteric inhibitors. Furthermore, MD simulation studies have been performed to understand the structural and functional dynamics of both sites. The best binding inhibitors identified in this study are also analysed by exploiting free energy calculations, which provide valuable results.

## 4.2 Materials and methods

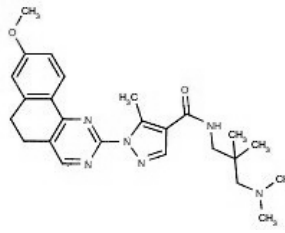
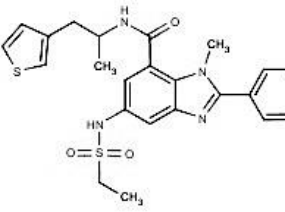
### 4.2.1 Receptor protein preparation

A recently reported crystallographic structure of DSPI with PDB ID: 5WYB was retrieved from the PDB database. The crystal structure refined at a resolution 2.25 Å consists of 272 residues. DSPI is an  $\alpha/\beta$  protein composed of six perpendicular antiparallel  $\beta$ -strands surrounded by eleven  $\alpha$ -helices. It can be split into two domains: the N-terminal spiral domain ( $\alpha 1$ – $\alpha 8$  and  $\beta 1$ – $\beta 6$ ) and the C-terminal trimerization domain ( $\alpha 9$ -end). The helix-helix contacts between the N-terminal extensions together with the trimerization domain of the neighboring monomer are shown in **Figure 4.1**, which stabilizes the homo-trimeric disk assembly<sup>223</sup>. The DSPI protein was exposed to energy minimization to eliminate the steric encounters and to relax the structure<sup>228</sup>. Altogether, minimization was conducted for 1500 rounds. To reduce critical encounters, 750 steps of steepest descent algorithm were initially executed, followed by 750 rounds of slow conjugate gradient method to eliminate the stern clashes, which persisted during the steepest minimization under Tripose Force Field (TFF) in UCSF Chimera. In both the algorithms, the step size was set to 0.02 Å, whereas Gasteiger charges were allocated to the enzyme<sup>229</sup>. After the minimization of DSPI, it was subjected to docking with the library of ligands.

## 4.2.2 Ligand library preparation and molecular docking

After the selection of target and binding site identification, one can conduct high-throughput virtual screening (HTVS) of ligand archives against the target site. For that purpose, 10,000 compounds were virtually screened using CHEMBRIDGE database<sup>230</sup>. These compounds were classified based on chemical properties, such as molecular weight, H-bond acceptor, H-bond donor, tPSA, and rotatable bonds, as presented in **Table 4.1**.

Table 4.1. ADMET and drug-related properties of top two ligand molecules of the normal and the predicted allosteric sites.

Structure	ID	Mol. Weight	Mol. Formula	Log P	RB	tPSA	H-bond Donors	H-bond Acceptors
	1019 5495	448.6	C25 H32 N6 O2	3.58	5	85.17	1	7
	1025 2273	482.6	C24 H26 N4 O3 S2	4.81	6	93.09	2	5

In addition to these compounds, previously reported 3-hydroxydecanoyl-CoA has been docked into the binding pocket of DSPI<sup>223</sup>, and also employed as controls in the current study to compare the behaviour of top-scoring compounds. Lipinski's rule of five was verified for all the compound ligands that passed the check by employing drug-like guidelines in Ligand Scout 4.1<sup>231</sup>. An online SWISS-ADME database was used to extort parameters for drug-like rules<sup>232</sup>. In the end, the MMFF94 force field in Ligand Scout was employed to minimize the subsequent number of inhibitors<sup>233</sup>. After applying the drug-like rules, the entire library was subjected to docking with x, y, z coordinates of active center

residue Glu118. It resulted in the identification of another pocket present in the vicinity of the active binding site to which the ligand preferably bound. In the current study, the potential allosteric site has been identified, which was observed to be competing with the active site for attachment of a ligand; therefore, the name competo-allosteric site has been coined. Further analysis was carried out on both the normal site and competo-allosteric sites to understand the mechanism of ligand binding fully. To select the best docking pose of inhibitors in both its binding sites, GOLD 5.2 (Genetic Optimization for Ligand Docking)<sup>129</sup> fitness score was determined. Visual molecular dynamics (VMD)<sup>234</sup>, Ligplot<sup>235</sup> and UCSF Chimera<sup>236</sup> were utilized to visualize the docking results.

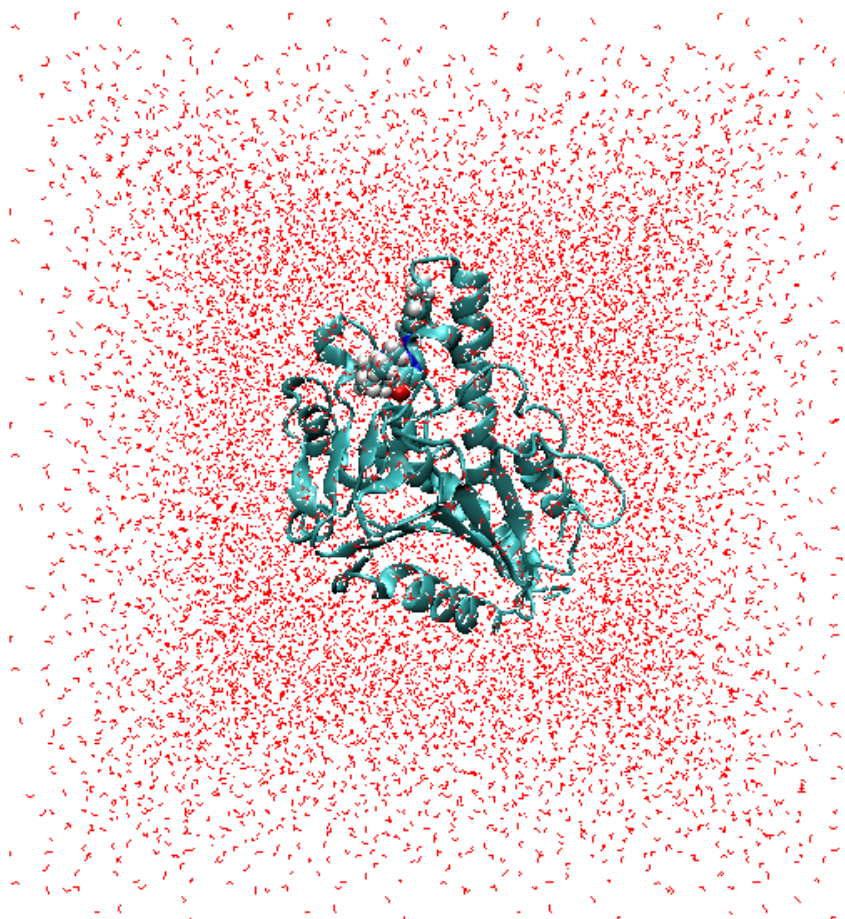


Figure 4.3. 3D structure representation of DSPI protein inside the TIP3P water box.

### 4.2.3 Pocket search

To validate the results obtained from docking and to identify the presence of different cavities of the DSPI enzyme, the Fpocket<sup>237</sup> and Cavityplus<sup>238</sup> were castoff, both of these are easily accessible and open-source pocket recognition software packages. Fpocket obtains the expertise from a firm structure, based on geometric constraints, whereas, a web server Cavityplus offers cavity detection and numerous purposeful analysis. It exploits the three-dimensional structure of a protein to reveal potential binding pockets on the surface and rank them based on ligandability and druggability scores. Compared to the other binding site detection methods, Cavityplus and Fpocket yield highly precise calculations in the bound as well as the unbound protein data sets<sup>238</sup>. An exceptional feature of Cavityplus is that it uses CavityScore to quantitatively determine the ligandability and Cavity DrugScore to ascertain the druggability of an identified binding cavity. The druggability value imitates the potential of a cavity to act as a worthy target for binding drug-like molecules. Whereas the ligandability value signifies the probability of aiming small ligands with elevated binding affinities to a definite cavity. Thus, the minimized PDB structure of DSPI was subjected to pocket search using Fpocket and Cavityplus to predict any druggable pockets that could be fundamental for protein's function. The results obtained from Cavityplus and Fpocket are presented in **Table 4.2** and **Table 4.3** that provide vital information on the possible druggable sites of DSPI.

### 4.2.4 Ligand topology and molecular dynamics simulations

Top-ranked docked complexes obtained from molecular docking were subjected to MD simulation to explore their conformational space and evaluate the binding potential of the proposed lead molecules. SANDER (Simulated Annealing with NMR-Derived Energy Restraints) module in AMBER 16.0 suite with force field FF14SB and GAFF was used to conduct molecular dynamics simulations<sup>239</sup>. MD simulations were conducted on multiple complexes (i) the previously reported crystal complex of DSPI-substrate (ii) a protein complex with a ligand bound to the normal binding site and (iii) a protein complex with a ligand bound to the proposed allosteric site. Docked complexes were initially subjected to energy minimization by 750 steps each of conjugate gradient and steepest descent algorithm through UCSF Chimera 1.10.1<sup>236</sup>.

Table 4.2. CavityPlus scores representing the druggable binding sites of DSPI.

<b>Fpocket Score</b>	<b>Ligand-free state</b>		<b>Ligand-bound to the normal binding site</b>		<b>Ligand-bound to Allosteric site</b>	
	<b>Normal site</b>	<b>Allosteric site</b>	<b>Normal site</b>	<b>Allosteric site</b>	<b>Normal site</b>	<b>Allosteric site</b>
<b>Score</b>	37.84	22.36	21.36	26.923	4.510	6.859
<b>Druggability score</b>	0.726	0.109	0.301	0.030	0.013	0.008
<b>Volume</b>	1832	803.7	412.5	951.542	618.8	450.1

Table 4.3. Differences in volume in the absence and presence of inhibitor at normal and competo-allosteric sites.

<b>No.</b>	<b>Phred. Max pKd</b>	<b>Phred. Avg pKd</b>	<b>Drug score</b>	<b>Druggability</b>
<b>1</b>	11.51	6.56	472.00	Druggable
<b>2</b>	11.39	6.52	2113.00	Druggable
<b>3</b>	7.41	5.16	-820.00	Undruggable
<b>4</b>	7.22	5.09	-1117.0	Undruggable
<b>5</b>	6.65	4.90	-1065.00	Undruggable
<b>6</b>	6.62	4.89	-1197.00	Undruggable
<b>7</b>	5.45	4.49	-1472.00	Undruggable

Energy minimization of the docked complexes was followed by ligand parameterization. Ligand forcefield was generated using the AM1-BCC charge method and topology files using the antechamber module of AMBER<sup>240</sup>. The energy minimization of the solvated systems was also done before conducting MD simulations. Each system was exposed to 1000 steps of conjugate gradient algorithm and 1500 steps of steepest descent algorithm with a nonbonded cut-off of 8 Å. After energy minimization, the system was heated from 0 to 300 K with the shackle of 5 kcal mol<sup>-1</sup> Å<sup>-2</sup> on carbon alpha atoms for 20 picoseconds. The time step for each calculation was set at 2 femtoseconds with

Langevin dynamics<sup>241</sup>. Heating was carried in the NVT ensemble under periodic boundary conditions, and H-atom bond interactions were ignored using SHAKE<sup>242</sup>. Following heating, the system was allowed to equilibrate by applying constraints at various intervals gradually. A time step of 2 ns and 100 ps was applied to equilibrate the systems<sup>243</sup>, whereas systems pressure was maintained using the NPT ensemble for 50 ps. In the end, the production run of 100 ns was carried out in the NVT ensemble. The time step of 2 fs for non-bonded interactions with cut off 8.0 Å was used during the production run. 3D structure of DSPI in TIP3P water box during the simulation is presented in **Figure 4.3**.

### 4.2.5 Simulation trajectories evaluation

The simulation trajectories were generated using CPPTRA<sup>244</sup> and analyzed to validate the conformational stability of docked complexes while snapshots at various nanoseconds were visualized through VMD<sup>234</sup>, UCSF Chimera<sup>236</sup> and TRAPP<sup>245</sup>. TRAPP (Transient pockets in proteins) is a tool that is used to evaluate and analyze the spatial and physicochemical properties of an identified pocket during the molecular dynamics simulation run. The opening and closing of transient sub-pockets along the MD trajectory can be examined using the pocket characteristics tab when exploring the TRAPP-pocket and simulation results. Other than that, different parameters were calculated for all the systems. These parameters include root mean square deviation (RMSD), root means square fluctuations (RMSF), the radius of gyration (Rg) and beta-factor ( $\beta$ -factor). The analysis was further followed by hydrogen bond characterization to illustrate the stability of complexes. Furthermore, the energy calculations were carried out using MMPBSA and MMGBSA in AMBER toolkit to estimate the ligand binding potential<sup>146</sup>. Free energies of systems were computed by employing MMPBSA and MMGBSA, which takes into account the energy differences between protein and ligand and that of the complex. Two methods, namely Poisson-Boltzmann (PB) and Generalized-Born (GB) were applied to conduct the analysis<sup>246</sup>. After every 0.2 ns, a total of 450 frames were extracted from the complete MD trajectory and exposed to MM(PB)SA calculation using MMPBSA.py module of AMBER 16<sup>146</sup>. To have deeper insights into the components, the hot spot amino acids that are significant in binding free energy were analysed. The binding free energy was therefore

fragmented into per residue and pair residues expending MMPBSA.py module of AMBER 16.

### 4.2.6 Validation of study with a positive control

Similar molecular docking and dynamics simulation protocol was implemented on all the predicted complexes. The two proposed complexes were compared to DSPI-substrate to understand the mechanism of normal and competo-allosteric binding sites.

## 4.3 Results and discussion

The current study provides two fundamental approaches critical for the inhibition of DSPI in *P. aeruginosa*. Apart from the inhibition of functional site as reported in the literature<sup>223</sup>, docking and MD simulation studies of DSPI were also carried out on the anticipated allosteric site. The results, however, encouraged us to analyze the inhibition mechanism of both the normal and competo-allosteric binding sites.

### 4.3.1 Docking analysis of DSPI

Docking evaluation determined that among the docked compounds, the best scoring compounds that bound with the normal binding site and the competo-allosteric site have a common benzamide-benzimidazole (BB) backbone. BB compounds have previously revealed to be active against MDR isolates of *P. aeruginosa* and efficiently reduced virulence<sup>247</sup>. Docking analysis of the normal site revealed that it possesses two well-conserved acidic residues Glu118 and Glu138. These two GLU residues are critical for catalysis and have been concluded as one of the structural features to differentiate the ECH hydration activity from the monofunctional ECI or DCI (dienoyl-CoA isomerase) activity<sup>248 221</sup>. In addition to the two catalytic residues Glu118 and Glu138, nearby cysteine residue Cys146 played a critical role in the current computational study. The BB nitro group established a volatile hydrogen bond with the hydroxyl group of Cys146 in DSPI, which was lying adjacent to the hydrophobic pocket of the normal binding site, as shown in **Figure 4.4b**. Among the docked compounds bound at the normal binding pocket, compound 10195495 exhibited the highest GOLD score of 68. The cavity analysis of normal binding site reveals interacting residues Ala70, Phe80, Phe90, Cys146, Leu143,

Leu144, Ala147, Gly119, Glu118, Leu136, Glu138, Gly116, Pro145, Cys119, Gly69, and Gly117 form the normal binding pocket of DSPI as shown in **Figure 4.4a**.

Molecular docking outcomes displayed hydrophobic, cation- $\pi$  interactions and formation of hydrogen bonding between side-chain amino acids and among beta sheets near the vicinity of the active site. These critical non-covalent binding contacts perform a substantial function in ligand detection, protein-drug communications, and structural steadiness<sup>249</sup>. We have therefore investigated the strength of all these forces that play a critical role in stabilizing the ligand-receptor complex. The critical residues of the normal binding site that are significant in hydrogen bonding with the ligand are Glu138, Gly115, Gly116, Ala70, and Cys146. Hydrogen bond donor and acceptor atoms were identified within a distance of less than 3.5 Å. An explicit hydrogen bond with a 3.319 Å distance between compound 10195495 and an O atom of Glu138 was identified. Protein residue Cys146 exhibited 3 H-bonds with N atoms of the ligand depicting 1.906Å, 2.375Å and 2.979 Å hydrogen bond distances, respectively. The impact of hydrophobic interactions was observed to be essential for producing a hydrophobic pocket in the vicinity of 10195495 with a maximum distance of 3.9 Å with residues Ala70, Gly115, Ala87, Ala83, Phe75, Ala68, Ala76, Pro145, Asp77, Gly78, Lys86, and Pro145. These hydrophobic residues are critical for the formation of a hydrophobic pocket that facilitates DSPI interaction with the docked compound N-[3-(dimethylamino)-2,2-dimethylpropyl]-1-(8-methoxy-5,6-dihydrobenzo[h]quinazolin-2-yl)-5-methyl-1H-pyrazole-4 carboxamide.

Another significant molecular interaction force in biological receptors is  $\pi$ -interactions<sup>250</sup> that was witnessed in the regular binding site. It is noticed that the heterocyclic ring of ligand 10195495 formed pi-pi stacked, pi-pi T-stacked and amide-pi stacked interactions with the side chain of Ala8, Phe75, and Phe90 as depicted in **Figure 4.4b**. In general, it is stated that the attractive interactions with heterocyclic ring are less sensitive to substituent effects than the corresponding non-heterocycles<sup>251</sup>. On the other hand, docking analysis of substrate CoA in comparison to the predicted normal site inhibitors revealed H-bonding with Ala87, Gly115, and Phe90. It comprised residues Ala87, Phe90, Gly115, Glu118, Leu143, Leu144, and Cys146. Weak hydrogen bonding with zero pi interactions were observed between DSPI and the substrate, although they



occupy the same binding pocket. The atom-wise interaction details of the highest-scoring compounds involved in hydrogen bonding are given in **Table 4.4**.

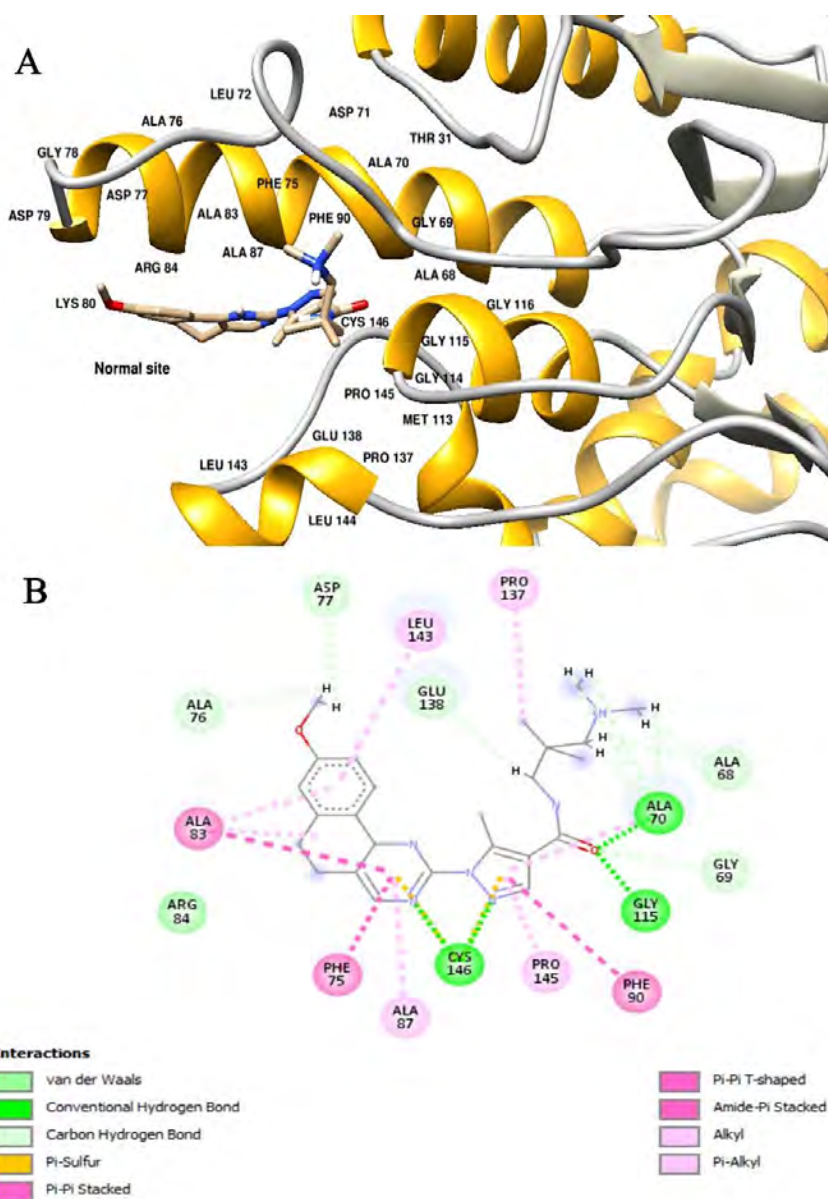


Figure 4.4. Docked inhibitor within the normal binding pocket. A) The docked pose of compound 10195495 highlighting critical residues of the normal binding pocket. Protein is in ribbons whereas ligand is in bond style. B) 2D depiction of the docked complex highlighting hydrogen bonds and cation- $\pi$  interaction through DS Visualizer.

Table 4.4. Interaction details of hydrogen bonding of docked complexes.

Compound	interacting atom of the ligand	interacting atom of the protein	Distance Å
<b>10195495</b> <b>Normal binding site</b>	H	GLU 138: O	3.319
	O	GLY 116: H	3.745
	O	GLY 115: H	1.936
	O	ALA 70: H	2.241
	N	CYS 146: H	1.906
	N	CYS 146: H	2.375
	N	CYS 146: H	2.979
<b>10252273</b> <b>Allosteric binding site</b>	H	LEU 121: O	1.916
	H	GLY 148: O	3.050
	O	ARG 126: H	2.330
	O	ARG 126: H	2.986
	O	ARG 98: H	1.993
	O	ARG 98: H	3.621

However, the compound with the highest score in potential allosteric site was 10252273, exhibiting a GOLD score of 81. Analysis of the docked complex at the predicted allosteric site revealed that it is composed of the residues Phe94, Ala147, Phe181, Gly48, Arg98, Glu118, His42, Ala122, Trp155, Arg222, Arg126, Ala52, Leu156 and Leu121 displayed in **Figure 4.5a**.

MD simulations analysis exhibited the presence of two additional critical residues Cys119 and Cys123 alongwith Glu118 and Cys146 that made this pocket even more stimulating. These two residues Cys119 and Cys123 have also been identified as crucial in the previous experimental studies by *Li Liu et al.*<sup>223</sup>. The predicted allosteric site interacting with compound 10252273 exhibited strong hydrogen bonding with the residues Leu121, Gly148, Arg126, and Arg98, as shown in **Figure 4.5b**. Hydrogen bond interactions were observed between Arg126 (2H-bond) and Arg98 (2H-bond) with O atoms of the ligand having bond distances of 2.33Å, 2.986Å, 1.993Å and 3.621Å respectively. It was also revealed that the heterocyclic ring of ligand 10252273 formed strong hydrogen bonding and cationic interactions with Arg222.

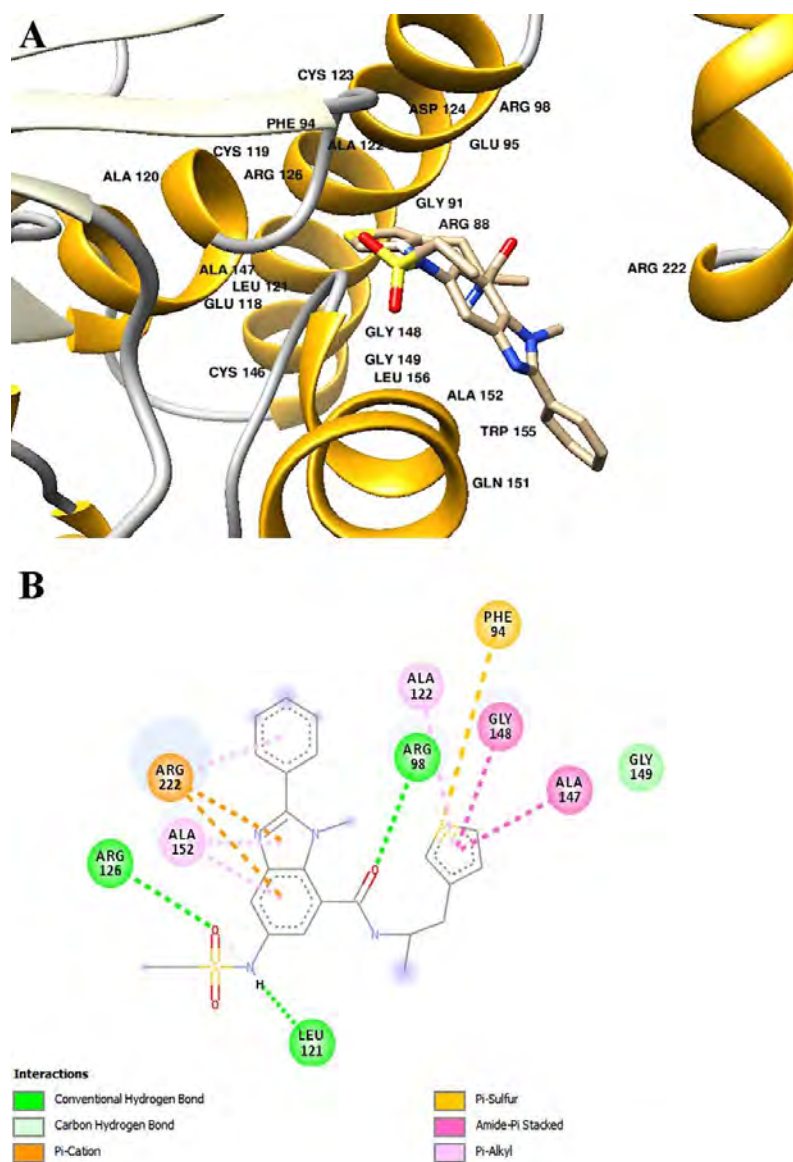


Figure 4.5. Docked inhibitor within the allosteric binding pocket. A) Docked pose of compound 10252273 highlighting critical residues of the allosteric binding pocket. Protein is in ribbons whereas ligand is in bond style. B) 2D depiction of the docked complex highlighting hydrogen bonds and cation- $\pi$  interaction through DS Visualizer.

One pi-sulfur interaction with Phe94, two amide-pi stacked interactions with Gly148 and Ala147, and one pi-alkyl interaction with Ala152 were also observed, which is presented in **Figure 4.5b**. Furthermore, Arg222 and Trp155 were observed to be essential for creating a hydrophobic pocket in the vicinity of ligand 10252273. The docked

complexes in the predicted allosteric binding site also showed variable interactions with  $\alpha 3$ ,  $\alpha 7$ , and  $\alpha 10$  from the neighboring subunit.

Results revealed that a common residue Glu118 in both the normal binding site and predicted allosteric sites appear to be competing for the ligand to attach as depicted in **Figure 4.6**. This phenomenon compelled us to classify the druggable sites of DSPI within the binding tunnel, which resulted in the identification of competo-allosteric site. The entire binding mechanism was dependent on the selection of atoms ('O' and 'OE1') of active center residue Glu118. Upon selection of 'O' atom of Glu118, the ligand preferred to bind to the allosteric site in the same binding tunnel, whereas the selection of 'OE1' atom led to the binding at normal site. However, the role of both the normal and predicted allosteric sites seemed critical while determining their binding mechanisms.

Comparative evaluation of all the docked complexes revealed higher GOLD scores at the proposed allosteric pocket, whereas the normal pocket yielded slightly lower GOLD scores. The highest GOLD score of 81 was attained for compound 10252273, which was docked against the allosteric pocket of DSPI, whereas the normal pocket exhibited the highest GOLD score of 68. Notably, the critical residue Glu118 played a vital role in the binding of inhibitors at both the normal and proposed allosteric binding sites. The current analysis indicated the presence of a site within site competing with each other upon ligand binding. The mechanism of both the hydrophobic allosteric pocket and the normal pocket, and how it can provide an alternative route to inhibit the mechanism of DSPI, has been further explored through MD simulations.

### 4.3.2 Crystal structure of DSPI

The overall structure of DSPI in complex with both the inhibitors was then compared with its ligand-free form and DSPI ligand binding domain in crystal structure, which was fused with R) 3-hydroxydecanoyl-CoA as illustrated in **Figure 4.7**. Results revealed that there was no obvious conformational change observed in DSPI when it was bound with inhibiting compounds at both the sites separately compared to when it was fused with a substrate.

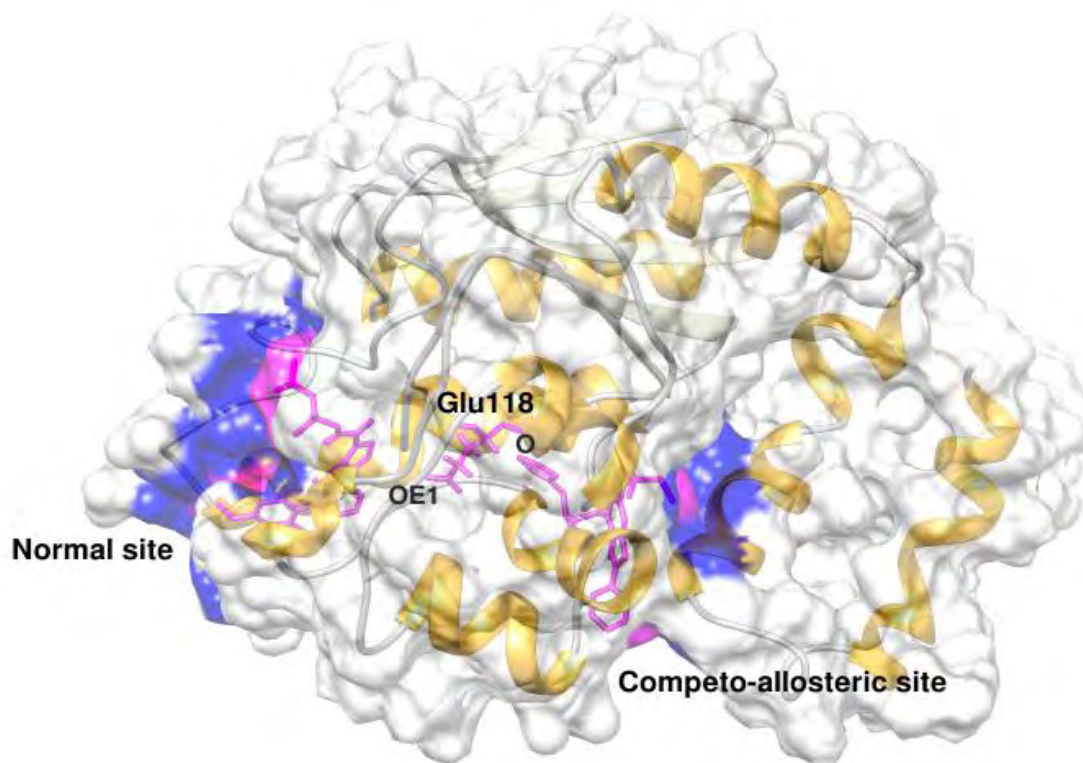


Figure 4.6. The normal binding site and the competo-allosteric site in the same binding tunnel competing with each other for ligand binding. Electronegative atom “OE1” interacted with a ligand bound at the normal binding site, whereas interactions between “O” atom of Glu118 and ligand attached at the allosteric site were observed.

However, subtle native conformational changes were observed in the region of helices  $\alpha 9$  (residues 208 – 223) when compared the normal site complex to the ligand-free DSPI. The residue Glu138 was observed to be present in the form of beta-sheets to make direct hydrophobic contact with DSPI, making a triad with Cys146 and the binding tunnel passing through the active site in all the docked complexes, as shown in **Figure 4.7**.

### 4.3.3 Druggability analysis

The identification of the binding cavities by Fpocket together with the prediction of Cavityplus assisted in understanding the principles of molecular binding and allosteric modulation. Binding cavities on protein surfaces are imperative for protein function because they expedite the binding of the protein to other biological macromolecules such as nucleic acids and proteins, or small molecules such as metabolites and drugs<sup>252</sup>.

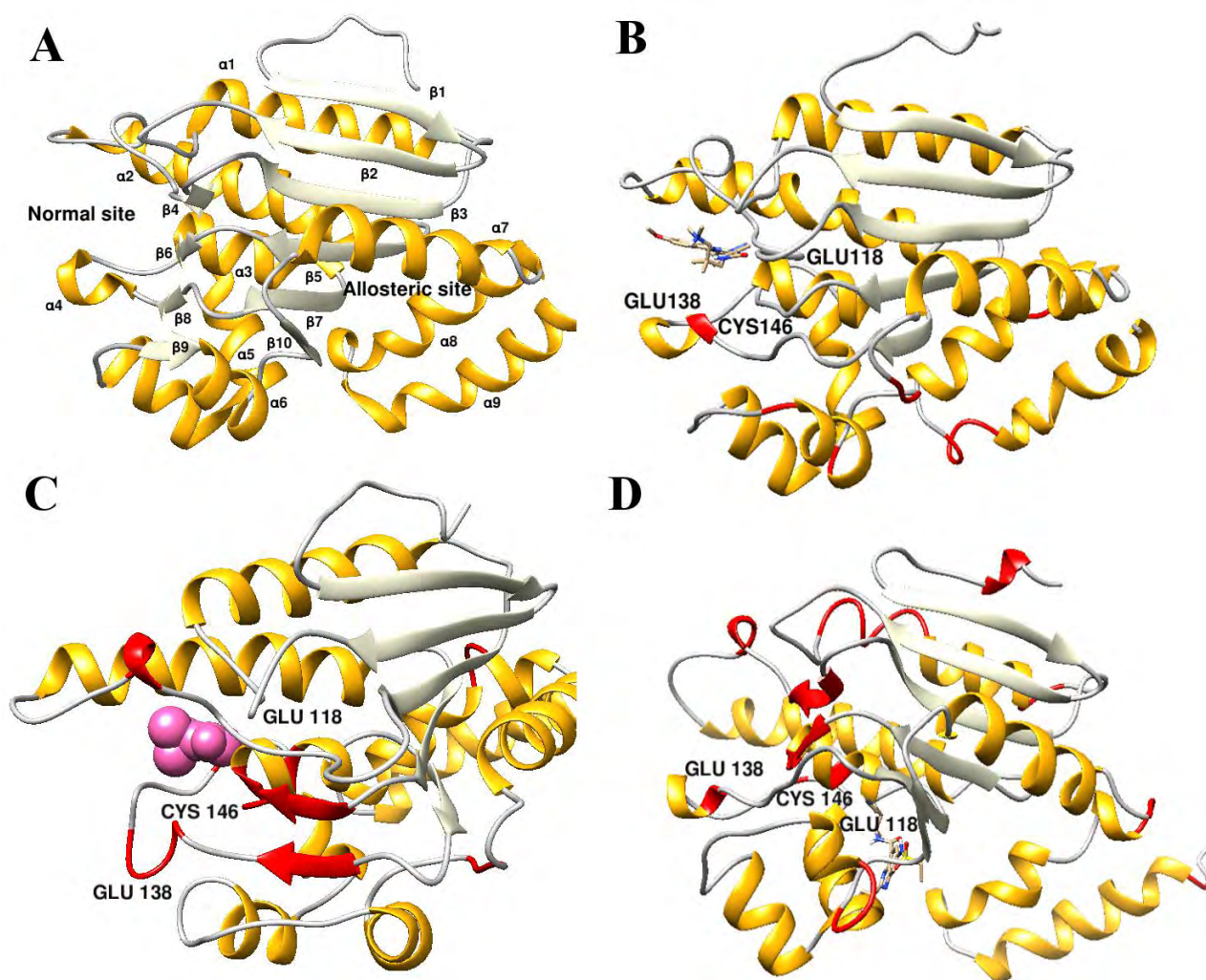


Figure 4.7: Structural changes upon ligand binding at the normal and the competo-allosteric site during docking. Structural rearrangements are mentioned in red with the critical residues highlighted in each conformation. A) DSPI without ligand B) 10195495 docked at the normal site C) DSPI with substrate D) 10252273 docked at the competo- allosteric site.

Computational identification of protein cavities has been contemplated as a vital step for efficient annotation of proteins and structure-based drug design<sup>253</sup>. In the current study, Fpocket predicted 11 cavities, whereas Cavityplus detected 7 cavities, out of which only two were categorized as putative druggable binding sites based on the druggability prediction score given by both the programs. The best-ranked sites were the site 1 that indicated the presence of potential allosteric site and site 2, which corresponded to the

normal binding site. Cavityplus and Fpocket analysis given in **Table 4.2** and **Table 4.3** revealed significant results. **Table 4.2** displayed the values obtained from Cavityplus in which Phred. Max pKd value indicates the ligandability of a cavity-binding site. A value of less than 6.0 suggests that this may not be a suitable binding site. Whereas, the results obtained by Fpocket are presented in **Table 4.3**, in which the score indicates the number assigned by the Fpocket to the predicted sites in the given structure (the higher the score, the better the binding site). The druggability value indicates the possibility of a cavity binding site to be druggable or not. Inspection of residues of both the sites revealed the presence of critical residues Glu118, Cys131, Glu138, and Cys146, which were also indicated during docking analysis. According to both the programs, normal binding pocket, and the predicted allosteric pocket were the only druggable pockets. However, Fpocket indicated changes in the normal binding cavity when ligand was bound at the allosteric site, which failed to detect the normal cavity. The disappearance of the normal cavity upon ligand binding at the allosteric site suggested the possibility of disordering in the residues that are critical for the inhibition of DSPI. This unique case of competitive inhibition between two sites refer to the lower inhibitory activity where all active sites on the protein subunits are altered when an allosteric inhibitor binds to it (illustrated in **Figure 4.8**).

#### 4.3.4 Analysis of MD simulation trajectories

MD studies for both the complexes and DSPI-substrate were carried out to enlighten a credible mechanism of action for the conventional and predicted competo-allosteric inhibitors 10195495 and 10252273. Molecular dynamics simulation findings serve as an influential tool to observe the intimate conformational details taking place in biological systems<sup>224</sup>. As the structure of a protein determines its function, the conformational dynamics of protein molecules play a critical role in defining the function of that particular protein. A thorough understanding of the structure and dynamics of a biological macromolecule is, therefore considered essential in understanding its functional flexibility<sup>254</sup>. Therefore, to further analyze the dynamics of DSPI, root mean square deviations (RMSD), root mean square fluctuations (RMSF), the radius of gyration (Rg), and B-factor values were plotted. All these values were obtained through the 100 ns trajectories. The

precision of our simulated complexes was evaluated through a comparison of the RMSD, RMSF, and energy values with the values of a control i-e DSPI-substrate complex

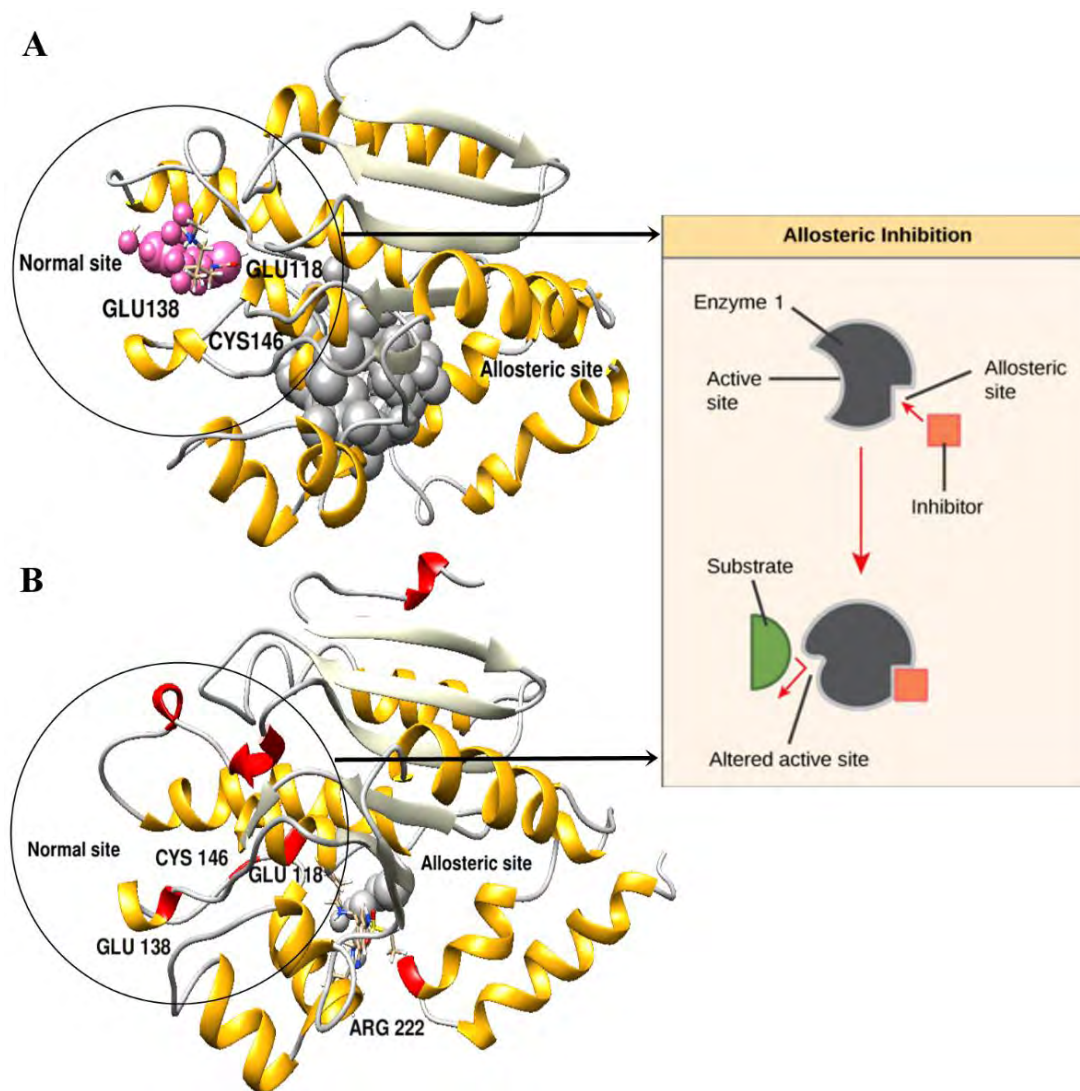


Figure 4.8: Detection of druggable cavities by CavityPlus and Fpocket A) Druggable binding sites upon ligand binding at the normal site with the critical residues labeled, normal site is shown in pink and allosteric site shown in grey color B) Druggable binding sites upon ligand binding at competo-allosteric site with the critical residues labeled and allosteric site shown in grey color. The structural rearrangement of critical residues at the normal binding site is shown due to which the software failed to identify its presence.



Backbone RMSD analysis of DSPI-substrate indicated a steady expansion during the first 3.5 ns, and conformational changes during 0 ns - 10 ns, 30 ns - 40 ns, and 90 ns - 99 ns indicated structural rearrangements over the entire simulation period. The average RMSD for the DSPI-substrate complex was found to be 2.26 Å when computed for 100 ns. Whereas, the values of RMSF were 1.17 Å and B-factor 56.4 Å, which indicated flexibility in residues that were involved in the formation of active site as depicted in **Figure 4.9**. Simulation results of normal binding site docked with the substrate revealed the widening of the pocket. The fluctuations throughout the simulation run were observed which were due to the movement in a bottom loop of the active site, comprising the residue Glu138. Due to the movement in the loop, the substrate kept moving away from the active site indicating the flexibility in this region presented in **Figure 4.10**.

The structural analysis of a proposed inhibitor bound at the normal pocket revealed significant movement along the ligand to maintain the electrostatic connections. Movement of loop residues (71-79) induced a conformational change in the normal pocket but kept the ligand within the active site showing strong bonding as compared to the substrate. However, the RMSD trajectory showed an increasing trend for the first 0 ns - 10 ns, which depicted the structural rearrangements initiated due to the ligand binding. The movement of ligand was also observed during 30 ns - 40 ns, which came back to its original position right after 40 ns and stayed intact for the rest of the simulation, as presented in **Figure 4.11**.

This phenomenon explains the change in RMSD from 30 ns - 40 ns as depicted in **Figure 4.9a**. When estimated from 100 ns, the average RMSD was found to be 2.73 Å. The maximum RMSD 3.93 Å was observed between 70 ns and 80 ns, which took place due to the fluctuation of amino acids present in the  $\alpha 7$  and  $\alpha 10$  regions of the C-terminal. These  $\alpha$ -helix residues consistently displayed higher B-factor values, i.e., 69 Å with a maximum value of Ala243. Amino acid residues present in the first and last regions displayed particularly higher fluctuations, which illustrated the flexible C terminal of this protein structure. The maximum value of 8.1 Å and an average value of 1.24 Å during the 100 ns run were revealed by RMSF values, representing the binding loop region residues Lys1 and Ala243, presented in **Figure 4.9b**.

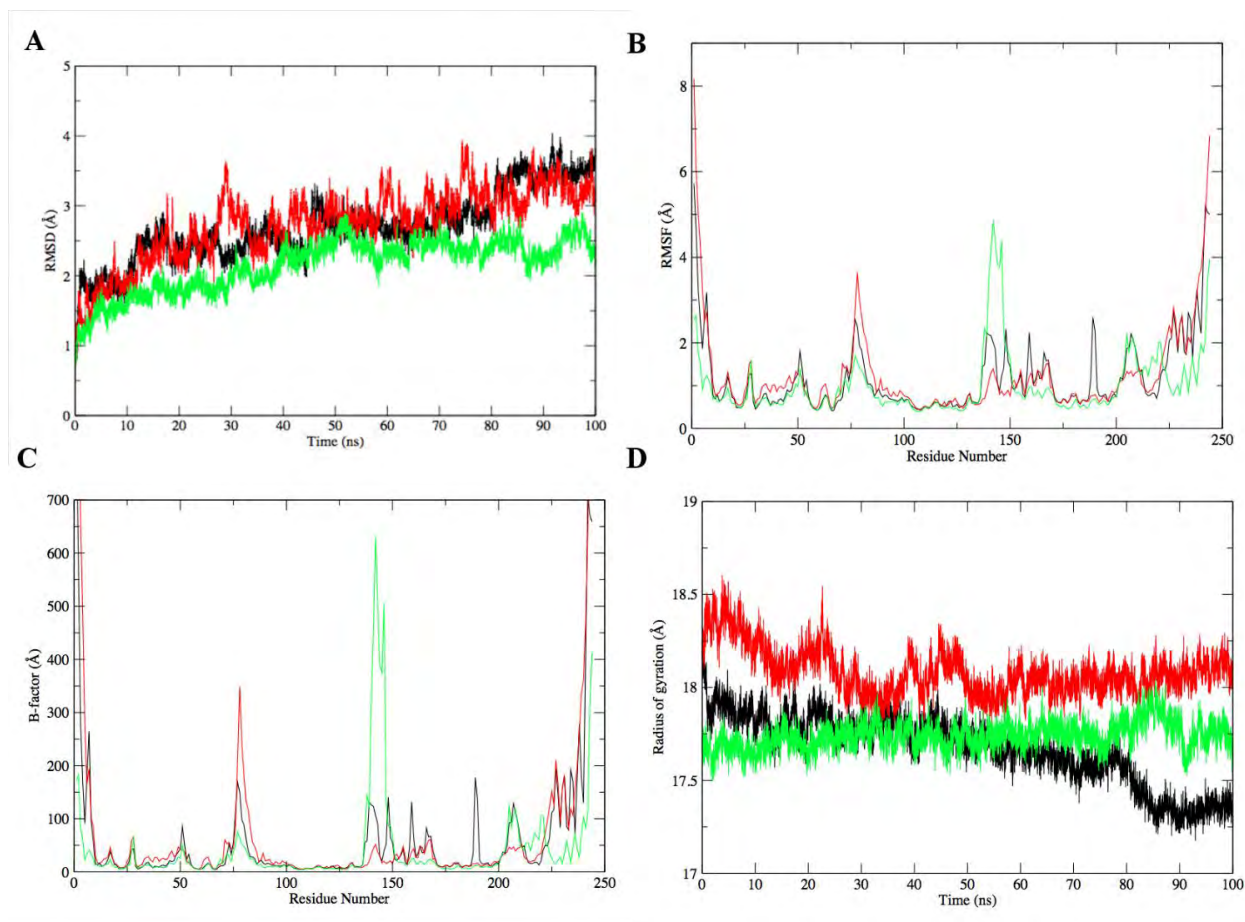


Figure 4.9. Simulations analysis of resulting trajectories of a substrate, ligand bound at the normal and compete-allosteric site. A) Deviation of the backbone depicted with root means square B) deviation of individual residue depicted as root mean square fluctuation. C) disordered regions and thermal stability of protein as B-factor. D) and net volume of the DSPI depicted with a radius of gyration. Black color represents a substrate used as controls, red color represents ligand bound at the normal site, and green color is the representation of a ligand at the compete-allosteric site.

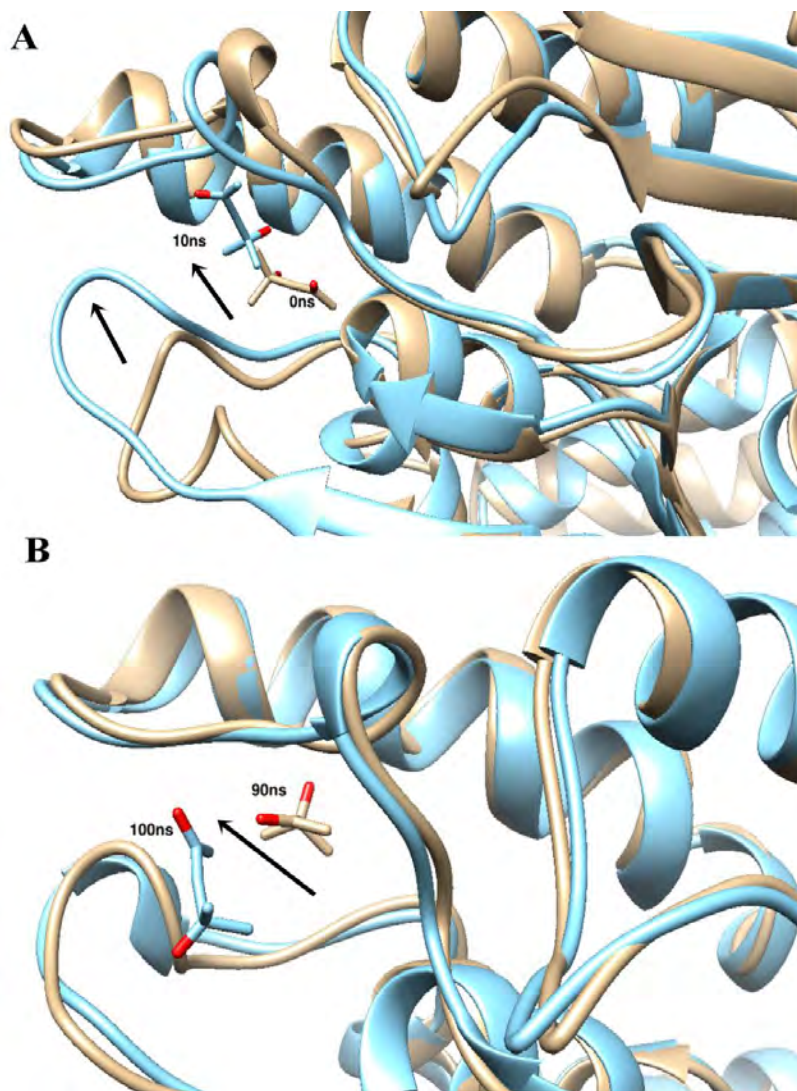


Figure 4.10. Structural analysis of a substrate at the normal binding site. A) Movement of a bottom loop as indicated with an arrow during 0 ns -10 ns. 0 ns trajectory is brown in color and 10 ns are shown in blue color. B) Movement of the substrate away from the binding pocket during 90 ns – 100 ns. 90 ns trajectory is brown in color and 100 ns are shown in blue color.

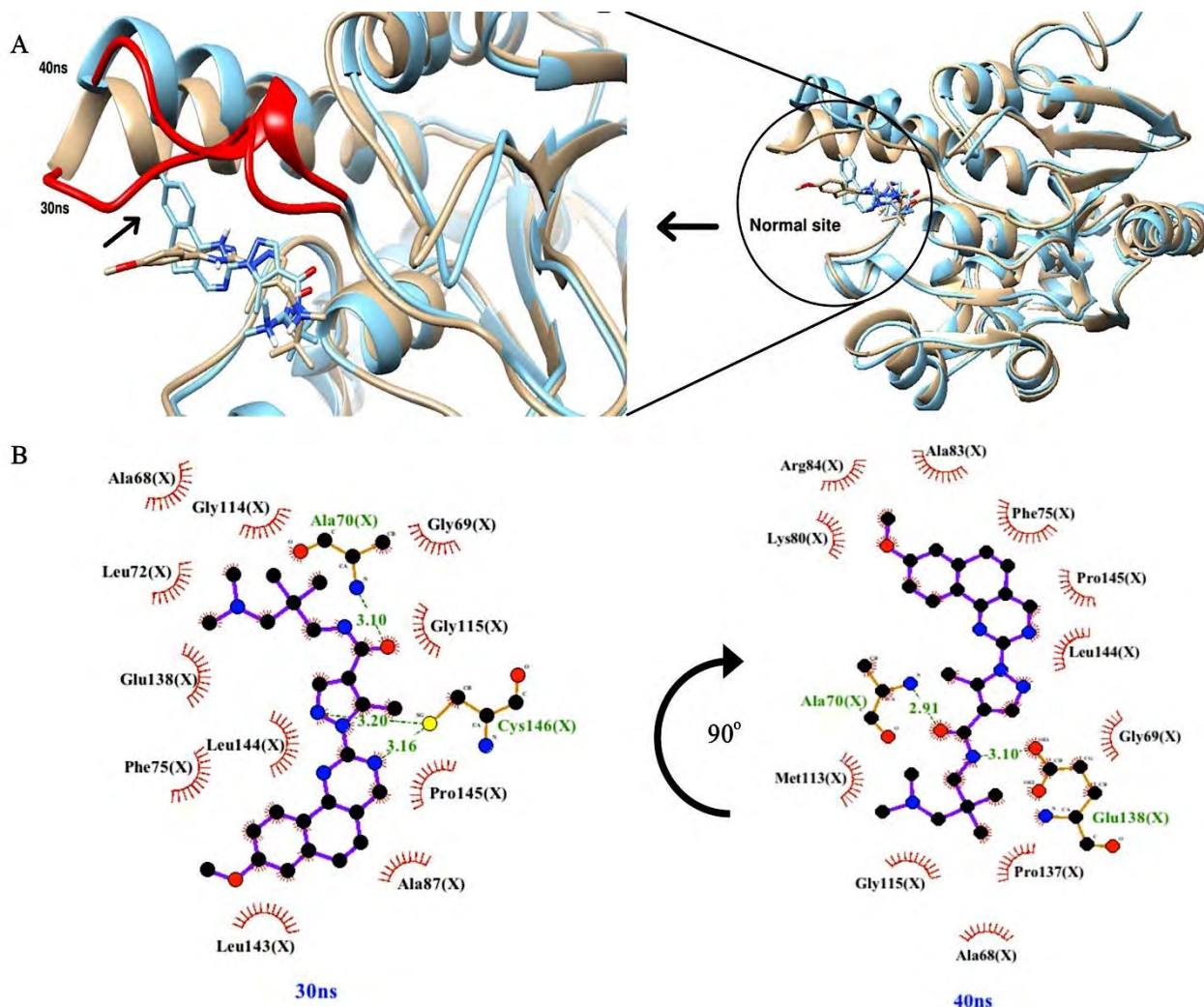


Figure 4.11. MD simulation trajectory analysis of ligand 10195495 at the normal binding site. Movement of the ligand and loop residues (71-79) during 30 ns – 40 ns are depicted **A)** Superimposition of 30 ns (brown color) – 40 ns (blue color) snapshots indicating the structural changes. **B)** Ligplot images generated at 30 ns and 40 ns to depict the movement of ligand and residues around the active pocket.

### 4.3.5 Competo-allostery

The competo-allosteric complex, to which the ligand was bound at the predicted allosteric site, exhibited an increasing trend for the first 0 ns – 10 ns. The reason for structural flexibility might be the fluctuations induced in C-terminal residues, as it was relatively a flexible region of DSPI protein reported in <sup>223</sup>. RMSD increased initially to the maximum value but remained extremely stable throughout the simulation run of 100 ns. The average

RMSD computed after 100 ns was observed to be 2.1 Å, whereas the overall mean value of RMSF was 1.01 Å. Regions comprising two residues Val141 and Ala243 exhibited maximum RMSF value of 4.8 Å due to higher fluctuations. However, the average B-factor value obtained was 41.8 Å<sup>2</sup>. The B-factor also indicated higher values for Val141 and Ala243 (629 Å<sup>2</sup>). Lastly, the RMSF of the DSPI-substrate complex and the predicted allosteric complex were compared to observe structural insights induced due to the fluctuations of residues. We observed rigidity of residues when ligand 10252273 was bound at the allosteric site. Reductions in the maximum peak of fluctuations from approximately 8 Å to barely 4 Å were revealed, which suggested fewer fluctuations when the ligand was attached to that the allosteric site.

Significant structural flexibility was observed at both the sites affecting the interaction of critical residues with the ligand molecules. Therefore, the most vibrant and flexible part of the protein, i.e. the helical regions were analyzed<sup>255</sup>. Modification of the helical secondary structure into a loop and vice versa was observed at different stages, throughout the 100 ns simulation run. Particular changes observed in the normal pocket residues were between Glu138 and Cys146. They were observed to be involved in the hydrogen exchange as a result of structural fluctuations in the protein. As previously comprehended, the fundamental aspect rather responsible for the secondary structures of proteins is the intra-molecular hydrogen bonding<sup>256</sup>. Various hydrogen bond interactions were observed during simulations such as the ligand 10195495, bound at the normal site, fluctuated around the predicted docking poses to maintain H-bond interactions with residues Ala70 (during the 100% of the simulation), similarly Gly115 during the initial simulation phase (20% of the simulation) and Ala68 interacted in the last 50% of the simulations. Further interactions between the H-bond donor and H-bond acceptor residues Cys146 (30% of the simulation) and the H-bond acceptor side-chain residues Glu138 (70% of the simulation) were observed. Despite structural rearrangements and ligand movement within the normal site, the proposed compound remained in the pocket, unlike the substrate that moved away from the binding site.

On the other hand, the detailed analysis of the predicted allosteric complex at different instances also illustrated significant structural changes. All the active site residues determined by docking were changed into Arg224, Glu223, Gln219, and Lys215 except

Phe94, Gly148, Trp155, Arg222, and Ala152. They were located in the proximity of the ligand molecule and were observed contributing actively to the interactions. Strong hydrogen bonding was observed throughout the simulation run between Arg222 and the proposed ligand bound at the allosteric site with a distance of 1.913, 2.184, 3.479, 3.997, 3.017 and 3.065 respectively. Another important parameter, the radius of gyration (Rg) was also computed to investigate the compactness and stability of a protein structure. The higher value of Rg indicates a less compact structure, whereas smaller Rg values depict the stable packing of a protein structure<sup>257</sup>. For the normal binding site, structural equilibrium was attained at 18.08 Å. Greater Rg was detected during 0 ns –10 ns (18.6 Å) exhibiting consistency with the values of RMSD. However, an average Rg witnessed for the proposed allosteric complex was 17.7 Å, which infers that both the docked complexes exhibited a stable and compact system.

Moreover, the energy values extracted from the frames of the simulation run of BB compound 10195495 bound at the normal site and compound 10252273 bound at the allosteric site were extracted. The predicted BB inhibitors showed stability throughout the simulation run therefore they are of primary importance. BB compounds have previously shown to reduce virulence in mice and have curbed serious infections caused by MDR strains of *P. aeruginosa*. Thus, the predicted BB inhibitors predicted in this study exhibit the potential to act as promising drugs in the future.

### 4.3.6 Validation of competo-allostery

Comparative MD simulation analysis of both the sites revealed subtle conformational changes at diverse time intervals throughout a simulation run. Widening of the C terminal loop was observed specifically when a ligand was bound at the predicted allosteric site. These changes possibly affected the area of the normal binding pocket, thus disturbing its conformation for regular substrate binding. This ligand rearrangement also displaced Cys146, a critical residue involved in the formation of a normal pocket from its position by 8.247 Å, as mentioned in **Figure 4.12**.

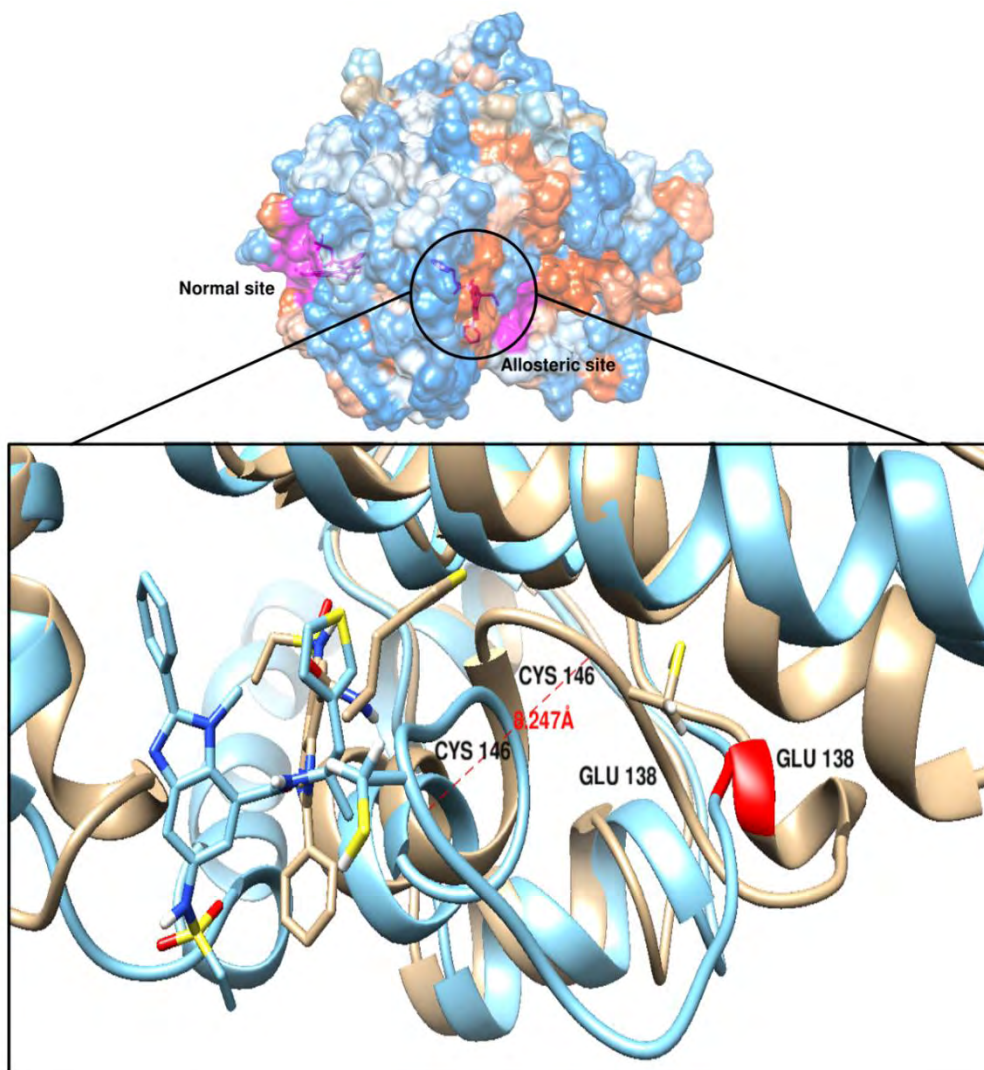


Figure 4.12. MD simulation trajectory analysis of the competo-allosteric site at 0 ns and 100 ns. Displacement of critical residue Cys146 from original position by 8.247 Å and change of Glu138 from loop to helices is depicted, while a ligand 10252273 is bound to the allosteric site.

Another conformational change, which was possibly instigated by the breakdown of intra hydrogen bonds of the helical structure of the protein, gave rise to the formation of a loop. Therefore, the conversion of Glu138 to loop during the simulation run might be critical for the functioning of protein as illustrated in **Figure 4.13**.

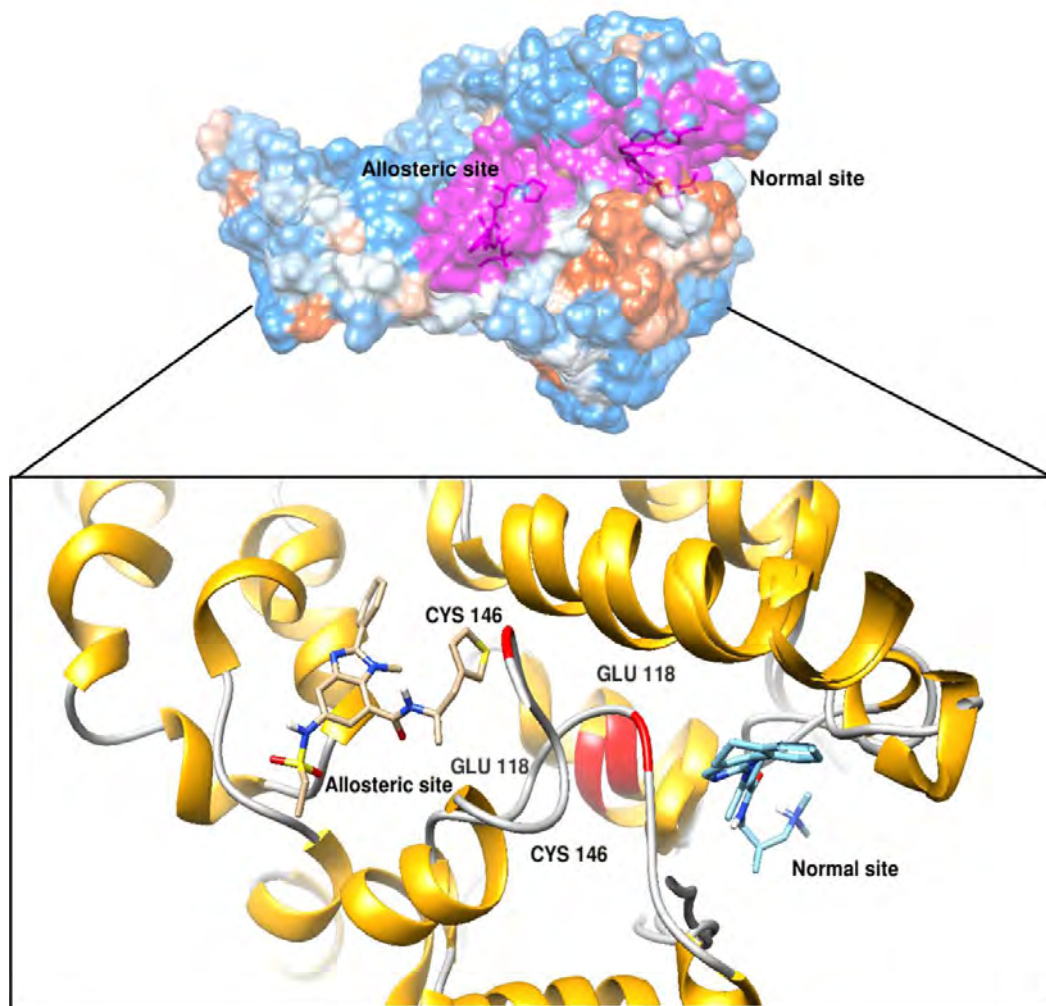


Figure 4.13. Comparative MD simulation trajectory analysis of the competo-allosteric site and normal site at 100 ns. The back view of the protein is presented in a hydrophobic surface style presenting the complete binding tunnel in magenta color with two pockets. Displacement of critical residues Cys146 and Glu138 at the normal binding site after 100 ns is clearly depicted in the close view. The residue Cys146 moves towards the right side and Glu138 moves to the left side away from the normal binding pocket, thus widening the normal site.

One possible reason for this phenomenon might be the structural rearrangements in  $\beta$  sheets that were formed by the alignment of  $\beta$  strands observed during MD simulation analysis. The formation of hydrogen bonds was observed between the carbonyl oxygen of one strand and the backbone nitrogen present in another strand between residues Met113, Tyr111, Ser67, and Phe66. Thus, it was inferred that the displacement and modification of



residue Glu118 could be the result of conformational pressure exerted by the formation  $\beta$  sheets on residue Glu118, lying next to it as depicted in **Figure 4.13**. To further explore the dynamics of both the pockets, TRAPP analysis of MD simulation trajectories was conducted.

### 4.3.7 TRAPP analysis of MD simulation trajectories

Some interesting differences with the conventional site were observed while analyzing the allosteric complex during the MD trajectory. To validate these changes, we examined different areas of DSPI along the MD trajectory using TRAPP software. We chose one out of five frames of the simulation trajectory as input for TRAPP. We first considered the conventional cavity, which revealed the flexibility of the residues (71 – 79) that comprised of loops exposed to the solvent, as stated previously in our MD analysis. The flexibility in this region indicated the chances of the opening of this site more often than the allosteric site when the ligand was attached to the normal site. Whereas, we could only comprehend the opening of the allosteric site in 25% of the total snapshots of the simulation as depicted in **Figure 4.14b**. The major transformations in the region of sub-pocket 2, which represents a normal site, appeared in the last half of the MD trajectory.

The movement of substrate during the MD simulation run in which the ligand gradually moved away from the binding site confirmed the opening of normal site relatively more often than the predicted allosteric site, as depicted in **Figure 4.14**. However, when the ligand was bound to the anticipated allosteric site, the software completely failed to identify the normal binding site because of the structural changes and displacement of residues, induced upon ligand binding. Overall, we observed a stiffness of the allosteric conformational state during the simulation. All the indicators observed so far refer to the allosteric theory that suggests that the entropy of a system can be reduced by ligand binding to maintain the stable conformation of the protein, inhibiting its movement and thus altering the target behavior<sup>224</sup>. To fully understand the dynamics of these critical residues and to determine the binding order of both the ligands and protein, we carried out binding free energy calculations using the MM-PBSA and MM-GBSA methodology based on the MD simulations.

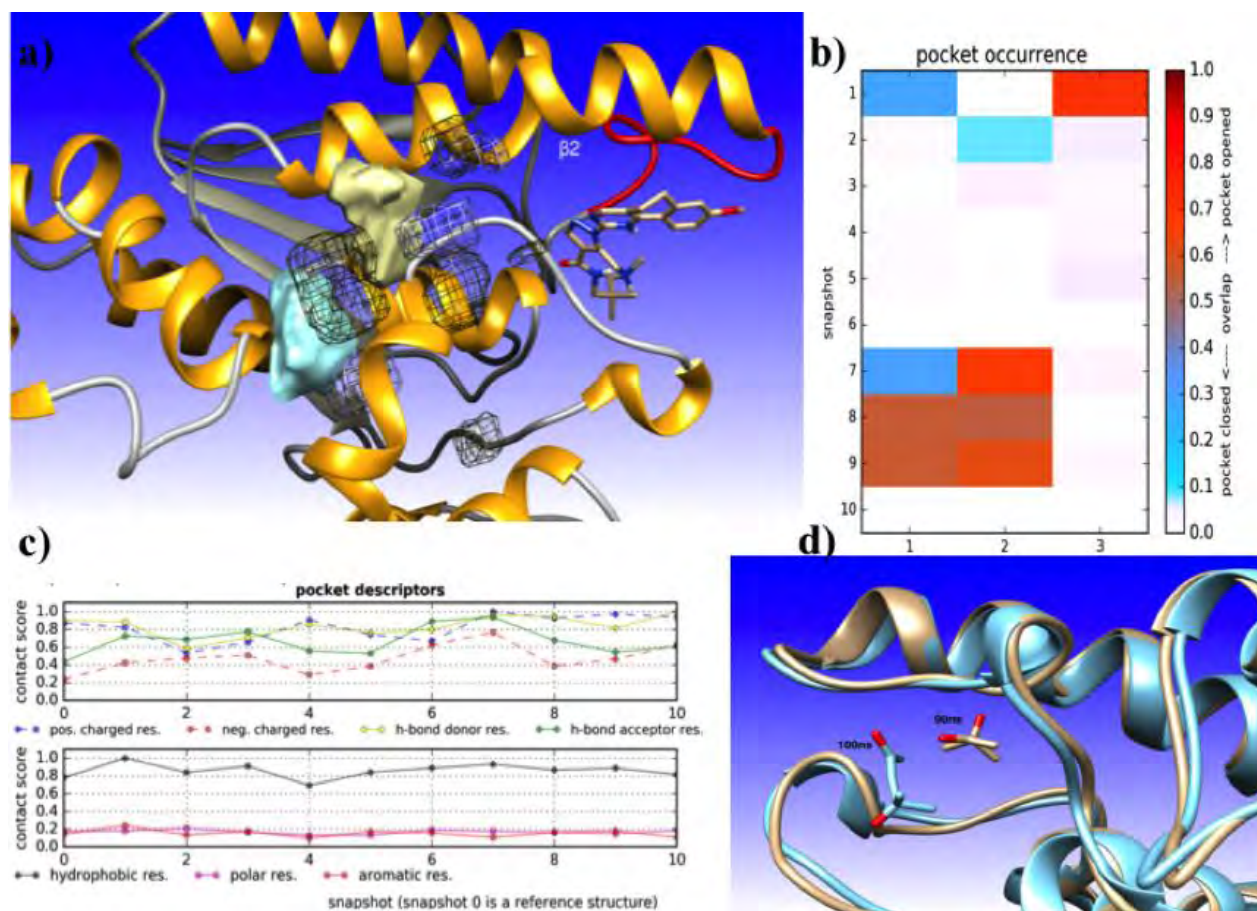


Figure 4.14. Analysis of the pocket dynamics in MD trajectories using TRAPP software. A) The reference structure (PDB code: 5wyb) and representative MD snapshots of the docked normal complex and the competo-allosteric complex are shown respectively. Residues (71 – 79) are shown in red, whereas sticks represent ligand bound at the normal site. Transient/conserved regions present in 50% of the simulation are represented in mesh scheme, whereas the pocket occurrence is shown in the solid scheme. B) Graph representing the opening of transient regions during MD simulations where column 2 represents the normal pocket, and column 3 represents the competo-allosteric pocket. C) The type of contacts that residues are making with the binding site during MD simulation d) Movement of the substrate away from the normal binding site during 100 ns simulation due to the flexibility of the side loop.

Table 4.5: MM/GBSA and MM/PBSA value for the docked trajectories of DSPI at the normal site, the competo-allosteric site, and the substrate that has been used as a control.

Energy component	Allosteric site		Normal site		DSPI- SUBSTRTE Normal site	
	MM/GBS A (kcal/mol)	MM/PBS A (kcal/mol)	MM/GBS A (kcal/mol)	MM/PBS A (kcal/mol)	MM/GBS A (kcal/mol)	MM/PBS A (kcal/mol)
$E_{VDW}$	-46.73	-46.73	-48.21	-48.21	-15.26	-15.26
$E_{ELEC}$	-32.35	-32.35	-142.34	-142.34	-11.07	-11.07
$E_{POLAR}$	---	-32.61	---	-32.80	---	-12.63
$E_{DISP}$	---	56.16	---	57.95	---	19.48
$E_{TOTAL}$	-40.37	-7.37	-42.71	-1.98	-10.35	1.18
$G_{GAS}$	-79.08	-79.08	-190.56	-190.56	-26.34	-26.34
$G_{SOLV}$	38.71	71.71	147.85	188.58	15.99	27.52

### 4.3.8 Binding free energy analysis

The MM/PB(GB)SA methods in AMBER were castoff to calculate the binding free energies of the three systems. **Table 4.5** summaries the binding free energy and its contributed components computed by MM/PB(GB)SA, and the entropy contributions obtained for each system. As listed in **Table 4.5**, the MM/PBSA calculated binding free energies were -7.37 of ligand-bound at the proposed allosteric site, -1.97 of the ligand-bound at the normal site and 1.18 kcal/mol of the substrate-bound at the normal site. However, the MM/GBSA computed binding free energies were -40.37, -42.71, and -10.35 kcal/mol of 10252273 at an allosteric site, 10195495 at the normal site and CoA substrate at the normal site, respectively. Both MM/PBSA and MM/GBSA computations signified that solvation contributions were unfavorable within the three systems. Looking at the conformations and locating the free hydrogen bond donor and acceptor could best provide the reason for higher solvation<sup>258</sup>. By analyzing the free energy components, it was revealed that inhibitor 10195495 can make extremely strong hydrogen bond connections with the residues Ala68, Ala70, Phe75, Gly115, Glu138 and Cys146 of DSPI,

whereas inhibitor 10252273 can form H-bonds with residues Leu121, Arg126, Gly148 and Arg222 that is located near the C-terminal of DSPI.

Furthermore, strong hydrophobic interactions were present between DSPI and its inhibitors. It was observed that both EVDW and EEL derived the promising interactions for both 10252273 and 10195495 bindings to DSPI. There were two hydrophobic interactions observed at normal site which were formed between the N-[3-(dimethylamino)-2,2-dimethylpropyl] of ligand 10195495 and Glu138 and between (8-methoxy-5,6-dihydrobenzo[h]quinazolin-2-yl) of 10195495 and residues (71-79) of DSPI, whereas LIGAND10252273 bound at the predicted allosteric site was mainly responsible for hydrophobic interactions between 1H-benzimidazole-7-carboxamide and residues Arg98, Ala122, Trp155 and Arg222 of DSPI. It was also observed that Ala83, Phe75, and Phe90 could form three stable pi-pi interactions with two aromatic rings that are almost parallel of ligand 10195495, bound at the normal site. These interactions of the side chain amino acids are critical in determining the structure of a protein, as they provide stability to the protein structure and are also involved in various enzymatic reactions<sup>259</sup>. Pocket residues, which are more stable in the structure, are mostly the aromatic ones. The ligand 10252273 bound at the predicted allosteric site exhibited one pi-pi stacked interaction with Ala147 and Gly148 and one pi-sulfur interaction with Phe94 and Arg222. However, the critical residues Glu138 and Cys146, involved in protein binding, confirmed the binding potential between 10195495 bound at the normal pocket and DSPI through energy contributions. Whereas, the other two residues Trp155 and Arg222, which have revealed interactions with 10252273, bound at the allosteric site, exhibited stronger energy contribution than 10195495. If we have to summarize based on these residual bonding, we can concur that the inhibitor 10195495, bound at the normal site, has the potential to block the binding site of DSPI. Whereas, the inhibitor bound at the anticipated allosteric site can easily adapt to the potential surface of DSPI and inhibit the mechanism by disturbing the critical residues, which are crucial for the binding of a substrate, thus limiting its attachment to the host-binding site.

## 4.4 Concluding remarks

The primary objective of this study was to identify and develop competitive inhibitors against DSPI, which can control DSF associated pathogenicity and is critical for protein dynamics and subunit interactions. Targeting multiple sites as presented in the current study suggest that both the conventional and allosteric binding pockets of DSPI will aid in addressing the problem of multi-drug resistance. Combinations of the free geometry-based algorithm Fpocket and Cavityplus alongwith the molecular docking have endorsed the identification of a new competo-allosteric binding site. The predicted site existed within the same binding tunnel as the normal binding site, possibly competing for the attachment of ligands. The active center residue Glu118, however, played a critical role in ligand binding. MD simulations and free energy calculations were further implemented to analyze the structural mechanisms of potential inhibitors. Simulation studies revealed that docking at the competo-allosteric site resulted in the displacement of critical residues that are essential for the functioning of DSPI. The disorderedness of residues resulted in the widening of the normal binding pocket, whereas the competo-allosteric site exhibited stiffness during the simulation run. Structural rearrangements in  $\beta$  sheets were also observed, which could be exerting conformational pressure on Glu118 located adjacent to it, hence the displacement in the subsequent residue. However, the formation of various cation- $\pi$  interactions and hydrogen bonding was observed between the protein and ligands induced due to the fluctuations in a protein. The per-residue energy decomposition was calculated to determine the favorable and unfavorable interactions of each residue with an inhibitor. The analysis of the dynamics in binding free energy suggested that the major contributions to inhibitors binding to DSPI were the vdW energy components exhibited by Ala83, Phe75, Phe90, Trp155, and Arg222. The predicted inhibitors have indispensable H-bond acceptors or donors to interact with the residues Ala68, Ala70, Phe75, Gly115, Glu138, Cys146, Leu121, Arg126, Gly148, and Arg222. Compounds with benzamide-benzimidazole (BB) backbone emerged as promising ligands against both the normal and the allosteric binding pockets and therefore, should be explored for their activity against *P. aeruginosa* experimentally. In conclusion, the binding of normal ligand might be affected due to the conformational changes induced by the potential allosteric compound 10252273. It concurs that widening phenomenon and disruption of the normal binding site and thus

inhibition of competo-allosteric site at the cost of the normal binding site is significant and noticeable outcomes. This study has provided a profound understanding of the binding mode and dynamics of inhibitors with DSPI, which may be useful in the development of potentially therapeutic drug.

This research work has been published in *Journal of Biomolecular Structure and Dynamics* by Taylor and Francis publishers and can be found in the publication section of thesis.

---

## CHAPTER 5

---

# Quantum Dynamics and Bi Metal Force Field Parameterization Yielding Significant Antileishmanial Targets

## 5. BI-METAL FORCE FIELD PARAMETERIZATION

### 5.1 Background

According to the World health organization (WHO), protozoan parasitic diseases from the genus *Trypanosoma* and *Leishmania* particularly visceral leishmaniasis, has reportedly caused more than 90% new cases in 2020<sup>63</sup>. Due to limited number of treatment options and rapidly evolving drug resistance to available drugs, it has resulted in more than 500,000 cases annually with greater than 50,000 mortality rates globally, which includes 69 different countries including Europe, Middle East, and South America<sup>65,260</sup>. More precisely, WHO has categorized it as one of the top mortality potential outbreaks that recently occurred in 10 countries namely, Brazil, China, Ethiopia, Eritrea, India, Kenya, Somalia, South Sudan, Sudan, and Yemen<sup>261,262</sup>. However, to curb leishmaniasis, multiple molecular studies targeted the most common and critical pathway, trypanothione metabolic pathway, which carries a unique thiol-based metabolic system different from humans, referred as to trypanothione (T(SH)<sub>2</sub>)<sup>263–265</sup>. The substantial role of this pathway in myriad of reactions comprise defense against oxidative damage, redox, homeostasis and replication<sup>66,266–268</sup>. Two widely circulated drug targets namely; trypanothione synthetase amidase (TSA) and trypanothione reductase (TR) play a central role in (T(SH)<sub>2</sub>) pathway. (T(SH)<sub>2</sub>) is synthesized in a two-step process; first it undergoes catalysis from glutathione (GSH) and spermidine (Spd) exclusively driven by TSA whereas TR, in the second step regenerates (T(SH)<sub>2</sub>) from trypanothione disulfide (TS<sub>2</sub>) in the presence of NADPH<sup>265,269</sup>.

Commonly used drugs in the treatment of leishmaniasis that target TSA and TR include the famous pentavalent antimonial, amphotericin B, miltefosine and paramomycin, each with its own efficacy and toxicity limitations<sup>262,270,271</sup>. These drugs most commonly target thiol-based redox system of parasites presenting TSA and TR as suitable anti-trypanosomatid agents. Apart from difficult administration regimen of these drugs, their continuous and long-term use has resulted in parasitic resistance in multiple strains resulting in dramatic decrease in their efficacy. Amidst continuous efforts after genetic and chemical validation in design of effective and less toxic inhibitors, multiple studies have proposed chemotherapy with metal containing compounds namely pentavalent antimonials



including sodium stibogluconate and meglumine antimonite<sup>272–274</sup>. Pentavalent antimonial however offer costly and onerous treatment procedures leading to unsolicited damage done to body by antimony Sb (III) alongwith the ever-emerging drug resistance<sup>64,275–277</sup>.

In light of the aforementioned facts, this particular study aims at targeting both the enzymes of (T(SH)<sub>2</sub>) pathway namely TSA and TR with novel metalloids. Bismuth (Bi) that lies below antimony (Sb) according to the periodic table, tend to share multiple electronic and physical features with Sb. Counterintuitively the least toxic among three metals (As, Sb, Bi) that exist in two oxidation states +III and +V is Bi<sup>278–280</sup>. Despite the closeness of Bi to Sb according to the periodic table, there is scarcity of both computational and experimental work on Bi. Meanwhile, highly defined organometallic complexes designed for targeted diseases are in development against multiple antimicrobial and anticancer agents<sup>270,281,282</sup>. Similarly, oral formulations namely bismuth subsalicylate are commonly used against *Helicobacter pylori* in the treatment of gastrointestinal ailments<sup>283,284</sup>. Despite the growing demand of molecular investigations with metalloids, these compounds are not fully characterized however main hindrance observed in computational analysis especially with molecular dynamics (MD) simulations arise due to the absence of relevant force field parameters.

This study however lays basis on our previous experimental study, which synthesized heteroleptic triorganobismuth(V) biscarboxylates of type [BiR<sub>3</sub>(O<sub>2</sub>CR')<sub>2</sub>] as anti-leishmanial therapeutic agents<sup>285</sup>. These compounds were fully characterized by elemental analysis that underwent antileishmanial assay followed by cytotoxicity profiling and X-ray crystallographic investigations. We have extended the experimental study and generated force field parameters of two bismuth compounds with different chemistry, which are investigated in complex with TSA and TR using QM MD methods, gaining pace in the development of novel metallic geometries<sup>286–288</sup>. Furthermore, to compute force field parameters, we exploited Seminario techniques and bonded methods of QM, the DFT that was used to generate [BiR<sub>3</sub>(O<sub>2</sub>CR')<sub>2</sub>] parameters with precise information about electronic structure of atoms around the metal center<sup>288,289</sup>. We also calculated force field parameters of meglumine antimonite to generate its topology with both the enzymes for comparative insights into dynamics of Sb and Bi compounds. This study thus reports force field parameters of bi(V) metalloids with pentagonal bipyramidal molecular geometry and

pentavalent antimonial; meglumine antimonite. Workflow and tools used in the generation and validation of Bi and meglumine antimonite parameters are mentioned in **Figure 5.1**. Findings shed light on experimentally verified new chemical structures particularly bismuth metalloids targeting key enzymes TSA and TR of (T(SH)<sub>2</sub>) pathway that will certainly aid in inhibiting parasitic redox metabolism and the infectious period of pathogenic trypanosomatids to overcome drug resistance.

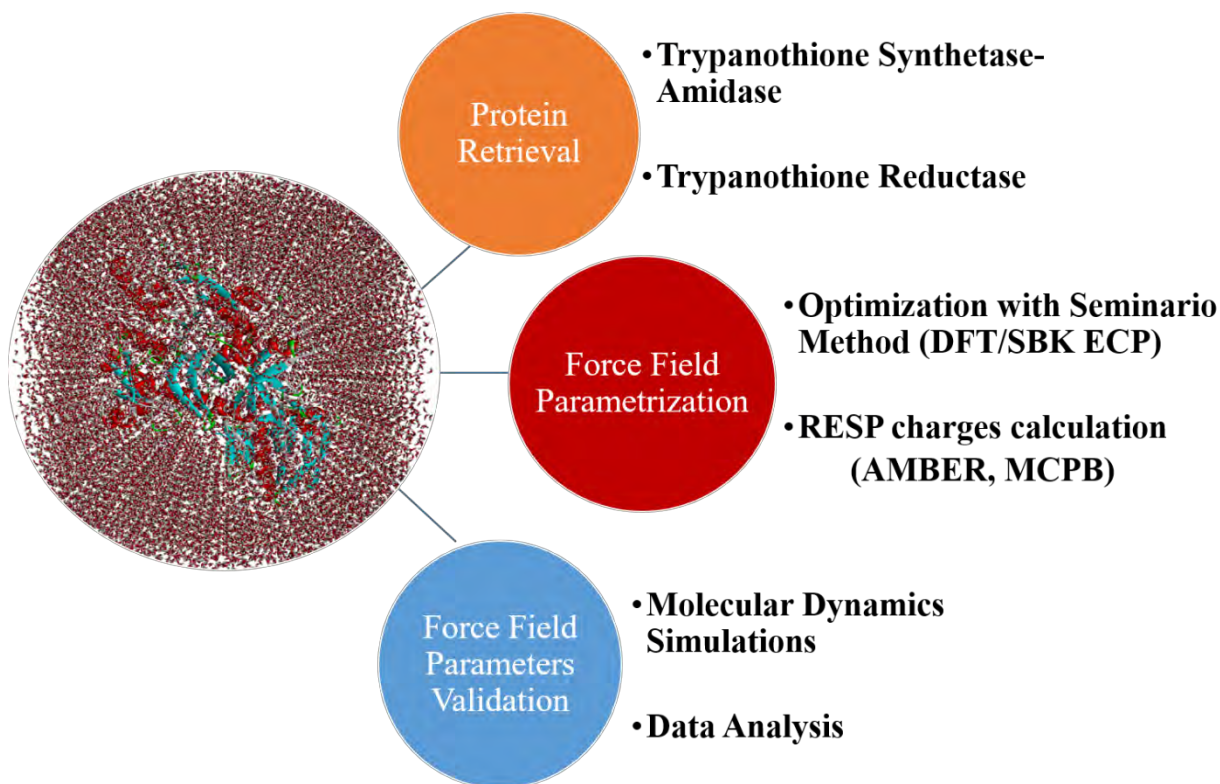


Figure 5.1: Workflow and tools used in the generation and validation of [BiR<sub>3</sub>(O<sub>2</sub>CR')<sub>2</sub>] force field parameters for TSA and TR of (T(SH)<sub>2</sub>) pathway. Seminario methods SBKJC ECP level of theory was employed to determine bond angles, bond lengths, and dihedrals for Models (1-3). For validation of geometric structures defining the coordination geometry of [BiR<sub>3</sub>(O<sub>2</sub>CR')<sub>2</sub>] models, all atom MD simulations were employed.

## 5.2 Materials and methods

### 5.2.1 Experimentally analysis of Bi(V) metalloids

In conjugation with our previous experimental synthesis and complete elemental analysis, we have employed QM techniques to determine binding potential of Bi metalloids with TSA and TR. Experimental study modified [SbAr<sub>3</sub>(O<sub>2</sub>CR)<sub>2</sub>] comprising Ar = *m*- or *p*-tolyl<sup>285</sup>, which are the prominent antileishmanial agents in practice and proposed the modified bismuth compounds as a series of [BiAr<sub>3</sub>(O<sub>2</sub>CR)<sub>2</sub>] demonstrated in **Figure 5.2**. All these compounds were productively synthesized using salt metathesis reaction, which exhibited higher stability and anti-leishmanial activity with lower IC<sub>50</sub> values (see **Table 5.1**).

Table 5.1: Anti-leishmanial activity of Bi(V) Model-1 and Model-2 with respective free binding energies.

Compound No.	Antileishmanial activity <i>Leishmania tropica</i> KWH23		<i>Leishmania infantm</i> Trypanothione Reductase (TR) $\Delta G$	Trypanothione Synthetase-Amidase (TSA) $\Delta G$
	% Mortality	IC <sub>50</sub> ( $\mu$ g/mL)		
<b>Model 1</b>	89	0.71	-9.5684	1.7110
<b>Meglumine Antimoniate</b>	-	-	-2.5153	22.0349
<b>Model 2</b>	93	0.45	-26.8282	-12.3653
<b>Amphotericin B</b>	99.5 $\pm$ 0.50	0.36 $\pm$ 0.04	-	-

Furthermore, the toxicity profile revealed all synthesized compounds (except 3 and 7) safe with low LD<sub>50</sub> values even at 50% viability with concentration level as high as 20  $\mu$ g/mL. We extended the experimental study and subjected these eight compounds to molecular docking with GOLD suite<sup>290</sup> targeting two enzymes TSA and TR. X-ray crystal structures with PDB ID: 2VOB and 4APN for TSA and TR were retrieved respectively; that targeted triangular cavity of TSA as a binding site whereas the interface domain of TR was targeted. Lastly, the meglumine antimonite (C<sub>7</sub>H<sub>18</sub>NO<sub>8</sub>Sb) was docked using the same

parameters with both the enzymes, which was used as a control during MD simulations analysis.

### 5.2.2 Novel force field parameters

Two Bi(V) compounds; Bis(*o*-bromobenzoato)triphenyl bismuth(V) referred as Model-1 and Bis(4-methylsalicylato) tris(*p*-tolyl) bismuth(V) referred as Model-2 were screened from docking, which were then subjected to geometry optimization alongwith C<sub>7</sub>H<sub>18</sub>NO<sub>8</sub>Sb as Model-3. All these models (1-3) were first optimized with the Seminario method, which exploits the bonded model method implemented in AmberTools 16 and Python-based metal center parameter builder (MCPB.py) that supports more than 80 metal ions<sup>131,142</sup>. Theoretical details of MCPB and its protocol are given in section 2.42. of this thesis. Prior to geometry optimization, ligands, proteins, and metals are protonated followed by input file preparation with Avogadro for Models (1-3)<sup>291</sup>.

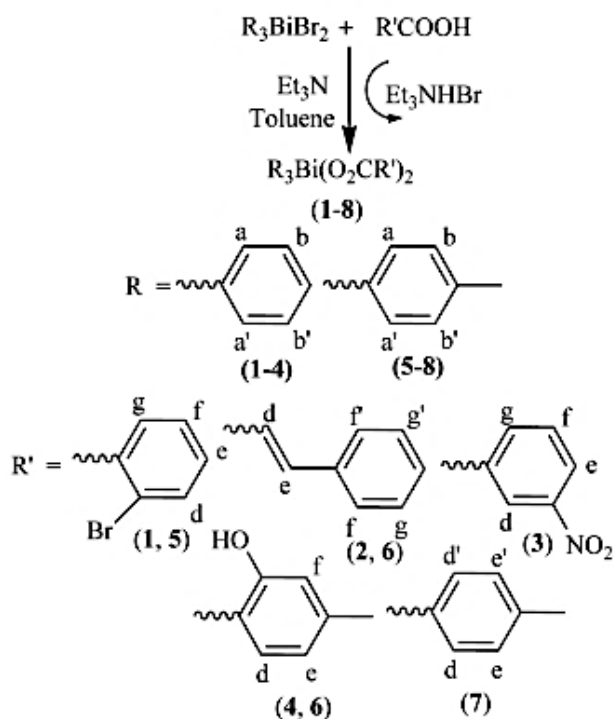


Figure 5.2: Synthesis of eight molecular geometries comprising Bi(V). Image sourced from our previous study<sup>285</sup>.

For geometry optimization using GAMESS-US<sup>84,85,292,293</sup>, we employed hybrid DFT method and electrically polarized basis set SBKJC coupled with ECP. The SBKJC basis set is particularly designed to handle metals of group 14 (C–Sn), 15 (N–Sb), 16 (O–Te) and 17 (F–I) that describe unperturbed system using valence double-zeta pseudopotential basis set proposed by Stevens and coworkers<sup>294–296</sup> 105. First step of QM calculations generated three fingerprint files (standard, small, and large models) of each model, which contains information about the metal ion and ligating atoms whose parameters do not exist in AMBER force field. To find a local minimum of small and large models, similar basis set was employed for geometry optimization and force constant calculations, which was then visualized using VMD to reaffirm bond coordination to metals<sup>234</sup>.

Furthermore, to derive metal geometry force field parameters, sub-matrices of Cartesian Hessian matrix were employed alongwith the retrieval of information regarding bonds and force constants by harmonic potential fitting<sup>142</sup>, which was determined by AMBER to provide potential energy of each position using equation 5.1 given below:

$$V(r^N) = \sum_{bonds} k_b(l - l_0)^2 + \sum_{angles} k_a(\theta - \theta_0)^2 + \sum_{dihedrals} \sum_n \frac{1}{2} V_n [1 + \cos(n\omega - \gamma)] + \sum_{j=1}^{N-1} \sum_{i=j+1}^N f_{ij} \left\{ \epsilon_{ij} \left[ \left( \frac{r_{oij}}{r_{ij}} \right)^{12} - 2 \left( \frac{r_{oij}}{r_{ij}} \right)^6 \right] + \frac{q_i q_j}{4\pi\epsilon_0 r_{ij}} \right\} \quad (5.1)$$

The first and second term in eq(1) estimate the probability of bending and stretching of bonds whereas the third term defines parameterization of torsion angles. Moreover, the Lennard Jones (LJ) potential and Coulomb potential relate the involvement of vdW and non-bonded electrostatic interactions<sup>131,297</sup>. LJ parameters are displayed for all three models (1-3) in **Table 5.2**. Nevertheless, the last step of modeling was performed with highly regarded method; the restrained electrostatic potential (RESP) fitting technique for assigning partial charges using a default Merz–Kollman RESP with defined radius of 2.8 Å, generally assigned to the metal centers<sup>298</sup>. As a result, a topology and coordinates files are generated by performing tleap modeling which sourced ff14SB force field to retrieve known parameters<sup>299</sup>.

### 5.2.3 Force field parameters validation and analysis

All parameters derived from AMBER force field and Seminario approaches were subjected to MD simulations to evaluate the generated parameters of all three systems (model 1-3). Missing parameters provided by optimization and force contacts calculations from GAMESS-US generated the topology for each system by Leap modeling with AMBER. All these systems were then solvated with TIP3P cubic box with dimensions 12 Å that underwent energy minimization comprising 500 cycles for hydrogen atoms and 1000 cycles for the water box to remove steric clashes. The system was then subjected to heating using a two-step canonical ensemble with restraints on the backbone and restraint weight 5 kcal/mol/Å<sup>2</sup> that gradually raised the temperature to 300 K using Langevin dynamics. Subsequently, the next step equilibrated the system for 100 ps followed by the pressure restraints in NPT ensemble with 1 atm and cutoff set to 8.0 Å. However, the long-range electrostatic interactions are dealt with Particle Mesh Ewald (PME)<sup>123,300</sup> method. Production run was carried out in 2 replicas each for 1 μs on both the Model-1 and Model-2 in complex with TSA.

Whereas the production run for 1 μs was separately performed on Model-1 in complex with the second protein: TR. Furthermore, three mutation models alongwith the control drug was carried out for 100 ns each. However, to analyse the resulting trajectories and structures, the Root mean square of deviation (RMSD), Root mean square fluctuation (RMSF), Radius of gyration (Rg), and Beta-factor graphs were generated. The resulting trajectories were further analysed for subsequent ligand movement in each system using Axial frequency distribution (AFD) tool followed by Radial distribution function (RDF) analysis. RDF based on hydrogen bond interactions calculates the density distribution of one atom in reference to another atom lying at a particular distance. Furthermore, to assess the molecular determinants of respective binding affinities, we calculated free binding energy of all complexes using MMPBSA.py module of AMBER<sup>301</sup>.

Table 5.2. The LJ parameters for three models (1-3) computed using MCPB.py with GAMESS-US.

<b>Bismuth Model-1</b>			
<b>Atom Type</b>	<b>Rmin/2 (Å)</b>	<b>ε (kcal/mol)</b>	<b>References</b>
<b>M1</b>	2.1850	0.5180	Adopted from atom type Bi3+3 from UFF (Rappe et al. JACS, 114, 10024)
<b>Y3</b>	1.9080	0.2100	cp C DLM 11/2007 well depth from OPLS replacing 0.0860
<b>Y4</b>	1.9080	0.2100	cp C DLM 11/2007 well depth from OPLS replacing 0.0860
<b>Y5</b>	1.9080	0.2100	cp C DLM 11/2007 well depth from OPLS replacing 0.0860
<b>Y6</b>	1.6612	0.2100	OPLS
<b>Y7</b>	1.6612	0.2100	OPLS
<b>Bismuth Model-2</b>			
<b>Atom Type</b>	<b>Rmin/2 (Å)</b>	<b>ε (kcal/mol)</b>	<b>References</b>
<b>M1</b>	2.1850	0.5180	Adopted from atom type Bi3+3 from UFF (Rappe et al. JACS, 114, 10024)
<b>Y3</b>	1.9080	0.2100	cp C DLM 11/2007 well depth from OPLS replacing 0.0860
<b>Y4</b>	1.9080	0.2100	cp C DLM 11/2007 well depth from OPLS replacing 0.0860
<b>Y5</b>	1.9080	0.2100	cp C DLM 11/2007 well depth from OPLS replacing 0.0860
<b>Y1</b>	1.6612	0.2100	OPLS
<b>Y6</b>	1.9080	0.0860	OPLS
<b>Y7</b>	1.9080	0.0860	OPLS
<b>Y2</b>	1.6612	0.2100	OPLS
<b>Bismuth Model-3</b>			
<b>Atom Type</b>	<b>Rmin/2 (Å)</b>	<b>ε (kcal/mol)</b>	<b>References</b>
<b>M1</b>	2.2100	0.4490	Adopted from atom type Sb3+3 from UFF (Rappe et al. JACS, 114, 10024)
<b>Y5</b>	1.6612	0.2100	OPLS
<b>Y6</b>	1.6612	0.2100	OPLS
<b>Y7</b>	1.6612	0.2100	OPLS
<b>Y8</b>	1.6612	0.2100	OPLS

### 5.2.4 Axial frequency distribution (AFD)

Theoretical overview of AFD to decipher the dynamics of positional shifts and changes in orientation of ligand with respect to protein coordinate planes over the period is explained in Section 2.5.3. AFD is indigenously developed, designed and implemented in our lab that holds the capability to provide significant information about the distribution of interacting atoms<sup>149</sup>. MD simulations trajectories with critical residues lying within 5.0 Å boundary cutoff with atomic center of mass are considered during the calculations. Function of AFD that calculates relative coordinate positions of X-axis and Y-axis relative to centroid on protein or ligand are discussed in detail in Section 2.5.3. Resulting AFD graphs contain 3D histograms depicting bi-molecular distribution of interacting atoms, which are depicted in forthcoming section of results.

## 5.3 Results and discussion

### 5.3.1 Force field parameterization reveal bidentate chelating effect

Proteins with metal coordinating geometries are dependent on well-optimized states and force field parameters to undergo MD simulations. Both bismuth complexes namely, Model-1 and Model-2 attained the local minima at optimization steps 349 and 240, respectively demonstrated in **Figure 5.3**. Both these ligands exhibit bidentate coordination modes around the Bi metal center while attaining pentagonal bipyramidal geometry. Notably, the experimental analysis demonstrated similar findings and mentioned the ability of Model-2 to attain bidentate/monodentate coordination geometry that can extend its interactions leading to distorted octahedral/pentagonal molecular geometry. Furthermore, the bond distances between Bi-C and Bi-O atoms for both models (Model-1 and Model-2) are in agreement with the experimentally derived X-ray crystal structure analysis that validate the optimization results<sup>285</sup>.



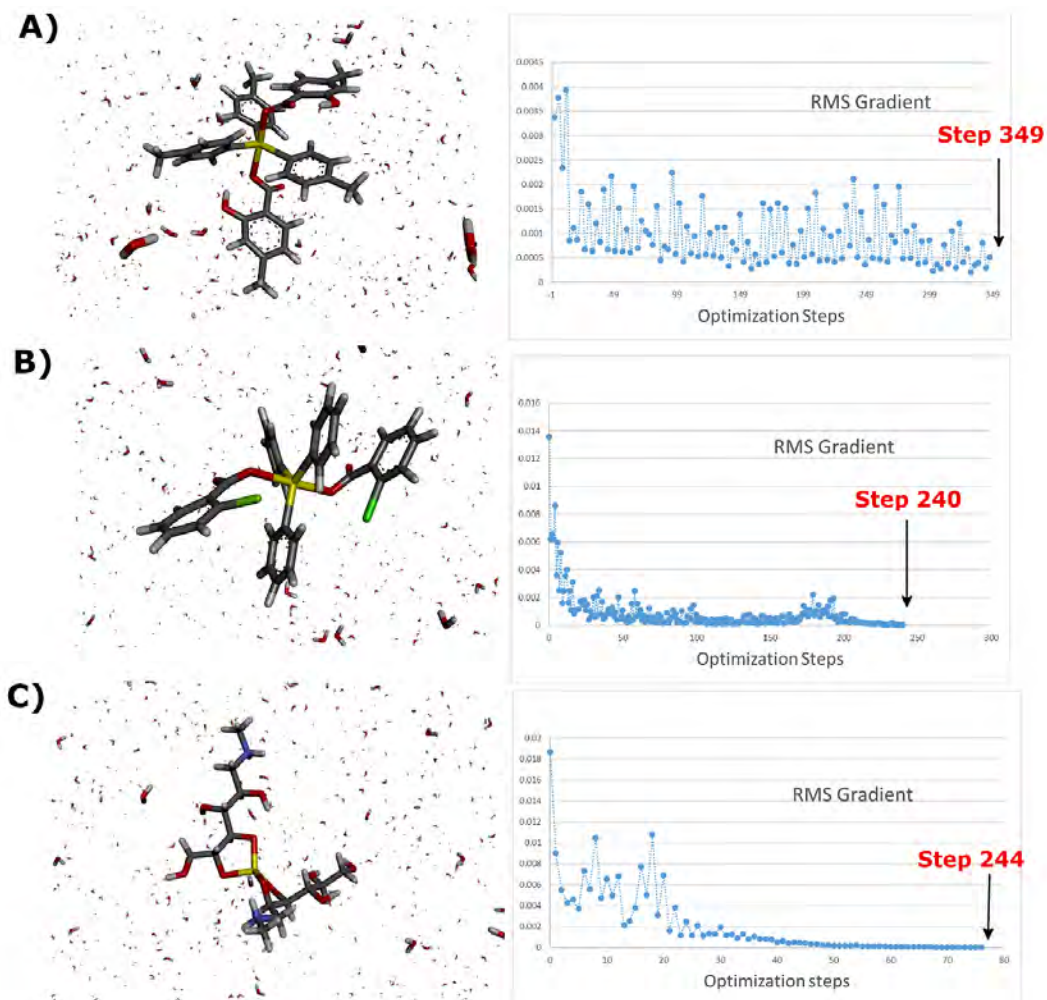


Figure 5.3: Parameterization of Bi(V) Model-1 and Model 2 along with Sb(V) meglumine antimonite ( $C_7H_{18}NO_8Sb$ ) with Seminario approach. A-C) 3D representation of optimized geometries of Model-1, Model-2, and meglumine antimonite, respectively. The geometries are optimized with SBKJC basis set coupled with ECP level of theory. Graphs represent energy potential calculated with GAMESS-US demonstrating starting point with the lowest energy level (step) mentioned in each graph.

Bond distances for Bi-C and Bi-O for Model-1 correspond to 2.12-2.2 Å presented in **Table 5.2** whereas Model-2 exhibits extended bond distances that ranges between 1.4 to 3.0 Å. The difference in bond distance between the two models are probably due to the ortho OH group present in Model-2 illustrated in **Table 5.2** that participates in making

extended interactions with the neighboring atoms. Model-2, however, has also been reported as the most active compound with  $IC_{50}$  0.45 (0.573  $\mu$ M) in antileishmanial activity, which highlights the role of OH group at alpha position leading to hydrogen bonding with alkyl substituents that enhances lipophilicity of this compound.

### 5.3.2 RESP charges

Furthermore, the RESP charges calculated for each atomic interaction with the Bi(V) center retrieved from the optimized structures are illustrated in **Figures (5.4-5.6)**.

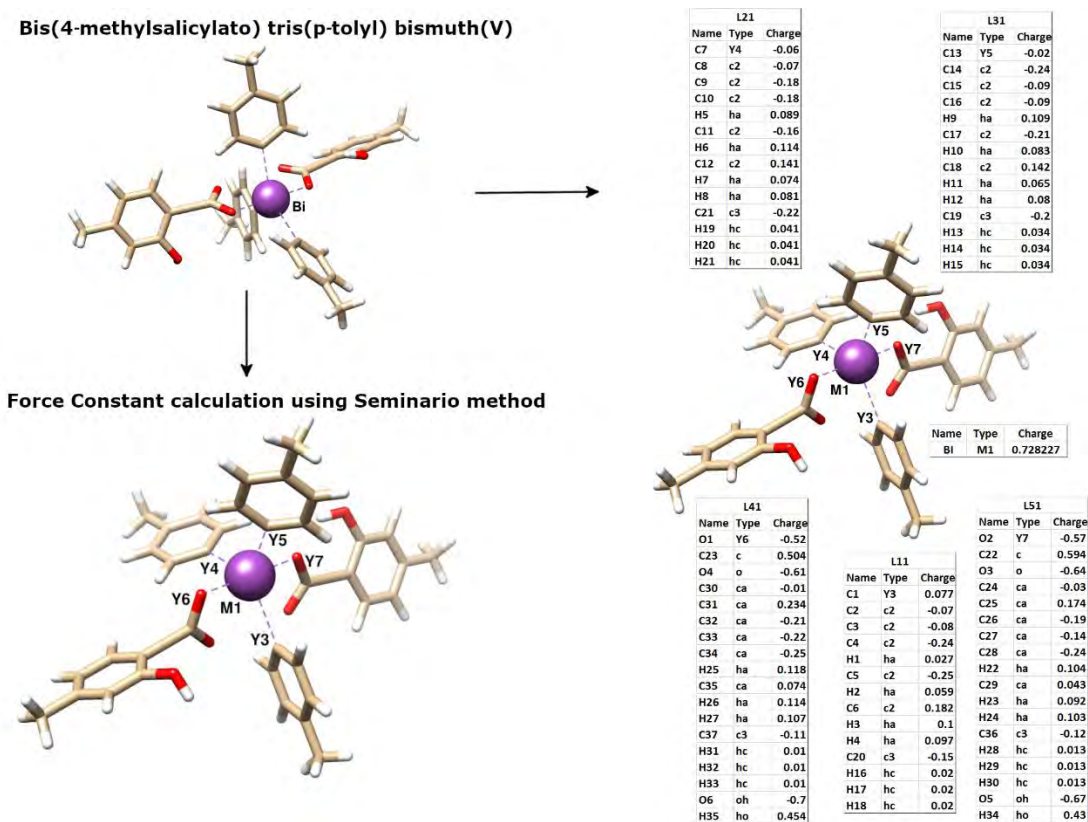


Figure 5.4: Calculation of RESP charges for Model-1 calculated with QM DFT methods using SBKJC ECP basis set. The metal center and interacting atoms are labelled.

Table 5.3: Average bond length (Å) and average internal angles (°) calculated with <sup>1</sup>QM <sup>2</sup>DFT methods using SBKJC <sup>3</sup>ECP basis set for the molecular models [BiAr<sub>3</sub>(O<sub>2</sub>CR)<sub>2</sub>] and meglumine antimonite (C<sub>7</sub>H<sub>18</sub>NO<sub>8</sub>Sb).

Geometry		Bond Length (Å)		Angle (°)		
Model System		Organo-bismuth(V) carboxylates				
Optimized Model Number	Bond Description	SBK ECP		Angle Description	SBK ECP	
		Average Equilibrium Bond Length (Å)	Force constant (kcal.mol <sup>-1</sup> .Å <sup>-2</sup> )		Average Equilibrium Angle [Θ <sub>eq</sub> ] (°)	Force constant [KΘ] (kcal.mol <sup>-1</sup> .rad <sup>-2</sup> )
<b>Bismuth Model 1</b>	M1-Y1	2.1937	77.3	M1-Y1-c	127.26	101.99
	M1-Y2	2.194	74.1	M1-Y2-c	130.01	107.63
	M1-Y3	2.147	144.6	M1-Y3-c2	119.4	167.64
	M1-Y4	2.1449	144.8	M1-Y4-c2	119.44	170.34
	M1-Y5	2.1479	149.3	M1-Y5-c2	119.69	132.05
	Y1-c	1.2183	637.7	Y1-M1-Y3	90.45	129.36
	Y3-c2	1.307	625	Y1-M1-Y4	91.68	79.1
	Y4-c2	1.307	625	Y1-M1-Y5	86.76	145.43
	Y5-c2	1.307	625	Y2-M1-Y1	173.52	157.58
	Y6-ca	1.3984	461.1	Y2-M1-Y3	93.93	96.91
	Y7-ha	1.086	345.8	Y2-M1-Y4	89.61	108.89
	c -Y2	1.2183	637.7	Y2-M1-Y5	87.02	144.11
	c -Y6	1.4906	345.9	Y4-M1-Y3	126.09	112.28
	ca-Y7	1.3984	461.1	Y5-M1-Y3	115.98	99.45
					Y5-M1-Y4	117.92
<b>Bismuth Model 2</b>	M1-Y1	2.1937	77.3	M1-Y1-c	127.26	101.99

	M1-Y2	2.194	74.1		M1-Y2-c	130.01	107.63
	M1-Y3	2.147	144.6		M1-Y3-c2	119.4	167.64
	M1-Y4	2.1449	144.8		M1-Y4-c2	119.44	170.34
	M1-Y5	2.1479	149.3		M1-Y5-c2	119.69	132.05
	Y1-c	1.2183	637.7		Y1-M1-Y3	90.45	129.36
	Y3-c2	1.307	625		Y1-M1-Y4	91.68	79.1
	Y4-c2	1.307	625		Y1-M1-Y5	86.76	145.43
	Y5-c2	1.307	625		Y2-M1-Y1	173.52	157.58
	Y6-ca	1.3984	461.1		Y2-M1-Y3	93.93	96.91
	Y7-ha	1.086	345.8		Y2-M1-Y4	89.61	108.89
	c -Y2	1.2183	637.7		Y2-M1-Y5	87.02	144.11
	c -Y6	1.4906	345.9		Y4-M1-Y3	126.09	112.28
	ca-Y7	1.3984	461.1		Y5-M1-Y3	115.98	99.45
					Y5-M1-Y4	117.92	99.22
	<b>Model System</b>	<b>Meglumine antimoniate</b>					
<b>Antimony Model 3</b>	M1-Y5	1.9953	174.9		M1-Y5-c3	117.45	122.03
	M1-Y6	2.0899	99.4		M1-Y6-c3	119.14	119.1
	M1-Y7	1.9914	181		M1-Y7-c3	114.14	106.37
	M1-Y8	2.0115	149.7		M1-Y8-c3	115.3	103.23
	c3-Y5	1.3165	449.9		Y6-M1-Y5	76.55	140.65
	c3-Y6	1.3165	449.9		Y7-M1-Y5	104.2	154.4
	c3-Y7	1.3165	449.9		Y7-M1-Y6	83.68	112.25
	c3-Y8	1.3165	449.9		Y8-M1-Y5	82.08	102.85
					Y8-M1-Y6	148.44	152
					Y8-M1-Y7	79.33	134.83

<sup>1</sup>QM: quantum mechanics, <sup>2</sup> DFT: density functional theory, <sup>3</sup> ECP: effective core potential

First and foremost, the difference in partial atomic charges of Bi metal center in both the models namely Model-1 and Model-2 was discrete alongwith the difference in charges in interacting atoms. The difference occurred due to larger electrostatic environment around the Bi center in Model-2. These variations hold crucial position particularly at the binding site to provide stability to metal center. These results however are validated through MD simulations of TR and TSA in complex with metal-coordinated ligands, which is explained in forth coming sections whereas **Figure 5.4-5.6** illustrate the resulting optimized parameters of all three models (1-3) used in this study.

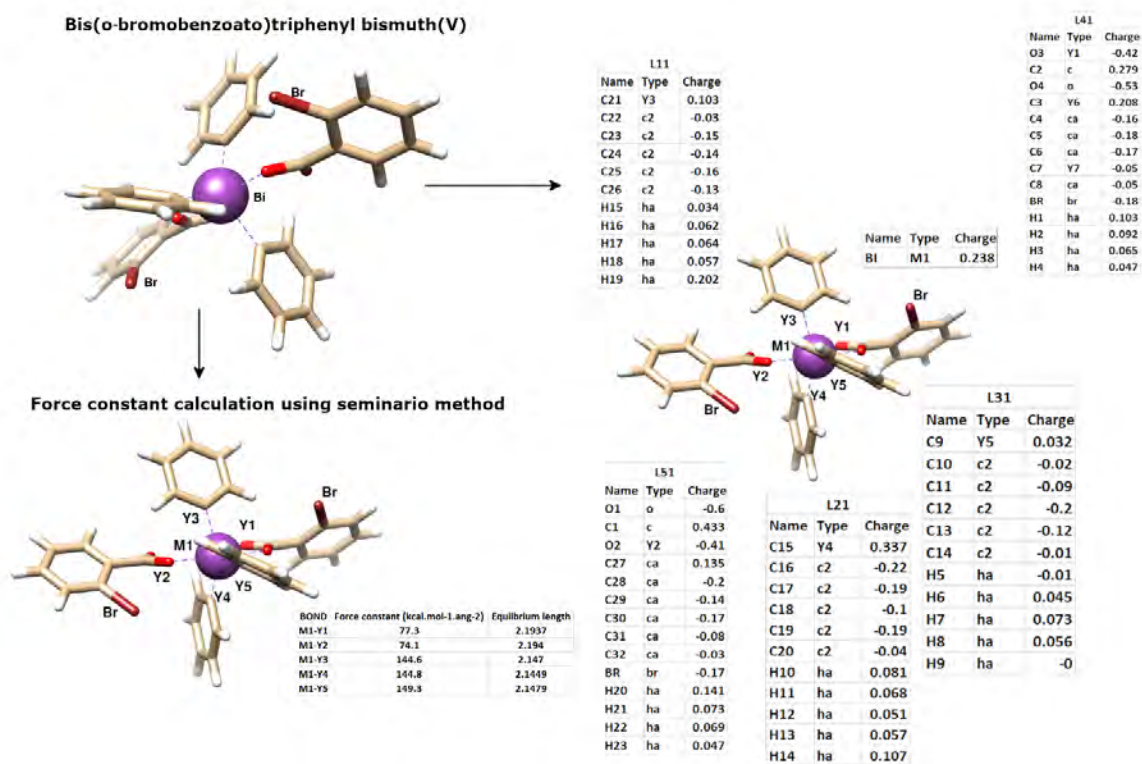


Figure 5.5: Calculation of RESP charges for Model-2 calculated with QM DFT methods using SBKJC ECP basis set. The metal center and interacting atoms are labelled.

### 5.3.3 SBKJC ECP at a glance

SBKJC basis set derived by Stevens and coworkers encompassing the valence double-zeta potential set coupled with ECP has been employed in this study to optimize Bi and Sb metalloids. SBKJC particularly deals with large sets of systems comprising elements of

higher period number covering atoms from mostly group 14-17 (C-Sn, N-Sb, O-Te, and F-I). Bi Model-1 and Model-2 prior to SBKJC optimization exploited LANL2DZ as basis set that led to unconverged geometries particularly for Bi systems. Whereas SBKJC when coupled with ECP generated converged calculations for both Bi and Sb that reached their local minima.

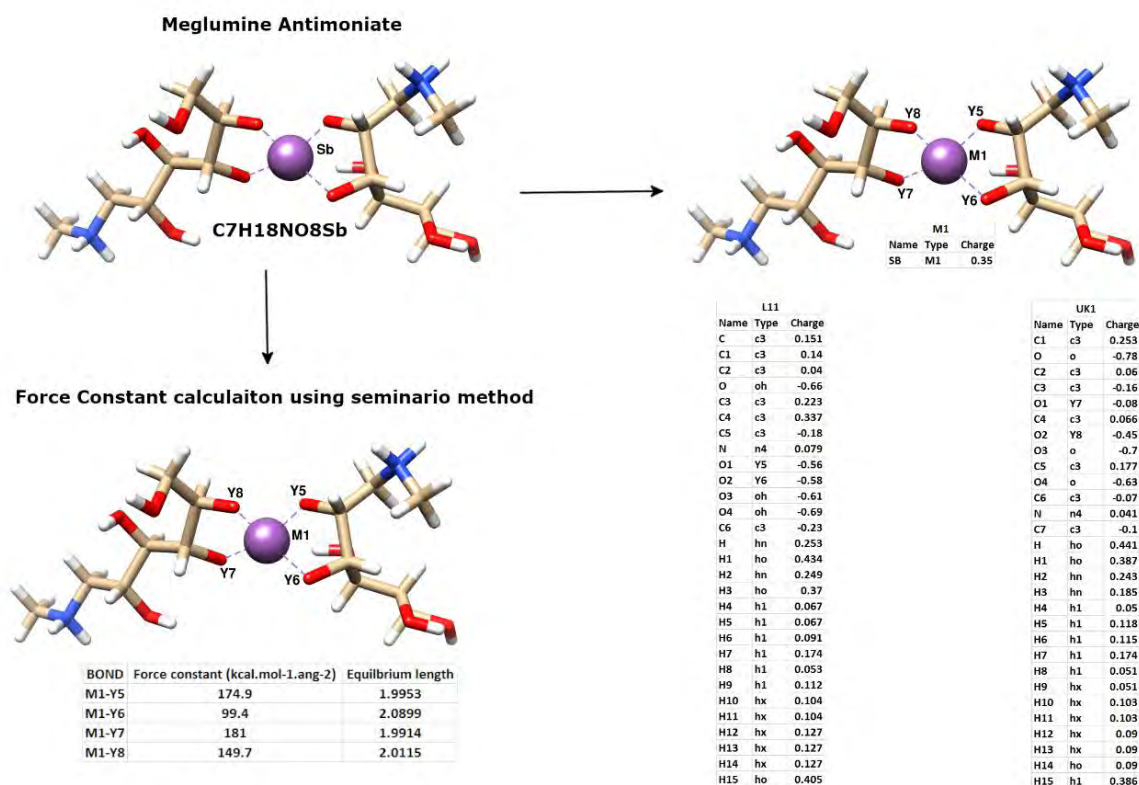


Figure 5.6: Calculation of RESP charges for meglumine antimonite (C<sub>7</sub>H<sub>18</sub>NO<sub>8</sub>Sb) calculated with QM DFT methods using SBKJC ECP basis set. The metal center and interacting atoms are labelled.

The resulting geometries particularly bond lengths lay close to experimental values of Bi compounds. Furthermore, a recent study on SBKJC conducted by *Luciano et al.* suggested the use of pseudopotential with SBKJC that can directly impact the contribution of inner electrons and Raman intensities, but the study did not incorporate Bi atoms in its data set<sup>105</sup>. Current study, however, proposes Bi metalloids with pentagonal geometries for further analysis, which if/must be considered for optimization with methods like SBKJC

ECP with pseudopotential referred as pSBKJC that will effectively lower the computational cost expended for heavy nucleus comprising large number of electrons.

### 5.3.4 Validation of force field parameters

The optimized models were validated in all atom MD simulations that require well-optimized geometries for metal coordinated systems. All three models including the control meglumine antimoniate were exploited in complex with TSA and TR using MD simulations to shed light on the binding dynamics of Bi(V) compounds on enzymes of T(SH)<sub>2</sub> pathway.

#### 5.3.4.1 Modulation of trypanothione synthetase amidase by Arg

TSA model contains ADP, 2 Mg<sup>+</sup> ions and an analogue of GSH necessary for biosynthesis and hydrolysis of T(SH)<sub>2</sub>. The triangular active site of synthetase comprise three sub-domains S1 for ADP and Mg<sup>+</sup>, S2 for binding of GSH and S3, a spermidine or glutathionyl-spermidine binding site. Recent studies have reported crystal structures of TSA bound with ATP, Mg<sup>+</sup> and an inhibitor comprising structural moieties similar to spermidine or glutathionyl-spermidine in their structures. In this study, we exploited organo-bismuth(V) carboxylates as inhibitors, which revealed discrete results and remodeled the mode of ligand binding. Visual inspection of MD simulations mentioned in **Figure 5.7** demonstrate overlaid crystal structure with all its sub-domains highlighted.

Detailed analysis of all three models (1-3) illustrates that ligand dynamics are largely dependent on the residue Arg569 lying at the bottom of the binding site. Simulations run in 2 replicas for 1 μs each on Model-1 are depicted in **Figure 5.8** and **Figure 5.9**, which reveal distinct movement of Arg569 to interact with the OH group present on “LIG604” chain of bismuth model. Ligand movement from vertical to horizontal position influences ARG569 to interact with the residue Arg313, a catalytic residue that is significant for the activity of TSA. Model-1 exhibited mean RMSD value of 1.5 Å while maximum and minimum values range from 1.3 Å to 2.5 Å depicted in **Figure 5.10**. Variations in positioning of ortho group in LIG604 chain of Model-1 over the time of 1 μs appears crucial that tends to interact with Arg569, leading to stronger interactions between Arg569 and Arg313 is depicted in **Figure 5.8**.

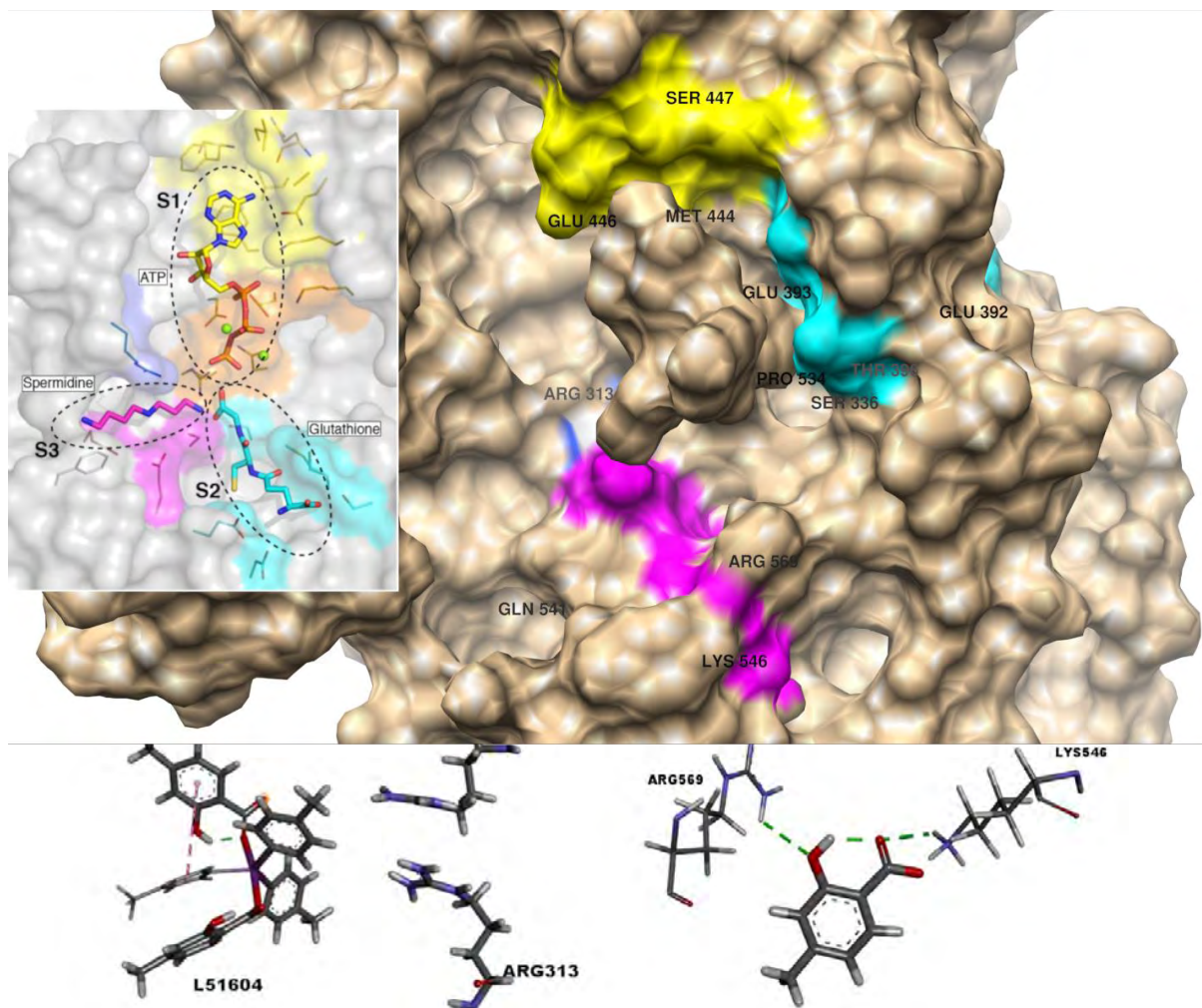


Figure 5.7: Visual inspection of active site of Trypanothione Synthetase-Amidase with sub-domains labelled. The crystal structure is depicted in grey surface whereas the Bi(V) bound complex after MD simulations is represented with brown surface.

Notably, the strictly conserved residues important for catalysis of ATP at S1 and orientation of spermidine at S3 comprising Arg313, Ser336, and Cys341 (non-conserved) are affected due to the dynamics of Arg569 upon ligand binding **Figure 5.12**. Findings from MD simulations not just highlight the critical role of Arg569 but also indicate the presence of possible allosteric site S4 near the catalytic site S3 of TSA that have been reported in multiple experimental studies<sup>302,303</sup>. In the same context, the study conducted by *Oliver et al.* reports the possibility of an allosteric site<sup>304</sup>, concurrent with the current



study that should undergo experimental and NMR crystallography in future studies especially in connection to the orientation of Arg569 (horizontally aligned).

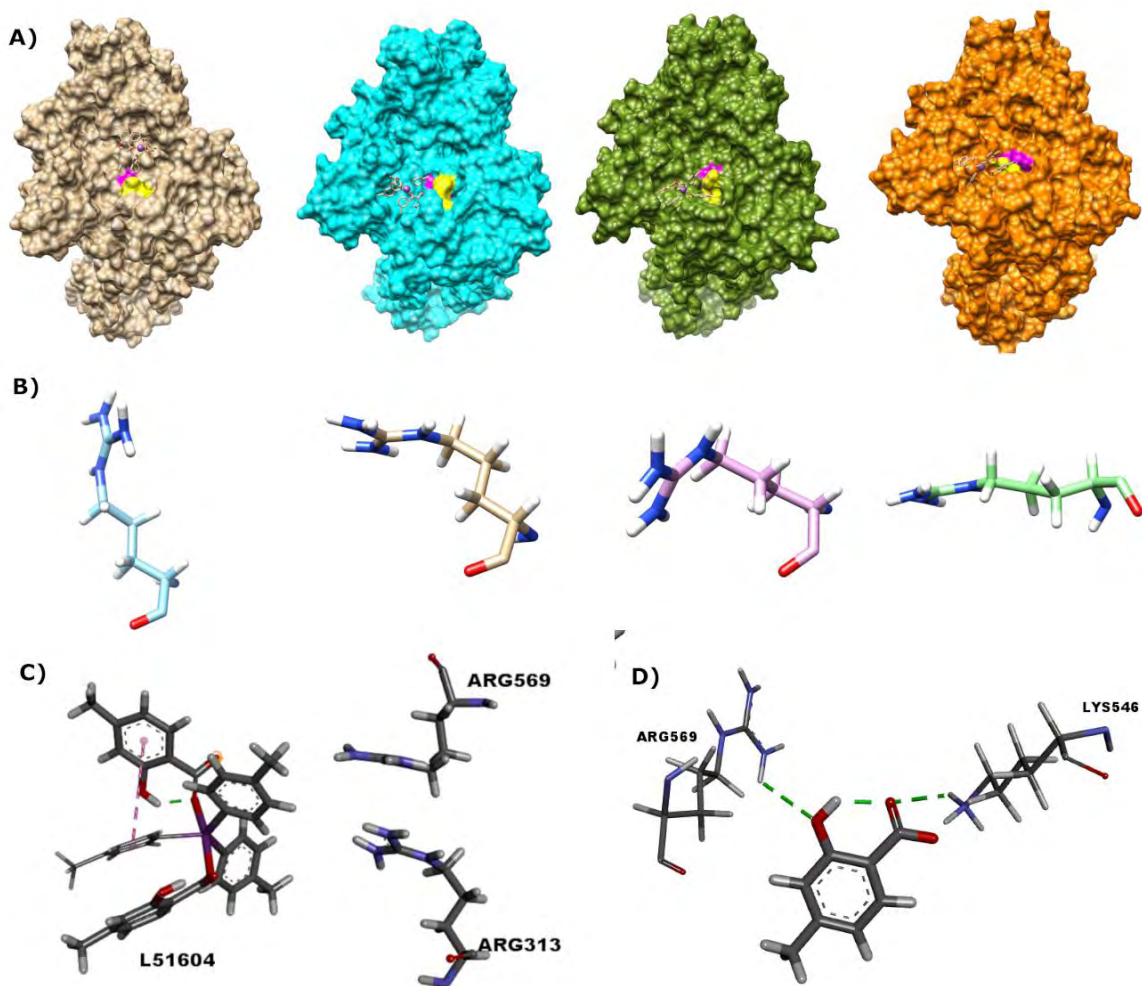


Figure 5.8: Visual representation of Arg569 and ligand dynamics during MD simulations of 1  $\mu$ s in complex with Model-1. A) snapshots taken at 10 ns, 100 ns, 500 ns, and 1  $\mu$ s depict movement of Model-1 from pocket S3 to S4. B) Representation of Arg569 at 10 ns, 100 ns, 500 ns, and 1  $\mu$ s exhibiting the role of Arg569 in modulating ligand dynamics. C) Snapshot taken at 10 ns with critical residues of protein and chains of Model-1 highlighted. D) Snapshot taken at 1  $\mu$ s depicting interaction of OH present at LIG604 of Model-1 with both Arg313 and Arg569.

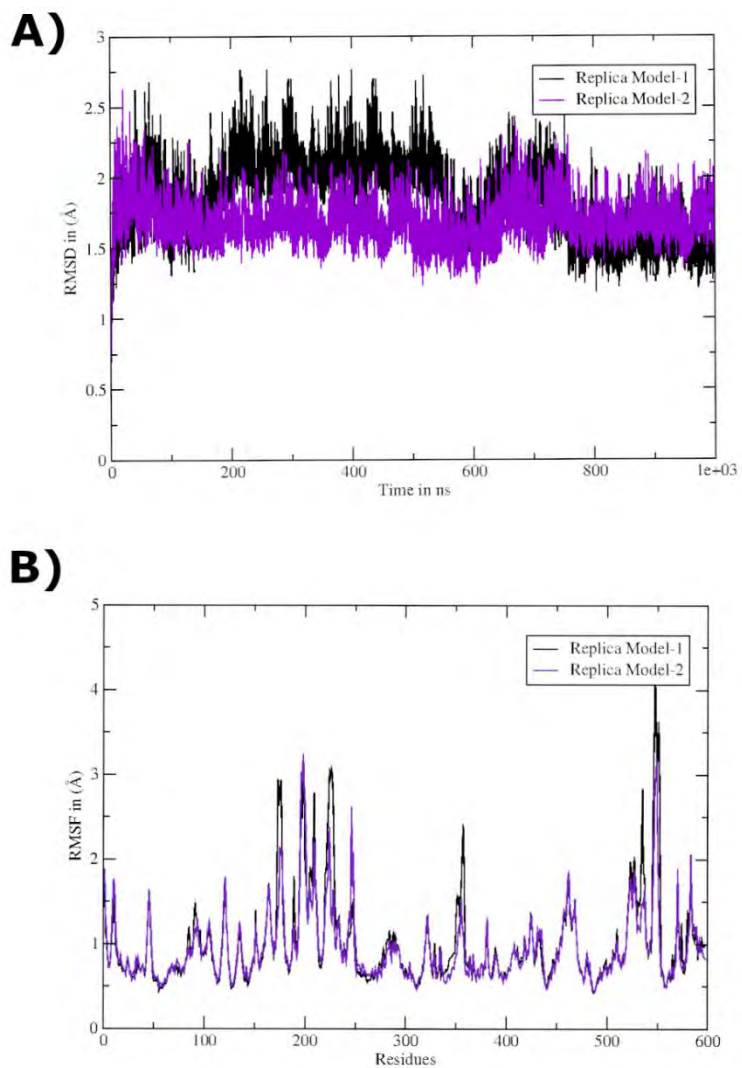


Figure 5.9. Replica simulations for 1  $\mu$ s of both Model-1 and Model-2 in complex with TSA. Bismuth Model-1 stayed intact till the end of simulations while making strong interactions with OH of ligand and Arg313. Bismuth Model-2 however, exhibited similar ligand dynamics and shifted to nearby pocket S4. A) Root mean square deviation B) Root mean square fluctuations C) Beta-factor D) Radius of gyration.

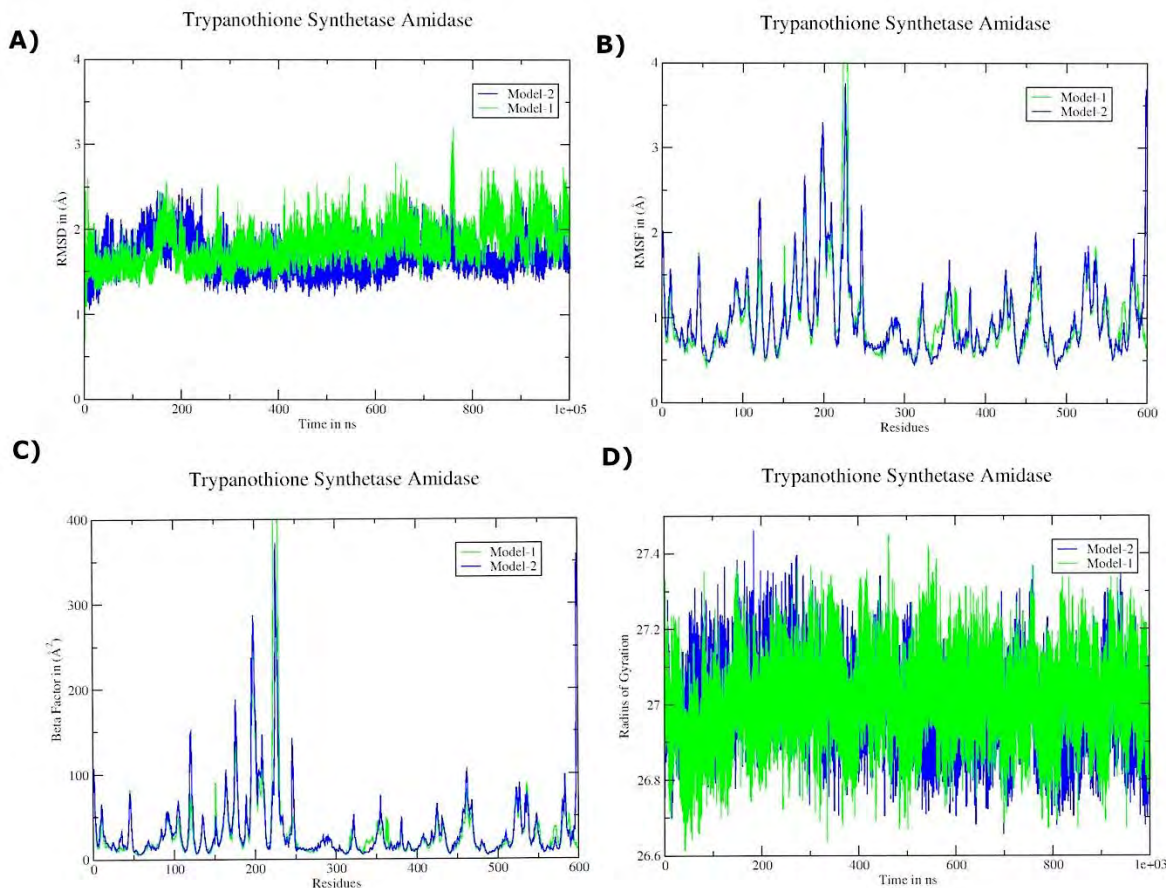


Figure 5.10: Trajectory analysis of Model-1 and Model-2 in complex with trypanothione synthetase-amidase carried out on 1  $\mu$ s MD simulations. A) Root mean square deviation B) Root mean square fluctuations C) Beta-factor D) Radius of gyration.

#### 5.3.4.2 Insights into dynamics of Arg569

To reaffirm the role of Arg569, we induced mutations in TSA giving rise to three mutated models (1-3), which were run for 100 ns each. Single mutation of residue Arg569 to Glu569 led to the mutated Model-1 whereas mutated Model-2 comprise 4 residues of pocket S4 that exhibited stronger interactions depicted in **Figure 5.12** including Arg569. Mutated Model-3 however signifies 4 mutated residues as Model-2 but keeps Arg569 non-mutated. Mutated residues namely Lys546, Tyr551, Phe328, and Leu543 comprise the S4 pocket, which would not affect the binding dynamics of S3.

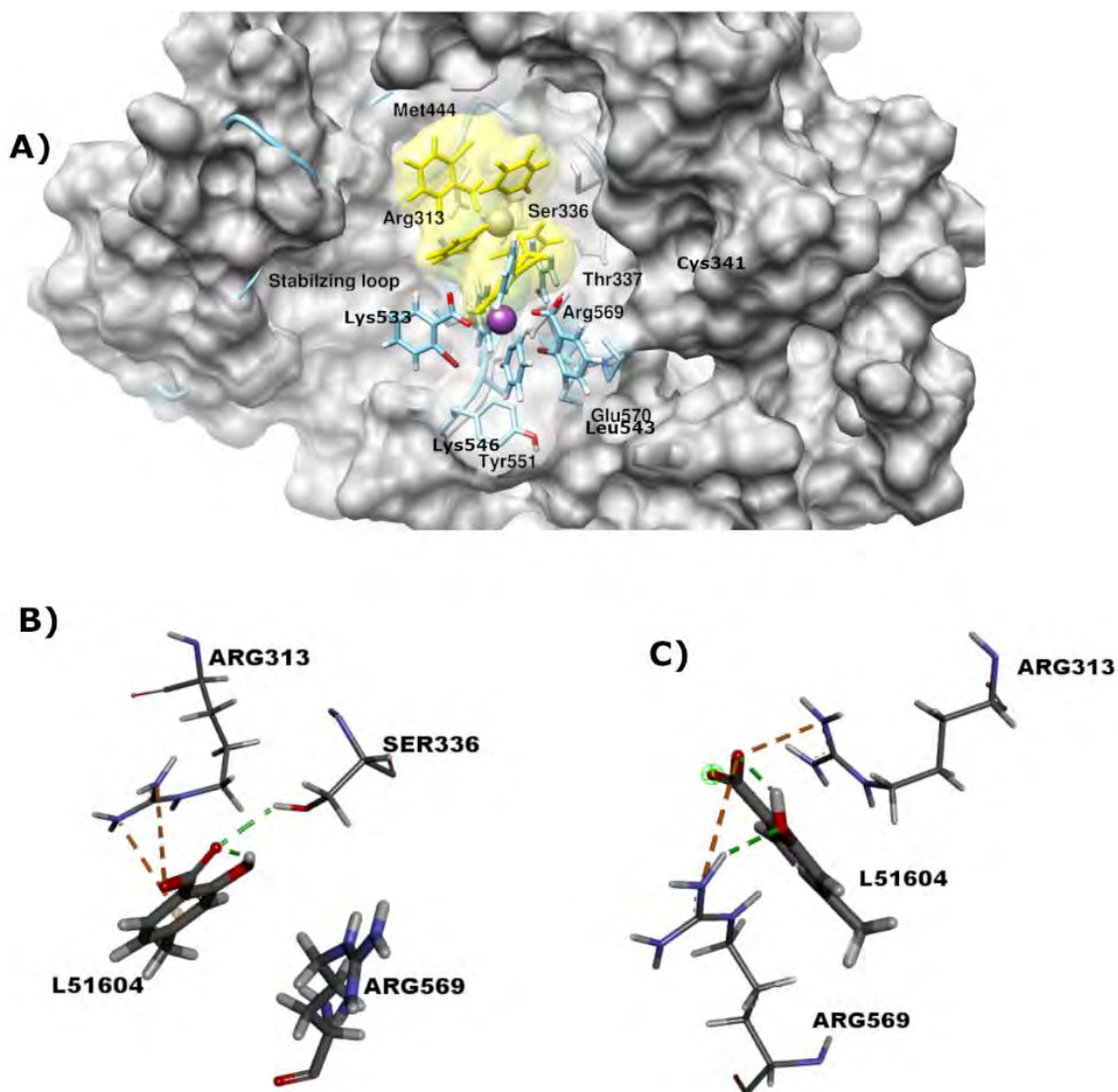


Figure 5.11: A) Snapshots of Model-2 overlapped to depict the movement of a ligand from position S3 to S4. B) Interactions diagram of replica simulations at 1  $\mu$ s of Model-1 in complex with trypanothione synthetase-amidase. C) Interactions diagram of replica simulations at 1  $\mu$ s of Model-2 in complex with trypanothione synthetase-amidase.

Interestingly, **Figure 5.12** supported by the **Figure 5.13** signifies the detachment of ligand in all models with Arg569 substituted with Glu569 whereas Arg569 in mutated Model-3 reaffirms the significance of this residue, which maintained interactions with the bismuth Model-1 till 100 ns. Overall RMSD of all systems fluctuated between maximum

and minimum value of 1.5 Å to 2.5 Å, respectively. We also put emphasis on the importance of OH in a ligand that oriented the activity of Arg569 by exhibiting strong hydrogen bonding with the ligand instead of Ser336, another significant residue for establishing and stabilizing the transition state. These findings reveal that Arg569 that is essential for the stability of transition state in a synthetase reaction, is completely occupied by bismuth containing compounds.

Furthermore, we compared snapshots and simulations results of control drug meglumine antimoniate. **Figure 5.14** comprising RMSD, RMSF, beta-factor and Rg graphs clearly depict the movement of Model-3 away from the active site of TSA. Despite the presence of Arg313, model-3 was unable to retain the binding site due to failure in establishing contacts with Arg569. However, to support our findings and to have insights into the rearrangement of Arg569 in complex with models (1-3) alongwith the reported pentavalent antimony drugs, we carried out CPPTRAJ analysis to identify the native contacts that are important for stabilization at both sites (S3 and S4).

**Figure 5.15** of native contacts depict residues that maintained interactions in maximum number of frames with distance less than 4 Å. Interacting residues observed at 10 ns are mostly the conserved residues of S3 pocket comprising Arg569, Ser3346, Glu392, Glu393, Met444, and Pro571 with maximum contact points in simulation frames. These interacting partners were however changed with the ligand movement comprising Glu569, Phe328, Ala531, Lys533, Gln541, Tyr551, and Ile553 observed at 100 ns. Common residues that maintained interactions till 1 µs are Tyr551, Lys546, Phe328, Ile553, and Arg569, which underwent mutations given in **Figure 5.12**.

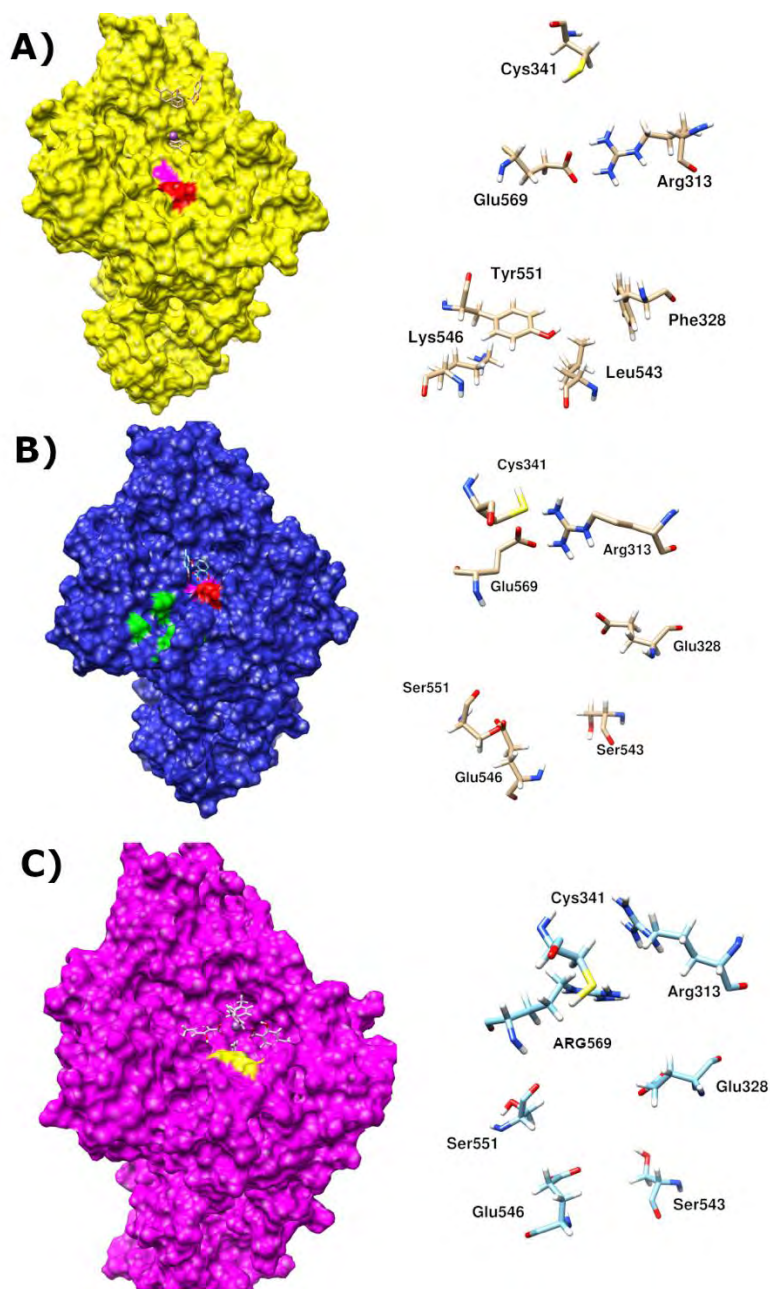


Figure 5.12: Mutated models to understand the role of Arg569 in anchoring the bismuth models (1-3). A) Mutated Model-1 at 100 ns with single mutation of residue Arg569 to Glu569. B) Mutated Model-2 with 4 mutations at S4 pocket comprising Lys546, Tyr551, Phe328, and Leu543 including Arg569 at 100 ns. C) Mutated Model-3 with 4 mutations at S4 pocket comprising Lys546, Tyr551, Phe328, and Leu543 with Arg569 non-mutated.

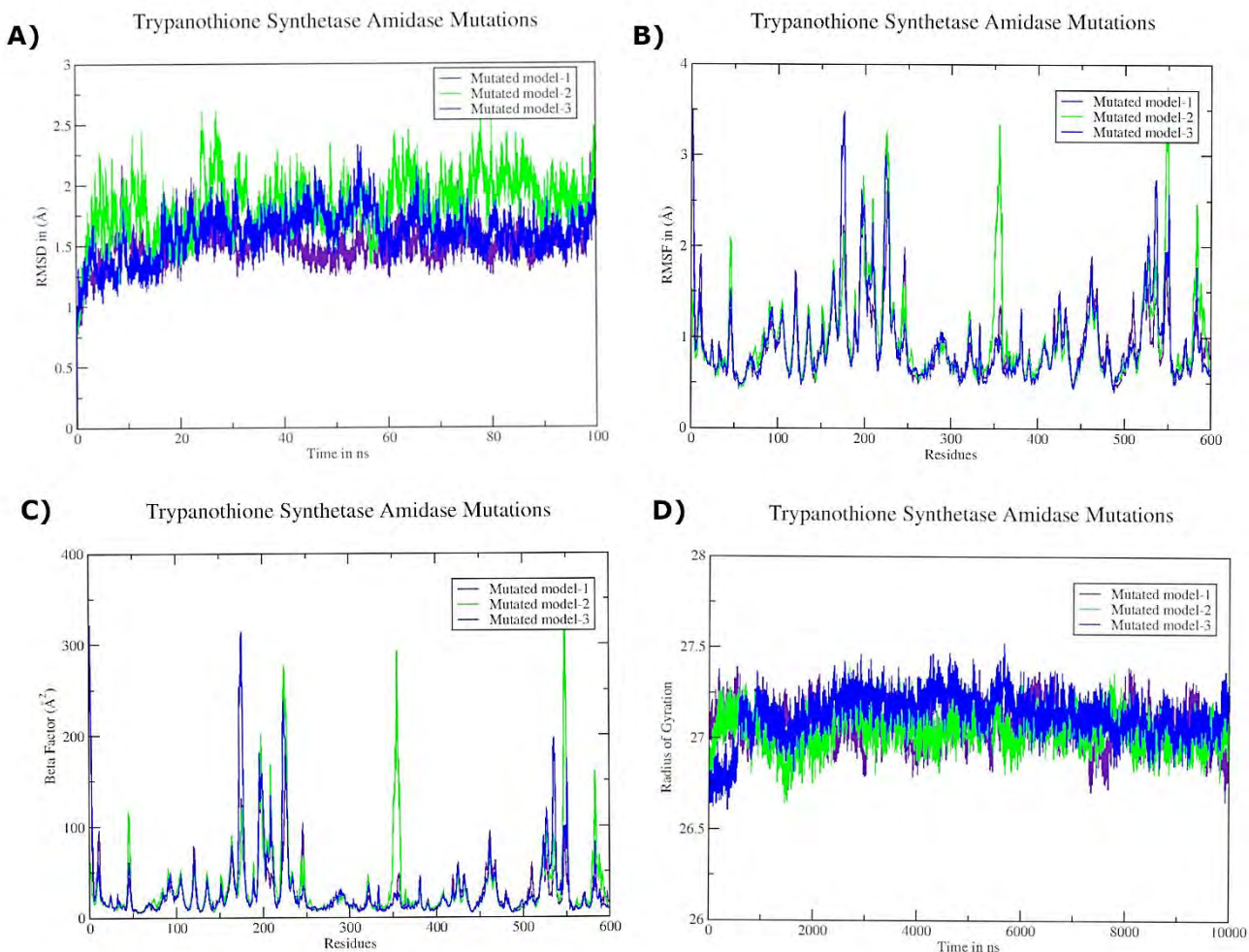


Figure 5.13: Trajectory analysis of mutated models (1-3) in complex with trypanothione synthetase-amidase carried out on 100 ns MD simulations. A) Root mean square deviation B) Root mean square fluctuations C) Beta-factor D) Radius of Gyration.

Furthermore, to monitor the change in orientation of Arg569 and estimate the involvement of hydrogen bond interactions in imparting stability, we applied RDF and AFD. RDF and AFD clearly expose the ligand shift from one chain to another in Model-1 along with the atom distribution along the simulation path that contributed to extended interactions at different time intervals (ns). **Figure 5.16** shows Arg569 simulations at 10 ns that exhibited highest peak at 3.4 Å with  $g(r)$  value of 0.02 with “LIG603” chain of bismuth Model-1. Whereas RDF at the end of simulations at 1  $\mu$ s exhibited higher and

stronger density peaks while interacting with “LIG604” chain of bismuth model-1 that carries the ortho group.

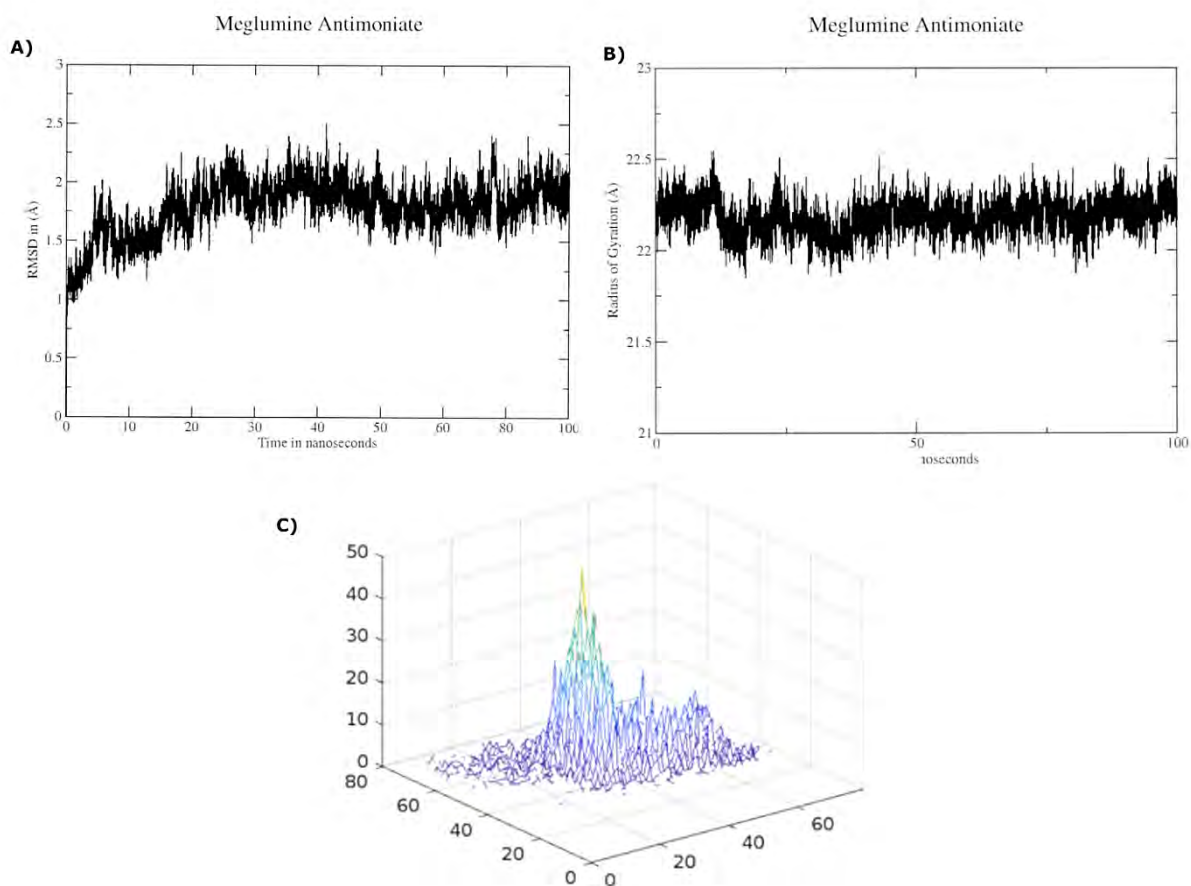


Figure 5.14. MD simulations analysis of pentavalent antimonial; Meglumine antimoniate in complex with trypanothione synthetase-amidase. A) RMSD B) Radius of gyration (Rg) C) AFD graph generated from trajectories of 100 ns MD simulations.

Similarly, Model-2 in complex with TSA exhibited similar pattern with maximum peak at 4.2 Å with  $g(r)$  value of 0.7 at 10 ns and the distance of 2.6 Å with  $g(r)$  value of 0.3 at 1 μs is observed. These results provide powerful insights into the hydrogen bond interactions throughout the simulations that directly impact the ligand dynamics connected with the Arg569.



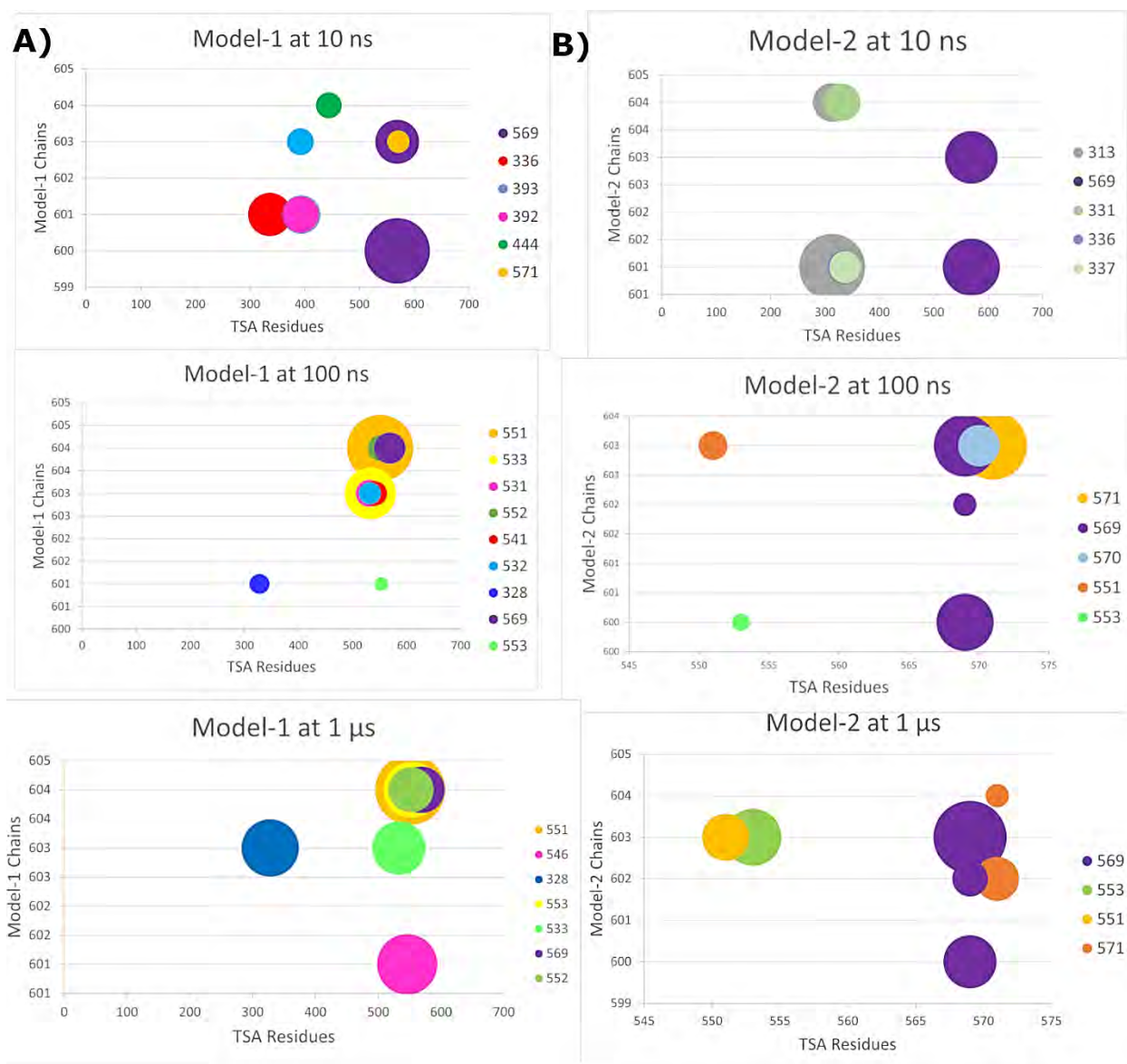


Figure 5.15. Native contacts established by bismuth Model-1 and Model-2 with pockets of TSA at different time intervals of 1  $\mu$ s MD simulations. A) Interacting residues of both sites (S3 and S4) of TSA in complex with bismuth Model-1 at 10 ns, 100 ns, and 1  $\mu$ s. B) Interacting residues of both sites (S3 and S4) of TSA in complex with bismuth Model-2 at 10 ns, 100 ns, and 1  $\mu$ s.

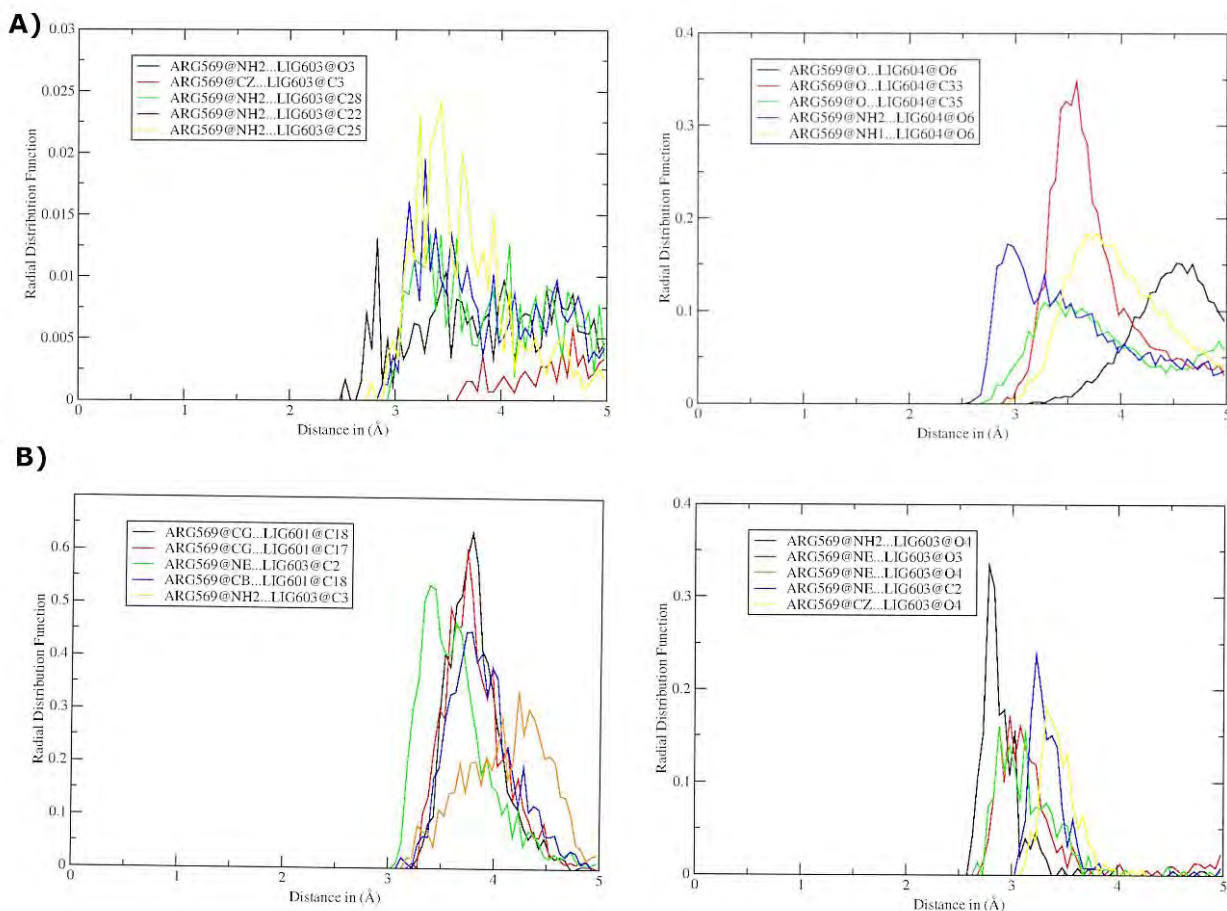


Figure 5.16. Radial distribution functions carried out on bismuth Model-1 and Model-2 at 10 ns and 1  $\mu$ s. A) RDF calculated for bismuth Model-1 with OH group present. B) RDF calculated for bismuth Model-2.

Moreover, Arg569 dynamics are best depicted in **Figure 5.17** representing movement of Arg569 over the simulations. Interactions observed at 10 ns between Glu569@NH2 and LIG603@O3 exhibited variations in binding pattern between different atoms of Arg569 and LIG603. Whereas peaks and density distributions keep increasing over the time depicted in snapshots taken at 100 ns and 1  $\mu$ s of Model-1. These sharper peaks and higher density distribution indicate stability of model-1 at S4 position where Arg569 lies horizontally while making interactions with Arg313. MD simulations snapshots also reveal change in dynamics of Cys341 due to movement of Arg569.

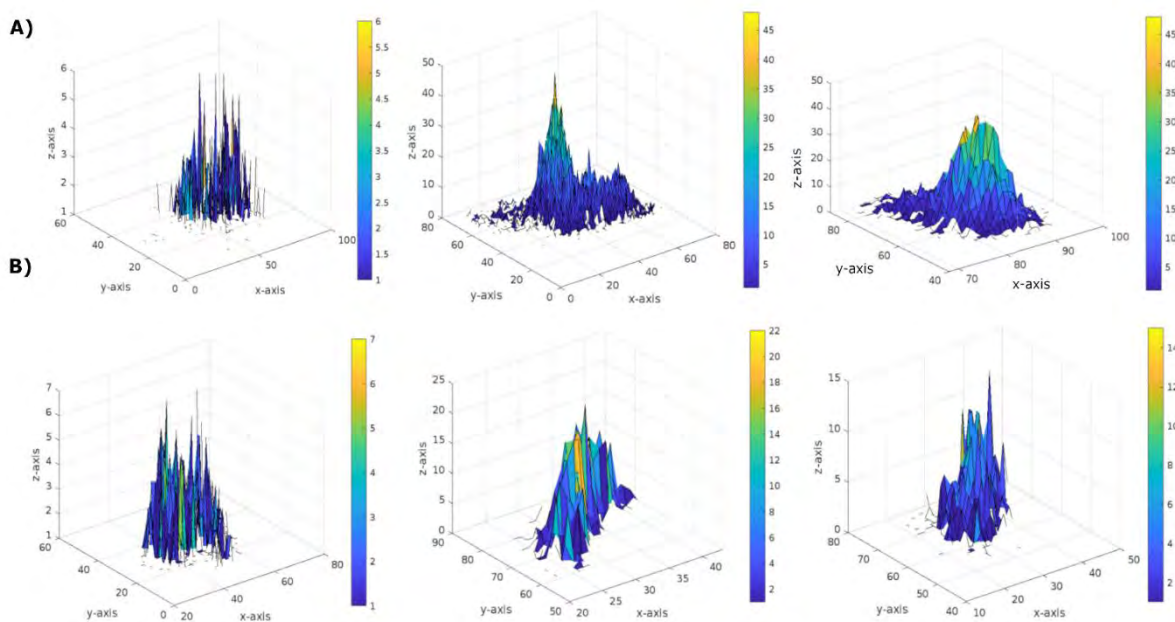


Figure 5.17. AFD results of Model-1 and Model-2 with trypanothione synthetase-amidase calculated over 1  $\mu$ s MD simulations each indicating period of positional shifts of Arg569. A) AFD of Model-1 at 10 ns, 500 ns, and 1  $\mu$ s. B) AFD of Model-2 at 10 ns, 500 ns, and 1  $\mu$ s.

These graphs indicate strong intermolecular forces between Model-1 and the Arg residues (Arg569 and Arg313) where the ligand is sandwiched between the two residues signifying the role of OH sidechain. These findings also point to the fact that any change in one of these residues can completely affect the dynamics of ligand binding. Overall analysis of all three bismuth models (1-3) in complex with TSA highlight the role of Arg569 that appears as a driving force for such ligand dynamics that can critically affect the inhibitory activity of this enzyme.

#### 5.3.4.3 Molecular basis of Bi(V) with trypanothione reductase

Bismuth containing compounds are further investigated with the second protein: TR of T(SH)<sub>2</sub> pathway. The X-ray crystal structure used in MD simulations (PDB ID 4APN) comprise the NADPH and FAD present in each monomer of a dimer. Whereas, the catalytic site for trypanothione molecule or inhibitor is characterized by the presence of two Cys residues accompanied by a His residue that is critical not just for inhibitory studies but for

dimerization as well<sup>206,308</sup>. MD simulations run for 1  $\mu$ s reveal that bismuth containing compounds bound at the interface of two chains act as competitive inhibitor of FAD that occupies the position where glutathione tail binds. Role of Cys52 and Cys57 residues of TR, however, is noteworthy which moves closer to the metalloid bound ligand over the period demonstrated in **Figure 5.18**.

Distance profile created from 100 ns MD simulations trajectories, exhibit decrease in distance from 6.9 to 5.4 Å between Cys52 and the model-1 whereas Cys72 revealed distances ranging from 6.9 to 3.5 Å. In a review study reported by *Baiocco et al.* it is clearly reported that Bi(V) and Sb(V) drugs are less toxic and 10-times more effective against TR, which in current study occupied two catalytic cysteine residues and His residue in the interface while exhibiting strong potential to inhibit TR<sup>304,308</sup>. Findings suggest that Bi(V) comparatively yields better results in terms of making interactions with neighboring residues belonging to 2-fold symmetric active site due to its pentagonal coordinating geometry.

Furthermore, it is observed that in the design of metal inhibitors of TR, several metals have exhibited inhibitory role with noteworthy IC<sub>50</sub> values such as Sb(III), Au(I) and AF (1-thio-b-d-glucopyranosato-(triethylphosphine)gold 2,3,4,6-tetraacetate) with similar binding mechanism but with toxicity issues<sup>309-311</sup>. Kinetic studies have disclosed higher functional characteristics of Au(I) and AF compared to Sb(III) that is Ki = 50 nM, 155 nM and 1.5  $\mu$ M, respectively<sup>269</sup>. This study, however, validates the reaction mechanism at computational level whereas the experimental analysis suggests that tris(*p*-tolyl)<sub>3</sub>Bi analogues hold the capability to inhibit with higher IC<sub>50</sub> and mortality percentage that correlates with data observed in antimony(V) dicarboxylate inhibitory studies<sup>312</sup>. Overall, the comparative free energy analysis of all models that underwent MD simulations alongwith their experimental IC<sub>50</sub> values are exhibited in **Table 5.1** with both trypanothione enzymes, which clearly prioritize Model-1 for further analysis.

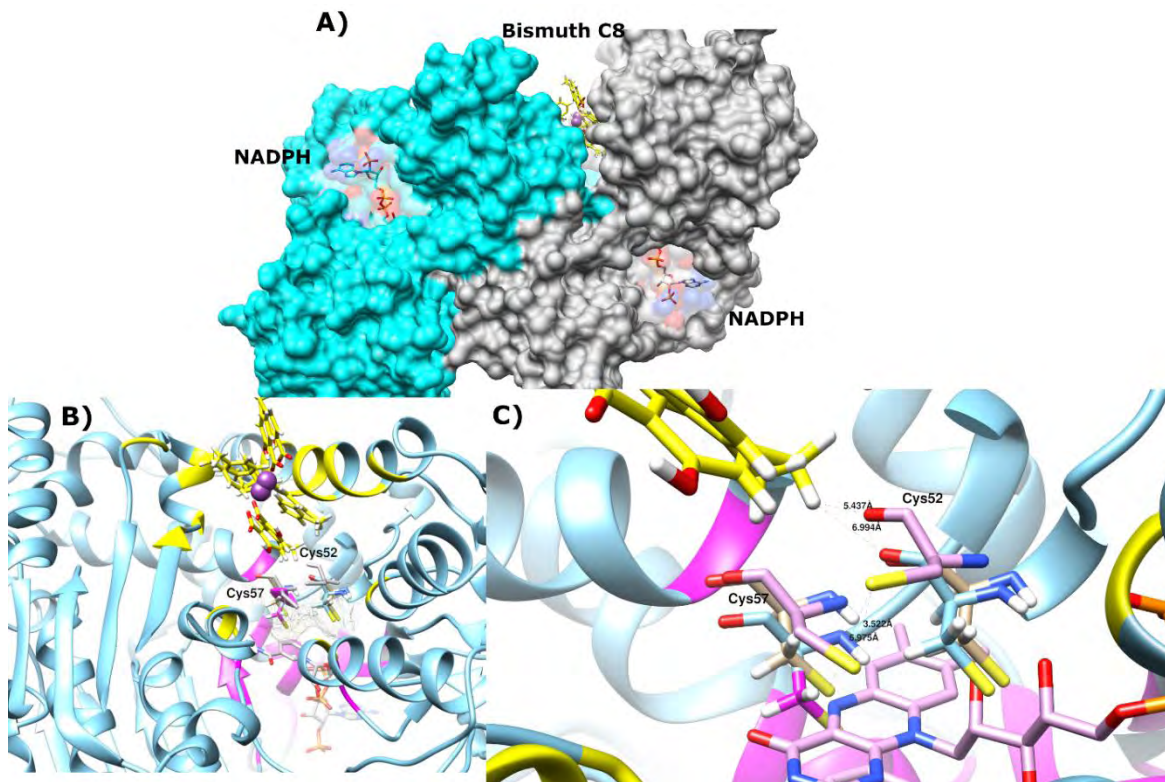


Figure 5.18. Depiction of molecular interactions demonstrated by Model-2 with hotspot residues of conserved binding cleft of TR A) Depicts overall 3D structure of TR with NADPH and Model-2 bound with FAD B) Close-up view of overlapped snapshots extracted from 10 ns and 100 ns trajectories with Model-2 highlighted in yellow whereas FAD lying behind the cavity is exhibited in elemental color C) Close-up view of distance profile between the Cys52 and Cys57 over the period.

## 5.4 Concluding remarks

While the unique systems of T(SH)<sub>2</sub> metabolism serve as valuable template in the design of selective anti-trypanosomatid agents, limited treatment options of parasitic diseases are obtainable. In the recent years, emerging drug resistance against present drugs particularly pentavalent antimonial emphasize on collective measures to explore novel inhibitors with varying chemical environment. One of the foremost strategies is to design chemical compounds capable of inhibiting multiple targets of redox homeostasis T(SH)<sub>2</sub> pathway. The available crystal structures lay strong basis to elucidate structural information of TSA and TR to design and optimize inhibitors to target the conserved binding clefts.

Nevertheless, application of dual drugs or single-targeted drugs open avenues to disrupt these metabolic pathways at multiple points. However, another foremost strategy to interfere antimicrobial resistance (AMR) is to design new formulations particularly with metalloids offering less toxicity that will act as a preamble of variation in novel drug discovery methods.

This study therefore manifests experimentally determined anti-leishmanial Bi(V) metalloids recently published in our previous work<sup>285</sup>, which are not only parametrized for the first time but to date is the first computational study that have provided powerful insights into binding potential of metalloids with enzymes of trypanothione pathway. These compounds were synthesized with salt metathesis reaction that underwent variety of analytical analysis for structural characterization such as X-ray crystallography, NMR spectroscopy and demonstrated higher antileishmanial activity with lower cytotoxicity compared to amphotericin B.

We have extended the experimental study by employing QM calculations with SBKJC ECP level of theory to retrieve novel force field parameters of Bi(V) compounds synthesized as series of [BiAr3(O2CR)2] alongwith a known Sb(V) drug, meglumine antimoniate. Force field parameterization revealed bidentate chelating behaviour of both Bi(V) models (Model-1 and Model-2), particularly Model-2 exhibited pentagonal bipyramidal geometry with higher binding affinity due to presence of subsalicylate in its structure. Moreover, the reported distances in experimentally determined X-ray crystal structure are in agreement with distances observed in optimized models illustrated in **Table 5.2**, thus validating the choice of a basis set. Such a parameterization at the hub of an inorganic metal centers and specifically bi-inorganic complex will give rise to further parameterization of new metals of biological relevance and can be considered as baseline importance of this work.

Furthermore, MD simulations of 5  $\mu$ s to elucidate conformational dynamics and binding potential of Sb(V) and Bi(V) containing compounds revealed role of Arg569 in modulating the ligand dynamics. Interestingly, the presence of ortho group in a bismuth Model-1 has a crucial role in bridging two Arg residues: Arg569 and Arg313 of the binding site. These findings are supported by comprehensive interaction analysis, RDF, AFD, and

binding free energy calculations. Similar findings have been revealed by experimental study that categorized Model-1 with higher antileishmanial activity and lower toxicity profile. It has been emphasized that OH group lying at alpha position is actively involved in making interactions with neighboring residues, which may improve the lipophilicity of this compound.

However, with the intention of targeting multiple enzymes of the same pathway, similar compounds were subjected to MD simulations with TR. TR that contains NADPH and FAD in a dimer structure holds the binding cavity at the interface of two chains. Proposed study targeted the critical cysteine residues Cys52 and Cys57 that moved closer to the Bi(V) models during MD simulations, thus occupying the area where glutathione tail of FAD attaches for its regular function<sup>304</sup>. Noticeably, similar behaviour yielded by Bi and Sb metalloids point to analogous electronic structures of these metals with the ability to extend interactions as bidentate or monodentate structures probably due to occurrence of these metalloids in the same group according to the periodic table, which presents Bi as less toxic than Sb<sup>278,279,313</sup>.

Similarly, the critical role of bismuth complexes is not only evident but there is striking opportunity of these complexes to perform better than their counterparts. Reaffirmation of structural attributes of bismuth in this context is of utmost medicinal importance. In conclusion, this study deciphers the impact of novel metalloids that can effectively cater drug resistance and toxicity issues for leishmaniasis and other diseases if applied in the context of biologically relevant enzymes.

This research work has been published in *Journal of Chemical Information and Modeling* by the ACS publishers and can be found at publications section of this thesis.

---

## CHAPTER 6

---

*Senna Makki* and other Active  
Phytochemicals: Myths and Realities behind  
Covid19 Therapeutic Interventions



## 6 MYTHS AND REALITIES BEHIND COVID19 THERAPEUTIC INTERVENTIONS

### 6.1 Background

Due to continuously evolving genetic makeup of the SARS-CoV-2 virus and its ability to spread rapidly, it has taken a huge toll on individuals, communities and societies across the world by ruthlessly affecting over 340 million people globally leading to 5.5 million deaths as of 20<sup>th</sup>, January 2022 <sup>314</sup>. However, several vaccines worldwide namely; Oxford–AstraZeneca, Pfizer-BioNTech, Sinopharm-BBIBP, Moderna, Sinovac, Johnson & Johnson, and mRNA-1273 (developed by Moderna Inc.), have been given authorization on an emergency basis due to overwhelmed health systems that have caused widespread social and economic disruption <sup>315</sup>. Despite the rollout of vaccines to the general public, the trend in the daily number of cases reported is still on the higher side signifying the end of the SARS-CoV-2 pandemic as implausible <sup>316,317</sup>. One of the foremost reasons is the unavailability of vaccines especially in low-income and middle-income countries leading to a standstill to achieve global control of SARS-CoV-2 <sup>318</sup>. Another big reason is that a large number of people are reluctant to get a vaccine shot rather they believe in using herbal medicines as an alternative cure to SARS-CoV-2 <sup>319</sup>. Nevertheless, traditional medicinal plants have a vast history in treating infectious diseases. For example, malaria was treated for a very long time with *Artemisia Annu* (sweet wormwood) in China and *Cinchona Officinalis* (Cinchona tree) in South America <sup>320</sup>. Another example is the use of Chinese traditional medicine *Lianhuaqingwen* in the treatment of SARS-CoV-2 exhibiting inhibition of virus replication in a dose-dependent manner with IC<sub>50</sub> of 411.2 ug/ml <sup>321</sup>. Thus, the role of herbal medicines in these unprecedented times of ongoing pandemic has resulted in a global catastrophe that cannot be ignored.

While the effectiveness of some medicinal plants has been scientifically proven, there is a global tendency for self-medication with different herbal medicines without proper scientific evidence. There has been a myth regarding the use of famous *Senna* tea in treatment of Covid19 that has eventually lead to its excessive use followed by a drastic hike in prices <sup>322,323</sup>. It is generally used as an herbal tea made from *Senna* pods or leaves

cultivated in different countries having different species commonly known as *Alexandrian Senna*, *Tinnevelly Senna*, *Indian Senna*, and *Sanna Makki*. The plant extracts of different species consists of many active anthraquinones and flavonoids including sennosides, aloemodin, rhein, iso-rhamnetin and kaempferol<sup>324,325</sup>. Limitation of long term use of *Senna* is reported to be concomitant with dehydration and diarrhea<sup>326</sup>. Apprehensions on the propagation of misleading information about its use in Covid19 treatment were enhanced through social and mainstream media without sufficient scientific evidence<sup>327</sup>. It is of utmost importance to remove ambiguity about using *Senna* tea in Covid19 treatment, which can rather aggravate the symptoms by causing irritated bowl linings, dehydration, and electrolyte imbalance that can ultimately be fatal<sup>328,329 330</sup>.

The scope of this study, therefore, serves to analyze potential binding of particularly those phytochemicals that have been suggested to inhibit the major protease of SARS-CoV-2, 3-Chymotrypsin-Like Protease (3CL<sup>pro</sup>) *in vitro* with IC<sub>50</sub> 0 – 10 μM in comparison with the phytochemicals present in *Senna*. Inhibition of 3CL<sup>pro</sup> is crucial in viral lifecycle and design of SARS-CoV and SARS-CoV-2 inhibitors<sup>168</sup>. It is highly conserved among the SARS-CoV viruses and displays 96% similarity with the zoonotic genome, especially the bat coronavirus<sup>331,332</sup>. To further explore the possibility of chemical compounds of *Senna* to be active against other Covid19 protein targets, we elucidated its structural properties with additional essential proteins of SARS-CoV-2 namely; spike protein, helicase nsp13, and RdRp nsp12. The findings of this study will assist in distinguishing potential phytochemicals from a group of known and social media acclaimed plant based Covid19 treatments based on comparative structural dynamics. Moreover, compounds proposed in this study will hold a rationale to inhibit both PL<sup>pro</sup> and 3CL<sup>pro</sup> and provide avenues to use the scaffolds of these molecules in the design of more specific SARS-CoV-2 inhibitors in the future.

## 6.2 Materials and methods

The complete workflow of the current study is mentioned in **Figure 6.1**.

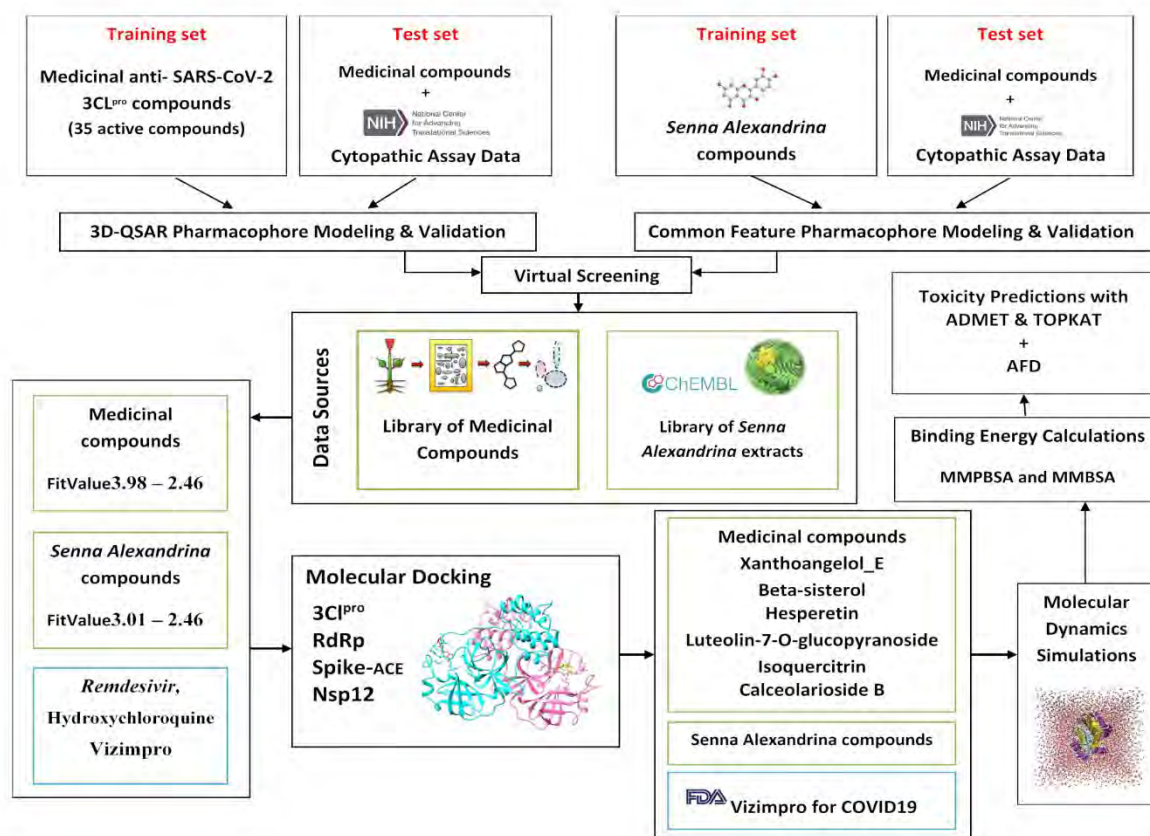


Figure 6.1. Workflow of the current study to identify potential phytochemicals against Covid19 drug targets from a list of known and social media acclaimed natural products.

## 6.2.1 Dataset collection for pharmacophore modeling

### 6.2.1.1 Training set

Two training sets were required for the generation of two pharmacophores namely; 3D-QSAR pharmacophore and common feature pharmacophore. A dataset consisting of diverse structural information with *in vitro* data on medicinal plants that have exhibited high potential in inhibiting 3CL<sup>pro</sup> was collected from different resources and used for the generation of 3D-QSAR pharmacophore<sup>333–335</sup>. The inhibitory studies conducted on SARS-CoV-2 reported the IC<sub>50</sub> value of chloroquine between 1.13 to 5.47 μM<sup>336</sup>, thus establishing a threshold to collect only those medicinal compounds that exhibited IC<sub>50</sub> value from 0 – 15 μM. Whereas, *Senna* compounds constituting phenolic acids, flavonoids,

and coumarins with the highest quantity of benzoic acid as well as anthraquinones were used in the training set to generate a common feature pharmacophore.

### 6.2.1.2 Test set

To validate the generated pharmacophores, we investigated both the known active and inactive medicinal compounds between  $IC_{50}$  values 1.2  $\mu$ M to 226  $\mu$ M. Moreover, to randomize the test set, a set of 77 known active and inactive FDA-approved compounds recently released against 3CL<sup>pro</sup> by the National Center for Advancing Translational Sciences (NCATS) ("SARS-CoV-2 cytopathic effect (CPE)", 2021)<sup>337</sup> were also added in the test set. To keep the study consistent with experimental results, we particularly added the controls reported in multiple *in vitro* studies including hesperetin (8.3  $\mu$ M), aloemodin (132  $\mu$ M), apigenin (280.8  $\pm$  21.4  $\mu$ M), luteolin (20.0  $\pm$  2.2  $\mu$ M), quercetin (23.8  $\pm$  1.9  $\mu$ M), and remdesivir (5  $\mu$ M)<sup>338</sup>.

## 6.2.2 Pharmacophore modeling

All the protocols such as; 3D-QSAR pharmacophore modeling, common feature pharmacophore modeling, ligand pharmacophore mapping, and feature mapping were carried out with the BIOVIA Discovery Studio (DS)<sup>190</sup>. In this study, we generated two pharmacophore models; **1)** 3D-QSAR pharmacophore model for biologically active phytochemicals reported against 3CL<sup>pro</sup> and **2)** a common feature pharmacophore for *Senna* compounds with no reported experimental activity with a given target. 3D-QSAR pharmacophore generation protocol that is designed to generate predictive pharmacophores based on ligands with known activity against a specific biological target was run with input ligands set to a training set of 27 active phytochemicals against 3CL<sup>pro</sup>. The HypoGen algorithm generated 200 conformations with an energy threshold for each ligand maintained within a 10 kcal/mol energy range that were further optimized using simulated annealing. The ligands in the dataset used pre-defined 'Activ' and 'Uncert' values. 'Activ' refers to the tested biological values of the input ligands ( $IC_{50}$ ). Whereas; 'Uncert' that is the uncertainty value was set to 1.5 implying the variation between experimental and estimated values during model generation up to two times and also affects the regression fitting of the pharmacophores during optimization. Moreover, to determine the best features that should be considered during the pharmacophore models generation, we used

a Feature mapping tool that maps solvent-accessible features and identifies all possible locations of the selected pharmacophore features on the given ligand. The parameters for “Max” and “Min” in the feature mapping protocol were set to 5 and 1, respectively. The results exhibited hydrogen bond acceptor (HBA), hydrogen bond donor (HBD), hydrophobic (HYD), positive ionizable (PI), and ring aromatic (RA) features as commonly mapped features from the training set compounds.

However, in the absence of biologically predicted values for *Senna* compounds against 3CL<sup>pro</sup>, a common feature pharmacophore was generated with the phytochemicals of *Senna*. We assumed all compounds to be equally active that were considered as reference ligands exhibiting HBA, HBD, HYD, PI, and RA as common features as a result of the feature mapping tool analysis. The protocol carried out both the model generation with a training set and validation with a test set simultaneously. The output file lists the SD file for each pharmacophore aligned to the ligands and the receiver operating characteristic (ROC) curve exhibiting the trade-off between sensitivity and specificity of selected pharmacophores. Each pharmacophore uses the FitValue property to ascertain which ligand uses the maximum features for mapping. Higher FitValue is indicative of more features mapped in a suitable conformation.

### 6.2.3 Pharmacophore validation

Two methods: the cost analysis and test set analysis were used to determine the best 3D-QSAR pharmacophore models. A test set of ligands with similar receptor binding that was not used for model generation was employed to assess the ability of generated pharmacophores to estimate activity of test ligands. The protocol to generate a 3D-QSAR pharmacophore model for the given training set and validation with a test set takes place simultaneously in BIOVIA DS resulting in a detailed report with 10 hypothesis models generated with different statistical parameters. The output file contains an SD file of the input ligands aligned to each pharmacophore with a report summary that includes regression statistics and a plot of LogEstimate vs. LogActiv for the test ligands to quickly determine the best pharmacophore with the ability to predict the activity of test ligands. Whereas; for the cost analysis, the overall cost of each hypothesis was calculated by summing these 3 cost factors; 1) FitValue property that indicates the total number of

features mapped that are HBA, HBD, HYD, PI, and RA **2)** high correlation coefficient ( $r^2$ ), **3)** lowest total cost while exhibiting highest cost difference and **4)** low root mean square deviation (RMSD) values. Another method ligand pharmacophore mapping protocol was run with the test ligands as input to validate the performance of selected pharmacophores and return an estimated value that should be close to the experimental values. It anticipates the activity of selected pharmacophore based on a decent correlation coefficient with the test set ligands and 95% cross-validation confidence.

However, to determine the best common pharmacophore model and to quickly determine the matches, a ligand profiler protocol was used with input data set to test set that was mapped against the generated common feature pharmacophores. Ligand profiler generates a heat map to quickly determine the best set of ligands mapped against a pharmacophore based on the FitValues. From the heat map, the pharmacophores that do not map to any of the test set compounds can be easily identified, making the selection of pharmacophores easier with higher FitValue and more relevant alignment. The selected validated pharmacophores could be used for lead identification from the molecular libraries.

#### **6.2.4 Virtual screening for lead identification**

The selected 3D-QSAR pharmacophore model was used to screen a library of 2,287 compounds comprising alkylated chalcones, phlorotannins, tanshinones, bioflavonoids, and flavonoids. Whereas, the common feature pharmacophore model was used to screen a library of in-house built *Senna* compounds collected using the ChEMBL similarity searching tool<sup>339</sup> against sennosides and anthraquinones present in *Senna*. We chose 3D-QSAR pharmacophore model Hypo1 and the common feature pharmacophore model 10 as a 3D query to screen the input ligands against each pharmacophore feature present in the query to extract the more relevant pharmacophore models. The screen library protocol in BIOVIA DS was used with the minimum features' parameter set to 3, the maximum features parameter set to 4, and the maximum subset of pharmacophore parameter set to 100. This suggests that 100 pharmacophore subsets of all possible 3 and 4 feature pharmacophore from the 5 features will be used for screening. The resulting subset of both the libraries was then subjected to molecular docking.

### 6.2.5 Molecular docking

LibDock algorithm of BIOVIA DS was run to dock the screened ligands from 3D-QSAR pharmacophore of phytochemicals and common feature pharmacophore consisting of *Senna* compounds separately. The screened compounds against 3D-QSAR pharmacophore were reported specifically as anti-3CL<sup>pro</sup> ligands with known biological activity, thus they were not tested for other Covid19 targets and subjected to docking into the active site HIS164 of 3CL<sup>pro</sup><sup>182</sup>. LibDock calculates a hotspot map for the given receptor site containing polar and apolar groups, which are used to generate favorable ligand-receptor interactions followed by the energy minimization step. Due to the conformational differences in the monomeric and dimeric structure of 3CL<sup>pro</sup> as suggested in the literature<sup>340</sup>, we subjected all the complexes to MD simulations with the monomer; whereas, only those compounds were tested with dimer that were unstable with monomer. Moreover, due to the absence of any experimental data on screened compounds sennoside A, B, C, and D of *Senna* against 3CL<sup>pro</sup>, we expanded our research scope and chose four additional proteins that are crucial for the survival of SARS-CoV-2 namely; spike protein (PDB: 6LZG), helicase nsp13 (PDB: 6JYT), RdRp nsp12 (PDB: 6M71) and 3CL<sup>pro</sup> (PDB: 6LU7). In order to validate further, based on dynamics and conformational changes, we selected the three FDA-approved drugs approved against Covid19 namely; remdesivir, hydroxychloroquine, and vizimpro<sup>341</sup>, which were used as a control. The top-scoring compounds from each dataset were then subjected to molecular dynamics (MD) simulations with Amber16<sup>342</sup>.

### 6.2.6 Molecular dynamics simulations

MD simulations were carried out on the active phytochemicals, vizimpro and *Senna* compounds to check the behavior of protein with their proposed ligands. There were 6 phytochemicals and vizimpro in complex with 3CL<sup>pro</sup>, 2 complexes of spike protein (docked at both the regular and allosteric site), helicase nsp13, RdRp nsp12, and 3CL<sup>pro</sup> with *Senna* compounds. For this purpose, parameter/topology files were generated using the LEaP program followed by the system preparation by neutralizing it with counter ions (Na<sup>+</sup>/Cl<sup>-</sup>). TIP3P tetrahedral solvation box was adjusted for 12 Å and General Amber Force Field (GAFF) and ff14SB was used to get insights into the intermolecular and

intramolecular interactions. Furthermore, in the next step, preprocessing was performed for all the systems with 500 steps and 1000 cycles of minimization with 200kcal/mol/Å<sup>2</sup>. The whole system's atoms were again minimized for 1000 cycles with 5kcal/mol/Å<sup>2</sup> by applying restraints on carbon alpha atoms, while 300 minimization steps were run for non-heavy atoms to further relax the system. The system was slowly heated with restraints on the backbone and restraint weight 5 kcal/mol/Å<sup>2</sup> using Langevin dynamics till 300 K. The system was then equilibrated for 100 ps to make it stabilized according to the environment. The pressure was sustained through the NPT ensemble allowing the restraint weight of 5kcal/mol/Å<sup>2</sup>. All these systems then underwent production run of minimum 200 ns with a non-bounded cut-off set to 8.0 Å. However, only those systems were extended that exhibited instability in their RMSD trend.

### 6.2.7 Trajectories analysis

The generated trajectories were analyzed through Amber CPPTRAJ module 16 to observe the stability of the complex. Different parameters such as RMSD, root mean square fluctuations (RMSF), beta-factor (β-factor), and radius of gyration (Rg) were calculated. The generated graphs and trajectories were analyzed using the Visual Molecular Dynamics<sup>234</sup> and Chimera<sup>236</sup>.

### 6.2.8 Binding free energies

Binding free energies were calculated using the MMPBSA/GBSA package of Amber16<sup>239</sup>. Theoretical background of binding free energy calculations is presented in Section 2.5.1. The generated trajectories of MD simulations were subjected to MM(PB/GB)SA.py module<sup>146</sup>. The system works by calculating the energy difference between complex and unaided protein and ligand. The MMPBSA.py module was used to generate the prmtop files of protein, ligand, and complex, which subsequently follow the total binding energies calculation and decomposition binding free energy calculations. The total 450 frames each after every 0.2 seconds were mined from the entire MD trajectories and exposed to MMPBSA calculations. The two methods Poisson-Boltzmann (PB) or Generalized-Born (GB) approaches were used to accomplish the analysis. The binding free energy provides information about the significant residues that help to analyze the components that participated in keeping the protein and ligand intact.



Furthermore, these binding energies were decomposed into per residue and pair residue using the MMPBSA.py module of Amber 16.

### **6.2.9 Axial frequency distribution**

Furthermore, AFD provided in Section 2.5.3 was employed to have insights about the positioning of ligand with respect to coordinates.

### **6.2.10 Toxicity analysis**

ADMET protocol of BIOVIA DS software was used to calculate the ADMET properties of selected compounds whereas; TOPKAT suite of BIOVIA DS software carried out the toxicity prediction based on built-in and validated rodent models. The parameters such as solubility level, absorption level, blood-brain barrier (BBB) penetration level, plasma protein binding (PPB) prediction with a cutoff score of -2.209, CYP2D6 (cutoff score 0.161), and hepatotoxic prediction using a cutoff value of -4.154 were calculated. Moreover, the TOPKAT calculated toxicity based on validated models present in BIOVIA DS such as; FDA rodent carcinogenicity test, the prediction of tumorigenic dose rate 50 (TD50) of a drug, rat maximum tolerated dose (MTD), test rat oral acute median lethal dose (LD50) of a chemical, prediction of rat chronic lowest observed adverse effect level (LOAEL), ocular and skin irritancy.

### **6.2.11 Network pharmacological analysis**

Last but not the least, network pharmacological approach was used to decipher the signaling pathways associated with target proteins of proposed phytochemicals against Covid19. Proposed phytochemicals including *Senna* compounds were subjected to <http://www.swisstargetprediction.ch/> to identify the drug targets. Whereas, the DisGeNET (<http://www.disgenet.org/>) disease target prediction analysis platform was used to find the drug targets of Covid19. Drug targets that were common between Covid19 and phytochemicals were selected and merged by Cytoscape3.9.1 software to construct an active ingredient-key targets Covid19 network.

## 6.3 Results and discussion

### 6.3.1 Pharmacophore modeling

Ligand-based 3D-QSAR pharmacophore modeling resulted in the generation of 10 hypotheses that aligned to the ligands present in training set. The best hypothesis Hypo1 was selected based on the highest correlation value of 0.74, highest cost difference of 115.21, and the lowest RMSD of 1.39 Å. The statistical values of 10 hypotheses are summarized in **Table 6.1**. The highest cost difference values indicate the ability of pharmacophore to predict estimated values with respect to experimental values with 90% significance. The selection of best pharmacophore model was also based on the highest FitValue of 4.36 that is based on the alignment of training set ligands to the pharmacophore.

Table 6.1: Statistical parameters of top 10 3D-QSAR pharmacophore hypotheses generated using HypoGen algorithm.

Hypothesis No.	Total Cost	Cost Difference <sup>a</sup>	RMSD <sup>b</sup>	Correlation	Features <sup>c</sup>
1	125.43	115.2	1.39	0.741	HBA, HP, RA
2	129.24	111.39	1.44	0.729	HBA, HP, RA
3	137.88	102.76	1.52	0.707	HBA, HP, RA
4	141.68	98.961	1.55	0.697	HBA, HP, RA
5	145.10	95.537	1.57	0.691	HBA, HP, RA
6	145.21	95.429	1.58	0.689	HBA, HP, RA
7	146.72	93.917	1.60	0.682	HBD, HP
8	153.04	87.594	1.65	0.667	HBA, HP, RA
9	154.81	85.827	1.68	0.660	HBA, HP, RA
10	157.02	83.620	1.75	0.653	HBD, HP

The null cost and the fixed cost are 240.64 and 109.19, respectively

<sup>a</sup> Cost difference between the null and the total cost

<sup>b</sup> RMSD, root mean square deviation

<sup>c</sup> Abbreviation used for features: HBA, hydrogen bond acceptor; HYD, hydrophobic; RA, Ring Aromatic.

Four common features consisting of 1 HBA, 2 HYD, and 1 RA were observed in Hypo1. It was noted that all the features of pharmacophore were mapped to the most active medicinal compound xanthoangelol\_E having IC<sub>50</sub> = 1.2 ± 0.4 μM, depicted in **Figure 6.2**. Moreover, a list of Hypo1 estimated and experimental values with their corresponding error values against medicinal compounds are also given in **Table 6.2**. Interestingly, it was also

noted that among the four features, only RA was missing from other active phytochemicals endorsing the importance of HBA and HYD features, which might be responsible for the experimental activity.

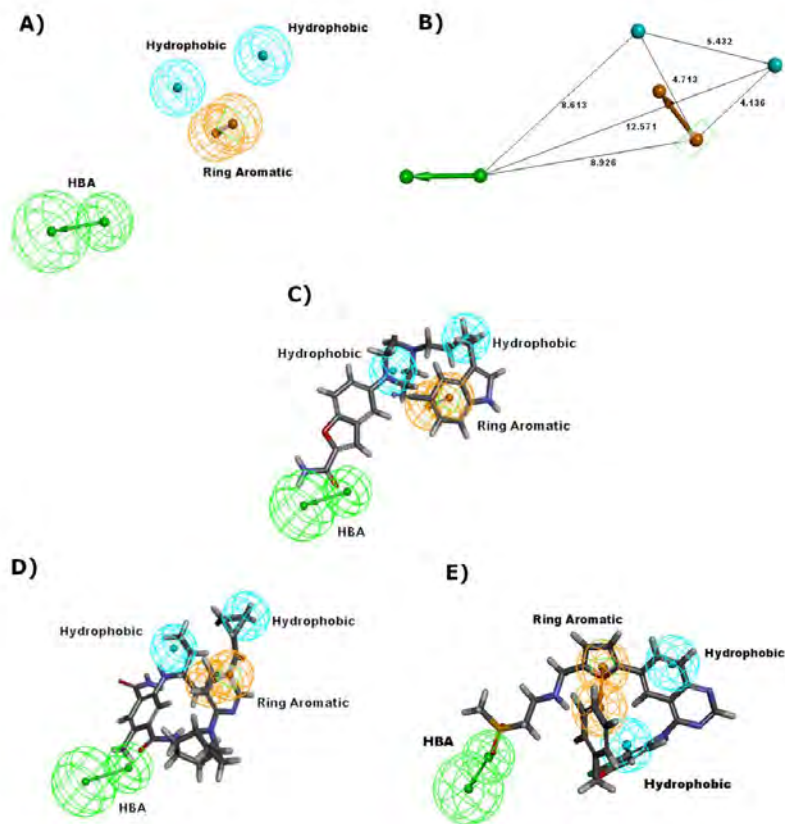


Figure 6.2 3D-QSAR pharmacophore model of compounds comprising alkylated chalcones, phlorotannins, tanshinones, bioflavonoids, and flavonoids. **A)** 3D-QSAR pharmacophore exhibits four common features consisting of 1 hydrogen bond acceptor (HBA), 2 hydrophobic (HYD), and 1 ring aromatic (RA) **B)** 3D-QSAR pharmacophore model with distance between chemical features. **C)** The most active medicinal compound; xanthoangelol\_E from the training set mapped with the highest FitValue of 4.36 **D)** The top compound, vilazodone mapped against 3D-QSAR pharmacophore with the highest FitValue of 3.56 from the test set. **E)** The second top compound lapitinib with a FitValue of 3.54 mapped against 3D-QSAR pharmacophore from the test set.

However, in the case of *Senna* compounds, it was observed that the common feature pharmacophore no. 10 aligned with the training set compounds with highest FitValues exhibiting 3 HBA and 1 RA features. The compound isoquercetin mapped to the common feature pharmacophore with highest FitValue of 0.975 as displayed in **Figure 6.3**. However, it is noteworthy that the presence of hydrophobic pockets and basic residues in 3CL<sup>pro</sup> have been reported in the literature<sup>182</sup>, highlighting the significance of hydrophobic features, which is missing in the case of common feature pharmacophore.

Table 6.2: Predicted and experimental IC<sub>50</sub> values of the training set compounds based on the 3D-QSAR Hypothesis 1 pharmacophore model.

Name	FitValue	Predicted IC <sub>50</sub> (μM)	Experimental IC <sub>50</sub> (μM)	Error	Status	Mapping
Xanthoangelol_E	4.36	1.60	1.20	1.40	active	[6 20 12 9]
Hesperetin	3.68	6.60	8.30	1.50	active	[1 23 14 *]
Iguesterin	3.08	8.10	2.70	3.10	active	[2 25 4 *]
Dieckol	3.14	5.70	2.70	2.10	Moderately active	[12 37 33 *]
Tanic acid	2.12	61	3.00	20	moderately active	[11 * * 61]
Psoralidin	3.71	5.30	4.20	1.30	moderately active	[5 23 17 *]
Tomentin	3.00	7.90	5.00	1.60	moderately active	[3 32 21 *]
Pristimerin	3.07	6.70	5.50	1.20	moderately active	[2 33 24 *]
Amentoflavone	3.00	8.00	8.30	-1.0	moderately active	[9 21 * 13]
Tingenone	2.81	12	9.9	1.20	moderately active	[3 25 5 *]
Betulinic acid	3.03	7.30	10	-1.40	moderately active	[1 31 14 *]
Diplacone	3.11	6.1	10	-1.70	moderately active	[6 29 16 *]
Celastrrol	2.74	15	10	1.40	moderately active	[4 16 18 *]
Dihydro tanshinone I	2.18	53	14	3.70	moderately active	[* 15 * 1]
Mimulone	3.13	5.80	14	-2.50	moderately active	[5 22 15 *]

\*Refers to the missing features.

### 6.3.2 Validation of pharmacophore models

Validation of any 3D-QSAR hypothesis model is primarily based on the cost analysis of two theoretical values **1)** total cost value and **2)** null cost value. A good quality pharmacophore has a cost difference of 40 to 60-bit score representing 70 – 90%

confidence level along with other important parameters such as lowest RMSD and the highest correlation values. However, the 3D-QSAR model selected in this study represents the probability of more than 90% correlation among the data sets with the highest total cost difference 115.21 and highest correlation value 0.74, exhibiting a pharmacophore model with high prediction ability for lead identification.

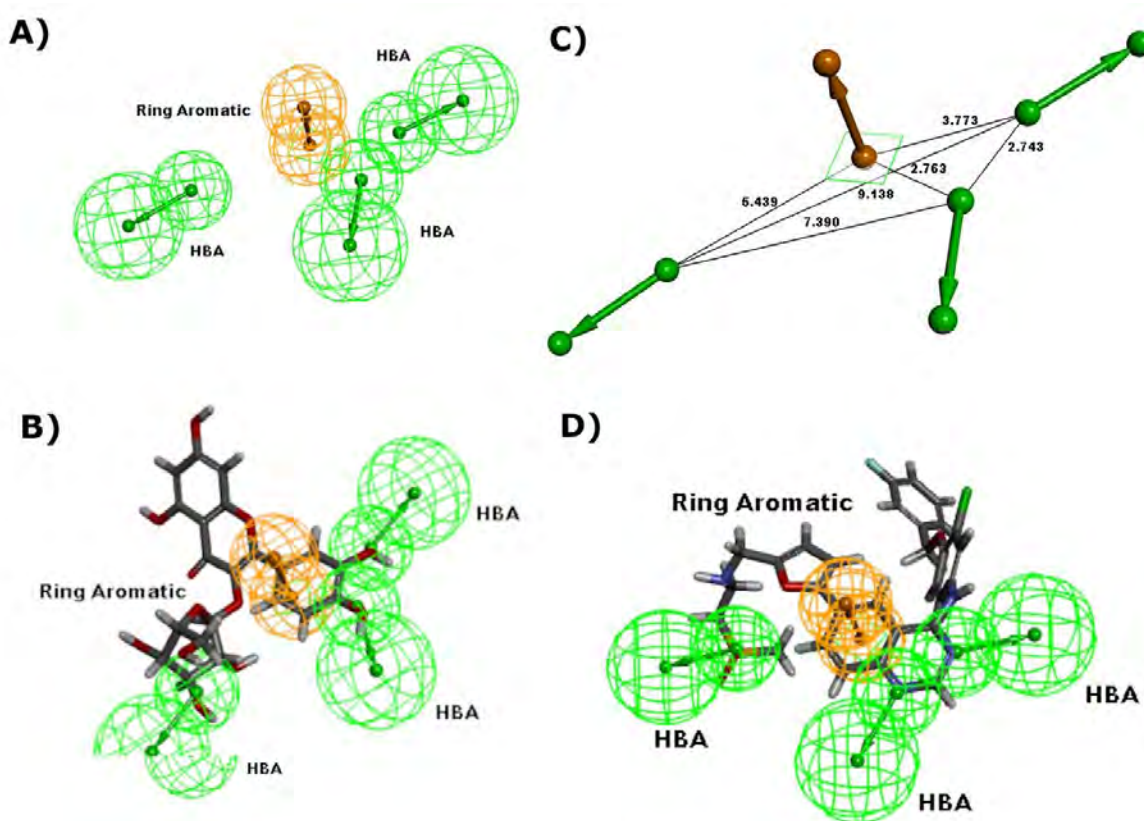


Figure 6.3. Common feature pharmacophore of *Senna* compounds A) Results exhibit four common features consisting of 3 hydrogen bond acceptors (HBA) and 1 ring aromatic (RA) features B) Common feature pharmacophore model with distance between chemical features. C) Isoquercetin mapped the common feature pharmacophore with highest FitValue of 0.99 from the training set. D) Compound with lowest FitValue.

Apart from the cost analysis of the training set, the 3D-QSAR pharmacophore model was validated using error values estimated between the experimental and estimated activity values generated as a result of the ligand pharmacophore mapping protocol. 33 test

set compounds mapped to Hypo1 pharmacophore with error value of  $\leq 10$  depicting order one difference between the experimental and estimated  $IC_{50}$  values. The statistical analysis indicated higher regression coefficient ( $R^2$ ) value of 0.646 for the test set while cross-validating the results with training set that displayed regression coefficient value  $R^2=0.495$ , depicted in **Figure 6.4**.

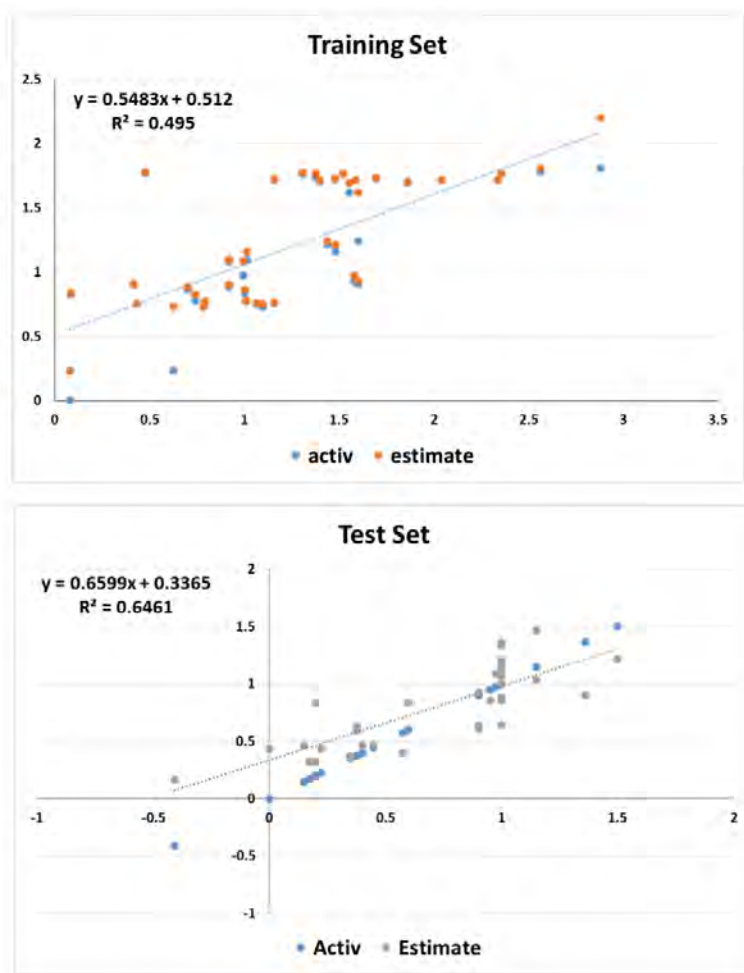


Figure 6.4. Correlation graph in logarithmic scale for experimental values vs. predicted values of training and test ligands that mapped the 3D-QSAR pharmacophore model Hypo1.

Moreover, the FDA-approved drugs, vilazodone and lapatinib both having  $IC_{50}$  of 10  $\mu$ M from the test set mapped the 3D-QSAR pharmacophore model highest FitValue of 3.56 as depicted in **Figure 6.2**. From these results, it was conceived that the presence of

chemical features HBA, HYD, and RA for 3CL<sup>pro</sup> inhibitory activity are crucial and are also found in FDA-approved drugs currently under clinical trials. Furthermore, in the case of common feature pharmacophore modeled for the *Senna* compounds, the ROC curve was used to evaluate the degree of false positivity of the model with known active and inactive compounds. The curve plots true positives against false positives and indicates if the model predicted active compounds higher than the inactive compounds. The AUC value lies between 0 and 1; 0 is indicative of a bad classifier, however, the selected model exhibited a fair accuracy score of 0.710 as presented in **Figure 6.5**. **Table 6.3** displays sensitivity and specificity values of the selected model with an ability to distinguish between active and inactive compounds.

Table 6.3 Statistical variations of common feature pharmacophore models.

Validation with known Active/Inactive compounds								
Pharmacophore	Total Active	Total Inactive	True Positives	True Negatives	False Positives	False Negatives	Sensitivity	Specificity
1	77	39	30	14	25	47	0.38	0.35
2	77	39	31	14	25	46	0.40	0.35
3	77	39	33	14	25	44	0.42	0.35
4	77	39	32	14	25	45	0.41	0.35
5	77	39	33	11	28	44	0.42	0.28
6	77	39	33	11	28	44	0.42	0.28
7	77	39	34	10	29	43	0.44	0.25
8	77	39	33	14	25	44	0.42	0.35
9	77	39	31	15	24	46	0.40	0.38
10	77	39	34	14	25	43	0.44	0.35

Additionally, the results of ligand profiler protocol exhibited mapping of 15 test set compounds accurately with the selected pharmacophore and labeled active compounds as red and inactive as blue that can be seen in **Figure 6.5**. It is therefore determined from the validation results that both pharmacophore models exhibited the capability to classify active and inactive compounds. The 3D-QSAR pharmacophore model however exhibited all the significant features that are required for binding of 3CL<sup>pro</sup>, while the common feature pharmacophore model failed to identify hydrophobicity as a common feature.

### 6.3.3 Virtual screening

The validated 3D-QSAR Hypo1 model and the common feature pharmacophore model No. 10 were used as a query to screen for new lead compounds from the medicinal library of 2,287 compounds and *Senna* compounds. The compounds from the virtual screening that best mapped to the pharmacophore models were selected based on the highest FitValues. The compounds with FitValue ranging from 3.98 – 2.46 from each library were selected and subjected to molecular docking.

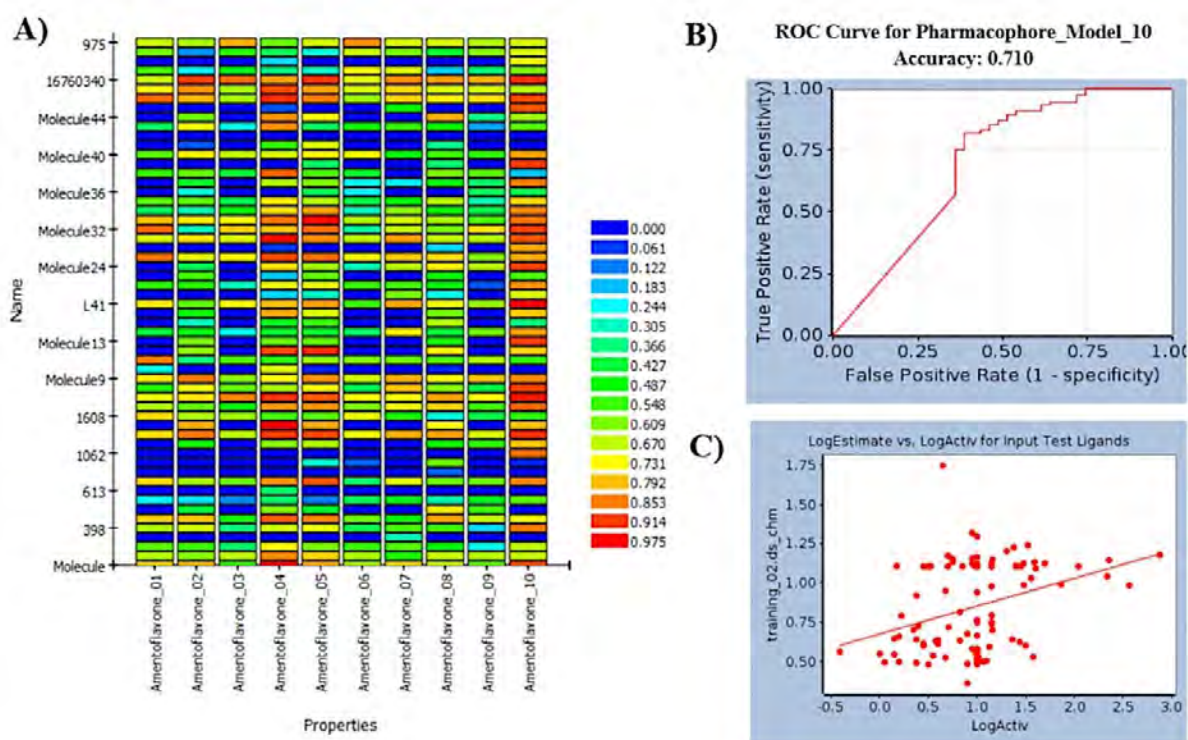


Figure 6.5. A) Heat map generated by the ligand profiler for validation of common feature pharmacophore model No. 10 with the test set B) ROC curves generated for the validation of common feature pharmacophore model with the test set C) Logarithmic graph between estimated and experimental values of the training set and test set of common feature pharmacophore.

### 6.3.4 Molecular docking

Since 3D-QSAR pharmacophore was generated with respect to only one target, the resulting compounds from virtual screening along with the 27 training set compounds of



the active phytochemicals were subjected to molecular docking with 3CL<sup>pro</sup>. The top six compounds; xanthoangelol\_E with the highest LibDock score of 202, beta-sitosterol with a score of 198, hesperetin with a score of 152, luteolin-7-O-glucopyranoside, isoquercetin, and calceolarioside\_B with LibDock score 124, 114, and 112 from the medicinal library were chosen, respectively. However, considering the fact that theoretically one of the tea ingredients of *Senna* may bind a different Covid19 protein and/or key cellular protein, it was necessary to expand our research to determine the binding potential of *Senna* compounds. Therefore, the *Senna* compounds screened for common feature pharmacophore that does not require a specific target for model building were subjected to docking with four additional proteins (both structural and non-structural) of Covid19. The standing of selected proteins in the structure of Covid19 virion is presented in **Figure 6.6**.

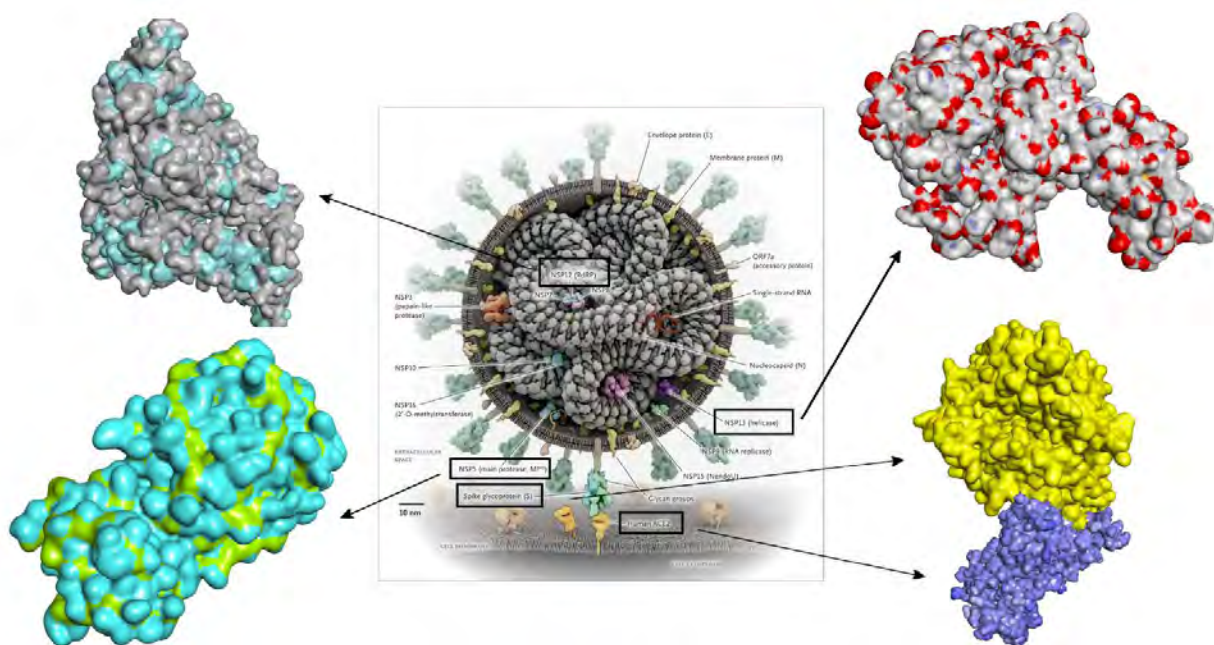


Figure 6.6 SARS-CoV-2 virion with the four selected proteins. The structure of virion is taken from <sup>343</sup>.

The docked compounds present in high quantity in *Senna* namely; sennoside A, B, C, and D were chosen for further analysis on the basis of Libdock score against each target protein. Herein; we also subjected three recently approved FDA drugs remdesivir, hydroxychloroquine, and vizimpro to molecular docking to validate results based on

comparative analysis. However, the topmost compound vizimpro with the highest docking score of 129 was further subjected to MD simulations to further validate representative pharmacophore models and demonstrate their efficiency.

#### 6.3.4.1 Active phytochemicals

The topmost compound, xanthoangelol\_E is an alkylated chalcone capable of inhibiting both 3CL<sup>pro</sup> and PL<sup>pro</sup> in a significant dose-dependent manner with IC<sub>50</sub> ranging from 1.2 ± 0.4 to 46.4 ± 7.8 μM<sup>344</sup>. Xanthoangelol\_E completely occupied the catalytic pocket of 3CL<sup>pro</sup> making interactions with all the sub-pockets S1, S2, S3, S4, and S5 as depicted in **Figure 6.7**. Whereas, the second and third topmost compounds; beta-sitosterol, and hesperetin, are phytochemicals with reported inhibitory activity for 3CL<sup>pro</sup> with IC<sub>50</sub> 115 μM and 8.3 μM, respectively<sup>345</sup>. Both these compounds exhibited strong hydrogen bond interactions with significant residues of 3CL<sup>pro</sup> such as Glu166, Thr190 and His164 presented in **Figure 6.7** while occupying the sub-pockets S3, S4 and S5. Beta-sitosterol also exhibited other significant interactions such as alkyl, pi-alkyl, and pi-pi T-shaped with residues Leu50, Leu167, Ala191, Met165, Pro168, and His41, respectively. Whereas, hesperetin not only exhibited interactions with the catalytic dyad but the –OH substitutes displayed strong hydrogen bond interactions with Arg489, Gln493, His464, and Leu442.

Furthermore, the fourth topmost compound is luteolin-7-O-glucopyranoside, which is a phytochemical essentially a derivative of luteolin and cynaroside. Luteolin is commonly known for its anti-inflammatory activities both *in vitro* and *in vivo* based on its pharmacologically competent mechanism of action<sup>346</sup>. The glucopyranoside ring of this compound targeted the sub-pockets S1 and S3 while exhibiting interactions with His163, Glu166, and Gln192 as depicted in **Figure 6.8** lying near the catalytic dyad (Cys145-His41). Whereas, the fifth compound, a hydroxycinnamic acid, calceolarioside\_B exhibited potential binding affinity with the sub-pockets S1, S2, and S3. The oxygen atoms of the ligand molecule have shown conventional hydrogen bond interactions with Asn142, His41, and Gly143 residues of the binding pocket.

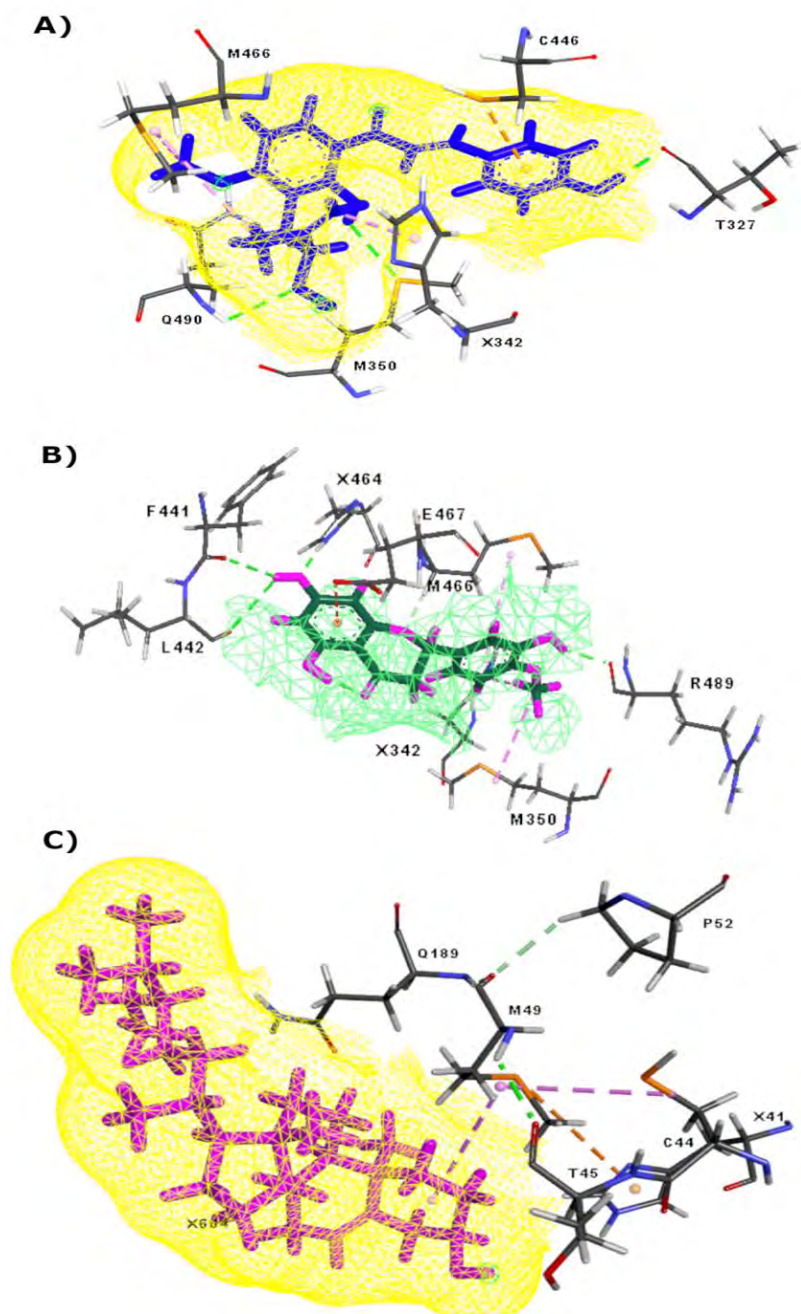


Figure 6.7. Preferred binding mode of active phytochemicals in the binding site of 3CLpro depicting two-dimensional (2D) docked complex with **A)** Xanthoangelol\_E having an  $IC_{50}$  value  $11.4 \pm 1.4 \mu M$  **B)** Hesperetin having an  $IC_{50}$  value  $8.3 \mu M$  **C)** Beta-sitosterol with an  $IC_{50}$  value  $1210 \mu M$ .

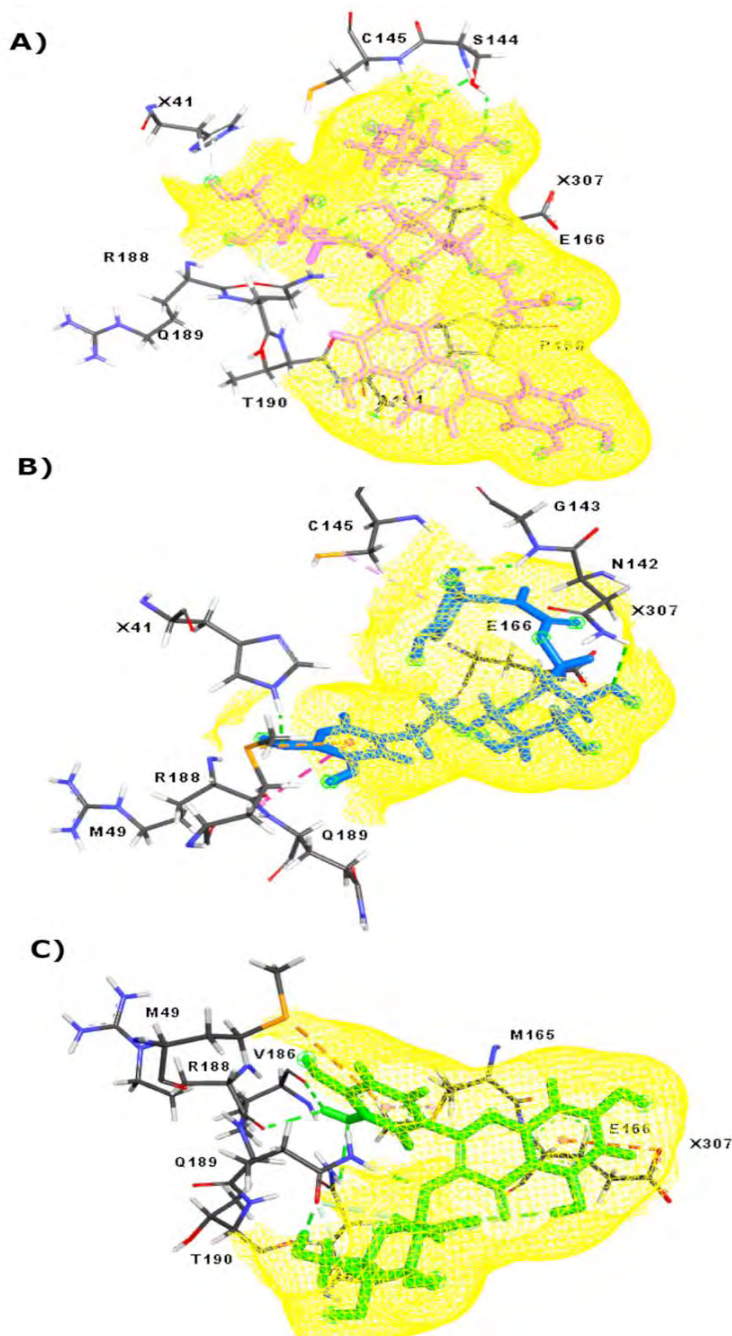


Figure 6.8. Preferred binding mode of active phytochemicals in the binding site of 3CLpro depicting two-dimensional (2D) docked complex with A) Luteolin-7-O-glucopyranoside B) Calceolarioside\_B C) Isoquercetin.

### 6.3.4.2 Senna compounds

To get insights into the binding potential of *Senna* compounds, they were subjected to docking with four additional essential proteins of SARS-CoV-2 to conclude and convey the larger significance of this study.

#### 3CL<sup>pro</sup>

The docking results of 3CL<sup>pro</sup> with *Senna* compounds presented in **Figure 6.9** exhibit conventional hydrogen bond interactions with residues Gly170, Gly138, Lys5, Val125, and GLU288 with Libdock score of 109. Compared to the docking results of active phytochemicals against 3CL<sup>pro</sup>, *Senna* has shown weak binding affinity and few intermolecular interactions suggesting that this might not be a potential lead compound for the inhibition of target protein.

#### Helicase Nsp13

Nsp13 is an interesting drug target as it plays a crucial role in the transcription-replication complex of CoVs. Docking of *Senna* compounds against helicase nsp13 has resulted in the Libdock score of 114. Significant hydrogen bond interactions of oxygen atoms of the ligand can be observed in **Figure 6.9** with residues Glu377, Ser312, Gln539, Ser541, Thr288, Arg445, and Glu321. Furthermore, Ala314 and Ala318 were involved in pi-alkyl interactions with benzene ring of the ligand playing a crucial role in adjusting and anchoring the ligand within the binding pocket.

#### RdRp Nsp12

Non-structural proteins such as nsp12 are highly conserved proteins, which are essential for viral infection. *Senna* compounds have shown a Libdock score of 102 against RdRp nsp12. Active pocket residues Trp617, Lys798, Asp760, Cys622, Lys551, and Lys621 have made crucial hydrogen bond interactions with the oxygen atoms of the ligand as depicted in **Figure 6.9**. Furthermore, the benzene ring of the ligand has made pi-anion interactions with Aap618.

## Spike protein

Spike protein aids in the attachment of virus to the host cell and thus is a significant drug target for inhibition studies. Docking of *Senna* compounds against receptor-binding domain (RBD) of spike protein bound with ACE2 receptor resulted in Libdock score of 118. The active site residues involved in crucial interactions with the protein are Asp30, Gly416, Arg408, His34, Ser494, Tyr495, Glu37, Ala387, and Tyr421. Significant hydrogen bond interactions of binding site residues with ligand oxygen atoms have firmly anchored the ligand within the active pocket as depicted in **Figure 6.9**.

Furthermore, several other intermolecular interactions such as pi-anion and pi-alkyl between receptor and ligand have also contributed to enhanced binding affinity. Moreover, to analyse the conformational changes in spike-ACE2 complex and to estimate the capability of *Senna* compounds to disrupt interactions between spike protein and ACE2 receptor, molecular docking at the allosteric site of spike protein has revealed a Libdock score of 126. Protein residues Ala330, His356, Glu357, Asp332, and Asn376 have exhibited strong hydrogen bonding interactions with the lead compound. However, Glu384 has exhibited pi-anion interactions with two benzene rings of the ligand.

### 6.3.5 Molecular dynamics simulations

All complexes including vizimpro (the control) were subjected to MD simulations to have insights into the dynamics and conformational stability of active phytochemicals in complex with the SARS-CoV-2 3CL<sup>pro</sup> and *Senna* compounds with 3CL<sup>pro</sup>, RdRp nsp12, helicase nsp13, and spike-ACE2.

#### 6.3.5.1 Analysis of active phytochemicals

The first compound beta-sitosterol exhibited noteworthy results during 200 ns of MD simulations. It possesses stability with both the chains A and B throughout simulations and moved even deeper in the binding pocket of 3CL<sup>pro</sup> as displayed in Fig 6. Interestingly, beta-sitosterol was observed making alkyl and pi-alkyl interactions more often with the residues of the active site with an average RMSD of 1.78 Å, Rg 22.2 Å and  $\beta$ -factor 31.6 Å as exhibited in **Figure 6.10**. The influence of electrostatic interactions in attaining

conformational stability has been explained in the literature several times <sup>347</sup>, proposing beta-sitosterol as an interesting candidate for further analysis.

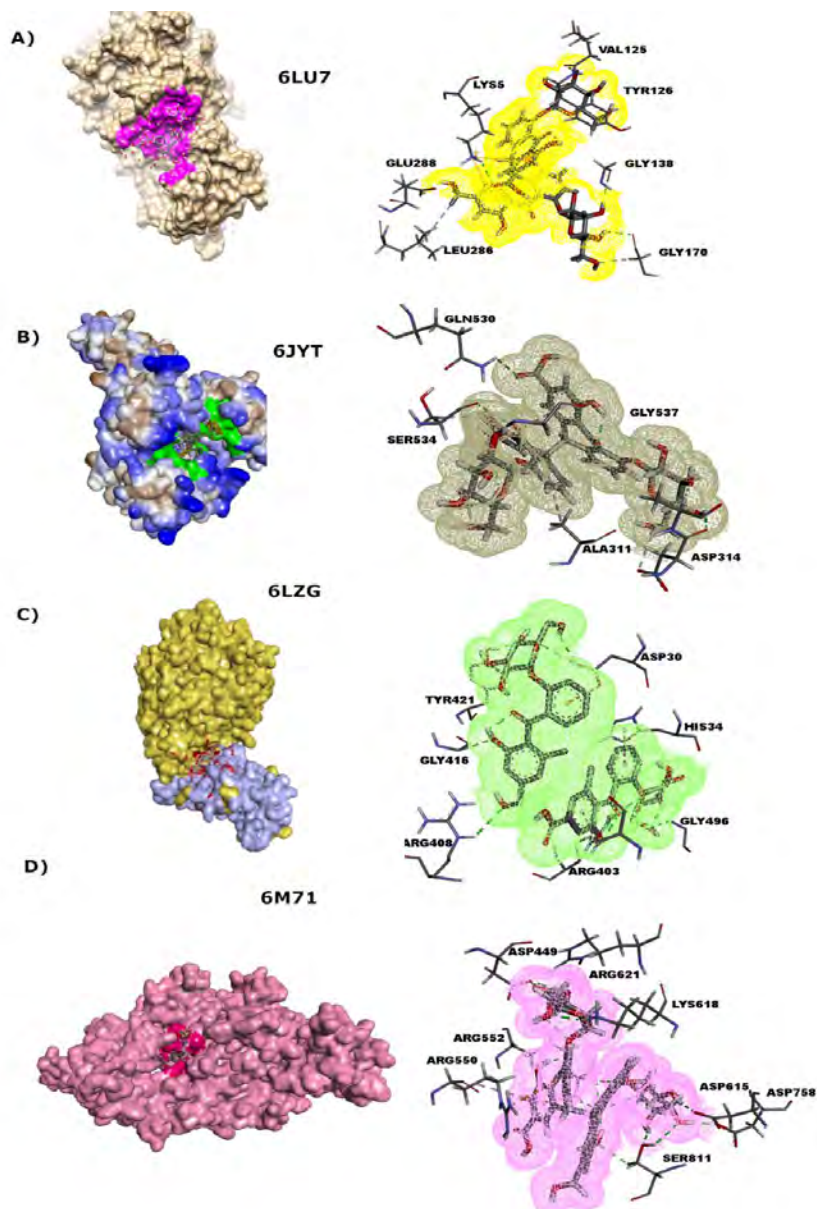


Figure 6.9. Preferred binding modes of sennosides docked with four essential proteins of SARS-CoV-2 depicting 2D binding interactions. **A)** 3CL<sup>pro</sup> **B)** Helicase nsp13 **C)** Spike protein-ACE2 receptor complex docked at two different sites **D)** RdRp nsp12.

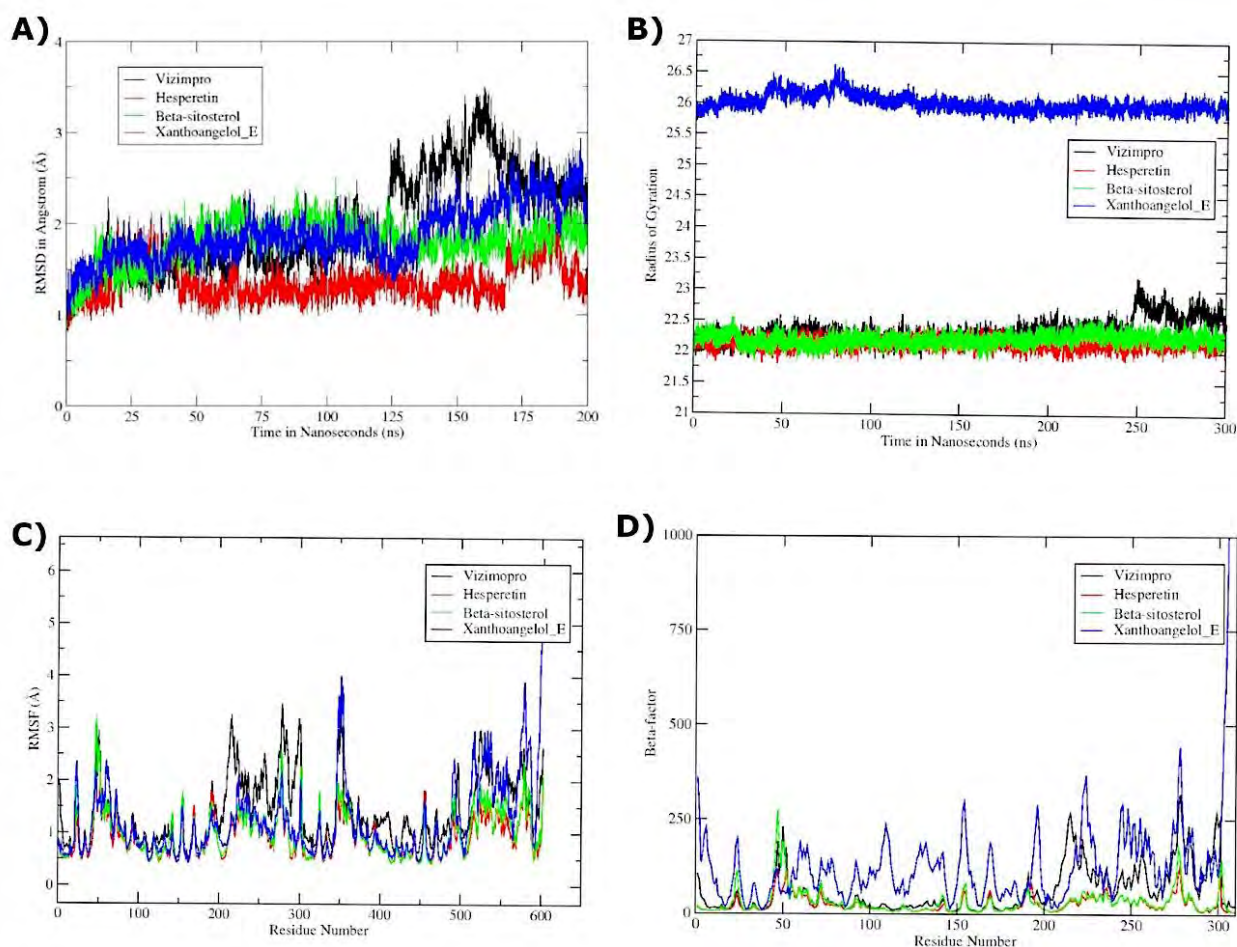


Figure 6.10. Insights into the MD simulations of vizimpro, hesperetin, beta-sitosterol, and xanthoangelol\_E for the time period of 200 ns each complex. **A)** RMSD in complex with 3CL<sup>pro</sup> **B)** Radius of gyration **C)** RMSF of 3CL<sup>pro</sup> residues **D)** Beta-factor.

Whereas, the second compound hesperetin was run for 200 ns and exhibited stability for the first 60 ns followed by a sudden increase in RMSD resulting in detachment of hesperetin from chain A, while remaining intact with chain B of the dimer as depicted in **Figure 6.11**. Average RMSD of 1.35 Å is shown in S5 Fig, which also exhibits the maximum fluctuations observed mainly in domain III with the Rg value 22.1 Å and  $\beta$ -factor 25.8 Å. Nonetheless, the role of critical residues such as His143, Phe140, Gln189, and Glu166 was again highlighted as they were involved in making significant interactions with chain B of 3CL<sup>pro</sup>.



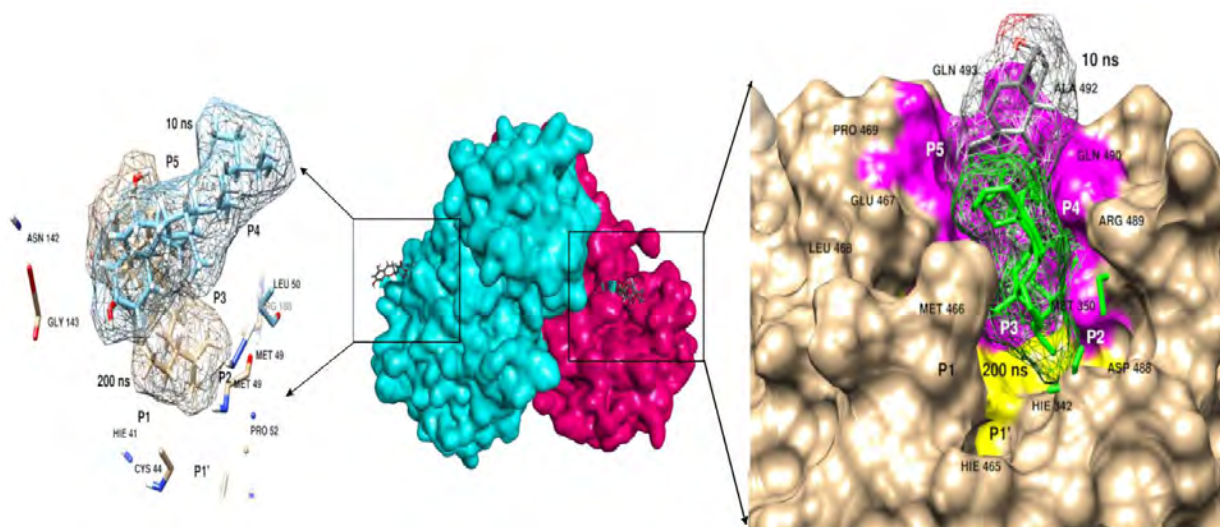


Figure 6.11. MD simulations of beta-sitosterol exhibited strong electrostatic interactions and stable conformational dynamics with both the chains of dimer 3CL<sup>pro</sup>.

Similarly, xanthoangelol\_E, the most active medicinal compound reported in experimental assays against 3CL<sup>pro</sup> exhibited the same behavior as hesperetin. However, increase in trend of RMSD graph was observed till 200 ns, which was extended to 300 ns to corroborate the structural dynamics. The ligand stayed intact with only chain B of the dimer protein displaying overall stability in protein structure as shown in **Figure 6.12**. However, the active site residues of chain B were actively involved in making interactions with xanthoangelol\_E with an average RMSD of 2.04 Å as displayed in **Figure 6.10**

Furthermore, the structural and conformational dynamics of luteolin-7-O-glucopyranoside during 200 ns exhibited extraordinary results with an average RMSD of 3.03 Å exhibiting the formation of 13 hydrogen bonds between glucopyranoside ring and the active site residues of 3CL<sup>pro</sup>. A significant increase was observed between 50 ns to 75 ns with the highest peak noted at 65<sup>th</sup> ns with an RMSD value of 6.07 Å. This noticeable change can be visually observed in simulation trajectories where increased bonding with the loop region (185-200 residues) that connects domain II to domain III caused the third domain to open up as displayed in **Figure 6.13**. Moreover, the number of bonds formed by the ligand significantly increased from 9 to 22, of which, 13 were hydrogen bonds while the rest comprised of C-H bonds and pi-alkyl bonds. The protein was seen to open up to

incorporate the ligand into its binding pocket completely at 10 ns forming and breaking after every 10 ns up to 75 ns. However, after 80 ns, strong hydrogen bonding was observed stabilizing the RMSD as presented in **Figure 6.10** making domain III returned to original position with the aid of residues Thr190 and Ala191 that kept the critical residues of the active site intact.

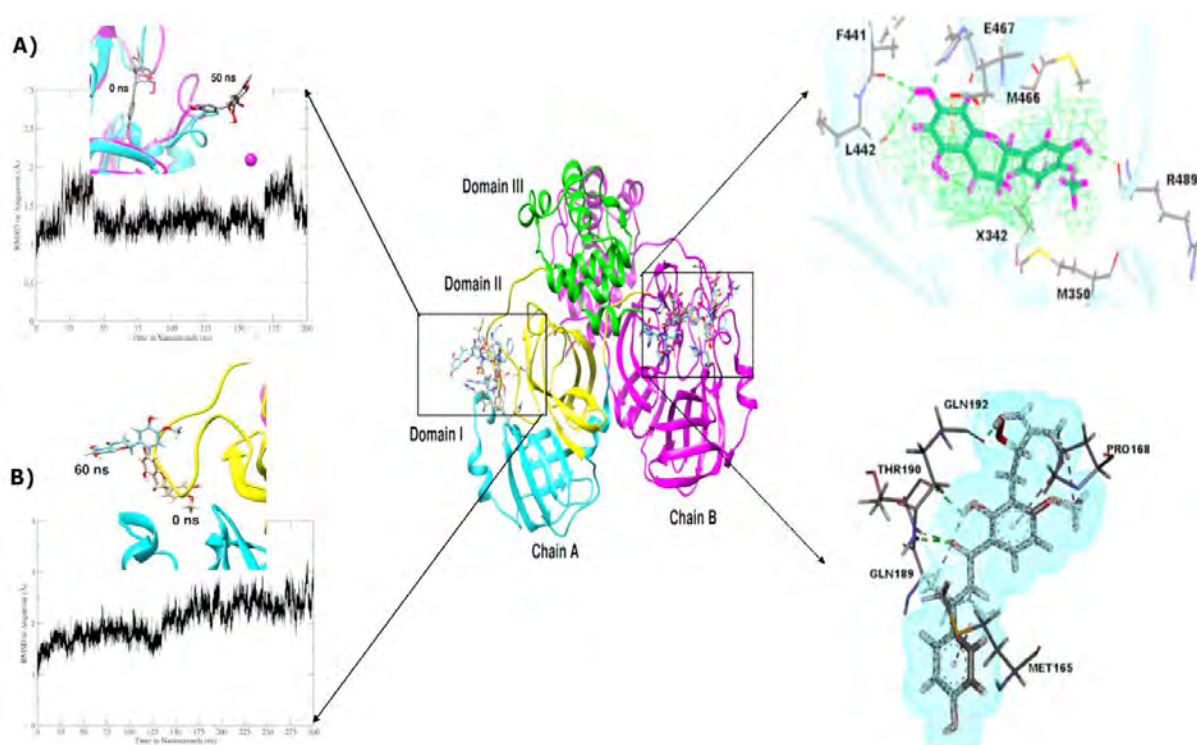


Figure 6.12. MD simulations analysis of Hesperetin and Xanthoangelol\_E A) Hesperetin detached itself from chain A due to structural dynamics in its cavity but stayed intact with chain B till 200 ns as displayed in the top-right image. B) Xanthoangelol\_E exhibited the same behavior with the chain while displaying strong hydrogen bond interactions and ligand movement deeper in the cavity of chain B till 300 ns, as presented in the bottom-right corner image.

The next simulation run with isoquercetin, exhibited fluctuations in domain II and domain III resulting in increased RMSD at 150 ns therefore MD simulations were extended to 300 ns to confirm the structural stability of this complex. However, after 200 ns, it was

observed that isoquercetin detached from the active site resulting in instability of the complex.

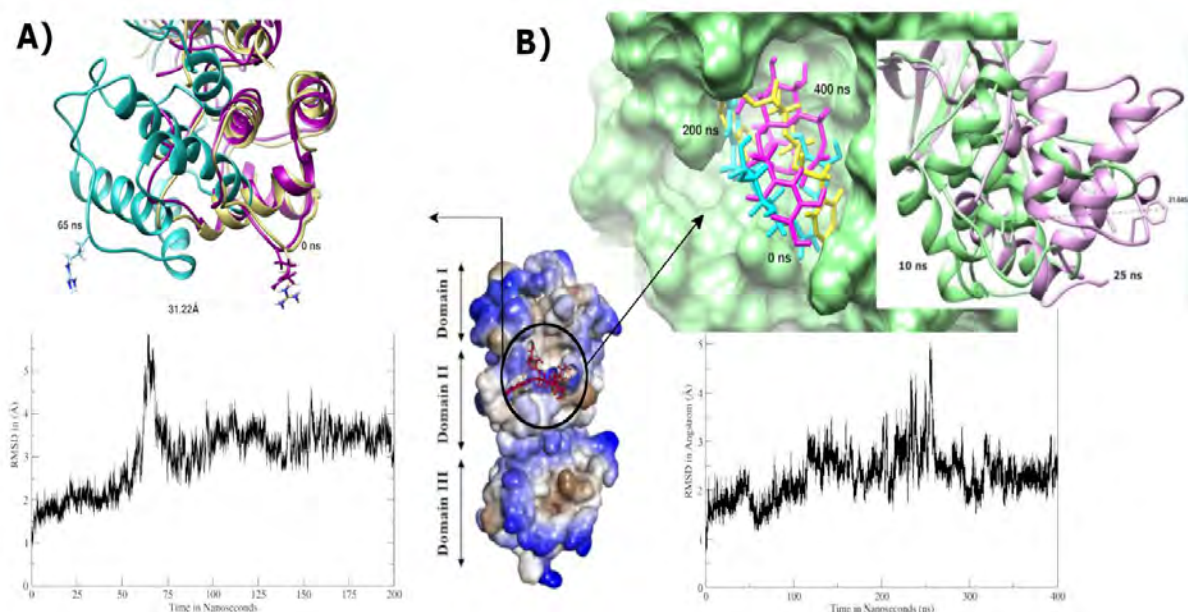


Figure 6.13. **A)** MD simulations analysis of luteolin-7-O-glucopyranoside for 200 ns. Snapshots from 0 ns, 60 ns, and 200 ns are superimposed depicting an increase in RMSD due to the domain movement. **B)** MD simulations analysis of calceolarioside\_B depicting ligand movement attempting to completely occupy the binding site thus leading to the increase in RMSD observed as a consequence of domain movement.

Furthermore, the last MD simulation run of calceolarioside\_B with 3CL<sup>Pro</sup> exhibited significant fluctuations in RMSD throughout the 200 ns run. The simulations were further extended to 400 ns to explore the stability of the compound in its binding pocket. Simulation trajectories suggested that the receptor-ligand Results yielded showed that a significant rise of RMSD at 250 ns is associated with domain III movement covering 21.6 Å from its initial position as depicted in **Figure 6.13**. The ligand adjusted itself in the binding pocket of the receptor to form strong hydrogen bond interactions with crucial residues Glu166, which play a central role in making interactions with a catalytic dyad (Cys145 and His41) and is critical for the proteolytic activity of the viral protein<sup>206,348</sup>. However, further insights into the simulation results show that the

domain moved back to its original position after 300 ns leading to stabilization in RMSD. All the 6 compounds were further compared with a control vizimpro based on MD simulation results, which exhibited the exact behavior between chain B (1-302 residues) of vizimpro and the dimer 3CL<sup>pro</sup>. The ligand from chain A drifted away from the active site after 150 ns. Whereas, the ligand tightly attached itself to chain B and completely occupied the active site while moving inside the cavity making even stronger interactions with the active site residues of the receptor. Our analysis was further extended to the calculation of binding free energies of all the 7 complexes using MMPBSA and MMGBSA calculations to conclude our study.

### 6.3.5.2 Analysis of Senna compounds

Five complexes were subjected to MD simulations comprising a span of 200 ns each. The first simulation run with 3CL<sup>pro</sup> exhibited detachment of sennoside (ligand) from the active site as depicted in **Figure 6.14**. However, the second most interesting complex with spike protein and ACE2 receptor was analysed with two different sites to identify the conformational changes if any. Ligand bound at RBD of spike protein exhibited stability till 200 ns exhibiting the inability of ligand to abrogate interactions between the spike protein and ACE2 receptor of SARS-Cov-2 as shown in **Figure 6.14**. However, the ligand docked at the allosteric site of ACE2 receptor resulted in protein fluctuations but eventually detached itself from the active site after 150 ns. As an outcome, interactions between spike protein and ACE receptor were not abolished that are essential for its inhibitory activity<sup>349,350</sup>. The same results were observed with RdRp nsp12 and helicase nsp13 complexes. None of the active sites retained sennosides probably due to the absence of hydrophobic interaction, which were reported in different studies as significant for inhibitory activity of SARS-CoV-2 proteins<sup>351,352</sup>. Moreover, the *Senna* compounds that remained intact with the protein even farther from the active site were still subjected to binding free energy profiles to get insights into the energetics between proteins and ligands; respectively.

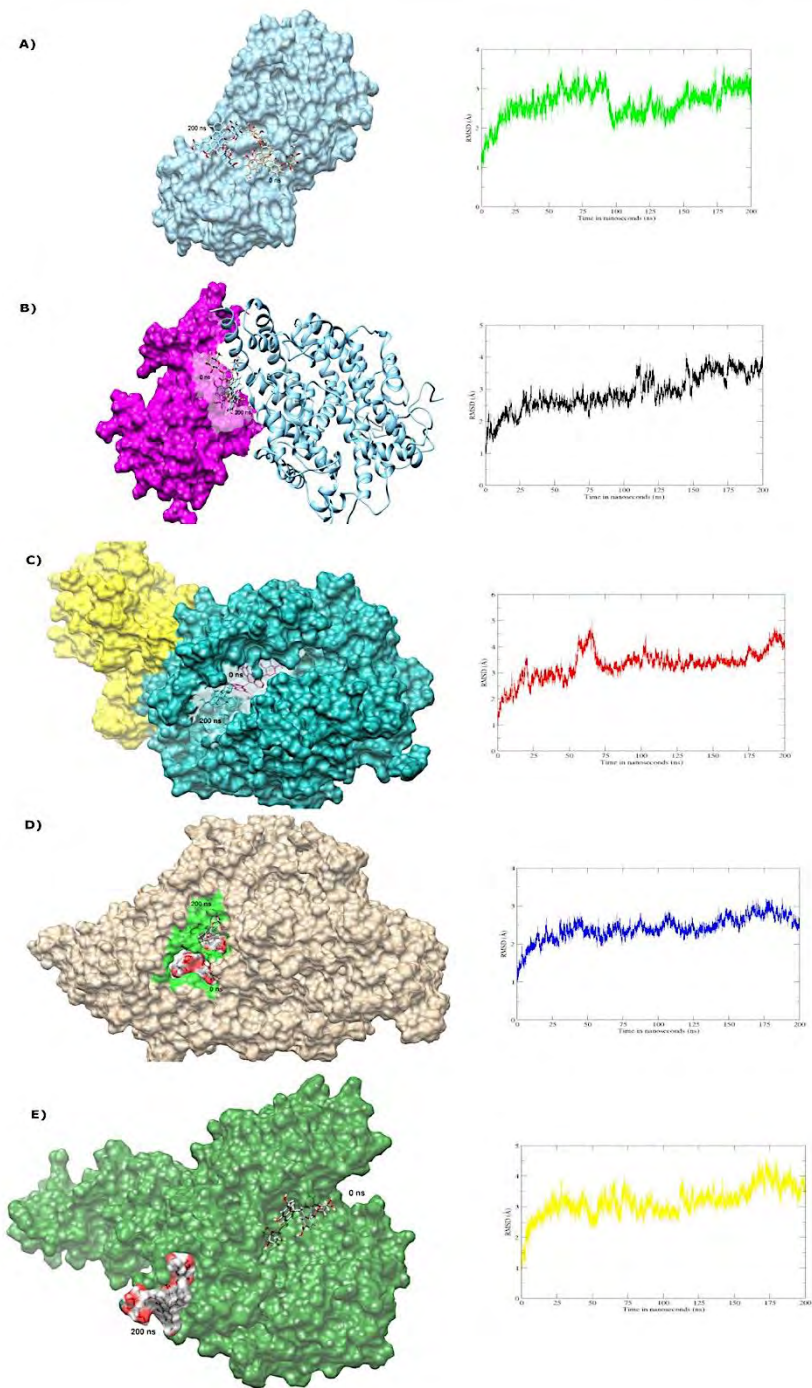


Figure 6.14. Insights into MD simulations of sennosides with **A)** 3CL<sup>pro</sup>, **B)** Spike-ACE2 with ligand attached at RBD, **C)** Spike-ACE2 with ligand attached at allosteric site, **D)** RdRp nsp12, and **e)** Helicase nsp13.

### 6.3.5.3 Binding free energy analysis

The end-point free energy calculations were performed to find energetics between active phytochemicals in complex with 3CL<sup>pro</sup>, *Senna* compounds in complex with RdRp and spike-ACE2, and vizimpro. The distribution of energetics of top three active phytochemicals xanthoangelol\_E, beta-sitosterol, and hesperetin as a result of MMGBSA calculations is mentioned in **Table 6.4**. The sum of binding free energy with a dimer 3D structure of 3CL<sup>pro</sup> exhibited impressive values ranging from -86.56 to -92.91 kcal/mol. The highest number of binding interactions resulted from the van der Waals interactions with values -163.69 to -172.99 kcal/mol between dimer and the selected ligands. However, the MMGBSA value of vizimpro, a control FDA-approved drug for SARS-CoV-2 exhibited a value of -52.80 kcal/mol. Moreover, the energetics of xanthoangelol\_E, beta-sitosterol, and hesperetin as a result of MMPBSA calculations mentioned in **Table 6.4** exhibited values ranging from -22.31 to -26.82 that were striking as compared to the control drug, vizimpro that was -9.56 kcal/mol.

Whereas, energetics of other three compounds namely; luteolin-7-O-glucopyranoside and calceolarioside B, and isoquercetin exhibited MMGBSA calculations that lied between -20.64 to -53.06i kcal/mol. The major contributions came as a result of van der Waals interactions with values ranging from -38.79 to -62.02 kcal/mol. Moreover, total binding energy values from MMPBSA calculations exhibited values ranging from 0.4745 to 21.0345 kcal/mol with mostly contributions from the van der Waals interactions that lied between -45.75 to -62.02 kcal/mol. Furthermore, free energy calculations of all three complexes with sennosides lied from 8.60 to 23.63 kcal/mol, which were comparatively weak as compared to active phytochemicals and the control drug, vizimpro.

Table 6.4. Binding free energy and its components in MM/GBSA and MM/PBSA for the active phytochemicals, Senna compounds, and vizimpro in complex with 3CLpro, RdRp, and spike-ACE2 proteins in kcal/mol.

Energy Components	Vizimpro 3CLpro	Beta-Sitosterol 3CLpro	Heperetin 3CLpro	Xanthoan gelol_E 3CLpro	Luteolin 3CLpro	Calceolarioside B 3CLpro	Isoquercetin 3CLpro	Sennoside 3CLpro	Sennoside RdRp	Sennoside Spike-ACE2
<b>MM/GBSA</b>										
<b>VDW</b>	-52.8713	-172.9954	-163.6940	-170.2654	-62.0288	-45.7566	-38.7973	-23.4553	-47.3276	-34.9620
<b>EEL</b>	67.9698	-604.9742	-672.0357	-610.7079	-8.5579	44.2002	123.7085	-15.2853	-133.0586	-34.9601
<b>EGB</b>	-61.5635	673.5643	720.7120	671.3829	25.4674	-29.4643	-100.7974	31.6589	147.1077	67.0213
<b>ESURF</b>	-6.3440	-22.6008	-21.9985	-22.0860	-7.9486	-5.2809	-4.7543	-2.8773	-7.6417	-4.9811
<b>DELTA G gas</b>	15.0985	-737.5308	-791.6253	-738.7731	-70.5867	-1.5564	84.9112	-38.7405	-180.3862	-69.9221
<b>DELTA G solv</b>	-67.9075	650.9634	698.7134	649.2969	17.5187	-34.7452	-105.5516	28.7816	139.4660	62.0402
<b>DELTA TOTAL</b>	-52.8090	-86.5674	-92.9119	-89.4762	-53.0680	-36.3016	-20.6405	-9.9590	-40.9203	-7.8819
<b>MM/PBSA</b>										
<b>VDW</b>	-52.8713	-172.9954	-163.6940	-170.2654	-62.0288	-45.7566	-38.7973	-23.4553	-47.3276	-34.9620
<b>EEL</b>	67.9698	-604.9742	-672.0357	-610.7079	-8.5579	44.2002	123.7085	-15.2853	-133.0586	-34.9601
<b>EPB</b>	-50.0416	595.4107	657.6581	587.1260	39.0509	-22.3992	-85.5626	29.4452	159.2216	63.4209
<b>ENPOLAR</b>	-34.9171	-124.0661	-116.7880	-119.7822	-41.3287	-26.2835	-24.6040	-15.9147	-36.8856	-25.2096
<b>EDISPER</b>	60.2918	243.8727	223.9269	236.2362	74.5756	50.7137	46.2899	33.8181	72.2494	55.3440
<b>DELTA G gas</b>	15.0985	-737.5308	-791.6253	-738.7731	-70.5867	-1.5564	84.9112	-38.7405	-180.3862	-69.9221
<b>DELTA G solv</b>	-24.6669	715.2173	764.7971	703.5800	72.2978	2.0309	-63.8767	47.3485	194.5854	93.5553
<b>DELTA TOTAL</b>	-9.5684	-22.3135	-26.8282	-35.1931	1.7110	0.4745	21.0345	8.6080	14.1991	23.6332

### 6.3.5.4 Axial frequency distribution

AFD was carried out on those complexes that exhibited conformational changes/movements in ligand-receptor complex to attain stability during MD simulations. The findings were consistent with MD simulations analysis that exhibited change in orientation of hesperetin while forcing itself to move deeper into the binding cavity while making interactions between His164@NE2 and the ligand atoms O6. Hesperetin displayed higher density distribution with His143 at the beginning of the simulation, which was later shifted to His41 of the second chain covering more surface area but decreased density distribution as exhibited in **Figure 6.15**.

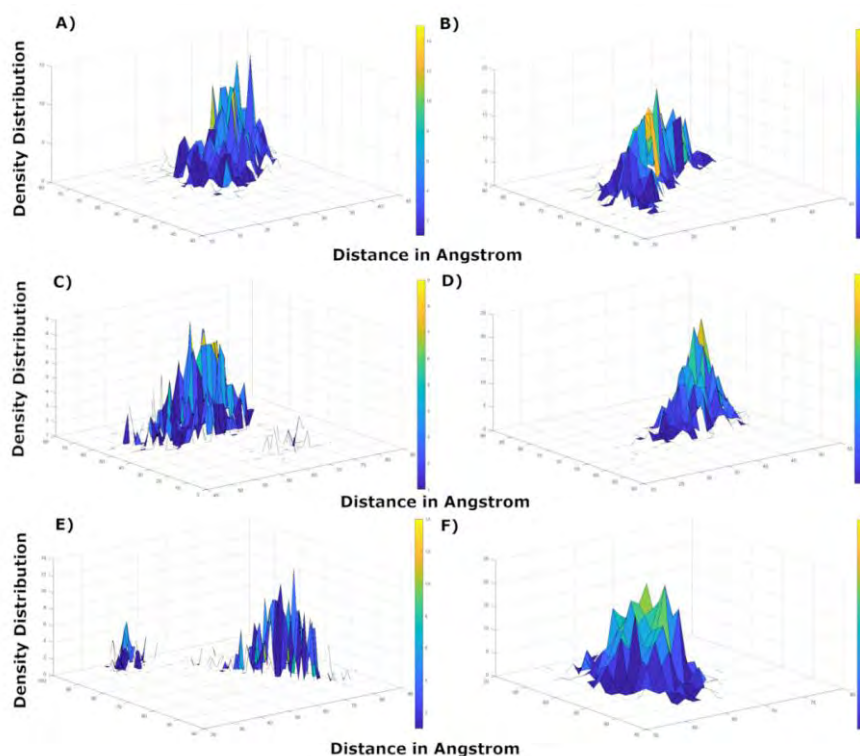


Figure 6.15. AFD plots to compare point of coordinates and geometry between the active phytochemicals **A)** Hesperetin at 10 ns, **B)** Hesperetin at 200 ns, **C)** Xanthoangelol\_E at 10 ns, **D)** Xanthoangelol\_E at 200 ns, **E)** Vizimpro at 10 ns, and **F)** Vizimpro at 200 ns.



Similarly, xanthoangelol\_E and vizimpro exhibited weak hydrogen bonding with His residues in the first 10 ns however it displayed higher density distribution later while retaining stable interactions with the same residue. Both the ligands displayed movement around the active site as seen in **Figure 6.15** and exhibited stronger interactions at the end of simulations. Moreover, luteolin-7-O-glucopyranoside and calceolarioside\_B also exhibited hydrogen bonding between two His residues (His41@O of Chain A and His143@HE2 of chain B) and ligand atoms H35 and O13 in the first 10 ns. **Figure 6.16** exhibits instabilities in density distribution between calceolarioside\_B atoms and His residues however the fluctuations in distances are representative of ligand movement between the two chains.

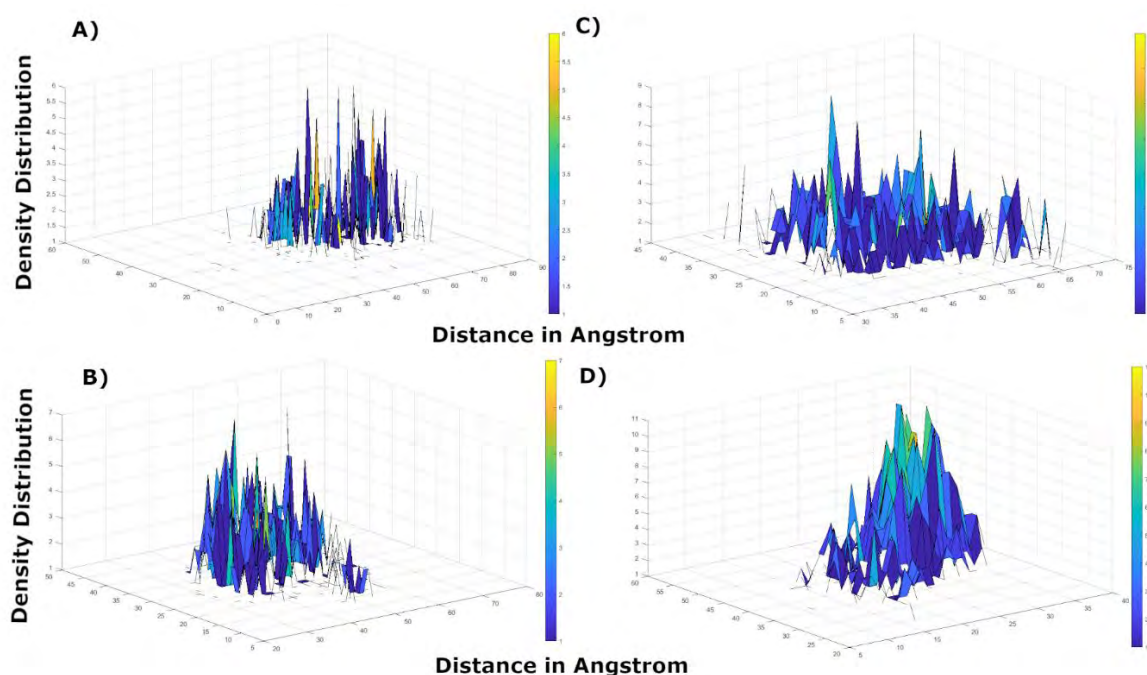


Figure 6.16. AFD plots to compare point of coordinates and geometry of **A)** Calceolarioside\_B at 10 ns, **B)** Calceolarioside\_B at 400 ns, **C)** Luteolin-7-O-glucopyranoside at 10 ns, and **D)** Luteolin-7-O-glucopyranoside at 200 ns.

Whereas, lutelolin exhibited strong hydrogen bonding with maximum density distribution together with decrease in distance between His143 and the ligand atoms till

the end of MD simulations (200 ns), presenting luteolin as more stable than calceolarioside\_B. The results from AFD highlight the significance of His residues present in both the chains of 3CL<sup>pro</sup> that participated in maintaining the stability of all the complexes under study.

### 6.3.6 Pharmacokinetic profiling analysis

#### 6.3.6.1 ADMET analysis

The ADMET analysis exhibited good absorption values of xanthoangelol\_E and hesperetin indicating good ability of both the compounds to enter blood circulation as compared to beta-sitosterol, and *Senna* compounds including sennoside A and sennoside B as displayed in **Table 6.5**.

Notably, only hesperetin presented less blood-brain barrier (BBB) penetration ability to penetrate CNS as compared to other active phytochemicals that displayed high or very high BBB values. Moreover, hesperetin and beta-sitosterol exhibited good solubility values as compared to xanthoangelol\_E, and calceolarioside\_B. Furthermore, xanthoangelol\_E and beta-sitosterol emerged as non-inhibitors of CYP2D6 exhibiting negative hepatotoxicity and greater than 90% ability to bind to plasma proteins.

#### 6.3.6.2 Toxicity analysis

The results of TOPKAT are compared with the FDA-approved drugs for the purpose of protocol validation and comparative analysis given in **Table 6.6**. The toxicity analysis suggested two active phytochemicals; xanthoangelol\_E, and hesperetin as non-carcinogens and non-mutagen as compared to beta-sitosterol and *Senna* compounds. Moreover, the TD50 rat model exhibited values ranging from 148 – 0.19 mg/Kg<sup>-1</sup> body weight as compared to remdesivir that displayed TD50 value 0.96 mg/Kg<sup>-1</sup> body weight. Most of the *Senna* compounds exhibited high TD50 values as compared to hesperetin and beta-sitosterol. Moreover, the active phytochemicals exhibited rat MTD values ranging from 2.62 – 0.05 g/Kg body weight while beta-sitosterol displayed lowest MTD values 0.03 g/Kg body weight. Comparatively, FDA-approved drugs including XL-888, vilazodone, and remdesivir presented MTD values of 0.24, 0.93 and 0.09-g/Kg body weights, respectively.

7

Furthermore, the oral LD50 and rat chronic LOAEL values of active phytochemicals stayed within the range of 11.27 – 0.62 g/Kg body weight and 0.29 – 0.001 g/Kg body weight, respectively. However, the LOAEL of beta-sitosterol was lower than other active phytochemicals. Notably, *Senna* compounds came out as ocular irritants but predicted the values of skin irritancy as non-moderate. The statistical data of TOPKAT analysis is exhibited in **Table 6.6**.

Table 6.5. ADMET properties of chemical compounds present in *Senna* in comparison with the active phytochemicals and FDA-approved drugs.

Name	<sup>a</sup> Absorption level	<sup>b</sup> BBB level	<sup>c</sup> Solubility Level	<sup>d</sup> CYP2D6	<sup>e</sup> Hepatotoxicity	<sup>f</sup> PPB
Cynaroside	3	4	3	FALSE	TRUE	FALSE
Gallic acid	0	3	4	FALSE	TRUE	FALSE
Benzoic acid	0	3	4	FALSE	TRUE	FALSE
Kaempferol	0	3	3	FALSE	TRUE	FALSE
Isorhamnetin	0	4	3	FALSE	TRUE	FALSE
Psoralen	0	2	3	FALSE	TRUE	FALSE
Syringic acid	0	3	4	FALSE	TRUE	TRUE
Vanillic acid	0	3	4	FALSE	FALSE	FALSE
Senoside A	3	4	2	FALSE	TRUE	FALSE
Senoside B	3	4	3	FALSE	TRUE	FALSE
Xanthoangelol E	0	4	2	FALSE	FALSE	TRUE
Beta-sisterol	3	4	3	FALSE	FALSE	TRUE
Hesperetin	0	3	3	TRUE	TRUE	FALSE
Calceolarioside B	3	4	1	FALSE	FALSE	FALSE
Isoquercetin	3	4	3	FALSE	FALSE	FALSE
Luteolin	0	4	3	TRUE	TRUE	FALSE
Vilazadone	1	4	2	FALSE	TRUE	FALSE
Lapatinib	2	4	3	FALSE	TRUE	TRUE
XL-888	1	4	3	FALSE	TRUE	TRUE
Hydroxychloroquine	0	1	3	TRUE	TRUE	FALSE
Remdesivir	3	4	2	FALSE	TRUE	FALSE

<sup>a</sup>Absorption level: (0, good; 1, moderate; 2, poor; 3, very poor), <sup>b</sup>Blood brain barrier (BBB) level; (0, very high; 1, = high; 2, medium; 3, low; 4, very low), <sup>c</sup>Solubility level ( 0, extremely low; 1, very low; 2, low; 3, good; 4, optimal), <sup>d</sup>CYP2D6 prediction: (cutoff score 0.161), <sup>e</sup>Hepatotoxicity prediction: (cutoff score -4.154), <sup>f</sup>Plasma protein binding (PPB) value: (cutoff score -2.209 presenting >90% binding ability of compounds to the plasma protein.

Table 6.6 Toxicity properties of chemical compounds present in *Senna* in comparison with the active phytochemicals and FDA-approved drugs calculated with TOPKAT.

Name	FDA Rodent Carcinogenicity	<sup>a</sup> Carcinogenic potency TD50 Rat	<sup>b</sup> Rat MTD feed	<sup>c</sup> Oral LD50	<sup>d</sup> RAT chronic LOAEL	Ames prediction	Skin irritancy	Ocular irritancy
<b>Cynaroside</b>	Non-Carcinogen	12.65	1.23	1.35	0.03	Non-Mutagen	None	Moderate
<b>Gallic acid</b>	Carcinogen	101.13	1.85	1.29	0.29	Non-Mutagen	None	Moderate
<b>Benzoic acid</b>	Single-Carcinogen	148.56	1.15	1.60	0.28	Non-Mutagen	None	Moderate
<b>Isorhamnetin</b>	Non-Carcinogen	11.72	0.69	1.20	0.11	Mutagen	None	Mild
<b>Kaempferol</b>	Non-Carcinogen	54.54	1.03	0.95	0.14	Mutagen	None	Moderate
<b>Psoralen</b>	Multi-Carcinogen	16.52	0.05	0.27	0.01	Non-Mutagen	Mild	Mild
<b>Syringic acid</b>	Non-Carcinogen	47.00	0.40	1.84	0.16	Non-Mutagen	None	Moderate
<b>Vanillic acid</b>	Non-Carcinogen	77.02	0.38	2.38	0.19	Non-Mutagen	None	Moderate
<b>Sennoiside A</b>	Non-Carcinogen	0.37	1.99	11.27	0.08	Non-Mutagen	None	Mild
<b>Sennoiside B</b>	Non-Carcinogen	0.37	1.99	11.27	0.08	Non-Mutagen	None	Mild
<b>Xanthoangelol_E</b>	Non-Carcinogen	131.03	0.46	3.70	0.10	Non-Mutagen	Mild	Mild
<b>Beta-sisterol</b>	Single-Carcinogen	0.71	0.03	1.57	0.001	Non-Mutagen	Moderate	None
<b>Hesperetin</b>	Non-Carcinogen	8.66	0.45	0.925	0.07	Non-Mutagen	None	Mild
<b>Calceolarioside B</b>	Non-Carcinogen	2.17	2.62	5.56	0.05	Non-Mutagen	Mild	Mild
<b>Isoquercetin</b>	Non-Carcinogen	4.54	1.75	0.84	0.07	Non-Mutagen	None	Moderate
<b>Luteolin</b>	Non-Carcinogen	140.46	0.83	0.77	0.11	Non-Mutagen	None	Mild
<b>Vilazadone</b>	Non-Carcinogen	0.93	0.13	1.17	0.02	Non-Mutagen	None	Moderate
<b>Lapatinib</b>	Non-Carcinogen	9.62	0.15	2.22	0.01	Non-Mutagen	None	Mild
<b>XL-888</b>	Non-Carcinogen	0.24	0.08	0.74	0.02	Non-Mutagen	None	Moderate
<b>Hydroxychloroquine</b>	Non-Carcinogen	1.30	0.357	0.20	0.03	Mutagen	None	Severe
<b>Remdesivir</b>	Non-Carcinogen	0.96	0.09	0.27	0.001	Non-Mutagen	Mild	None

<sup>a</sup>Tumorigenic dose rate 50 TD50 in unit mg/kg body weight, <sup>b</sup>Maximum tolerated dose MTD in unit g/kg body weight, <sup>c</sup>Median lethal dose LD50 in unit g/kg body weight, <sup>d</sup>Lowest observed adverse effect level LOAEL in unit g/kg body weight.

### 6.3.7 Network pharmacological analysis

482 Covid19 drug target genes were predicted along with 8 xanthoangelol\_E drug target genes, 44 target genes for beta-sitosterol, 88 for hesperetin, 24 for calceolarioside-B, 100 for luteolin, and only 2 for sennosides. Moreover, to generate a network of common interactions between target genes of Covid19 and phytochemicals, only those drug targets were selected that were common between both the groups as presented in **Figure 6.17**. Active phytochemicals that were most actively involved in interactions were beta-sitosterol, hesperetin, and luteolin. However, the sennosides failed to exhibit any interactions with Covid19 drug target genes.

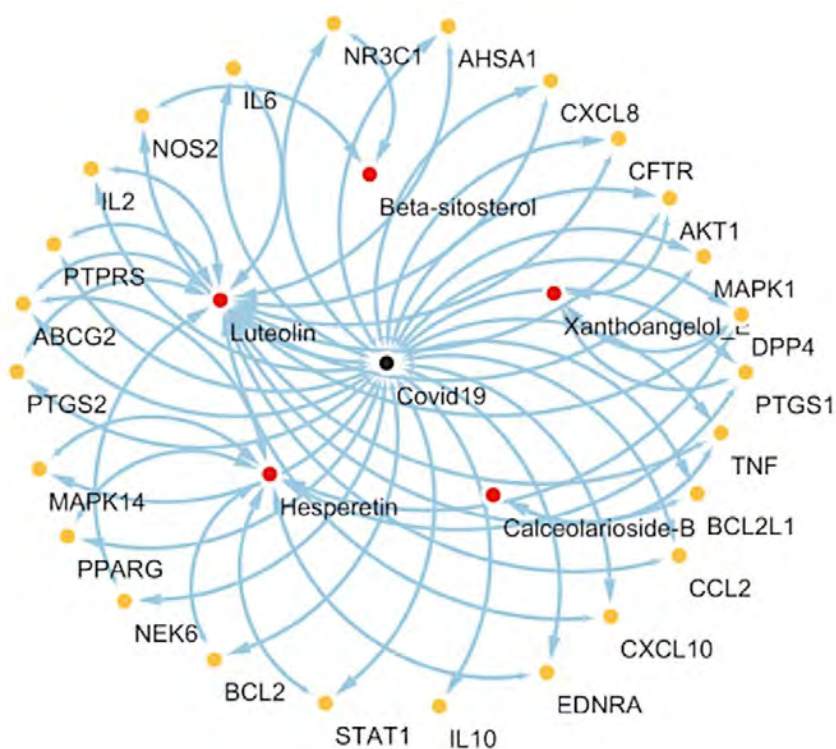


Figure 6.17. Medicinal compounds disease-target-network. Red dots represent the five-screened active phytochemicals and yellow dots represent the drug targets common between the proposed active phytochemicals and Covid19.

The Network pharmacological analysis also highlighted the significance of proposed compounds by identifying common drug targets with Covid19 (presented in

**Figure 6.16).** The phytochemicals hesperetin, luteolin, and xanthoangelol\_E exhibited the maximum number of interactions and identified AKT1, PTGS1, TNF, and DPP4 as the most affected drug targets. The roles of these kinases, oxidoreductases, upregulation of DPP4, and inhibition of PI3K/AKT signaling pathway have been highlighted in multiple studies in the treatment of Covid19 <sup>353–355</sup>.

## 6.4 Concluding remarks

While the spread of SARS-CoV-2 is inevitable despite the availability of different vaccines <sup>356</sup>, it is imperative to explore every possible treatment to curb this viral disease. Based on viral studies conducted in clinical trials by the U.S. Food and Drug Administration, 2020, the use of combination therapy has been highly recommended such as lopinavir, ritonavir in combination with chloroquine, hydroxychloroquine, and interferon-alpha since they have exhibited potential in the treatment of SARS-CoV-2 infection <sup>357,358</sup>. Similarly, the combination therapy with natural products has delivered promising results while targeting the specific stages of viral life cycle critical for its survival <sup>359,360</sup>. It is therefore indispensable to expand the treatment options and include medicinal plants in our research.

In the current study, we derived two pharmacophore models 1) a 3D-QSAR pharmacophore model focused on active phytochemicals that have exhibited biological activity ( $IC_{50}$ ) against 3CL<sup>pro</sup> with less or no toxicity, and 2) a common feature pharmacophore model derived from *Senna* compounds due to its popularity in India, Pakistan, China, Thailand, Singapore, South East Asia, and inhabitants of these regions residing in the United States, U.K, and Europe as Covid19 treatment. The ligand-based pharmacophore models were validated with FDA compounds in clinical trials for inhibition of main proteases released by the NCATS <sup>337</sup>. 3D-QSAR pharmacophore model identified HBA, HYD, and RA as common features from the training set of active phytochemicals and validated with a test set. Whereas, a common feature pharmacophore model lacked a significant attribute of hydrophobic groups in its framework that is essential for the bioactivity of 3CL<sup>pro</sup> <sup>349,350</sup>. Moreover, the 3D-QSAR pharmacophore also mapped to the FDA-approved drugs vilazodone and lapatinib from the test set that are currently in clinical trials for SARS-CoV-2. Vilazodone is a novel anti-depressant and its use in combination with ritonavir and lopinavir that works by affecting the CYS3A4 is reported to inhibit

3CL<sup>pro</sup> with IC<sub>50</sub> values below 15 μM<sup>361–363</sup>. Whereas; lapatinib suppressed the SARS-CoV-2 cytopathic effect and cleaved clustering of N protein in MRC5 (human pulmonary fibroblast cell line), thus exhibiting the potential to block 3CL<sup>pro</sup><sup>364</sup>. The above results validate the ability of 3D-QSAR pharmacophore to predict the activity of test ligands as active and inactive. Thus, a 3D-QSAR pharmacophore model comprising all the fundamental features for 3CL<sup>pro</sup> activity proved to be superior to the common feature pharmacophore.

Furthermore, the MD simulations and binding free energy analysis conducted on screened compounds using 3D-QSAR pharmacophore identified xanthoangelol\_E, hesperetin and beta-sitosterol as promising inhibitors of 3CL<sup>pro</sup> exhibiting binding energy values of -35.1 kcal/mol, -26.9 kcal/mol, and -22.3 kcal/mol respectively. Beta-sitosterol displayed hydrophobic interactions with both the chains of a dimer throughout 200 ns probably because of the hydrophobic constituents in its chemical structures. It is noteworthy that xanthoangelol\_E and hesperetin displayed higher binding energies than beta-sitosterol even though they stayed intact with only one chain of the dimer. The findings of MD simulations revealed the significance of hydrophobic interactions in keeping the ligands intact with a dimer while it has been previously established both computationally and experimentally that only one chain of dimer 3CL<sup>pro</sup> is active at a time<sup>340</sup>. In agreement with the simulations studies, experimental analysis conducted by Cheng-Wen Lin *et al.*, 2005 on the inhibitory activity of main proteases also revealed xanthoangelol\_E as the most active compound against 3CL<sup>pro</sup> and PL<sup>pro</sup> with IC<sub>50</sub> values (11.4 ± 1.4 μM) and (1.2 ± 0.4 μM) respectively<sup>344</sup>. In another study by Park *et al.* 2016, hesperetin and beta-sitosterol were reported to be capable of inhibiting main protease dose-dependently in both the cell-free and cell-based assays with the IC<sub>50</sub> value of 8.3 μM and 115 μM, respectively<sup>345</sup>. Keeping in view the scope of this study and capability of these compounds in experimental assays to inhibit both the 3CL<sup>pro</sup> and PL<sup>pro</sup>, we also subjected PL<sup>pro</sup> to molecular docking followed by 50 ns MD simulations on top complexes, which can be used as a lead to design more specific dual inhibitors in future. The structural insights of these compounds might offer clues for development of anti-SARS-CoV-2 drugs and could be used in combination as alternate medicine to prevent Covid19 infection.

In comparison, the secondary metabolites like sennosides A, B, C, and D present in higher percentage in *Senna*<sup>325</sup> exhibited instability and weak binding affinity during computational analysis against 3CL<sup>pro</sup>. Furthermore, to explore the possibility of binding of *Senna* compounds with other Covid19 target proteins, we expanded the prospect of our research. The findings suggested that *Senna* compounds failed to act as a candidate of high ligand affinity capable of disrupting contact between the spike protein RBD and ACE2 receptor. Moreover, these sennoside ligands completely left binding sites of all other targets namely helicase nsp13, spike-ACE2, and 3CL<sup>pro</sup> except RdRp nsp12, which also resulted in displacement of sennoside with weak binding energy (14.199 kcal/mol). The ADMET and TOPKAT protocols have also marked few *Senna* compounds as carcinogens and mutagens after undergoing rat carcinogenicity, TD50, LD50, and LOAEL tests. In conclusion, these findings discredit the use of *Senna* tea as whole with all its chemical constituents in Covid19 treatment, which can rather be harmful in the absence of insufficient clinical data.

However, as an outcome of this work, it is suggested as a matter of general global dissemination that *Senna* tea has nothing to do with the killing of the SARS-CoV-2. This unintentionally held us responsible for deaths of geriatric patients particularly, via diuresis/dehydration/kidney failure through overconsumption of *Senna* tea. Negation of false claim through scientific research is necessary not only to reduce overall burden but at the same time uncertified facts when disseminated through the electronic and print media, is and can remain a curse under the situation of deadly pandemic <https://twitter.com/i/status/1262403722006724608>. Statements without proper workout from renowned personalities are cherry on top that may have disastrous impact to an already poverty and/or illiteracy hit regions of the world, which is avoidable<sup>365</sup>. While our analysis has a limitation of providing a predictive viewpoint of *Senna* compounds in the absence of experimental data on this plant, further clinical analysis should be considered and implemented in the future. Our study hints and thus recommends that the use of media to propagate any unscientific thought or actions without scientific curation and clarification must be discouraged worldwide. This also urges the need for a scientific body from the WHO platform to control the propagation of scientific information in a manner to prevent



a wider community worldwide from spreading unchecked information under the disguise of scientific nomenclature.

This research work has been published in *PLoS ONE* and can be found at publications section of this thesis.

---

## **CHAPTER 7**

---

# **Dynamics of Water-Mediated Interaction Effects on the Stability and Transmission of Omicron**

## 7 DYNAMICS OF WATER-MEDIATED INTERACTIONS EFFECTS ON OMICRON

### 7.1 Background

Two years into the Covid19 pandemic, world is once again confronting upward surge with yet another variant; Omicron threatening to worsen transmissibility rate, diagnosis, re-infection and performance of vaccines due to multiple mutations<sup>366,367</sup>. World is acknowledging Omicron to be far more transmissible and agile in evading immune defense system compared to previous mutated variants especially the Delta variant. Variants that emerged in these two years and are categorized as variants of concern (VoCs) by WHO (<https://www.who.int/activities/tracking-SARS-CoV-2-variants>) are Alpha (B.1.1.7 lineage), Beta (B.1.351), Gamma (P.1), Delta (B.1.617.2), and now Omicron (BA.1, BA.1.1 and BA.2).

Delta variant has predominated global epidemiology of SARS-CoV-2 prevailing 99.8% of analysed sequences uploaded to GISAID database (<https://www.gisaid.org/hcov19-variants/>). Delta variant acquired 10 mutations in spike protein whereas Omicron has exhibited 32 mutations including 15 mutations in receptor binding domain (RBD), 3 deletions and one insertion. Different studies have reported the effect of mutations on binding between the ACE2 receptor and spike protein leading to disparity in rate of transmission and virulence over the period of time<sup>368,369</sup>. To study the effect of individual mutations on binding affinity of ACE2, Starr *et al.* conducted a systematic experimental study, which categorized 9 mutations (S371L, S373P, S375F, K417N, G446S, E484A, G496S, Q498R, Y505H) as decreasing and other 6 mutations (G339D, N440K, S477N, T478K, Q493K, N501Y) involved in increasing deleterious effects of the variant due to enhanced binding affinity<sup>370</sup>. Moreover, higher binding affinity of recently reported mutations D614G have been linked with increased rate of transmission and viral load in Covid19 patients<sup>371</sup> whereas deleted residues in Delta variant 157-158 were connected with antibody escape<sup>372</sup>. Furthermore, commonly found mutations among other variants particularly Omicron that exhibited significant structural changes in combination and are particularly linked with cell tropism effecting receptor recognition

pattern include N679K, N501Y and P681H. Additional mutations not only appeared at RBD that is directly involved in cell entry of SARS-CoV-2 resulting in enhanced attachment to its receptor but also played critical role in priming of the protein. These two major events; prefusion to the postfusion stage of viral life cycle were drastically effected by subsequent mutations in sub-domains of spike protein as mentioned in multiple studies<sup>373,374</sup>.

Therefore, to unveil the molecular basis for a higher number of mutations in each wave, this study compares the dynamic differences between SARS-CoV-2 variants of concern and wild-type with specific interest on the omicron variant, through MD simulations. These comparisons were done by considering SARS-CoV-2 as a trimer, choosing a single monomer, and considering just the receptor binding domain (RBD) of VoCs alone. The findings highlight the significant role of hydration forces in providing stability with particular emphasis on mutations-induced intra/intermolecular changes in solution and molecular determinants responsible for relative binding affinities. Moreover, the 3 amino acid insertion (EPE) in Omicron BA.1 is proposed to hold a precarious position in forecasting the impact of bulk mutations on conformational dynamics. Complete coherence of structural mutations and outcomes of MD simulations further strengthens the possible relation between mutations and viral fitness that will significantly aid in understanding the molecular basis of additional mutations in new variants. Furthermore, the research data also tends to examine the significant role of hydration forces in guiding the structure, stability, function, and dynamics of VOCs, a subject that yet remains unexplored in present studies.

## 7.2 Materials and methods

### 7.2.1 Predicting the impact of multiple point mutations

DynaMut, a comprehensive suite for protein motion and flexibility analysis<sup>375</sup> was used to explore molecular consequences of mutations in different VoCs. The tool implements Normal mode analysis (NMA) using ENCoM and Bio3D approaches to analyze protein motions. It also considers the vibrational entropy changes that influence protein dynamics and stability. For protein dynamics analysis, structure of wildtype spike protein was given as input. The ‘Mutation list’ option was then used to upload the list of mutations for each

VoCs for batch processing. The server then uses consensus prediction method, which includes performance metrics, machine-learning algorithms to explore the impact of protein mutations on interactions with other molecules.

### 7.2.2 Mutant structure modeling

SARS-CoV-2 S-ACE2 complex (PDB ID: 7df4), was selected as a suitable template to model the WT. Three-Dimensional (3-D) structure of WT and all variants of Covid19 were generated using SWISS-MODEL (<https://swissmodel.expasy.org/>). SWISS-MODEL is an automated server that predicts 3D structure of proteins using homology modeling techniques. Mutated amino acid sequences for all variants were entered and the template was selected for each variant respectively. PDB ID: 7a94 showed highest homology to all input sequences and was selected as a template to generate 3D-structures of Alpha (B.1.1.7), Beta (B.1.351), Gamma (P.1), Delta (B.1.617.2), and Omicron (B.1.1.529).

Alpha variant has 3 deletions (H69, V70 and Y144) and 7 single mutations namely (N501Y, A570D, D614G, P681H, T7161, S982A and D1118H). Beta variant is associated with several mutations in spike, including 3 deletions (L241, L242 and A243) and 8 single mutations (L18F, D80A, D215G, K417N, E484K, N501Y, D614G and A701V). Deletion at H69 and V70 positions are not present in Beta variant. In Gamma variant, however several single mutations (L18F, P26S, T20N, D138Y, R190S, K417T, E484K, N501Y, D614G, H655Y and T1027I) are observed but no deletions have been reported. 6 Spike mutations in Delta variant are observed at positions (T19R, L452R, T478K, D614G, P681R and D950N). In addition to these, 2 deletions (E156 and F157) are also associated in Delta variant. Titers against Delta variant were reported to be around 2-fold lower in comparison to Alpha and WT. Omicron is a newly discovered and most mutated Covid19 variant. It includes 6 deletions (H69, V70, Y144, G142, V143, and N211). There are 29 single point mutations in Omicron i-e: A67V, T95I, Y145D, K417N, S477N, T478K, E484A, N501Y, D614G, H655Y, P681H, G339D, S371L, S373P, S375F, N440K, G446S, Q493R, G496S, Q498R, Y505H, T547K, N679K, N764K, D796Y, N856K, Q954H, N969K and L981F and one insertion at position 214EPE. 15 mutations are present in RBD and 10 mutations occurred at Receptor Binding Motif (RBM), which interacts directly with the ACE2 receptor. Mutations in Omicron are not evenly distributed. Omicron spike is 3 amino acids

less in comparison to the WT. The study of mutations was divided in three sets i.e., trimer, monomer, and isolated RBD. The RBD domain of all variants was truncated from the mutated full-length S proteins, which is an important domain for ACE2 binding to analyze separately. Mutations in Alpha, Beta, Gamma and Omicron are listed in Table 1 whereas mutations in RBD domain are highlighted in **Table 7.1**.

### 7.2.3 Molecular dynamics simulations

MD simulations were performed using AMBER (Assisted model building with energy refinement) forefield<sup>239</sup>. System of the complex in preprocessing step was prepared using the antechamber program of AMBER. Multiple simulations were performed to investigate dynamic behavior and conformational space of proteins, particularly intermediate states or transitory states that are crucial roles in defining binding or unbinding process of ACE2 and SARS-CoV-2 variants. MD simulations were performed for 2800 ns in total for WT and Omicron trimer, monomer of all variants and RBD of each variant in complex with ACE2 receptor, respectively.

Topology of the complex was extracted using the ff14SB force field and the system was solvated by placing complexes in a cubic box of 12 Å with TIP3P water box, which was minimized for 1000 steps. Utilizing the Langevin dynamics, entire system was heated for 20 picoseconds (ps) at 300 K with 1 atm, which was maintained at that temperature. The SHAKE algorithm was utilized to constraint the bonds involved between hydrogen atoms and heavy atoms whereas for heating NVT ensemble was utilized. Furthermore, system pressure was maintained with time scale of 50-ps using NPT ensemble. However, for production run the unbounded interfaces cut-off radius of 8.0 Å was set by using Berendsen algorithm with NVT ensemble. CPPTRAJ<sup>244</sup> module of AMBER was used to evaluate system simulation trajectories whereas for analyzing and visualization of trajectories of MD simulations after every production run, the VMD suite<sup>234</sup> was utilized.

Table 7.1: Mutations in Alpha, Beta, Gamma, Delta, and Omicron.

Alpha, V1 (B.1.1.7)	Beta, V2 (B.1.351)	Gamma, V3 (P.1)	Delta (B.1.617.2)	Omicron (B.1.1.529)
<b>Shared Mutations</b>				
<b>S:H69-</b>	S:L18F	S:L18F	S:L452R	S:A67V
<b>S:V70-</b>	S:L241-	S:P26S	S:T478K	S:H69-
<b>S:Y144-</b>	S:L242-	S:K417T	S:D614G	S:V70-
<b>S:N501Y</b>	S:A243-	S:E484K	S:P681R	S:T95I
<b>S:D614G</b>	S:K417N	S:N501Y	S:D950N	S:Y144-
<b>S:P681H</b>	S:E484K	S:D614G		S:Y145D
<b>S:D1118H</b>	S:N501Y	S:H655Y		S:K417N
	S:D614G	S:T1027I		S:S477N
	S:A701V			S:T478K
				S:E484A
				S:N501Y
				S:D614G
				S:H655Y
				S:P681H
<b>Other Mutations</b>				
<b>S:A570D</b>	S:D80A	S:T20N	S:T19R	S:G142-
<b>S:T716I</b>	S:D215G	S:D138Y	S:E156-	S:V143-
<b>S:S982A</b>		S:R190S	S:F157-	S:N211-
				S:G339D
				S:S371L
				S:S373P
				S:S375F
				S:N440K
				S:G446S
				S:Q493R
				S:G496S
				S:Q498R
				S:Y505H
				S:T547K
				S:N679K
				S:N764K
				S:D796Y
				S:N856K
				S:Q954H
				S:N969K
				S:L981F

## 7.2.4 Binding energy calculations

To compute free energies, Poisson–Boltzmann or Generalized Born and Surface Area Continuum Solvation (MM/PBSA and MM/GBSA) methods were used<sup>146,301</sup>, which can be found in Section 2.5.1.

## 7.2.5 Principle component analysis (PCA)

Principal component analysis (PCA) was used to perform advanced analysis of MD simulations trajectories. PCA is a significant method used for investigating protein structural changes and movement along the subspace during MD simulations. PCA analysis is a statistical approach that allows researchers to extract large-scale collective movements of atoms in simulations, which are frequently linked to biological function and biophysical features. First and last 10 ns trajectories of each run were utilized for calculating PCA with CPPTRAJ module of AMBER.

## 7.3 Results and discussion

### 7.3.1 Protein thermodynamics and mutational effects

Based on results of NMA, we predicted comparative thermodynamic effect of mutations on stability and flexibility of spike protein of SARS-CoV-2. To get insights into the effect of mutations on structural dynamics of VoCs under consideration, DynaMut calculated differences in free energy ( $\Delta\Delta G$ ) and variations in vibrational entropy energy ( $\Delta\Delta S_{\text{vib}}$  ENCoM) between the WT and VoCs presented in **Figure 7.1**. Out of 5 studied variants, 22 substitutions; namely D614G, P681R, N501Y, K417N, L452R, D950N, Q954H, Q498R, G446S, G339D, L981F, N764K, Y505H, A67V, G496S, D215G, D1118H, T7161, A570D, H655Y, R190S, and T1027I resulted in dynamic behavior with increasing  $\Delta\Delta G$  values that resulted in overall protein flexibility. Whereas NMA results revealed 6 substitutions: namely N856K, Y145D, T547K, L18F, D80A, and D138Y as stabilizing leading to increase in rigidity in protein structure. Interestingly, another 17 substitutions; namely N679K, N440K, S375F, T478K, E484A, D796Y, S373P, T95I, Q493R, P681H, S477N, S371L, N969K, A701V, S982A, T20N, and P26S revealed themselves as destabilizing but caused overall decrease in flexibility of protein.



Out of these substitutions, there are 15 mutations reported in RBD of Omicron including 5 shared mutations mentioned in **Table 7.1**. While discussing shared mutations lying at RBD, substitution at K417N in all other variants except Gamma that substituted Asn417 with Thr exhibited comparatively higher  $\Delta\Delta G$  ENCoM value of -0.159 kcal/mol than -0.264 kcal/mol imparting flexibility to the structure. This could be one of the foremost reasons that both K417N and K417T are associated with decrease in ACE2 binding affinity in experimental studies<sup>368</sup> and alternations at K417 tend to affect the binding affinity of class I and II antibodies at the RBD<sup>376</sup>. Whereas, substitution at E484A exhibited unstable values with  $\Delta\Delta G$  ENCoM 0.078 kcal/mol in Omicron compared to variants Beta and Gamma that exhibited stability with  $\Delta\Delta G$  ENCoM values 0.637 kcal/mol. Notably, variations in vibrational entropy might prove substantial in defining role of this immunodominant residue, which facilitates antibody escape identified in different lineages of SARS-CoV-2<sup>369,377</sup>.

Moreover, T478K that evolved in variants Omicron and Delta revealed itself as destabilizing but led to increase in rigidity of protein. Due to the presence of T478K at RBM, less accessible region of RBD, these residues that tend to make interactions in open conformational state of spike protein deliver compactness that can impact antigenicity<sup>378,379</sup>. Current study has also predicted thermodynamic effect of unique mutations present in Delta variant such as L452R lying at RBD that led to increased flexibility with  $\Delta\Delta G$  ENCoM value 0.299 kcal/mol. Multiple studies have reported evolution of this residue as a direct result of viral adaptation in response to multitude immunity<sup>379,380</sup>. It is a noteworthy substitution holding capability to neutralize multiple antibodies thus prompting the need to study the impact of these phenotypic changes in detail. Two more substitutions from Delta D950N and T19R exhibited maximum structural changes in turn leading to increased flexibility. Omicron on the other hand exhibited many new substitutions. We categorized it to four clusters based on their locations. Cluster I refer to substitutions S371L, S373P, and S375F, which contributed to decrease in protein flexibility altogether. Cluster II refers to Q493R, G496S, both increasing protein flexibility followed by Q498R that counteracted the effect of previous two mutations by decreasing the vibrational entropy. Cluster III consists of N856K, N969K, T547K, and D796Y, which contributed to decreased flexibility according to Dynamut results. Cluster IV, however, has

G339D, N440K, G446S, and Y505H substitutions, which are the most significant ones, leading to increase in vibrational entropy except N440K.

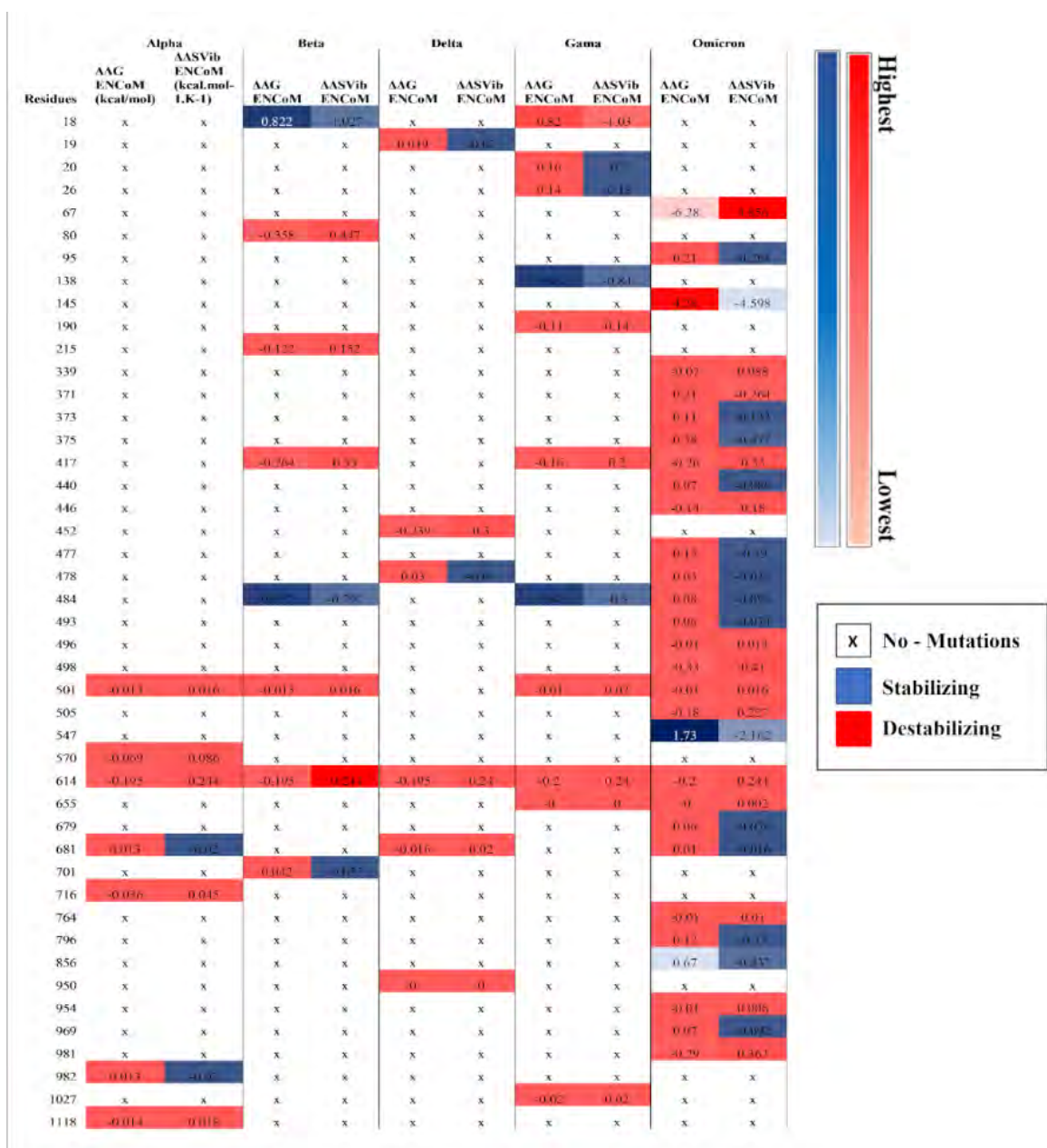


Figure 7.1. Normal mode analysis (NMA) of Dynamut predicted comparative thermodynamic effect of mutations on stability and flexibility of spike protein of all VoCs. Differences in free energy ( $\Delta\Delta G$ ) and variations in vibrational entropy ( $\Delta\Delta S_{vib}$  ENCoM) between the WT and other VoCs are mentioned from lowest to highest.

These results are in coherence with literature that associates residues of cluster I, II and IV with improved stability whereas; cluster III is linked to probable weak fusogenicity<sup>381</sup>. Results yielded define combined and independent effect of these substitutions lying at RBD on thermodynamics of protein. Although subsequent mutations including loss of some important residues in Omicron drastically effect thermodynamics of spike protein, it compensated the overall effect by making other interactions, which seems to facilitate the protein to hide from antibody immune response<sup>382</sup>.

Lastly, conserved residues involved in cleavage of spike protein, such as P681H in Alpha and Omicron that existed in Delta as P681R exhibited contradicted results. P681H exhibited stabilizing values  $\Delta\Delta G_{\text{ENCoM}}$  0.013 kcal/mol whereas P681R exhibited destabilizing values  $\Delta\Delta G_{\text{ENCoM}}$  -0.016 kcal/mol. Significance of mutation 681 that lies at furin cleavage site cannot be denied due to its presence with the neighboring residues D614G<sup>371</sup>. Both these substitutions have been regarded as critical in defining the rate of infection in different lineages<sup>383</sup>. Moreover, it has been observed that  $\Delta\Delta G$  values depending on the mutated residue effect the overall dynamics of protein that impact binding equilibrium of interacting partners; namely S1 and S2 subunits, which is associated with antibody immune escape in literature<sup>379</sup>.

### 7.3.2 Mutations-induced intra/intermolecular changes in solution

To further have insights into the effect of each mutation on intermolecular interactions with neighboring residues and solvent, MD simulations was carried out on all VoCs. Comparative analysis of overall protein RMSD presented in S1-Fig yielded interesting results during 100 ns MD simulations of RBD, furin cleavage site, NTD and RBM, which are discussed in detail. While discussing mutations at RBD site, the most significant substitution at N501Y exhibited maximum number of hydrogen bonds with neighboring residues until 100 ns namely, Lys335, Gly496, Gly498, and Gln506 with an additional hydrogen bond seen in Omicron with Tyr495. Similarly, K417N also exhibited maximum hydrogen bonds in Omicron variant with residues Tyr421, Asn422, and Gln409 while sustaining a covalent bond with Ile418 until 100 ns. Comparatively, substitution K417T in Gamma appears approx. 1-fold less collaborating while displaying 2 hydrogen bonds with Tyr421 and Asn422. Moreover, charged substitutions E484K and T478K exhibited higher

number of interactions with water molecules and neighboring cysteine residues namely Cys448, Cys468, and Cys488 in Beta, Gamma and Omicron depicted in **Figure 7.2E**. Compared to other variants, Delta substitution at L452R exhibited strong hydrogen bonding with residues Tyr419, Asn420, Asp465, and Ser467 until 100 ns, depicting enhanced binding affinity with ACE2 receptor. Notably, remaining substitutions in Omicron exhibited higher number of bonds with water residues while only S477N, Q498R, and Y505H sustained it until 100 ns of MD simulations depicted in **Figure 7.2A**.

Furthermore, newly acquired substitutions in cluster I and II of Omicron primarily G496S and Q498R revealed 2-fold increase in interactions. These enhanced interacting moieties observed in Omicron are predominantly due to hydrophobic and hydrophilic contacts particularly at RBD-up region including Q493R, G496S, Q498R, N501Y, and Y505H followed by S371L, S373P, and S375F. Higher number of positively charged residues present at the interface of Omicron is displayed in **Figure 7.2E** compared to other variants while harboring a loss of K417N that participated significantly in establishing interactions in Delta variant.

Lastly, previous studies reported the significance of distal region furin site and D614G<sup>371</sup> that displayed strong hydrogen bonding with Ala647 in both Delta and Omicron whereas, P681R in Delta expressed comparatively less water mediated interactions as compared to P681H in Omicron exhibiting 3-fold stronger interactions with water. These water mediated interactions may provide one of the reasons for enhanced stability of Omicron compared to Delta as reported in multiple studies<sup>384,385</sup>. In this context, other significant substitutions of furin site and NTD were also analysed. N-terminal substitution in Delta namely T19R displayed strong hydrogen bonding with ACE2 receptor namely, Asp251, Ser253, Ser254, and Trp256 compared to Omicron N-terminal substitutions A67V, T95I, and Y145D that revealed higher number of non-covalent interactions in this region. Although Delta and Omicron both impart stronger contacts in this region as depicted in S2-Fig, Omicron is seen participating more actively to hold the S1 and S2 subunits together before splitting apart followed by its cleavage and subsequently release into the cell<sup>386,387</sup>. Furthermore, Omicron also holds an additional 3-residue insertion at position 214 (ins214EPE) at furin site that exhibited strong hydrogen bonding with

Asp788, Gln793, and Gly794. However, the role of ins214EPE in Omicron needs more corroboration, which is discussed in detail in forthcoming sections.

### 7.3.3 Molecular determinants responsible for relative binding affinities

RBD region of spike protein that directly interacts with ACE2 receptor carries maximum number of mutations thus playing an important role in viral transmissibility and adaptability<sup>388</sup>. Increased number of mutations at RBD of Omicron is certainly correlated with its ability to facilitate cell entry. We calculated RMSD of reported mutations and binding affinities of RBD of all VoCs. Substitutions exhibiting significant changes were then compared by performing PCA to assess residual structural contribution. Delta RBD exhibited 5-fold increased binding affinity than WT and 2.8-fold increased affinity than Omicron RBD as depicted in **Figure 7.3C**. Results comprising isolated RBD of all VoCs attached with ACE2 receptor exhibited highest RMSD for Omicron residues Asn477, Lys478, and Arg484 → Ala compared to Arg484 → Lys in Alpha and Gamma as depicted in **Figure 7.3A**. These two residues, Arg484 and Lys478 both added a positive charge and exhibited different mobility for Omicron compared to other VoCs when PC1 and PC2, the projections of essential subspace were plotted (**Figure 7.3D and 3E**). Whereas Omicron Tyr501 and Asn417 exhibited, lowest RMSD compared to other VoCs but higher than its WT Asn501 and Lys417.

Both residues exhibited similar cluster distribution although K417N added a negative charge while N501Y added a positive charge (**Figure 7.3B**). Overall cluster projection revealed that Omicron and Alpha exhibited similar conformer distribution along the subspace whereas Delta, Gamma and Beta sampled in opposite direction (**Figure 7.4E and 4F**). Apart from shared mutations, newly acquired mutations in Omicron cluster I exhibited lesser RMSD and robust binding affinity values when compared to WT. Similarly, cluster III was observed displaying low RMSD and higher binding affinity signifying more compact domain organization with the ability to impart positive charges as displayed in **Figure 7.4B**

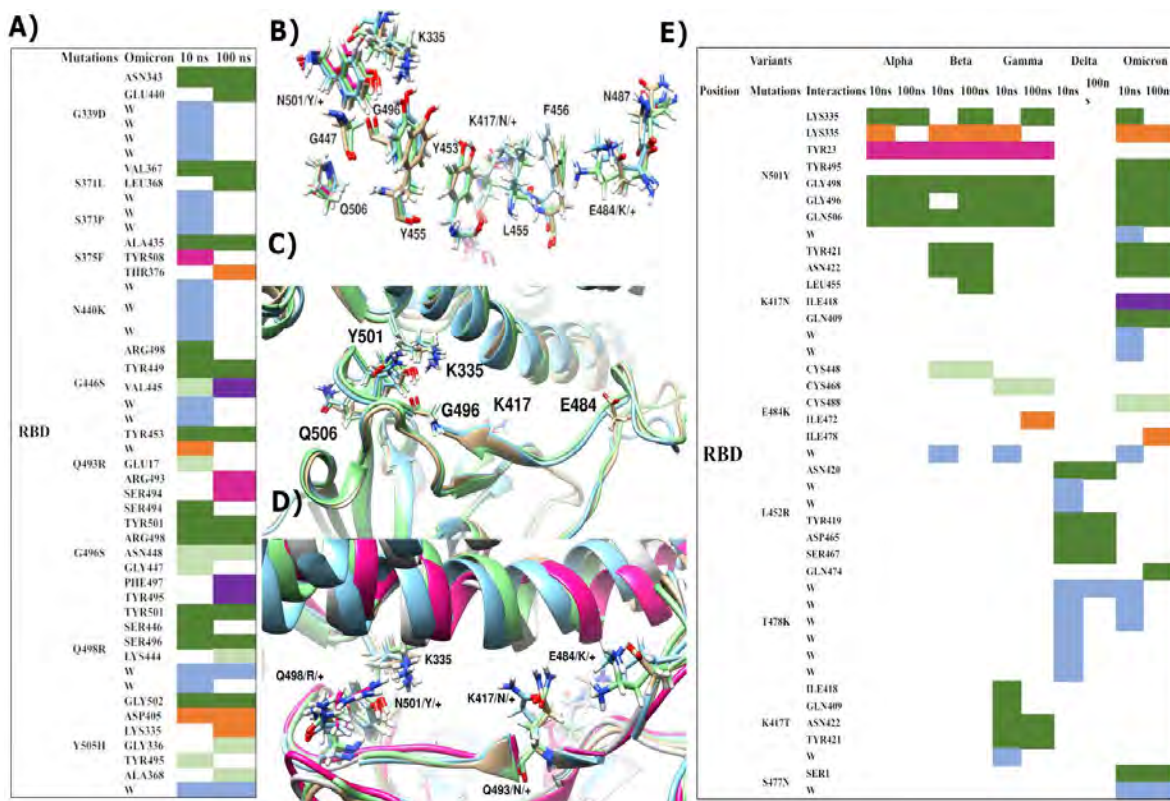


Figure 7.2. A) Intermolecular interactions of recently emerged mutations in Omicron with neighboring residues and solvent during 100 ns MD simulations **B)** Homologous and presumably constrained interacting residues among all VoCs exhibit significant interactions with induced mutations. (+/-) signifies the charge. **C)** Recently evolved mutations from cluster II reveal multiple interactions with neighboring residues **D)** Highly diverse group of residues prone to variations in all SARS-CoV-2 sublineages exhibit the capability to dramatically affect binding affinity. **E)** Intermolecular interactions of shared mutations among all VoCs with neighboring residues and solvent during 100 ns MD simulations where (w) represents interactions with water molecules.

Cluster II that is directly involved in ACE2 binding exhibited comparatively higher RMSD values but the same binding affinity pattern while imparting two positive charges. Moreover, residues including P681H/R and D614G, which are both positively charged along with ins214EPE that holds a significant standpoint with capability to impart two negative charges (**Figure 7.4B**). However, lower RMSD values and weak binding affinity

for ins214EPE was observed compared to WT (**Figure 7.4D**). To conclude, overall combined effect of Omicron substitutions signifies the importance of charge distribution in defining capability to reinforce stability due to higher number of mutations into polar residues.

### **7.3.4 Conformational rearrangements underpinning the active conformation**

Furthermore, to draw inferences about comparative structural and conformational rearrangements among different variants of spike proteins, simulations on the WT, Delta, Omicron, and ins214EPE were carried out. In all selected variants (trimer), the RBD remains in the up-configuration while binding to the receptor whereas RBD with no receptor exhibited a down-configuration. When comparing the monomer Omicron with Delta, a 45-degree conformational shift in ACE2 attachment site in Delta was observed primarily due to the substitution L452R exhibited in **Figure 7.5E**. Consequently, the architecture of up-RBD region deviated leading to a clockwise rotation, which subsequently drifted down-RBD faraway. Whereas much more compact organization was observed in Omicron intersubunits with addition of S371L, S373P, S375F and Q493R, G496S, Q498R, N501Y substitutions (**Figure 7.5E**), which seem to be the facilitator of active conformational state. Moreover, interactions between the ACE2 receptor and RBD domain remained more widespread in Omicron compared to Delta and WT. Surface area of receptor interacting with Omicron RBD had intensive hydrogen bond networks along with a salt bridge formed between Arg493 and Asp20. This interaction plays an important role in keeping the receptor compact and more interactive with Omicron RBD throughout the simulation run. Additionally, **Figure 7.7** exhibits another salt bridge formed between Asp145 and Arg247 of NTD triggering more stable conformational changes in Omicron.

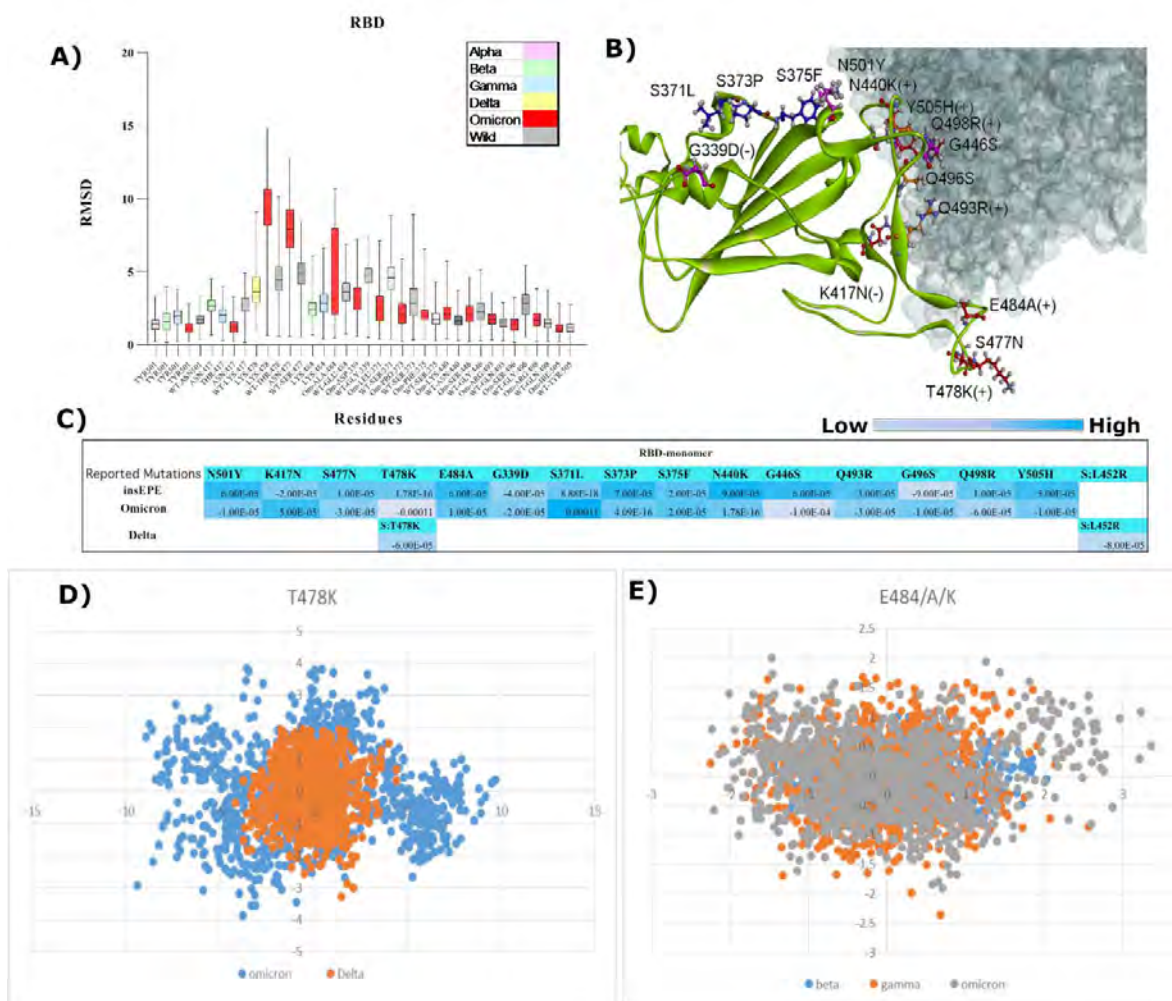


Figure 7.3. **A)** Comparative root mean square deviation (RMSD) of all VoCs and WT are represented by box plots. **B)** Snapshot of spike protein (green ribbon) exhibiting position of mutated residues at RBD (mutations belonging to different clusters are color coded) directly involved in making interactions with ACE2 receptor (grey surface) **C)** Comparative free binding energy profile of reported mutations at RBD **D)** Comparative PCA of Delta and Omicron mutation T478K exhibit opposite conformer distribution along the subspace **E)** Comparative PCA of Gamma, Delta and Omicron mutation E484/A/K exhibit varying conformer distribution along the subspace depending on the variant.



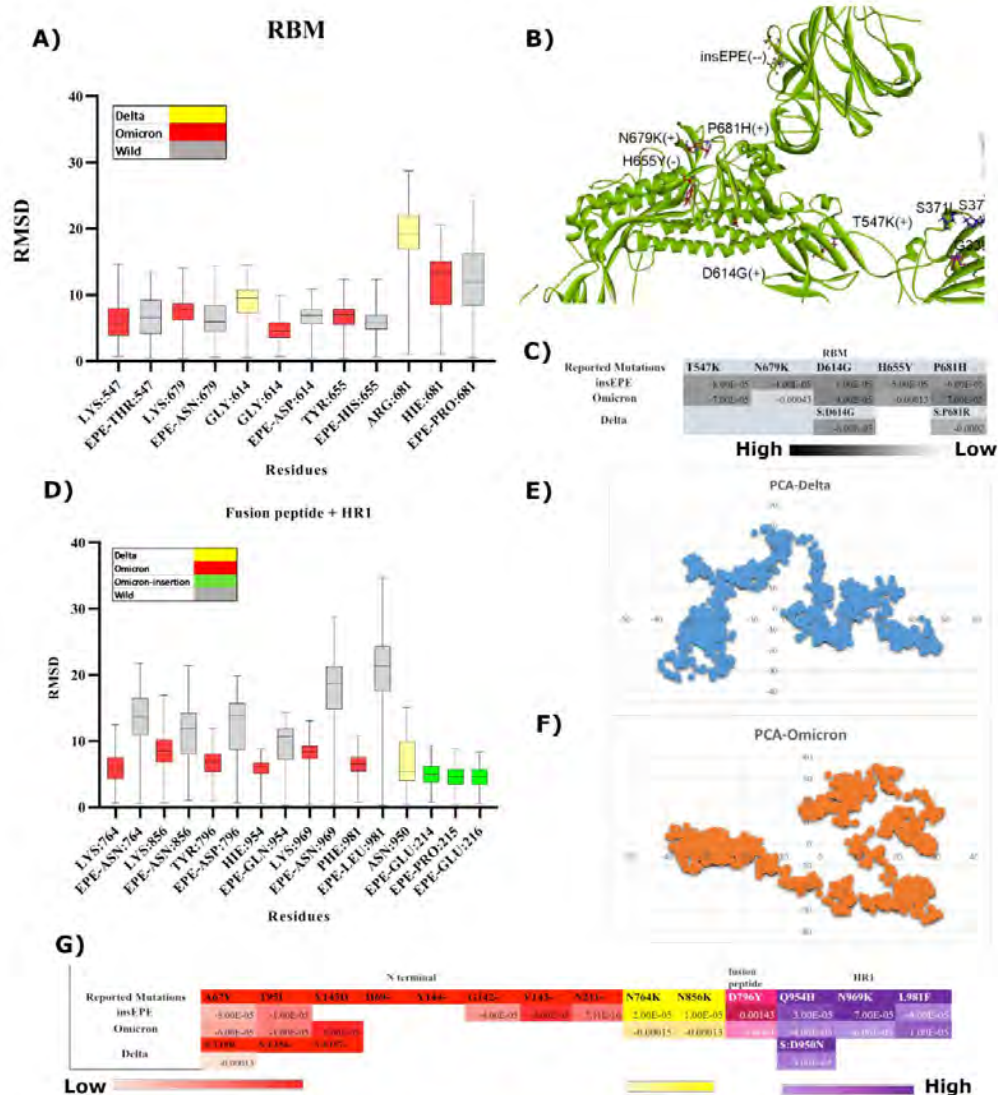


Figure 7.4. A) Comparative RMSD box plots of RBM of Delta, Omicron, and WT monomers **B)** Snapshot of spike protein (green ribbon) exhibit position of mutated residues at RBM critical for compact conformation of Omicron **C)** Comparative free binding energy profile of reported mutations at RBM **D)** Comparative RMSD box plots of mutated residues at fusion peptide site and HR1 along with insertion EPE lying at position 214 **E)** PCA of monomer Delta exploit different energy minima while sampling trajectories **F)** PCA of monomer Omicron sampling in completely opposite direction compared to Delta monomer. **G)** Comparative free binding energy profile of reported mutations at N-terminal, fusion peptide site and HR1.

### 7.3.5 Role of EPE insertion in Omicron

Multiple insertions in protein evolution over time play an important role in surfacing novel protein architectures<sup>389</sup>. Number of insertions and deletions within the protein sequence is directly proportional to the evolutionary distance. As in case of VoCs, Omicron has the highest number of substitutions, unique insertions and deletions compared to other variants. To have insights into the effect of ins214EPE, we simulated it with all other Omicron mutations and compared it with the ins214EPE induced in WT. Simulation results while exploring conformational stability and compactness of spike protein suggested that Omicron has more stable structural orientation extensively interacting with the ACE2 receptor while forming improved intersubunit contacts. As an outcome, the ACE2 binding has caused notable and diverse structural shifts in different variants of spike protein.

The RBD-HR1-NTD have exhibited varying distances and altered angles in all four complexes depicted in **Figure 7.6**, which reflect the role of mutations in controlling structural orientations while keeping protein in active conformational state. Findings demonstrate 69.29 Å, 73.20 Å, 62.52 Å, and 56.83 Å angular distances between RBD-HR1-NTD of WT, Delta, Omicron, and ins214EPE monomers crucial for viral stability of spike protein that is necessary for viral transmission and immunogenicity. These findings propose that ins214EPE was necessary to better characterize the process of substitution in Omicron. Simulation analysis of WT with ins214EPE exhibited salt bridge interactions with neighboring Arg residues shown in **Figure 7.7 and 7.8**. In addition to this, six potential hydrogen bonds formed during simulation run. Ins214EPE occupied mainly the loop regions of NTD. In this way, insertion has not disturbed the folding of protein core structure while allowing the protein to explore its conformational space and develop novel substructures.

### 7.3.6 Water-mediated interactions enhance stability

Subsequent mutations of residues can increase or decrease the number of water molecules interacting with the core region of macromolecule resulting in gain or loss of protein stability<sup>390,391</sup>. In the current study, we have observed that water-mediated contacts kept on increasing and getting stronger with each upcoming Covid variant. For instance,

nearly all mutated residues of Omicron exhibited formation and breaking of hydrogen bond interactions with water throughout the simulation.

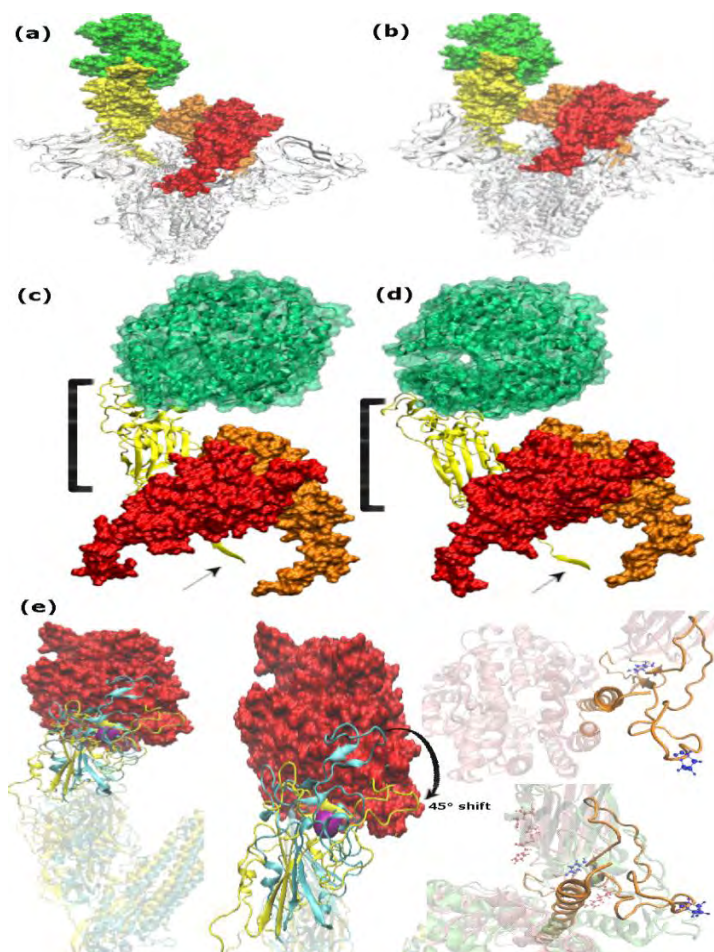


Figure 7.5. Conformational changes observed in different variants of spike protein during simulation run. **A)** WT trimer and **B)** Omicron trimer, highlighting receptor in green and the three RBD domains in orange, red and yellow. The ‘Up’ and ‘Down’ conformation of RBD is visible while interacting with the receptor and during no interaction, respectively. **C)** WT trimer **D)** Omicron trimer zoomed in view to show the difference in structural compactness and stability. **E)** Comparison of structural and conformational changes that occur during the binding of Delta and Omicron variants to ACE2 receptor. Zoomed in view of superimposed RBD domain and HR1 peptide where purple surface depicts L452R.

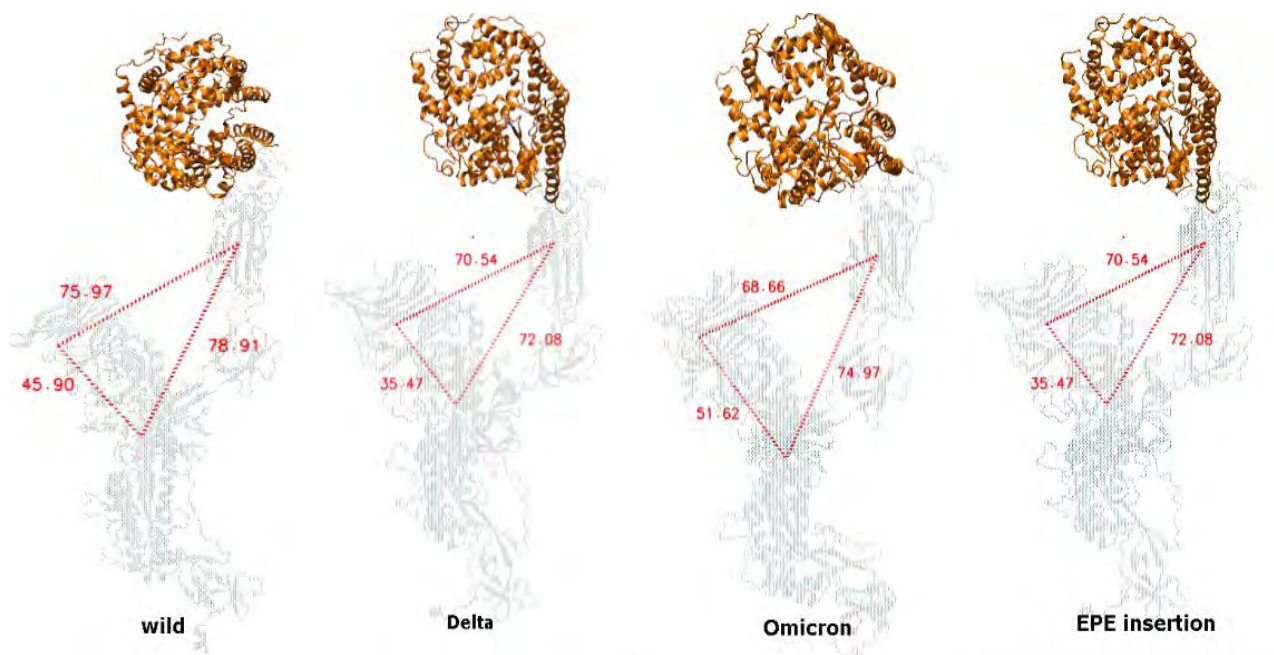


Figure 7.6. Monomers at 100 ns simulation run each. Insets representing the diverse structural shifts and altered angles formed (RBD-HR1-NTD) in the variants that were triggered by ACE2 binding. Orange ribbon displays the receptor.

However, if we look at the simulation analysis of WT and early-stage variants of Covid such as Alpha, Beta, Gamma, and Delta, the interaction of water molecules with mutated residues can be seen minimal or not at all. Water is an integral component of biomolecular systems that mediates hydrogen bonds and electrostatic interactions<sup>390</sup>. Significant amount of research data highlights the invaluable role of hydration forces in guiding the structure, stability, function and dynamics of proteins<sup>390,392</sup>. Water regulates protein folding by defining hydrophobic interactions that glue hydrophobic residues stabilizing the folding process<sup>392</sup>. Water also interacts with protein backbone, surface residues, and sidechains while controlling the formation of hydrophobic cavities. Mutations of notable number of hydrophobic residues into hydrophilic residues has resulted in increased water-mediated interactions in Omicron leading to more compact structure and stable behavior of the protein compared to other VoCs. Increased affinity of Omicron towards ACE2 receptor and improved role of solvent-mediated interactions has influenced its biological functionality. Consequently, Omicron being highly stable, and transmissible but much less infectious has been favored in the process of natural selection.

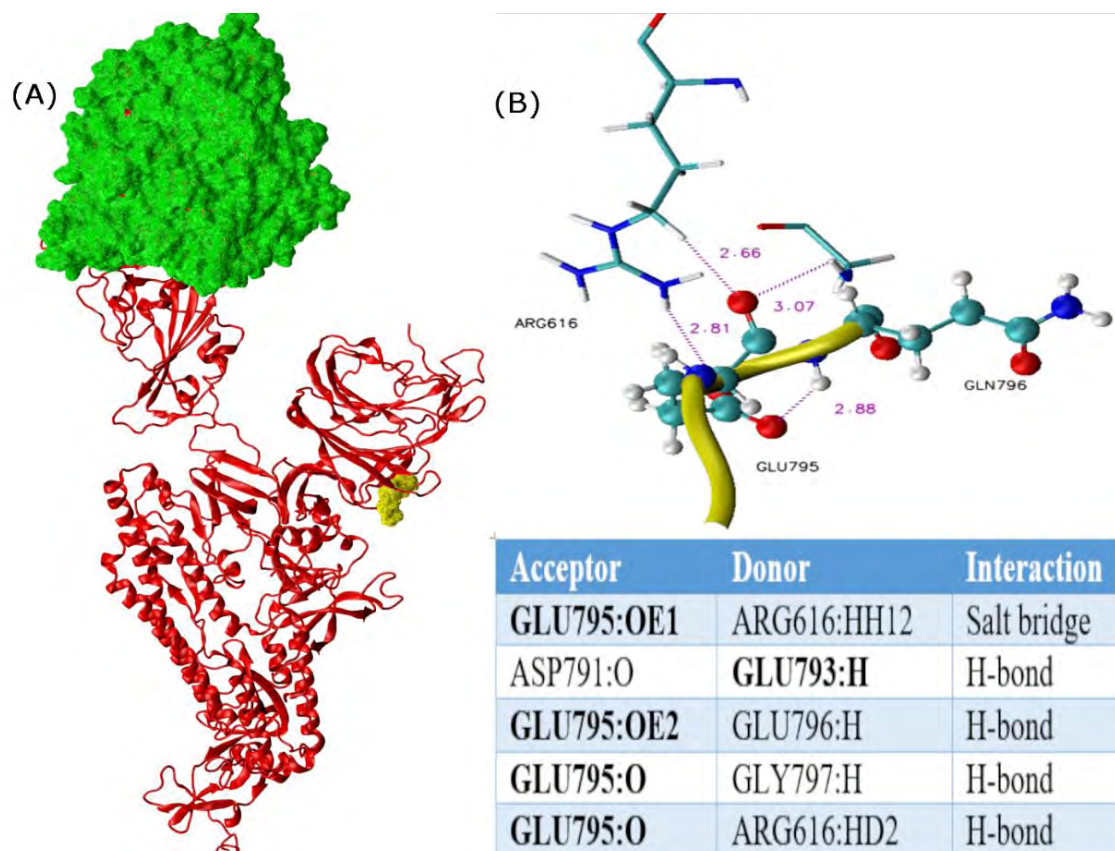


Figure 7.7. Intermolecular interactions surrounding the ins214EPE in the WT spike protein after 100 ns of simulation run. **A)** ACE2 receptor is in surf representation in green whereas the rest of the monomer is in ribbon representation **B)** Zoomed in view of ins214EPE and interacting protein residues forming salt bridge and hydrogen bond interactions.

## 7.4 Concluding remarks

Owing to the presence of isolated RBD, monomeric and trimeric Cryo-EM structures of spike protein in complex with ACE2, a comprehensive comparative mutational analysis on Omicron and other VoCs elucidated significant structural changes, which might act as facilitators in explaining higher risk of Omicron transmission rate and reveal interesting facts about its compromised viral fusion ability.

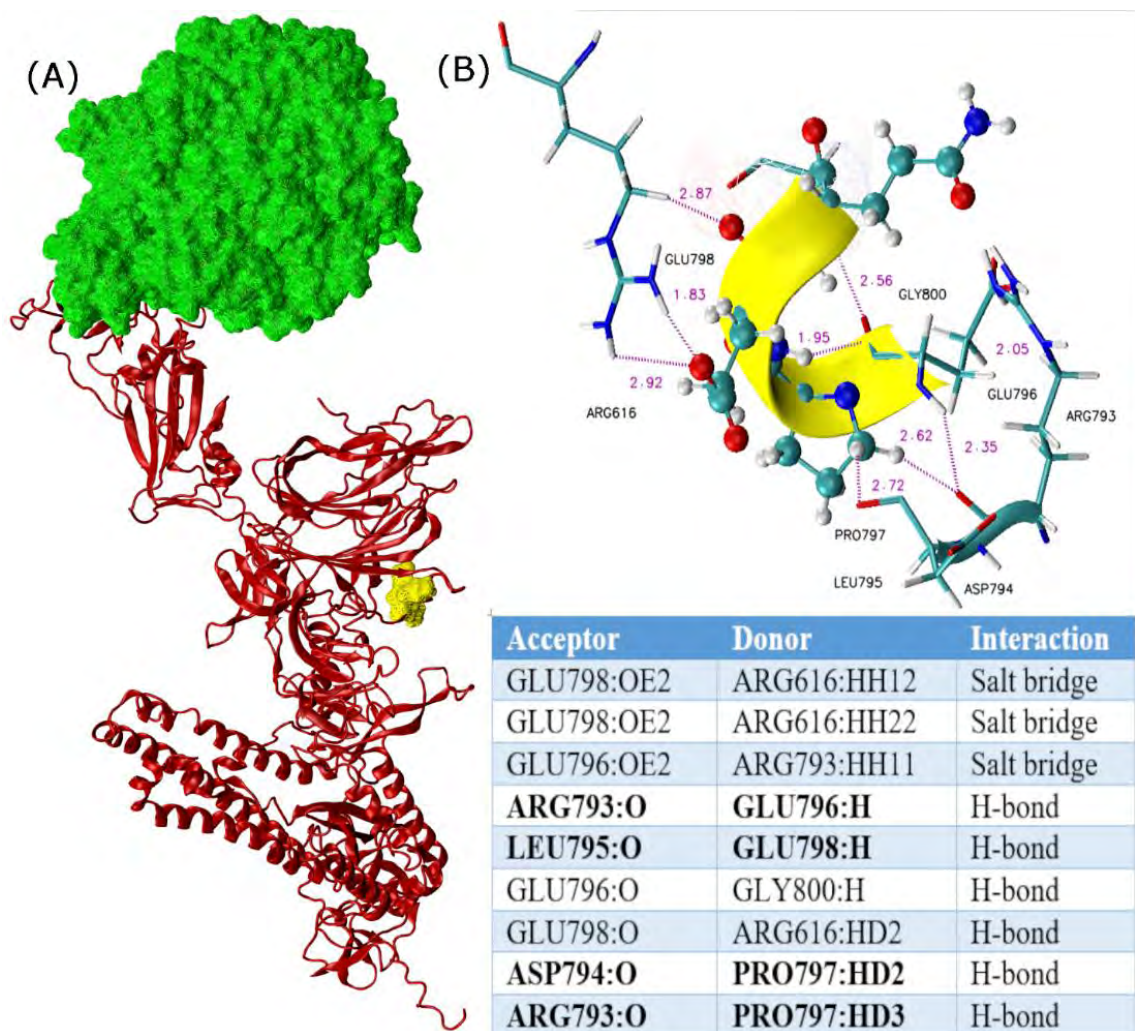


Figure 7.8. Intermolecular interactions surrounding the ins214EPE in the Omicron spike protein after 100 ns of simulation run. **A)** ACE2 receptor is in surf representation in green whereas the rest of the monomer is in ribbon representation **B)** Zoomed in view of ins214EPE and interacting protein residues forming salt bridge and hydrogen bond interactions.

Effect of independent mutations on thermodynamics of spike protein in all five variants revealed dynamic behavior of conserved mutations such as K417/N/T, E484/A/L, N501Y, D614G, and P681R/H.  $\Delta\Delta G$  values reveal that successive mutations at RBD including recently emerged Omicron clusters could be directly involved in enhanced transmissibility of Omicron. Interestingly, mutation P681H in Omicron forged decreased

NMA values compared to P681R in Delta that exhibited weak stability or loose attachment suggesting a direct link with enhanced replication and cleavage of S1 and S2 subunits of Delta as reported in previous studies<sup>378,383,393</sup>.

The above discussion is largely supported by *in silico* models and simulations carried out to disclose molecular basis of improved stability of Omicron. We characterized amino acids involved in making significant interactions with RBM+RBD based on their binding potential into different groups. Homologous residues exhibiting high binding potential in establishing strong interactions among all VoCs are Lys335, Gly447, Gly498, Gly496, Gln506, Leu455, Tyr449, Tyr453, Asn487, and Phe456 depicted in **Figure 7.2B**. Role of these conserved residues is presumably constrained due to their involvement in protein folding or ascertaining binding affinity for ACE2. Whereas other group of residues prone to undergo mutations in all sublineages are G446, Y505, K417, E484, and cluster II mentioned in **Figure 7.2C and 2D**. It is therefore deduced that residues that are characterized as molecular determinants participating in protein folding have comparatively less potential to mutate in upcoming variants of Omicron or Deltacron or any other variant. However, role of mutations at NTD and furin site that are associated with enhanced transmission rate of Delta and Omicron<sup>394,395</sup> particularly P681R that emerged in Delta and mutated into P681H in Omicron demonstrated 3-fold increased electrostatic interactions with water and enhanced hydrogen bonding depicted in S2-Fig and **Figure 7.4C**. These findings signify sturdier molecular bridges holding S1 and S2 subunits of Omicron together.

Further investigations on structural dynamics and conformational orientation during MD simulations reiterates compact intersubunits in Omicron compared to Delta that exhibited angular movements due to L452R depicted in **Figure 7.5E**. Similar cluster projection between Alpha and Omicron compared to Delta and other VoCs exploited different energy minima while sampling trajectories. Another significant finding anticipated to support compact domain organization in Omicron is unique ins214EPE. MD simulations revealed structural shifts and significant difference in angular distances between RBD-HR1-NTD of WT, Delta, Omicron, and ins214EPE monomers demonstrated in **Figure 7.6**. Ins214EPE is therefore crucial for viral stability of spike protein to understand biological consequences of recently acquired mutations. The

observed differences particularly between Omicron and Delta based on certain mutations directly affect protein stability and binding that shed light on possible reasons of divergence between transmission rate and fusogenicity of both the variants.

Current study likewise proposes substantial role of hydration forces based on influx of solvent-mediated interactions with each Covid variant. As far as Delta and other VoCs are concerned, no significant, solvent-mediated interactions give the impression. Thus, the interplay between protein and solvent is critical in shaping Omicron function and dynamics. Furthermore, Delta and Omicron expressed higher number of mutations into charged residues +4 and +9 respectively compared to their successors Alpha, Beta, and Gamma. Role of hydrations forces and positively charged residues explained by Nie *et. al* in previous studies support the fact that increased number of mutations in Omicron drastically effect binding capability of antibodies to these cationic patches on the interface of spike protein <sup>396</sup>.

Based on these findings, it has been discussed that mutational spread is positively related to viral fitness, which has been defined in literature <sup>397</sup>. For instance, current research data suggests that Covid19 variants employing hydration forces along with other electrostatic interactions are more compact; thus, play significant role in protein folding and function that are prevalent among the human population. However, results yielded also put forward those mutations in context of their positions, which compromise water-mediated interactions and destabilize the protein will be eliminated eventually. This study thus demonstrates an insight into structural and conformational changes in response to subsequent mutations based on their type and position and forecast the possibility of those amino acids to experience changes in future that appear as mutational drivers<sup>397,398</sup>.



## APPENDIX

Table A1: Optimized parameters of thiophene-core inhibitor with 6-31+G(d,p).

<b>Thiophene-core inhibitor</b>						
<b>Parameters</b>			<b>Parameters</b>			
<b>BOND</b>	<b>K(kcal.mol-1.ang-2)</b>	<b>Dist0(ang)</b>		<b>ANGLE</b>	<b>K(kcal.mol-1.rad-2)</b>	<b>Theta0(deg)</b>
<b>C -CA</b>	470	1.409		<b>CA-C -CA</b>	65	120
<b>C -CX</b>	315	1.522		<b>CA-C -OS</b>	70	120
<b>C -H4</b>	365	1.1		<b>CX-C -O</b>	80	120.4
<b>C -N</b>	490	1.335		<b>H4-C -O</b>	50	120.93
<b>C -O</b>	570	1.229		<b>N -C -O</b>	80	122.9
<b>C -OS</b>	450	1.323		<b>C -CA-CA</b>	65	120
<b>CA-CA</b>	470	1.4		<b>C -CA-HA</b>	50	120
<b>CA-CB</b>	470	1.404		<b>CA-CA-CA</b>	65	120
<b>CA-CM</b>	425	1.433		<b>CA-CA-HA</b>	50	120
<b>CA-HA</b>	365	1.08		<b>CB-CA-HA</b>	50	120
<b>CM-CM</b>	550	1.35		<b>CA-CM-CM</b>	65	117
<b>CM-CT</b>	315	1.51		<b>CA-CM-HA</b>	50	123.3
<b>CM-HA</b>	365	1.08		<b>CM-CM-CT</b>	70	119.7
<b>CT-CT</b>	310	1.526		<b>CM-CM-HA</b>	50	119.7
<b>CT-CX</b>	310	1.526		<b>CM-CT-CT</b>	65	111
<b>CT-H1</b>	340	1.09		<b>CM-CT-HC</b>	50	109.5
<b>CT-H2</b>	340	1.09		<b>CT-CT-CT</b>	40	109.5
<b>CT-HC</b>	340	1.09		<b>CT-CT-H1</b>	50	109.5
<b>CT-N</b>	335	1.449		<b>CT-CT-H2</b>	50	109.5
<b>CT-OH</b>	320	1.41		<b>CT-CT-HC</b>	50	109.5
<b>CT-OS</b>	320	1.41		<b>CT-CT-OH</b>	50	109.5
<b>CT-S</b>	225	1.81		<b>CT-CT-OS</b>	50	109.5
<b>CX-H1</b>	340	1.09		<b>CT-CT-S</b>	50	114.7

<b>H -N</b>	435	1.01			CX-CT-H1	50	109.5
<b>H -NT</b>	435	1.01			CX-CT-S	50	114.7
<b>HO-OH</b>	555	0.96			H1-CT-H1	35	109.5
					H1-CT-N	50	109.5
					H1-CT-S	50	109.5
					H2-CT-OS	50	109.5
					HC-CT-HC	35	109.5
					C -CX-CT	65	111.1
					C -CX-H1	50	109.5
					CT-CX-H1	50	109.5
					C -N -CT	50	121.9
					C -N -H	50	120
					CT-N -H	50	118.04
					H -NT-H	35	109.5
					CT-OH-HO	55	108.5
					C -OS-CT	60	117
					CT-S -CT	60	98.9

Table A2: Optimized parameters of nitrile-core inhibitor with 6-31+G(d,p).

<b>Nitrile-core Inhibitor</b>					
<b>Parameters</b>			<b>Parameters</b>		
<b>BOND</b>	<b>K(kcal.mol-1.ang-2)</b>	<b>Dist0(ang)</b>	<b>ANGLE</b>	<b>K(kcal.mol-1.rad-2)</b>	<b>Theta0(deg)</b>
<b>C -CA</b>	470	1.409	CB-CA-N2	70	123.5
<b>C -NC</b>	455	1.358	CB-CA-NC	70	117.3
<b>CA-CB</b>	470	1.404	N2-CA-NC	70	119.3
<b>CA-N2</b>	480	1.34	CA-CB-CB	65	117.3
<b>CA-NC</b>	485	1.339	CA-CB-NB	70	132.4
<b>CB-CB</b>	520	1.37	CB-CB-N*	70	106.2
<b>CB-N*</b>	435	1.374	CB-CB-NB	70	110.4
<b>CB-NB</b>	415	1.391	CB-CB-NC	70	127.7
<b>CB-NC</b>	460	1.354	N*-CB-NC	70	126.2
<b>CK-H5</b>	365	1.08	H5-CK-N*	50	123.05
<b>CK-N*</b>	440	1.371	H5-CK-NB	50	123.05
<b>CK-NB</b>	530	1.304	N*-CK-NB	70	113.9
<b>CT-CT</b>	310	1.526	CT-CT-CT	40	109.5
<b>CT-H1</b>	340	1.09	CT-CT-H1	50	109.5
<b>CT-HC</b>	340	1.09	CT-CT-HC	50	109.5
<b>CT-N*</b>	335	1.475	CT-CT-N*	50	109.5
<b>CT-N2</b>	335	1.463	CT-CT-N2	80	111.2
<b>CT-NT</b>	365	1.471	CT-CT-NT	80	111.2
<b>CT-OH</b>	320	1.41	CT-CT-OH	50	109.5
<b>CT-S</b>	225	1.81	CT-CT-S	50	114.7
<b>H -N2</b>	435	1.01	H1-CT-H1	35	109.5
<b>H -NT</b>	435	1.01	H1-CT-N*	50	109.5
<b>HO-OH</b>	555	0.96	H1-CT-N2	50	109.5
			H1-CT-NT	50	109.5

---

					H1-CT-S	50	109.5
					HC-CT-HC	35	109.5
					CB-N*-CK	70	105.4
					CB-N*-CT	70	125.8
					CK-N*-CT	70	128.8
					CA-N2-CT	50	123.2
					CA-N2-H	50	120
					CT-N2-H	50	118.4
					CB-NB-CK	70	103.8
					CA-NC-CB	70	112.2
					CT-NT-CT	50	109.5
					CT-NT-H	50	109.5
					CT-OH-HO	55	108.5

Table A3: Exp-2 inhibitor encompassing methyl oxy-enoate optimized parameters with 6-31+G(d,p).

<b>Methyl oxy enoate warhead</b>						
<b>Parameters</b>			<b>Parameters</b>			
<b>BOND</b>	<b>K(kcal.mol-1.ang-2)</b>	<b>Dist0(ang)</b>		<b>ANGLE</b>	<b>K(kcal.mol-1.rad-2)</b>	<b>Theta0(deg)</b>
<b>C -O2</b>	655	1.25		<b>O2-C -O2</b>	80	126
<b>CA-CA</b>	470	1.4		<b>CA-CA-CA</b>	65	120
<b>CA-CT</b>	315	1.51		<b>CA-CA-CT</b>	70	120
<b>CA-HA</b>	365	1.08		<b>CA-CA-HA</b>	50	120
<b>CC-CV</b>	510	1.375		<b>CT-CT-CT</b>	40	109.5
<b>CC-CW</b>	520	1.371		<b>CT-CT-H1</b>	50	109.5
<b>CT-CT</b>	310	1.526		<b>CT-CT-HP</b>	50	109.5
<b>CT-H1</b>	340	1.09		<b>CT-CT-N3</b>	80	111.2
<b>CT-HP</b>	340	1.09		<b>CT-CT-NT</b>	80	111.2
<b>CT-N*</b>	335	1.475		<b>CT-CT-OH</b>	50	109.5
<b>CT-N3</b>	365	1.471		<b>CT-CT-S</b>	50	114.7
<b>CT-NT</b>	365	1.471		<b>H1-CT-H1</b>	35	109.5
<b>CT-OH</b>	320	1.41		<b>H1-CT-N*</b>	50	109.5
<b>CT-S</b>	225	1.81		<b>H1-CT-OH</b>	50	109.5
<b>CV-NB</b>	410	1.394		<b>H1-CT-S</b>	50	109.5
<b>CW-H4</b>	365	1.08		<b>HP-CT-N3</b>	50	109.5
<b>H -N3</b>	435	1.01		<b>CC-CV-NB</b>	70	120
<b>H -NT</b>	435	1.01		<b>CC-CW-H4</b>	50	120
<b>HO-OH</b>	555	0.96		<b>CT-N3-H</b>	50	109.5
				<b>H -N3-H</b>	35	109.5
				<b>CT-NT-H</b>	50	109.5
				<b>CT-OH-HO</b>	55	108.5
				<b>CT-S -CT</b>	60	98.9

Table A4: Exp-1 inhibitor encompassing hydroxy methyl ketone (HMK) optimized parameters with 6-31+G(d,p).

<b>Hydroxy methyl ketone (HMK)</b>						
<b>Parameters</b>			<b>Parameters</b>			
<b>BOND</b>	<b>K(kcal.mol-1.ang-2)</b>	<b>Dist0(ang)</b>		<b>ANGLE</b>	<b>K(kcal.mol-1.rad-2)</b>	<b>Theta0(deg)</b>
<b>C -CM</b>	410	1.444		<b>CM-C -O</b>	80	125.3
<b>C -CT</b>	315	1.522		<b>CT-C -N</b>	70	116.6
<b>C -H4</b>	365	1.1		<b>CT-C -O</b>	80	120.4
<b>C -N</b>	490	1.335		<b>CT-C -O2</b>	70	117
<b>C -O</b>	570	1.229		<b>H4-C -O</b>	50	120.93
<b>C -O2</b>	655	1.25		<b>N -C -O</b>	80	122.9
<b>C -OH</b>	450	1.364		<b>O -C -OH</b>	80	120
<b>CA-CA</b>	470	1.4		<b>O2-C -O2</b>	80	126
<b>CA-CT</b>	315	1.51		<b>CA-CA-CA</b>	65	120
<b>CA-HA</b>	365	1.08		<b>CA-CA-CT</b>	70	120
<b>CD-CM</b>	550	1.35		<b>CA-CA-HA</b>	50	120
<b>CM-CT</b>	315	1.51		<b>C -CM-CT</b>	70	119.7
<b>CM-H4</b>	365	1.08		<b>C -CT-CT</b>	65	111.1
<b>CT-CT</b>	310	1.526		<b>C -CT-H1</b>	50	109.5
<b>CT-H1</b>	340	1.09		<b>C -CT-HC</b>	50	109.5
<b>CT-HC</b>	340	1.09		<b>CM-CT-CT</b>	65	111
<b>CT-N</b>	335	1.449		<b>CM-CT-H1</b>	50	109.5
<b>CT-NT</b>	365	1.471		<b>CT-CT-H1</b>	50	109.5
<b>CT-S</b>	225	1.81		<b>CT-CT-HC</b>	50	109.5
<b>H -N</b>	435	1.01		<b>CT-CT-N</b>	80	109.7
<b>H -NT</b>	435	1.01		<b>CT-CT-NT</b>	80	111.2
<b>HO-OH</b>	555	0.96		<b>CT-CT-S</b>	50	114.7
				<b>H1-CT-H1</b>	35	109.5
				<b>H1-CT-N</b>	50	109.5
				<b>H1-CT-NT</b>	50	109.5

---

					H1-CT-S	50	109.5
					HC-CT-HC	35	109.5
					C -N -CT	50	121.9
					C -N -H	50	120
					CT-N -H	50	118.04
					CT-NT-CT	50	109.5
					H -NT-H	35	109.5
					C -OH-HO	50	113

Table A5: Cartesian coordinates of E:I and E-I state of the inhibition process of thiophene-core inhibitors.

Thiophene-core inhibitor								
E:I				E-I				
Atom	x	y	z	Atom	x	y	z	
N	37.735	47.595	24.086	N	39.48	49.218	26.228	
HN	37.54	48.546	24.267	HN	38.584	49.246	26.711	
CA	38.503	47.336	22.753	CA	39.463	49.23	24.775	
HA	37.947	47.867	21.963	HA	38.632	49.871	24.448	
CB	39.905	48.069	22.744	CB	40.783	49.745	24.185	
HB1	40.295	47.948	21.72	HB1	40.71	49.731	23.087	
HB2	39.719	49.129	22.978	HB2	40.921	50.761	24.57	
CG	40.959	47.499	23.725	CG	41.915	48.877	24.656	
ND1	41.89	46.423	23.431	ND1	42.569	47.891	23.927	
CE1	42.608	46.242	24.472	CE1	43.613	47.264	24.682	
HE1	43.327	45.484	24.578	HE1	43.385	46.192	24.823	
NE2	42.273	47.174	25.471	NE2	43.463	48.013	25.946	
CD2	41.2	47.936	24.96	CD2	42.441	48.933	25.855	
HD2	40.688	48.72	25.457	HD2	42.13	49.576	26.634	
C	38.734	45.907	22.288	C	39.202	47.847	24.263	
O	38.919	45.658	21.087	O	38.361	47.127	24.814	
HE2	42.658	47.213	26.442	HD1	42.261	47.566	23.018	
N	47.116	44.337	26.21	N	47.031	42.245	27.14	
HN	46.705	44.744	25.367	HN	46.811	41.271	26.864	
CA	46.477	44.534	27.566	CA	46.341	42.942	28.252	
HA	46.939	45.405	28.058	HA	47.021	43.678	28.676	
CB	45.025	44.738	27.393	CB	44.983	43.663	27.842	
HB2	44.582	43.837	26.934	HB1	44.341	42.889	27.405	
HB1	44.58	44.915	28.38	HB2	44.503	44.06	28.751	
SG	44.742	46.104	26.354	SG	45.101	45.087	26.625	
C	46.547	43.336	28.45	C	46.11	41.847	29.259	
O	45.652	42.471	28.329	O	47.041	41.467	29.971	
C1	48.345	46.498	35.59	C1	48.381	49.221	33.322	
N1	47.558	46.604	34.391	N1	47.303	48.477	32.712	
HN1	48.018	46.809	33.486	HN1	46.854	48.811	31.876	
C2	46.222	46.424	34.456	C2	46.923	47.337	33.293	
O1	45.643	46.163	35.542	O1	47.531	46.954	34.317	
C3	45.395	46.57	33.243	C3	45.849	46.496	32.718	



<b>C17</b>	45.888	47.196	32.103			<b>C17</b>	45.211	46.795	31.514
<b>C4</b>	44.091	46.098	33.255			<b>C4</b>	45.492	45.357	33.433
<b>C5</b>	43.284	46.247	32.135			<b>C5</b>	44.5	44.516	32.955
<b>C6</b>	43.772	46.884	31			<b>C6</b>	43.871	44.806	31.758
<b>C7</b>	45.078	47.367	30.98			<b>C7</b>	44.217	45.936	31.022
<b>O2</b>	45.636	48.053	29.874			<b>O2</b>	43.479	46.101	29.796
<b>C8</b>	44.922	48.311	28.699			<b>C8</b>	43.732	47.223	28.936
<b>O3</b>	43.75	47.922	28.471			<b>O3</b>	42.836	46.796	27.902
<b>C9</b>	45.64	49.035	27.625			<b>C9</b>	45.059	47.411	28.305
<b>C10</b>	46.055	47.986	26.57			<b>C10</b>	45.67	46.658	27.344
<b>C11</b>	46.318	48.67	25.214			<b>C11</b>	46.827	47.432	26.764
<b>C12</b>	46.48	47.78	24.026			<b>C12</b>	47.163	47.222	25.379
<b>C13</b>	45.892	48.083	22.861			<b>C13</b>	47.726	48.235	24.728
<b>N2</b>	46.005	47.282	21.734			<b>N2</b>	48.066	48.102	23.486
<b>O5</b>	45.37	47.675	20.629			<b>O5</b>	48.273	49.185	23.073
<b>O4</b>	46.694	46.346	21.694			<b>O4</b>	48.076	46.951	23.142
<b>C14</b>	45.012	49.288	22.743			<b>C14</b>	47.995	49.533	25.365
<b>C15</b>	44.53	49.885	23.964			<b>C15</b>	47.399	49.833	26.502
<b>C16</b>	45.117	49.541	25.098			<b>C16</b>	46.416	48.87	26.969
<b>S1</b>	44.584	49.943	26.599			<b>S1</b>	45.887	48.912	28.604
<b>H2</b>	47.687	46.391	36.452			<b>H2</b>	49.144	48.515	33.682
<b>H3</b>	48.973	47.395	35.695			<b>H3</b>	47.985	49.788	34.178
<b>H4</b>	49.002	45.621	35.519			<b>H4</b>	48.82	49.915	32.594
<b>H5</b>	46.876	47.567	32.101			<b>H5</b>	45.488	47.664	30.973
<b>H6</b>	43.713	45.625	34.119			<b>H6</b>	45.977	45.134	34.342
<b>H7</b>	42.292	45.883	32.15			<b>H7</b>	44.225	43.652	33.506
<b>H8</b>	43.138	47.003	30.154			<b>H8</b>	43.108	44.157	31.393
<b>H10</b>	47.05	46.922	24.109			<b>H10</b>	46.98	46.311	24.907
<b>H11</b>	44.573	49.537	21.813			<b>H11</b>	48.655	50.223	24.907
<b>H12</b>	43.679	50.529	23.961			<b>H12</b>	47.575	50.753	27.001
<b>H13</b>	47.221	49.287	25.333			<b>H13</b>	47.682	47.235	27.341
<b>H13</b>	46.508	49.641	27.966			<b>H13</b>	45.533	48.991	26.335
<b>H14</b>	46.84	47.302	26.929			<b>H14</b>	43.156	45.932	27.505

Table A6: Cartesian coordinates of E:I and E-I state of the inhibition process of nitrile-core inhibitor.

Nitrile-core inhibitor								
E:I				E-I				
Atom	x	y	z	Atom	x	y	z	
N	38.446	48.06	28.006	N	39.029	47.643	27.653	
HN	39.433	48.006	27.741	HN	39.96	48.012	27.765	
CA	37.652	49.107	27.652	CA	37.916	48.528	27.448	
HA	37.026	49.335	28.514	HA	37.3	48.527	28.353	
CB	38.423	50.338	27.215	CB	38.406	49.958	27.174	
HB2	37.707	51.135	26.978	HB2	37.566	50.658	27.03	
HB1	39.047	50.621	28.076	HB1	38.981	50.282	28.052	
CG	39.318	50.092	25.989	CG	39.329	49.997	25.974	
ND1	40.455	49.204	25.813	ND1	40.252	48.976	25.594	
HD1	40.834	48.573	26.482	CE1	40.864	49.466	24.424	
CE1	40.912	49.401	24.506	HE1	41.551	48.939	23.807	
HE1	41.709	48.9	24.034	NE2	40.362	50.704	24.16	
NE2	40.133	50.371	23.943	HE2	40.595	51.272	23.371	
HE2	40.259	50.762	23.021	CD2	39.407	51.006	25.111	
CD2	39.149	50.756	24.852	HD2	38.827	51.903	25.144	
HD2	38.383	51.486	24.671	C	37.077	47.995	26.314	
C	36.741	48.568	26.582	O	36.55	48.759	25.487	
O	36.38	49.249	25.621	N	47.58	44.083	27.191	
N	47.808	44.022	27.217	HN	46.836	43.425	26.969	
HN	47.088	43.341	27.004	CA	47.545	44.942	28.314	
CA	47.746	44.896	28.298	HA	48.348	45.673	28.199	
HA	48.606	45.577	28.266	CB	46.268	45.677	28.368	
CB	46.474	45.71	28.189	HB1	46.337	46.375	29.195	
HB1	46.441	46.42	29.023	HB2	46.18	46.238	27.43	
HB2	46.505	46.282	27.242	SG	44.76	44.744	28.571	
SG	44.977	44.686	28.2	C	47.825	44.223	29.498	
C	47.851	44.169	29.512	O	48.988	44.352	29.899	
O	48.94	44.334	30.077	C30	45.322	48.209	34.333	
C30	45.216	48.165	34.112	C31	44.565	47.361	35.371	
C31	44.522	47.317	35.186	C32	45.075	45.91	35.317	
C32	45.085	45.886	35.148	C33	44.826	45.328	33.918	
C33	44.815	45.266	33.767	C34	45.583	46.169	32.882	
C34	45.507	46.114	32.693	C29	45.078	47.631	32.926	

<b>C29</b>	44.954	47.559	32.716			N28	45.786	48.39	31.935
<b>N28</b>	45.645	48.335	31.72			HAC	46.594	48.995	32.189
<b>HAC</b>	46.501	48.844	31.983			C25	45.389	48.304	30.617
<b>C25</b>	45.223	48.378	30.386			N24	44.39	47.577	30.279
<b>N24</b>	44.148	47.802	30.019			C23	43.868	47.495	28.89
<b>C23</b>	43.649	47.968	28.624			C27	43.544	46.059	28.416
<b>C27</b>	42.615	47.168	28.074			N35	42.47	45.843	27.768
<b>N35</b>	41.781	46.523	27.631			N22	44.751	48.209	27.901
<b>N22</b>	44.507	48.55	27.675			C21	45.782	49.024	28.386
<b>C21</b>	45.649	49.133	28.139			C26	46.065	49.053	29.656
<b>C26</b>	45.976	49.087	29.405			N20	47.106	49.938	29.903
<b>N20</b>	47.111	49.832	29.611			C19	47.446	50.478	28.789
<b>C19</b>	47.467	50.329	28.484			N18	46.684	49.916	27.759
<b>N18</b>	46.642	49.859	27.489			C17	46.587	50.363	26.414
<b>C17</b>	46.644	50.29	26.116			C16	47.129	49.312	25.322
<b>C16</b>	47.446	49.362	25.051			N06	48.61	48.969	25.324
<b>N06</b>	48.951	49.114	25.228			C01	49.128	48.176	26.483
<b>C01</b>	49.302	48.197	26.331			C04	50.674	47.917	26.322
<b>C04</b>	50.831	47.936	26.332			N03	51.379	49.157	26.353
<b>N03</b>	51.547	49.178	26.584			C15	52.811	48.915	26.2
<b>C15</b>	52.99	48.888	26.561			HAA	51.224	49.63	27.289
<b>HAA</b>	51.301	49.565	27.512			C02	50.903	49.954	25.231
<b>C02</b>	51.219	50.113	25.549			C05	49.372	50.22	25.318
<b>C05</b>	49.682	50.381	25.479			HC2	46.395	48.185	34.558
<b>HC2</b>	46.295	48.175	34.31			HC3	44.96	49.245	34.373
<b>HC3</b>	44.825	49.192	34.146			HC4	44.735	47.77	36.378
<b>HC4</b>	44.71	47.757	36.175			HC5	43.491	47.379	35.144
<b>HC5</b>	43.442	47.289	34.993			HC6	46.153	45.893	35.536
<b>HC6</b>	46.17	45.913	35.337			HC7	44.538	45.308	36.06
<b>HC7</b>	44.595	45.282	35.916			HC8	45.187	44.289	33.881
<b>HC8</b>	45.214	44.24	33.741			HC9	43.747	45.35	33.699
<b>HC9</b>	43.737	45.243	33.587			0HC1	45.409	45.751	31.881
<b>0HC1</b>	45.331	45.671	31.7			1HC1	46.656	46.142	33.112
<b>1HC1</b>	46.581	46.129	32.905			HC	44.005	47.629	32.679
<b>HC</b>	43.878	47.533	32.49			2HC1	48.168	51.246	28.686
<b>2HC1</b>	48.274	51.018	28.333			3HC1	45.51	50.509	26.2
<b>3HC1</b>	45.573	50.323	25.773			4HC1	47.126	51.324	26.305
<b>4HC1</b>	47.089	51.302	26.071			5HC1	46.925	49.769	24.343
<b>5HC1</b>	47.329	49.878	24.084			6HC1	46.55	48.386	25.408
<b>6HC1</b>	46.967	48.388	24.986			7HC1	48.945	48.709	27.423
<b>7HC1</b>	49	48.614	27.302			8HC1	48.629	47.211	26.519

---

<b>8HC1</b>	48.796	47.24	26.175			9HC1	50.875	47.393	25.392
<b>9HC1</b>	51.145	47.519	25.382			0HC2	51.035	47.316	27.173
<b>0HC2</b>	51.083	47.237	27.141			1HC2	51.105	49.401	24.293
<b>1HC2</b>	51.542	49.693	24.588			2HC2	51.438	50.914	25.224
<b>2HC2</b>	51.753	51.055	25.745			3HC2	49.069	50.827	24.469
<b>3HC2</b>	49.48	51.089	24.682			4HC2	49.169	50.767	26.248
<b>4HC2</b>	49.343	50.806	26.439			5HC2	53.002	48.38	25.262
<b>5HC2</b>	53.269	48.468	25.59			6HC2	53.345	49.876	26.203
<b>6HC2</b>	53.552	49.811	26.747			7HC2	53.159	48.307	27.048
<b>7HC2</b>	53.224	48.162	27.354			H30	44.506	48.16	26.915
<b>H30</b>	44.22	48.616	26.713			H31	42.311	44.903	27.381

**Table A7** Cartesian coordinates of E:I and E-I state of the inhibition process of Exp-1 inhibitors with methyl oxy-enoate warheads.

<b>Methyl oxy-enoate warhead</b>								
<b>E:I</b>				<b>E-I</b>				
<b>Atom</b>	<b>x</b>	<b>y</b>	<b>z</b>		<b>Atom</b>	<b>x</b>	<b>y</b>	<b>z</b>
C8	45.711	28.193	27.239		C8	43.662	27.447	29.426
C9	45.64	26.844	27.572		C9	43.388	26.191	29.956
C10	44.972	26.445	28.725		C10	42.327	26.026	30.837
C11	44.381	27.4	29.544		C11	41.54	27.116	31.188
C12	44.46	28.746	29.217		C12	41.813	28.375	30.656
C7	45.123	29.15	28.067		C7	42.876	28.536	29.773
C6	45.184	30.633	27.732		C6	43.185	29.88	29.185
N2	44.168	30.9	26.735		N2	42.395	30.045	28.08
C	43.099	31.861	26.752		C	41.293	30.793	28.136
N1	43.996	30.076	25.76		N1	42.544	29.443	26.914
C5	42.923	30.373	25.162		C5	41.52	29.766	26.244
C4	42.525	29.602	24.075		C4	41.327	29.338	24.969
O3	43.503	28.747	23.594		O3	42.371	28.753	24.315
O2	41.394	29.668	23.584		O2	40.23	29.349	24.454
C3	42.301	31.546	25.756		C3	40.698	30.653	27
N	41.126	32.173	25.309		N	39.598	31.323	26.599
H4	40.499	31.591	24.779		H4	38.931	30.841	26.025
C2	41.031	33.616	25.159		C2	39.872	32.703	26.278
O	40.927	33.196	23.927		O	40.935	32.598	25.235
C1	39.524	33.794	24.89		C1	38.611	33.289	25.791
O1	39.288	32.994	23.734		O1	38.153	32.507	24.747
H1	39.73	32.077	23.933		H1	38.085	31.505	25.158
HC	46.21	28.491	26.35		HC	44.47	27.568	28.758
HC1	46.093	26.111	26.943		HC1	43.989	25.368	29.686
HC2	44.912	25.412	28.976		HC2	42.116	25.063	31.245
HC3	43.866	27.105	30.417		HC3	40.732	26.987	31.861
HC4	44.012	29.467	29.843		HC4	41.203	29.213	30.927
HC5	45.019	31.257	28.613		HC5	42.912	30.682	29.913
HC6	46.154	30.826	27.256		HC6	44.212	29.916	28.869
HC7	42.95	32.645	27.421		HC7	40.967	31.403	28.939
HC8	38.952	33.412	25.752		HC8	37.884	33.275	26.601
HC9	39.26	34.831	24.711		HC9	38.764	34.307	25.466
H13	41.896	32.912	23.979		H13	41.745	32.184	25.732
N	44.682	33.876	25.454		N	44.809	32.153	23.417

## APPENDIX

<b>HN</b>	43.695	33.941	25.23			<b>HN</b>	43.932	32.542	23.398
<b>CA</b>	45.486	32.77	24.901			<b>CA</b>	44.96	30.975	22.687
<b>HA</b>	45.773	32.108	25.723			<b>HA</b>	45.344	30.246	23.392
<b>CB</b>	44.512	31.982	23.906			<b>CB</b>	43.545	30.408	22.167
<b>HB2</b>	45.095	31.139	23.521			<b>HB2</b>	43.755	29.441	21.699
<b>HB1</b>	43.653	31.62	24.5			<b>HB1</b>	42.952	30.286	23.066
<b>CG</b>	43.945	32.81	22.698			<b>CG</b>	42.663	31.19	21.191
<b>ND1</b>	42.553	33.196	22.507			<b>ND1</b>	41.632	32.09	21.584
<b>CE1</b>	42.454	33.864	21.286			<b>CE1</b>	40.947	32.43	20.374
<b>HE1</b>	41.574	34.264	20.863			<b>HE1</b>	40.121	33.062	20.304
<b>NE2</b>	43.734	33.875	20.718			<b>NE2</b>	41.58	31.775	19.283
<b>HE2</b>	43.968	34.253	19.799			<b>HE2</b>	41.322	31.806	18.269
<b>CD2</b>	44.63	33.227	21.627			<b>CD2</b>	42.625	30.999	19.862
<b>HD2</b>	45.67	33.07	21.461			<b>HD2</b>	43.253	30.323	19.333
<b>C</b>	46.838	33.252	24.272			<b>C</b>	46.026	31.152	21.603
<b>O</b>	47.917	32.988	24.834			<b>O</b>	47.111	30.526	21.73
<b>H8</b>	41.748	33.001	23.184			<b>N</b>	38.64	36.435	26.099
<b>N</b>	39.822	37.15	25.558			<b>HN</b>	37.69	36.244	26.449
<b>HN</b>	39.289	37.66	24.909			<b>CA</b>	39.765	36.363	27.083
<b>CA</b>	40.068	37.689	26.836			<b>HA1</b>	39.924	35.641	26.306
<b>HA1</b>	40.39	38.722	26.711			<b>CB</b>	40.983	35.464	27.424
<b>CB</b>	41.199	36.875	27.471			<b>HB2</b>	41.437	35.854	28.343
<b>HB2</b>	42.059	36.995	26.823			<b>HB1</b>	41.71	35.509	26.611
<b>HB1</b>	41.432	37.29	28.459			<b>SG</b>	40.546	33.687	27.712
<b>SG</b>	40.935	35.063	27.62			<b>C</b>	39.029	36.076	28.356
<b>C</b>	38.774	37.746	27.557			<b>O</b>	38.993	36.968	29.208
<b>O</b>	38.161	38.823	27.417			<b>HA2</b>	40.226	37.337	26.999

**Table A8.** Cartesian coordinates of E:I and E-I state of the inhibition process of Exp-2 inhibitors with hydroxy methyl ketone (HMK) warheads. .

<b>Hydroxy methyl ketone (HMK) warhead</b>							
<b>E:I</b>				<b>E-I</b>			
<b>Atom</b>	<b>x</b>	<b>y</b>	<b>z</b>	<b>Atom</b>	<b>x</b>	<b>y</b>	<b>z</b>
N	45.342	24.62	22.846	N	45.46	24.394	21.302
HN	44.413	24.874	22.609	HN	44.475	24.389	21.469
CA	45.939	23.378	22.382	CA	46.2	23.189	20.797
HA	46.456	22.878	23.211	HA	46.863	22.828	21.592
CB	44.925	22.428	21.678	CB	45.208	22.094	20.39
HB1	44.45	22.9	20.81	HB1	44.579	22.435	19.559
HB2	45.482	21.555	21.304	HB2	45.728	21.18	20.045
CG	43.905	21.898	22.592	CG	44.319	21.776	21.53
ND1	42.746	21.214	22.248	ND1	43.258	20.891	21.546
HD1	42.425	21.004	21.304	HD1	42.947	20.29	20.773
CE1	42.113	20.703	23.471	CE1	42.669	21.009	22.757
HE1	41.087	21.056	23.593	HE1	41.812	20.5	23.094
NE2	42.972	21.282	24.446	NE2	43.375	21.918	23.477
CD2	44.001	21.93	23.898	CD2	44.375	22.359	22.717
HD2	44.785	22.35	24.44	HD2	45.068	23.103	23.019
C	46.951	23.708	21.342	C	47.049	23.54	19.623
O	48.116	23.234	21.369	O	48.276	23.368	19.659
HE1	42.13	19.601	23.541	N	41.815	27.695	26.5
HE2	42.88	21.128	25.465	HN	42.486	28.363	26.467
N	40.183	28.068	26.569	CA	41.862	26.838	27.427
HN	40.583	27.596	25.809	CB	43.342	26.398	27.713
CA	40.749	28.176	27.713	HB2	43.999	26.941	27.03
CB	42.073	27.448	27.657	HB1	43.559	26.751	28.723
HB	42.339	26.88	26.795	SG	43.918	24.608	27.763
SG	43.063	27.493	28.872	C	41.95	27.761	28.537
C	40.634	28.639	28.962	O	42.791	28.689	28.467
O	41.083	28.78	30.104	HA	41.084	26.093	27.453
C	47.369	18.928	32.175	C	46.821	17.182	33.589
C1	46.626	18.277	33.153	C1	46.952	17.879	34.785
C2	46.169	18.979	34.265	C2	47.306	19.223	34.776
C3	46.458	20.333	34.396	C3	47.53	19.873	33.567
C4	47.204	20.982	33.419	C4	47.397	19.177	32.369
C5	47.658	20.279	32.309	C5	47.043	17.831	32.38

<b>C6</b>	48.456	20.965	31.242		<b>C6</b>	46.893	17.077	31.081
<b>N</b>	47.518	21.448	30.286		<b>N</b>	46.069	17.872	30.231
<b>C14</b>	46.651	22.474	30.5		<b>C14</b>	44.682	17.889	30.227
<b>N1</b>	47.305	20.922	29.051		<b>N1</b>	46.542	18.794	29.367
<b>C7</b>	46.355	21.582	28.515		<b>C7</b>	45.543	19.401	28.85
<b>C8</b>	45.978	21.335	27.156		<b>C8</b>	45.704	20.503	27.9
<b>O1</b>	46.418	20.307	26.661		<b>O1</b>	46.842	20.717	27.501
<b>O</b>	45.378	22.276	26.271		<b>O</b>	44.634	21.344	27.535
<b>C9</b>	45.889	22.574	29.446		<b>C9</b>	44.309	18.832	29.386
<b>N2</b>	44.851	23.422	29.355		<b>N2</b>	42.991	19.178	29.083
<b>H11</b>	44.87	24.25	29.856		<b>H11</b>	42.234	18.692	29.519
<b>C10</b>	43.734	23.104	28.653		<b>C10</b>	45.015	22.421	26.62
<b>O4</b>	43.606	22.02	28.065		<b>O4</b>	46.186	22.511	26.217
<b>C11</b>	42.618	23.997	28.577		<b>C11</b>	44.119	23.584	26.219
<b>C12</b>	41.665	23.61	27.736		<b>C12</b>	42.779	23.153	25.589
<b>C13</b>	40.459	24.362	27.481		<b>C13</b>	42.053	24.394	25.076
<b>O3</b>	39.704	24.02	26.551		<b>O3</b>	42.617	25.502	24.973
<b>O2</b>	40.117	25.455	28.208		<b>O2</b>	40.785	24.316	24.646
<b>HC</b>	47.715	18.394	31.321		<b>HC</b>	46.55	16.155	33.601
<b>HC1</b>	46.406	17.248	33.049		<b>HC1</b>	46.781	17.384	35.706
<b>HC2</b>	45.598	18.48	35.014		<b>HC2</b>	47.406	19.755	35.694
<b>HC3</b>	46.108	20.871	35.241		<b>HC3</b>	47.804	20.906	33.565
<b>HC4</b>	47.422	22.017	33.518		<b>HC4</b>	47.563	19.673	31.439
<b>HC5</b>	48.977	21.829	31.685		<b>HC5</b>	47.881	17.017	30.602
<b>HC6</b>	49.125	20.255	30.745		<b>HC6</b>	46.465	16.076	31.274
<b>HC7</b>	46.565	23.027	31.353		<b>HC7</b>	44.049	17.278	30.792



## PUBLICATIONS

### Published thesis work

1. **Naila Zaman**, and Syed Sikander Azam\*. (2023). Discrete Dynamics of Warhead Modulation on Covalent Inhibition of Oxyr: A QM/MM Study. *Journal of Physical Chemistry B*, 127, 27, 5993–6005.
2. **Naila Zaman**, and Syed Sikander Azam\*. (2023). Quantum Dynamics and Bi Metal Force Field Parameterization Yielding Significant Antileishmanial Targets. *Journal of Chemical Information and Modeling*, 63, 4, 1371–1385.
3. **Naila Zaman**, Nousheen Pervaiz, Rabia Farid, Afifa Navid, Ghulam Abbas, and Syed Sikander Azam\* (2022). Senna makki and other active phytochemicals: myths and realities behind covid19 therapeutic interventions. *PLoS ONE*, 17(6), e0268454.
4. **Naila Zaman**, and Syed Sikander Azam\*. (2019). From normal to competo-allosteric regulation: Insights into the binding pattern dynamics of DSPI protein of *Pseudomonas aeruginosa*. *Journal of Biomolecular Structure and Dynamics*, 39 (2), 538-557.

### Other publications

5. **Naila Zaman**, Rimsha Yousaf, Zahra Akhtar, and Syed Sikander Azam\*. (2023). Modulating Structural Dynamics of Dual Drugs for CDK4 Complex Addressing Prostate Cancer. *Journal of Molecular Liquids*, Volume 376, 15 April 2023, 121454
6. Kainat Gul, **Naila Zaman**, Syed Sikander Azam\*. (2023). Roxadustat and its failure: A comparative dynamic study. *Journal of Molecular Graphics and Modelling*. Volume 120, May 2023, 108422

7. Hassan Yousaf, Anam Naz, **Naila Zaman**, Ayesha Obaid, Faryal Mehwish Awan, and Syed Sikander Azam. (2023). Immunoinformatic and reverse vaccinology-based designing of potent multi-epitope vaccine against Marburgvirus targeting the glycoprotein. *Heliyon*, Volume 9, issue 8, E18059.
8. Azka Ahmad, Naila Zaman, Syed Sikander Azam\*. (2020). Deciphering the Molecular Basis of Thioredoxin Domain Underlying Dynamics of Sulfonamides through Comparative Molecular Dynamics Simulations. *Journal of Molecular Liquids*, 321, 114797.
9. Sajjad Ahmad, Afifa Navid, Rabia Farid, Ghulam Abbas, Faisal Ahmad, **Naila Zaman**, Nousheen Parvaiz, Syed Sikander Azam\*. (2020). Design of a Novel Multi Epitope-Based Vaccine for Pandemic Coronavirus Disease (COVID-19) by Vaccinomics and Probable Prevention Strategy against Avenging Zoonotics. *European Journal of Pharmaceutical Sciences*, 151, 105387
10. Sohaila Andleeb\*, Imtiaz-ud-Din\*, Muhammad Khawar Rauf, Syed Sikander Azam, Ihsan-ul Haq, Muhammad Nawaz Tahir, **Naila Zaman**. (2021). Structural Characterization, and Antileishmanial Activity of newly Synthesized Organobismuth(V) Carboxylates: Experimental and Molecular Docking Studies. *Journal of Biological Inorganic Chemistry*, 27 (1), 175-187.
11. Syed Sikander Azam\*, Ayman Sarosh, **Naila Zaman**, and Saad Raza. (2013). Role of N-acetylserotonin O-methyltransferase in bipolar disorders and its dynamics. *Journal of Molecular Liquids*, 182, 25-31.

## Research work in submission

**Naila Zaman**, Nousheen Parvaiz, Fouzia Gul, Rimsha Yousaf, Kainat Gul, and Syed Sikander Azam Zaman\*. (2022). Dynamics of water-mediated interaction effects on the stability and transmission of Omicron. *Scientific Reports*

## REFERENCES

- (1) Jamrozik, E.; Selgelid, M. J. Drug-Resistant Infection: Causes, Consequences, and Responses. In *Ethics and drug resistance: collective responsibility for global public health*; Jamrozik, E., Selgelid, M., eds.; Public health ethics analysis; Springer International Publishing: Cham, 2020; Vol. 5, pp 3–18.
- (2) WHO report on surveillance of antibiotic consumption <https://www.who.int/publications/i/item/who-report-on-surveillance-of-antibiotic-consumption>
- (3) Šámal, V.; Paldus, V.; Fáčková, D.; Mečl, J.; Šrám, J. The prevalence of antibiotic-resistant and multidrug-resistant bacteria in urine cultures from inpatients with spinal cord injuries and disorders: an 8-year, single-center study. *BMC Infect. Dis.* **2022**, *22* (1), 239.
- (4) Moghnieh, R.; Estaitieh, N.; Mugharbil, A.; Jisr, T.; Abdallah, D. I.; Ziade, F.; Sinno, L.; Ibrahim, A. Third generation cephalosporin resistant Enterobacteriaceae and multidrug resistant gram-negative bacteria causing bacteremia in febrile neutropenia adult cancer patients in Lebanon, broad spectrum antibiotics use as a major risk factor, and correlation with poor prognosis. *Front. Cell Infect. Microbiol.* **2015**, *5*, 11.
- (5) Protic, D.; Pejovic, A.; Djukanovic, N.; Toskovic, B.; Zdravkovic, M.; Todorovic, Z. Analysis of the third- and fourth-generation cephalosporin use for the treatment of infections caused by Gram-negative bacteria in hospital settings. *Int. J. Clin. Pract.* **2016**, *70* (12), 1033–1040.
- (6) Arumugham, V. B.; Gujarathi, R.; Cascella, M. Third Generation Cephalosporins. In *StatPearls*; StatPearls Publishing: Treasure Island (FL), 2022.
- (7) Tackling drug-resistant infections globally : final report and recommendations / the Review on Antimicrobial Resistance chaired by Jim O'Neill. | Wellcome Collection
- (8) Progress Report - AMR Industry Alliance <https://www.amrindustryalliance.org/progress-report/>
- (9) Abushaheen, M. A.; Muzahed; Fatani, A. J.; Alosaimi, M.; Mansy, W.; George, M.; Acharya, S.; Rathod, S.; Divakar, D. D.; Jhugroo, C.; et al. Antimicrobial resistance, mechanisms and its clinical significance. *Dis. Mon.* **2020**, *66* (6), 100971.
- (10) Reygaert, W. C. An overview of the antimicrobial resistance mechanisms of bacteria. *AIMS Microbiol.* **2018**, *4* (3), 482–501.
- (11) Birgand, G.; Moore, L. S. P.; Bourigault, C.; Vella, V.; Lepelletier, D.; Holmes, A. H.; Lucet, J. C. Measures to eradicate multidrug-resistant organism outbreaks: how much do they cost? *Clin. Microbiol. Infect.* **2016**, *22* (2), 162.e1–162.e9.

- 
- (12) Revitt-Mills, S. A.; Robinson, A. Antibiotic-Induced Mutagenesis: Under the Microscope. *Front. Microbiol.* **2020**, *11*, 585175.
- (13) Ghosh, A.; N, S.; Saha, S. Survey of drug resistance associated gene mutations in *Mycobacterium tuberculosis*, ESKAPE and other bacterial species. *Sci. Rep.* **2020**, *10* (1), 8957.
- (14) Mutation Rates and Antibiotic Resistance | Learn Science at Scitable <https://www.nature.com/scitable/topicpage/antibiotic-resistance-mutation-rates-and-mrsa-28360/>
- (15) Munita, J. M.; Arias, C. A. Mechanisms of antibiotic resistance. *Microbiol. Spectr.* **2016**, *4* (2).
- (16) Byrne, M. K.; Miellet, S.; McGlinn, A.; Fish, J.; Meedy, S.; Reynolds, N.; van Oijen, A. M. The drivers of antibiotic use and misuse: the development and investigation of a theory driven community measure. *BMC Public Health* **2019**, *19* (1), 1425.
- (17) Ventola, C. L. The antibiotic resistance crisis: part 1: causes and threats. *P T* **2015**, *40* (4), 277–283.
- (18) Founou, R. C.; Founou, L. L.; Essack, S. Y. Clinical and economic impact of antibiotic resistance in developing countries: A systematic review and meta-analysis. *PLoS One* **2017**, *12* (12), e0189621.
- (19) Nadimpalli, M. L.; Marks, S. J.; Montealegre, M. C.; Gilman, R. H.; Pajuelo, M. J.; Saito, M.; Tsukayama, P.; Njenga, S. M.; Kiiru, J.; Swarthout, J.; et al. Urban informal settlements as hotspots of antimicrobial resistance and the need to curb environmental transmission. *Nat. Microbiol.* **2020**, *5* (6), 787–795.
- (20) Raising awareness and educating on antimicrobial resistance <https://www.who.int/activities/raising-awareness-and-educating-on-antimicrobial-resistance>
- (21) Majumder, M. A. A.; Rahman, S.; Cohall, D.; Bharatha, A.; Singh, K.; Haque, M.; Gittens-St Hilaire, M. Antimicrobial stewardship: fighting antimicrobial resistance and protecting global public health. *Infect. Drug Resist.* **2020**, *13*, 4713–4738.
- (22) Antibiotic / Antimicrobial Resistance | CDC <https://www.cdc.gov/drugresistance/index.html>
- (23) Wu, D.; Ding, Y.; Yao, K.; Gao, W.; Wang, Y. Antimicrobial Resistance Analysis of Clinical *Escherichia coli* Isolates in Neonatal Ward. *Front. Pediatr.* **2021**, *9*, 670470.
- (24) Jain, P.; Bepari, A. K.; Sen, P. K.; Rafe, T.; Imtiaz, R.; Hossain, M.; Reza, H. M. High prevalence of multiple antibiotic resistance in clinical *E. coli* isolates from

---

Bangladesh and prediction of molecular resistance determinants using WGS of an XDR isolate. *Sci. Rep.* **2021**, *11* (1), 22859.

(25) Farhadi, M.; Ahanjan, M.; Goli, H. R.; Haghshenas, M. R.; Gholami, M. High frequency of multidrug-resistant (MDR) *Klebsiella pneumoniae* harboring several  $\beta$ -lactamase and integron genes collected from several hospitals in the north of Iran. *Ann Clin Microbiol Antimicrob* **2021**, *20* (1), 70.

(26) Odari, R.; Dawadi, P. Prevalence of Multidrug-Resistant *Klebsiella pneumoniae* Clinical Isolates in Nepal. *J. Trop. Med.* **2022**, *2022*, 5309350.

(27) Thuy, D. B.; Campbell, J.; Thuy, C. T.; Hoang, N. V. M.; Voong Vinh, P.; Nguyen, T. N. T.; Nguyen Ngoc Minh, C.; Pham, D. T.; Rabaa, M. A.; Lan, N. P. H.; et al. Colonization with *Staphylococcus aureus* and *Klebsiella pneumoniae* causes infections in a Vietnamese intensive care unit. *Microb. Genom.* **2021**, *7* (2).

(28) Seung, K. J.; Keshavjee, S.; Rich, M. L. Multidrug-Resistant Tuberculosis and Extensively Drug-Resistant Tuberculosis. *Cold Spring Harb. Perspect. Med.* **2015**, *5* (9), a017863.

(29) WHO announces updated definitions of extensively drug-resistant tuberculosis <https://www.who.int/news/item/27-01-2021-who-announces-updated-definitions-of-extensively-drug-resistant-tuberculosis>.

(30) Fact Sheets | Drug-Resistant TB | Multidrug-Resistant Tuberculosis (MDR TB) | TB | CDC <https://www.cdc.gov/tb/publications/factsheets/drtb/mdrtb.htm>.

(31) Zhou, F.; Yu, T.; Du, R.; Fan, G.; Liu, Y.; Liu, Z.; Xiang, J.; Wang, Y.; Song, B.; Gu, X.; et al. Clinical course and risk factors for mortality of adult inpatients with COVID-19 in Wuhan, China: a retrospective cohort study. *Lancet* **2020**, *395* (10229), 1054–1062.

(32) Chen, X.; Liao, B.; Cheng, L.; Peng, X.; Xu, X.; Li, Y.; Hu, T.; Li, J.; Zhou, X.; Ren, B. The microbial coinfection in COVID-19. *Appl. Microbiol. Biotechnol.* **2020**, *104* (18), 7777–7785.

(33) Zhou, P.; Liu, Z.; Chen, Y.; Xiao, Y.; Huang, X.; Fan, X.-G. Bacterial and fungal infections in COVID-19 patients: A matter of concern. *Infect. Control Hosp. Epidemiol.* **2020**, *41* (9), 1124–1125.

(34) Sharifipour, E.; Shams, S.; Esmkhani, M.; Khodadadi, J.; Fotouhi-Ardakani, R.; Koohpaei, A.; Doosti, Z.; Ej Golzari, S. Evaluation of bacterial co-infections of the respiratory tract in COVID-19 patients admitted to ICU. *BMC Infect. Dis.* **2020**, *20* (1), 646.

(35) Contou, D.; Claudinon, A.; Pajot, O.; Micaëlo, M.; Longuet Flandre, P.; Dubert, M.; Cally, R.; Logre, E.; Fraissé, M.; Mentec, H.; et al. Bacterial and viral co-infections in

---

patients with severe SARS-CoV-2 pneumonia admitted to a French ICU. *Ann. Intensive Care* **2020**, *10* (1), 119.

(36) Baron, S. A.; Devaux, C.; Colson, P.; Raoult, D.; Rolain, J.-M. Teicoplanin: an alternative drug for the treatment of COVID-19? *Int. J. Antimicrob. Agents* **2020**, *55* (4), 105944.

(37) Sodhi, M.; Etminan, M. Therapeutic Potential for Tetracyclines in the Treatment of COVID-19. *Pharmacotherapy* **2020**, *40* (5), 487–488.

(38) Yates, P. A.; Newman, S. A.; Oshry, L. J.; Glassman, R. H.; Leone, A. M.; Reichel, E. Doxycycline treatment of high-risk COVID-19-positive patients with comorbid pulmonary disease. *Ther Adv Respir Dis* **2020**, *14*, 1753466620951053.

(39) Oldenburg, C. E.; Doan, T. Azithromycin for severe COVID-19. *Lancet* **2020**, *396* (10256), 936–937.

(40) Hendrickx, S.; Van Bockstal, L.; Caljon, G.; Maes, L. In-depth comparison of cell-based methodological approaches to determine drug susceptibility of visceral Leishmania isolates. *PLoS Negl. Trop. Dis.* **2019**, *13* (12), e0007885.

(41) Muhaj, F. F.; George, S. J.; Nguyen, C. D.; Tying, S. K. Antimicrobials and resistance part II: Antifungals, antivirals, and antiparasitics. *J. Am. Acad. Dermatol.* **2022**, *86* (6), 1207–1226.

(42) Wijnant, G.-J.; Dumetz, F.; Dirx, L.; Bulté, D.; Cuypers, B.; Van Bocxlaer, K.; Hendrickx, S. Tackling drug resistance and other causes of treatment failure in leishmaniasis. *Front. Trop. Dis.* **2022**, *3*.

(43) Xin Yu, J.; Hubbard-Lucey, V. M.; Tang, J. Immuno-oncology drug development goes global. *Nat. Rev. Drug Discov.* **2019**, *18* (12), 899–900.

(44) Tracking the Global Pipeline of Antibiotics in Development, April 2020 | The Pew Charitable Trusts <https://www.pewtrusts.org/en/research-and-analysis/issue-briefs/2020/04/tracking-the-global-pipeline-of-antibiotics-in-development>.

(45) Beyer, P.; Paulin, S. The antibacterial research and development pipeline needs urgent solutions. *ACS Infect. Dis.* **2020**, *6* (6), 1289–1291.

(46) 2019 antibacterial agents in clinical development: an analysis of the antibacterial clinical development pipeline <https://www.who.int/publications/i/item/9789240000193> (accessed Aug 19, 2022).

(47) Rex, J. H.; Fernandez Lynch, H.; Cohen, I. G.; Darrow, J. J.; Outterson, K. Designing development programs for non-traditional antibacterial agents. *Nat. Commun.* **2019**, *10* (1), 3416.

- (48) Theuretzbacher, U.; Piddock, L. J. V. Non-traditional Antibacterial Therapeutic Options and Challenges. *Cell Host Microbe* **2019**, *26* (1), 61–72.
- (49) Fleitas Martínez, O.; Cardoso, M. H.; Ribeiro, S. M.; Franco, O. L. Recent Advances in Anti-virulence Therapeutic Strategies With a Focus on Dismantling Bacterial Membrane Microdomains, Toxin Neutralization, Quorum-Sensing Interference and Biofilm Inhibition. *Front. Cell Infect. Microbiol.* **2019**, *9*, 74.
- (50) Calvert, M. B.; Jumde, V. R.; Titz, A. Pathoblockers or antivirulence drugs as a new option for the treatment of bacterial infections. *Beilstein J Org Chem* **2018**, *14*, 2607–2617.
- (51) Kumar, A.; Ellermann, M.; Sperandio, V. Taming the Beast: Interplay between Gut Small Molecules and Enteric Pathogens. *Infect. Immun.* **2019**, *87* (9).
- (52) Venter, H. Reversing resistance to counter antimicrobial resistance in the World Health Organisation’s critical priority of most dangerous pathogens. *Biosci. Rep.* **2019**, *39* (4).
- (53) Rezzoagli, C.; Archetti, M.; Mignot, I.; Baumgartner, M.; Kümmerli, R. Combining antibiotics with antivirulence compounds can have synergistic effects and reverse selection for antibiotic resistance in *Pseudomonas aeruginosa*. *PLoS Biol.* **2020**, *18* (8), e3000805.
- (54) How AlphaFold can realize AI’s full potential in structural biology. *Nature* **2022**, *608* (7921), 8.
- (55) Callaway, E. What’s next for AlphaFold and the AI protein-folding revolution. *Nature* **2022**, *604* (7905), 234–238.
- (56) Zheng, X.; Cao, Q.; Cao, Q.; Mao, F.; Li, X.; Zhu, J.; Lan, L.; Li, J. Discovery of synergistic activity of fluoroquinolones in combination with antimicrobial peptides against clinical polymyxin-resistant *Pseudomonas aeruginosa* DK2. *Chinese Chemical Letters* **2020**, *31* (2), 413–417.
- (57) Shukla, A.; Shukla, G.; Parmar, P.; Patel, B.; Goswami, D.; Saraf, M. Exemplifying the next generation of antibiotic susceptibility intensifiers of phytochemicals by LasR-mediated quorum sensing inhibition. *Sci. Rep.* **2021**, *11* (1), 22421.
- (58) Heo, Y.-J.; Chung, I.-Y.; Cho, W.-J.; Lee, B.-Y.; Kim, J.-H.; Choi, K.-H.; Lee, J.-W.; Hassett, D. J.; Cho, Y.-H. The major catalase gene (*katA*) of *Pseudomonas aeruginosa* PA14 is under both positive and negative control of the global transactivator OxyR in response to hydrogen peroxide. *J. Bacteriol.* **2010**, *192* (2), 381–390.
- (59) da Cruz Nizer, W. S.; Inkovskiy, V.; Versey, Z.; Stempel, N.; Cassol, E.; Overhage, J. Oxidative Stress Response in *Pseudomonas aeruginosa*. *Pathogens* **2021**, *10* (9).

- (60) Zhang, J.; Adrián, F. J.; Jahnke, W.; Cowan-Jacob, S. W.; Li, A. G.; Jacob, R. E.; Sim, T.; Powers, J.; Dierks, C.; Sun, F.; et al. Targeting Bcr-Abl by combining allosteric with ATP-binding-site inhibitors. *Nature* **2010**, *463* (7280), 501–506.
- (61) Hassan, A. Q.; Sharma, S. V.; Warmuth, M. Allosteric inhibition of BCR-ABL. *Cell Cycle* **2010**, *9* (18), 3710–3714.
- (62) Abdel-Magid, A. F. Allosteric modulators: an emerging concept in drug discovery. *ACS Med. Chem. Lett.* **2015**, *6* (2), 104–107.
- (63) Leishmaniasis <https://www.who.int/news-room/fact-sheets/detail/leishmaniasis>.
- (64) De Brito, R. C. F.; Aguiar-Soares, R. D. de O.; Cardoso, J. M. de O.; Coura-Vital, W.; Roatt, B. M.; Reis, A. B. Recent advances and new strategies in Leishmaniasis diagnosis. *Appl. Microbiol. Biotechnol.* **2020**, *104* (19), 8105–8116.
- (65) Torres-Guerrero, E.; Quintanilla-Cedillo, M. R.; Ruiz-Esmenjaud, J.; Arenas, R. Leishmaniasis: a review. [version 1; peer review: 2 approved]. *F1000Res.* **2017**, *6*, 750.
- (66) Saccoliti, F.; Di Santo, R.; Costi, R. Recent advancement in the search of innovative antiprotozoal agents targeting trypanothione metabolism. *ChemMedChem* **2020**, *15* (24), 2420–2435.
- (67) Abiri, R.; Abdul-Hamid, H.; Sytar, O.; Abiri, R.; Bezerra de Almeida, E.; Sharma, S. K.; Bulgakov, V. P.; Arroo, R. R. J.; Malik, S. A Brief Overview of Potential Treatments for Viral Diseases Using Natural Plant Compounds: The Case of SARS-Cov. *Molecules* **2021**, *26* (13).
- (68) Rahman, M. M.; Islam, M. R.; Shohag, S.; Hossain, M. E.; Shah, M.; Shuvo, S. K.; Khan, H.; Chowdhury, M. A. R.; Bulbul, I. J.; Hossain, M. S.; et al. Multifaceted role of natural sources for COVID-19 pandemic as marine drugs. *Environ. Sci. Pollut. Res. Int.* **2022**, *29* (31), 46527–46550.
- (69) Soleymani, S.; Naghizadeh, A.; Karimi, M.; Zarei, A.; Mardi, R.; Kordafshari, G.; Esmacalzadeh, N.; Zargarán, A. COVID-19: General Strategies for Herbal Therapies. *J. Evid. Based Integr. Med.* **2022**, *27*, 2515690X211053641.
- (70) Marshall, G. R. Limiting assumptions in molecular modeling: electrostatics. *J. Comput. Aided Mol. Des.* **2013**, *27* (2), 107–114.
- (71) Gao, J. 9.9 quantum mechanical methods for enzyme modeling: accurate computation of kinetic isotope effects. In *Comprehensive Biophysics*; Elsevier, 2012; pp 149–161.



- (72) Alex, A. A. Quantum mechanical calculations in medicinal chemistry: relevant method or a quantum leap too far? In *Comprehensive medicinal chemistry II*; Elsevier, 2007; pp 379–420.
- (73) Kostal, J. Computational chemistry in predictive toxicology; *Advances in molecular toxicology*; Elsevier, 2016; Vol. 10, pp 139–186.
- (74) Wang, Y.; Guo, Y.; Qiang, S.; Jin, R.; Li, Z.; Tang, Y.; Leung, E. L. H.; Guo, H.; Yao, X. 3D-QSAR, Molecular Docking, and MD Simulations of Anthraquinone Derivatives as PGAM1 Inhibitors. *Front. Pharmacol.* **2021**, *12*, 764351.
- (75) Sadeghi, F.; Afkhami, A.; Madrakian, T.; Ghavami, R. QSAR analysis on a large and diverse set of potent phosphoinositide 3-kinase gamma (PI3K $\gamma$ ) inhibitors using MLR and ANN methods. *Sci. Rep.* **2022**, *12* (1), 6090.
- (76) Verkhivker, G. M.; Agajanian, S.; Hu, G.; Tao, P. Allosteric regulation at the crossroads of new technologies: multiscale modeling, networks, and machine learning. *Front. Mol. Biosci.* **2020**, *7*, 136.
- (77) Silva, G. M. da; Yang, J.; Leang, B.; Huang, J.; Weinreich, D. M.; Rubenstein, B. M. Covalent docking and molecular dynamics simulations reveal the specificity-shifting mutations Ala237Arg and Ala237Lys in TEM beta-lactamase. *PLoS Comput. Biol.* **2022**, *18* (6), e1009944.
- (78) Rabe von Pappenheim, F.; Wensien, M.; Ye, J.; Uranga, J.; Irisarri, I.; de Vries, J.; Funk, L.-M.; Mata, R. A.; Tittmann, K. Widespread occurrence of covalent lysine-cysteine redox switches in proteins. *Nat. Chem. Biol.* **2022**, *18* (4), 368–375.
- (79) Murphy, R. B.; Philipp, D. M.; Friesner, R. A. A mixed quantum mechanics/molecular mechanics (QM/MM) method for large-scale modeling of chemistry in protein environments. *J. Comput. Chem.* **2000**.
- (80) Schlick, T.; Portillo-Ledesma, S. Biomolecular modeling thrives in the age of technology. *Nat. Comput. Sci.* **2021**, *1* (5), 321–331.
- (81) Metropolis, N.; Rosenbluth, A. W.; Rosenbluth, M. N.; Teller, A. H.; Teller, E. Equation of state calculations by fast computing machines. *J. Chem. Phys.* **1953**, *21* (6), 1087.
- (82) Owen, A. B.; Tribble, S. D. A quasi-Monte Carlo Metropolis algorithm. *Proc. Natl. Acad. Sci. USA* **2005**, *102* (25), 8844–8849.
- (83) Levitt, M.; Hirshberg, M.; Sharon, R.; Daggett, V. Potential energy function and parameters for simulations of the molecular dynamics of proteins and nucleic acids in solution. *Comput Phys Commun* **1995**, *91* (1-3), 215–231.

- (84) Hu, L.; Ryde, U. Comparison of Methods to Obtain Force-Field Parameters for Metal Sites. *J. Chem. Theory Comput.* **2011**, *7* (8), 2452–2463.
- (85) Visscher, K. M.; Geerke, D. P. Deriving Force-Field Parameters from First Principles Using a Polarizable and Higher Order Dispersion Model. *J. Chem. Theory Comput.* **2019**, *15* (3), 1875–1883.
- (86) Hilborn, R. C. David J. Griffiths: recipient of the Robert A. Millikan Medal. *Am J Phys* **1997**, *65* (12), 1140–1140.
- (87) Wayback Machine  
<https://web.archive.org/web/20081217040121/http://home.tiscali.nl/physis/HistoricPaper/Schroedinger/Schroedinger1926c.pdf>.
- (88) Schöpf, H. G. Mehra, J. / Rechenberg, H., The Historical Development of Quantum Theory. Vol. 1, Part 1 & 2: The Quantum Theory of Planck, Einstein, Bohr and Sommerfeld: Its Foundation and the Rise of Its Difficulties, 1900–1925. Berlin-Heidelberg-New York, Springer-Verlag 1982. Part 1: XLVII, 372 S., DM 75, —. US \$ 31.30. ISBN 3-540-90642-8, Part 2: VI, 506 S., DM 85, —. US \$ 34.00. ISBN 3-540-90667-3. *Z. angew. Math. Mech.* **1983**, *63* (10), 522–522.
- (89) Essentials of Computational Chemistry: Theories and Models, 2nd Edition | Wiley  
<https://www.wiley.com/en-us/Essentials+of+Computational+Chemistry:+Theories+and+Models,+2nd+Edition-p-9780470091821>.
- (90) Schrödinger, E. An Undulatory Theory of the Mechanics of Atoms and Molecules. *Phys. Rev.* **1926**, *28* (6), 1049–1070.
- (91) Lieb, E. H. Thomas-Fermi and Related Theories of Atoms and Molecules. In *Rigorous atomic and molecular physics*; Velo, G., Wightman, A. S., eds.; Springer US: Boston, MA, 1981; pp 213–308.
- (92) Hohenberg, P.; Kohn, W. Inhomogeneous Electron Gas. *Phys. Rev.* **1964**, *136* (3B), B864–B871.
- (93) Kohn, W.; Sham, L. J. Self-Consistent Equations Including Exchange and Correlation Effects. *Phys. Rev.* **1965**, *140* (4A), A1133–A1138.
- (94) Ceperley, D. M.; Alder, B. J. Ground State of the Electron Gas by a Stochastic Method. *Phys. Rev. Lett.* **1980**, *45* (7), 566–569.
- (95) Becke, A. D. Density-functional exchange-energy approximation with correct asymptotic behavior. *Phys. Rev. A, Gen. Phys.* **1988**, *38* (6), 3098–3100.

- 
- (96) Becke, A. D. Density-functional thermochemistry. III. The role of exact exchange. *J. Chem. Phys.* **1993**, *98* (7), 5648.
- (97) Lee, C.; Yang, W.; Parr, R. G. Development of the Colle-Salvetti correlation-energy formula into a functional of the electron density. *Phys. Rev. B, Condens. Matter* **1988**, *37* (2), 785–789.
- (98) Van Lenthe, E.; Baerends, E. J. Optimized Slater-type basis sets for the elements 1-118. *J. Comput. Chem.* **2003**, *24* (9), 1142–1156.
- (99) Aldossary, A.; Head-Gordon, M. Non-iterative method for constructing valence antibonding molecular orbitals and a molecule-adapted minimum basis. *J. Chem. Phys.* **2022**, *157* (9), 094102.
- (100) Ebisawa, S.; Tsutsumi, T.; Taketsugu, T. Extension of natural reaction orbital approach to multiconfigurational wavefunctions. *J. Chem. Phys.* **2022**, *157* (8), 084118.
- (101) Magalhães, A. L. Gaussian-Type Orbitals versus Slater-Type Orbitals: A Comparison. *J. Chem. Educ.* **2014**, *91* (12), 2124–2127.
- (102) Weigend, F.; Ahlrichs, R. Balanced basis sets of split valence, triple zeta valence and quadruple zeta valence quality for H to Rn: Design and assessment of accuracy. *Phys. Chem. Chem. Phys.* **2005**, *7* (18), 3297–3305.
- (103) Schäfer, A.; Horn, H.; Ahlrichs, R. Fully optimized contracted Gaussian basis sets for atoms Li to Kr. *J. Chem. Phys.* **1992**, *97* (4), 2571–2577.
- (104) Li, W.-L.; Chen, K.; Rossomme, E.; Head-Gordon, M.; Head-Gordon, T. Optimized pseudopotentials and basis sets for semiempirical density functional theory for electrocatalysis applications. *J. Phys. Chem. Lett.* **2021**, *12* (42), 10304–10309.
- (105) Vidal, L. N.; Vazquez, P. A. M. Electrically polarized valence basis sets for the SBKJC effective core potential developed for calculations of dynamic polarizabilities and Raman intensities. *Theor. Chem. Acc.* **2012**, *131* (2), 1111.
- (106) Dubbeldam, D.; Walton, K. S.; Vlugt, T. J. H.; Calero, S. Design, parameterization, and implementation of atomic force fields for adsorption in nanoporous materials. *Adv. Theory Simul.* **2019**, *2* (11), 1900135.
- (107) Park, H.; Lee, S. H. Review on interfacial bonding mechanism of functional polymer coating on glass in atomistic modeling perspective. *Polymers (Basel)* **2021**, *13* (14).
- (108) Verlet, L. Computer “Experiments” on Classical Fluids. I. Thermodynamical Properties of Lennard-Jones Molecules. *Phys. Rev.* **1967**, *159* (1), 98–103.
-

- (109) Torrie, G. M.; Valleau, J. P. Monte Carlo free energy estimates using non-Boltzmann sampling: Application to the sub-critical Lennard-Jones fluid. *Chem. Phys. Lett.* **1974**, *28* (4), 578–581.
- (110) Fischer, N. M.; van Maaren, P. J.; Ditz, J. C.; Yildirim, A.; van der Spoel, D. Properties of Organic Liquids when Simulated with Long-Range Lennard-Jones Interactions. *J. Chem. Theory Comput.* **2015**, *11* (7), 2938–2944.
- (111) Kirkwood, J. G. Statistical mechanics of fluid mixtures. *J. Chem. Phys.* **1935**, *3* (5), 300–313.
- (112) Ezra, G. S. On the Statistical Mechanics of Non-Hamiltonian Systems: The Generalized Liouville Equation, Entropy, and Time-Dependent Metrics. *J Math Chem* **2004**, *35* (1), 29–53.
- (113) Hansen, J.-P.; McDonald, I. R. Statistical Mechanics. In *Theory of simple liquids*; Elsevier, 2013; pp 13–59.
- (114) Zheng, L.; Alhossary, A. A.; Kwoh, C.-K.; Mu, Y. Molecular dynamics and simulation. In *Encyclopedia of bioinformatics and computational biology*; Elsevier, 2019; pp 550–566.
- (115) Muralidhar, K. Monte Carlo Simulation. In *Encyclopedia of information systems*; Elsevier, 2003; pp 193–201.
- (116) Spreiter, Q.; Walter, M. Classical Molecular Dynamics Simulation with the Velocity Verlet Algorithm at Strong External Magnetic Fields. *J Comput Phys* **1999**, *152* (1), 102–119.
- (117) Basconi, J. E.; Shirts, M. R. Effects of temperature control algorithms on transport properties and kinetics in molecular dynamics simulations. *J. Chem. Theory Comput.* **2013**, *9* (7), 2887–2899.
- (118) Yong, X.; Zhang, L. T. Thermostats and thermostat strategies for molecular dynamics simulations of nanofluidics. *J. Chem. Phys.* **2013**, *138* (8), 084503.
- (119) Grest, G. S.; Kremer, K. Molecular dynamics simulation for polymers in the presence of a heat bath. *Phys. Rev. A, Gen. Phys.* **1986**, *33* (5), 3628–3631.
- (120) Paquet, E.; Viktor, H. L. Molecular dynamics, monte carlo simulations, and langevin dynamics: a computational review. *Biomed Res. Int.* **2015**, *2015*, 183918.
- (121) Kuksin, A. Y.; Morozov, I. V.; Norman, G. E.; Stegailov, V. V.; Valuev, I. A. Standards for molecular dynamics modelling and simulation of relaxation. *Mol. Simul.* **2005**, *31* (14-15), 1005–1017.

- (122) Cox, S. J. Dielectric response with short-ranged electrostatics. *Proc. Natl. Acad. Sci. USA* **2020**, *117* (33), 19746–19752.
- (123) Essmann, U.; Perera, L.; Berkowitz, M. L.; Darden, T.; Lee, H.; Pedersen, L. G. A smooth particle mesh Ewald method. *J. Chem. Phys.* **1995**, *103* (19), 8577.
- (124) Tzeliou, C. E.; Mermigki, M. A.; Tzeli, D. Review on the QM/MM methodologies and their application to metalloproteins. *Molecules* **2022**, *27* (9).
- (125) (19) (PDF) Multiscale modeling for complex chemical systems: Highlights about the Nobel Prize in Chemistry 2013 [https://www.researchgate.net/publication/287346580\\_Multiscale\\_modeling\\_for\\_complex\\_chemical\\_systems\\_Highlights\\_about\\_the\\_Nobel\\_Prize\\_in\\_Chemistry\\_2013](https://www.researchgate.net/publication/287346580_Multiscale_modeling_for_complex_chemical_systems_Highlights_about_the_Nobel_Prize_in_Chemistry_2013) (accessed Sep 6, 2022).
- (126) Charzewski, Ł.; Krzyśko, K. A.; Lesyng, B. Exploring Covalent Docking Mechanisms of Boron-Based Inhibitors to Class A, C and D  $\beta$ -Lactamases Using Time-dependent Hybrid QM/MM Simulations. *Front. Mol. Biosci.* **2021**, *8*, 633181.
- (127) Trott, O.; Olson, A. J. AutoDock Vina: improving the speed and accuracy of docking with a new scoring function, efficient optimization, and multithreading. *J. Comput. Chem.* **2010**, *31* (2), 455–461.
- (128) Bursulaya, B. D.; Totrov, M.; Abagyan, R.; Brooks, C. L. Comparative study of several algorithms for flexible ligand docking. *J. Comput. Aided Mol. Des.* **2003**, *17* (11), 755–763.
- (129) Jones, G.; Willett, P.; Glen, R. C.; Leach, A. R.; Taylor, R. Development and validation of a genetic algorithm for flexible docking. *J. Mol. Biol.* **1997**, *267* (3), 727–748.
- (130) de Vries, S. J.; van Dijk, M.; Bonvin, A. M. J. J. The HADDOCK web server for data-driven biomolecular docking. *Nat. Protoc.* **2010**, *5* (5), 883–897.
- (131) Cornell, W. D.; Cieplak, P.; Bayly, C. I.; Gould, I. R.; Merz, K. M.; Ferguson, D. M.; Spellmeyer, D. C.; Fox, T.; Caldwell, J. W.; Kollman, P. A. A Second Generation Force Field for the Simulation of Proteins, Nucleic Acids, and Organic Molecules. *J. Am. Chem. Soc.* **1995**, *117* (19), 5179–5197.
- (132) Kairys, V.; Jensen, J. H. QM/MM Boundaries Across Covalent Bonds: A Frozen Localized Molecular Orbital-Based Approach for the Effective Fragment Potential Method. *J. Phys. Chem. A* **2000**, *104* (28), 6656–6665.
- (133) Walker, R. C.; Crowley, M. F.; Case, D. A. The implementation of a fast and accurate QM/MM potential method in Amber. *J. Comput. Chem.* **2008**, *29* (7), 1019–1031.

- (134) Zalloum, W. A.; Zalloum, N. Comparative QM/MM Molecular Dynamics and Umbrella Sampling Simulations: Interaction of the Zinc-Bound Intermediate Gem-Diolate Trapoxin A Inhibitor and Acetyl-L-lysine Substrate with Histone Deacetylase 8. *J. Phys. Chem. B* **2021**, *125* (20), 5321–5337.
- (135) Dietschreit, J. C. B.; von der Esch, B.; Ochsenfeld, C. Exponential averaging versus umbrella sampling for computing the QM/MM free energy barrier of the initial step of the desuccinylation reaction catalyzed by sirtuin 5. *Phys. Chem. Chem. Phys.* **2022**, *24* (13), 7723–7731.
- (136) Šebesta, F.; Šebera, J.; Sychrovský, V.; Tanaka, Y.; Burda, J. V. QM and QM/MM umbrella sampling MD study of the formation of Hg(II)-thymine bond: Model for evaluation of the reaction energy profiles in solutions with constant pH. *J. Comput. Chem.* **2020**, *41* (16), 1509–1520.
- (137) Torrie, G. M.; Valleau, J. P. Nonphysical sampling distributions in Monte Carlo free-energy estimation: Umbrella sampling. *J Comput Phys* **1977**, *23* (2), 187–199.
- (138) Hoof, R. W. W.; van Eijck, B. P.; Kroon, J. An adaptive umbrella sampling procedure in conformational analysis using molecular dynamics and its application to glycol. *J. Chem. Phys.* **1992**, *97* (9), 6690–6694.
- (139) Bartels, C.; Karplus, M. Multidimensional adaptive umbrella sampling: Applications to main chain and side chain peptide conformations. *J. Comput. Chem.* **1997**.
- (140) Souaille, M.; Roux, B. Extension to the weighted histogram analysis method: combining umbrella sampling with free energy calculations. *Comput Phys Commun* **2001**, *135* (1), 40–57.
- (141) Kumar, S.; Rosenberg, J. M.; Bouzida, D.; Swendsen, R. H.; Kollman, P. A. THE weighted histogram analysis method for free-energy calculations on biomolecules. I. The method. *J. Comput. Chem.* **1992**, *13* (8), 1011–1021.
- (142) Li, P.; Merz, K. M. Mcpb.py: A python based metal center parameter builder. *J. Chem. Inf. Model.* **2016**, *56* (4), 599–604.
- (143) Peters, M. B.; Yang, Y.; Wang, B.; Füsti-Molnár, L.; Weaver, M. N.; Merz, K. M. Structural survey of zinc containing proteins and the development of the zinc AMBER force field (ZAFF). *J. Chem. Theory Comput.* **2010**, *6* (9), 2935–2947.
- (144) Li, W.; Wang, J.; Zhang, J.; Wang, W. Molecular simulations of metal-coupled protein folding. *Curr. Opin. Struct. Biol.* **2015**, *30*, 25–31.
- (145) Kollman, P. A.; Massova, I.; Reyes, C.; Kuhn, B.; Huo, S.; Chong, L.; Lee, M.; Lee, T.; Duan, Y.; Wang, W.; et al. Calculating structures and free energies of complex

- molecules: combining molecular mechanics and continuum models. *Acc. Chem. Res.* **2000**, *33* (12), 889–897.
- (146) Genheden, S.; Ryde, U. The MM/PBSA and MM/GBSA methods to estimate ligand-binding affinities. *Expert Opin. Drug Discov.* **2015**, *10* (5), 449–461.
- (147) Gohlke, H.; Case, D. A. Converging free energy estimates: MM-PB(GB)SA studies on the protein-protein complex Ras-Raf. *J. Comput. Chem.* **2004**, *25* (2), 238–250.
- (148) Levine, B. G.; Stone, J. E.; Kohlmeyer, A. Fast Analysis of Molecular Dynamics Trajectories with Graphics Processing Units-Radial Distribution Function Histogramming. *J Comput Phys* **2011**, *230* (9), 3556–3569.
- (149) Raza, S.; Azam, S. S. AFD: an application for bi-molecular interaction using axial frequency distribution. *J Mol Model* **2018**, *24* (4), 84.
- (150) Lister, P. D.; Wolter, D. J.; Hanson, N. D. Antibacterial-resistant *Pseudomonas aeruginosa*: Clinical impact and complex regulation of chromosomally encoded resistance mechanisms. *Clin. Microbiol. Rev.* **2009**, *22* (4), 582–610.
- (151) Azam, M. W.; Khan, A. U. Updates on the pathogenicity status of *Pseudomonas aeruginosa*. *Drug Discov. Today* **2019**, *24* (1), 350–359.
- (152) Xie, Y.; Chen, J.; Wang, B.; Peng, A.-Y.; Mao, Z.-W.; Xia, W. Inhibition of Quorum-Sensing Regulator from *Pseudomonas aeruginosa* Using a Flavone Derivative. *Molecules* **2022**, *27* (8).
- (153) Moura-Alves, P.; Puyskens, A.; Stinn, A.; Klemm, M.; Gühlich-Bornhof, U.; Dorhoi, A.; Furkert, J.; Kreuchwig, A.; Protze, J.; Lozza, L.; et al. Host monitoring of quorum sensing during *Pseudomonas aeruginosa* infection. *Science* **2019**, *366* (6472).
- (154) Zhou, L.; Zhang, Y.; Ge, Y.; Zhu, X.; Pan, J. Regulatory Mechanisms and Promising Applications of Quorum Sensing-Inhibiting Agents in Control of Bacterial Biofilm Formation. *Front. Microbiol.* **2020**, *11*, 589640.
- (155) Marshall, H. E.; Merchant, K.; Stamler, J. S. Nitrosation and oxidation in the regulation of gene expression. *FASEB J.* **2000**, *14* (13), 1889–1900.
- (156) Green, J.; Paget, M. S. Bacterial redox sensors. *Nat. Rev. Microbiol.* **2004**, *2* (12), 954–966.
- (157) Delaunay, A.; Pflieger, D.; Barrault, M. B.; Vinh, J.; Toledano, M. B. A thiol peroxidase is an H<sub>2</sub>O<sub>2</sub> receptor and redox-transducer in gene activation. *Cell* **2002**, *111* (4), 471–481.

- (158) Storz, G.; Tartaglia, L. A.; Ames, B. N. Transcriptional regulator of oxidative stress-inducible genes: direct activation by oxidation. *Science* **1990**, *248* (4952), 189–194.
- (159) Zheng, M.; Aslund, F.; Storz, G. Activation of the OxyR transcription factor by reversible disulfide bond formation. *Science* **1998**, *279* (5357), 1718–1721.
- (160) Hausladen, A.; Privalle, C. T.; Keng, T.; DeAngelo, J.; Stamler, J. S. Nitrosative stress: activation of the transcription factor OxyR. *Cell* **1996**, *86* (5), 719–729.
- (161) Jo, I.; Chung, I.-Y.; Bae, H.-W.; Kim, J.-S.; Song, S.; Cho, Y.-H.; Ha, N.-C. Structural details of the OxyR peroxide-sensing mechanism. *Proc. Natl. Acad. Sci. USA* **2015**, *112* (20), 6443–6448.
- (162) Kullik, I.; Toledano, M. B.; Tartaglia, L. A.; Storz, G. Mutational analysis of the redox-sensitive transcriptional regulator OxyR: regions important for oxidation and transcriptional activation. *J. Bacteriol.* **1995**, *177* (5), 1275–1284.
- (163) Aslund, F.; Zheng, M.; Beckwith, J.; Storz, G. Regulation of the OxyR transcription factor by hydrogen peroxide and the cellular thiol-disulfide status. *Proc. Natl. Acad. Sci. USA* **1999**, *96* (11), 6161–6165.
- (164) Kim, S. O.; Merchant, K.; Nudelman, R.; Beyer, W. F.; Keng, T.; DeAngelo, J.; Hausladen, A.; Stamler, J. S. OxyR: a molecular code for redox-related signaling. *Cell* **2002**, *109* (3), 383–396.
- (165) Paulsen, C. E.; Truong, T. H.; Garcia, F. J.; Homann, A.; Gupta, V.; Leonard, S. E.; Carroll, K. S. Peroxide-dependent sulfenylation of the EGFR catalytic site enhances kinase activity. *Nat. Chem. Biol.* **2011**, *8* (1), 57–64.
- (166) Truong, T. H.; Ung, P. M.-U.; Palde, P. B.; Paulsen, C. E.; Schlessinger, A.; Carroll, K. S. Molecular basis for redox activation of epidermal growth factor receptor kinase. *Cell Chem. Biol.* **2016**, *23* (7), 837–848.
- (167) Wind, S.; Schmid, M.; Erhardt, J.; Goeldner, R.-G.; Stopfer, P. Pharmacokinetics of afatinib, a selective irreversible ErbB family blocker, in patients with advanced solid tumours. *Clin Pharmacokinet* **2013**, *52* (12), 1101–1109.
- (168) Kim, Y.; Lovell, S.; Tiew, K.-C.; Mandadapu, S. R.; Alliston, K. R.; Battaile, K. P.; Groutas, W. C.; Chang, K.-O. Broad-spectrum antivirals against 3C or 3C-like proteases of picornaviruses, noroviruses, and coronaviruses. *J. Virol.* **2012**, *86* (21), 11754–11762.
- (169) Martí, S.; Arafet, K.; Lodola, A.; Mulholland, A. J.; Świderek, K.; Moliner, V. Impact of Warhead Modulations on the Covalent Inhibition of SARS-CoV-2 Mpro Explored by QM/MM Simulations. *ACS Catal.* **2022**, *12* (1), 698–708.



- (170) Yoshimori, A.; Miljković, F.; Bajorath, J. Approach for the design of covalent protein kinase inhibitors via focused deep generative modeling. *Molecules* **2022**, *27* (2).
- (171) Gehringer, M.; Laufer, S. A. Emerging and Re-Emerging Warheads for Targeted Covalent Inhibitors: Applications in Medicinal Chemistry and Chemical Biology. *J. Med. Chem.* **2019**, *62* (12), 5673–5724.
- (172) Hoffman, R. L.; Kania, R. S.; Brothers, M. A.; Davies, J. F.; Ferre, R. A.; Gajiwala, K. S.; He, M.; Hogan, R. J.; Kozminski, K.; Li, L. Y.; et al. Discovery of Ketone-Based Covalent Inhibitors of Coronavirus 3CL Proteases for the Potential Therapeutic Treatment of COVID-19. *J. Med. Chem.* **2020**, *63* (21), 12725–12747.
- (173) Pedre, B.; Young, D.; Charlier, D.; Mourenza, Á.; Rosado, L. A.; Marcos-Pascual, L.; Wahni, K.; Martens, E.; G de la Rubia, A.; Belousov, V. V.; et al. Structural snapshots of OxyR reveal the peroxidatic mechanism of H<sub>2</sub>O<sub>2</sub> sensing. *Proc. Natl. Acad. Sci. USA* **2018**, *115* (50), E11623–E11632.
- (174) Choi, H.; Kim, S.; Mukhopadhyay, P.; Cho, S.; Woo, J.; Storz, G.; Ryu, S. E. Structural basis of the redox switch in the OxyR transcription factor. *Cell* **2001**, *105* (1), 103–113.
- (175) Wan, F.; Shi, M.; Gao, H. Loss of OxyR reduces efficacy of oxygen respiration in *Shewanella oneidensis*. *Sci. Rep.* **2017**, *7*, 42609.
- (176) Oh, H.-Y.; Jalde, S. S.; Chung, I.-Y.; Yoo, Y.-J.; Jang, H.-J.; Choi, H.-K.; Cho, Y.-H. An antipathogenic compound that targets the OxyR peroxide sensor in *Pseudomonas aeruginosa*. *J. Med. Microbiol.* **2021**, *70* (4).
- (177) Singh, J.; Petter, R. C.; Baillie, T. A.; Whitty, A. The resurgence of covalent drugs. *Nat. Rev. Drug Discov.* **2011**, *10* (4), 307–317.
- (178) Copeland, R. A.; Pompliano, D. L.; Meek, T. D. Drug-target residence time and its implications for lead optimization. *Nat. Rev. Drug Discov.* **2006**, *5* (9), 730–739.
- (179) Tonge, P. J. Drug-Target Kinetics in Drug Discovery. *ACS Chem. Neurosci.* **2018**, *9* (1), 29–39.
- (180) Long, M. J. C.; Aye, Y. Privileged electrophile sensors: A resource for covalent drug development. *Cell Chem. Biol.* **2017**, *24* (7), 787–800.
- (181) Zhang, T.; Hatcher, J. M.; Teng, M.; Gray, N. S.; Kostic, M. Recent advances in selective and irreversible covalent ligand development and validation. *Cell Chem. Biol.* **2019**, *26* (11), 1486–1500.

- (182) Jin, Z.; Du, X.; Xu, Y.; Deng, Y.; Liu, M.; Zhao, Y.; Zhang, B.; Li, X.; Zhang, L.; Peng, C.; et al. Structure of Mpro from SARS-CoV-2 and discovery of its inhibitors. *Nature* **2020**, *582* (7811), 289–293.
- (183) Yang, H.; Xie, W.; Xue, X.; Yang, K.; Ma, J.; Liang, W.; Zhao, Q.; Zhou, Z.; Pei, D.; Ziebuhr, J.; et al. Design of wide-spectrum inhibitors targeting coronavirus main proteases. *PLoS Biol.* **2005**, *3* (10), e324.
- (184) Zhang, L.; Lin, D.; Sun, X.; Curth, U.; Drosten, C.; Sauerhering, L.; Becker, S.; Rox, K.; Hilgenfeld, R. Crystal structure of SARS-CoV-2 main protease provides a basis for design of improved  $\alpha$ -ketoamide inhibitors. *Science* **2020**, *368* (6489), 409–412.
- (185) Kummari, L. K.; Butler, M. S.; Furlong, E.; Blundell, R.; Nouwens, A.; Silva, A. B.; Kappler, U.; Fraser, J. A.; Kobe, B.; Cooper, M. A.; et al. Antifungal benzo[b]thiophene 1,1-dioxide IMPDH inhibitors exhibit pan-assay interference (PAINS) profiles. *Bioorg. Med. Chem.* **2018**, *26* (20), 5408–5419.
- (186) Kastrati, I.; Siklos, M. I.; Calderon-Gierszal, E. L.; El-Shennawy, L.; Georgieva, G.; Thayer, E. N.; Thatcher, G. R. J.; Frasca, J. Dimethyl fumarate inhibits the nuclear factor  $\kappa$ B pathway in breast cancer cells by covalent modification of p65 protein. *J. Biol. Chem.* **2016**, *291* (7), 3639–3647.
- (187) Rosa, A. C.; Benetti, E.; Gallicchio, M.; Boscaro, V.; Cangemi, L.; Dianzani, C.; Miglio, G. Analyzing cysteine site neighbors in proteins to reveal dimethyl fumarate targets. *Proteomics* **2019**, *19* (4), e1800301.
- (188) Bevilacqua, P. C.; Brown, T. S.; Nakano, S.; Yajima, R. Catalytic roles for proton transfer and protonation in ribozymes. *Biopolymers* **2004**, *73* (1), 90–109.
- (189) Mikulski, R. L.; Silverman, D. N. Proton transfer in catalysis and the role of proton shuttles in carbonic anhydrase. *Biochim. Biophys. Acta* **2010**, *1804* (2), 422–426.
- (190) BIOVIA Discovery Studio - BIOVIA - Dassault Systèmes® <https://www.3ds.com/products-services/biovia/products/molecular-modeling-simulation/biovia-discovery-studio/>.
- (191) ChemBridge | Screening Libraries | Targeted & Focused Libraries [https://www.chembridge.com/screening\\_libraries/targeted\\_libraries/index.php](https://www.chembridge.com/screening_libraries/targeted_libraries/index.php)
- (192) Asinex Covalent Library with over 50k molecules now available for SeeSAR • BioSolveIT <https://www.biosolveit.de/2021/09/20/asinex-covalent-library-with-over-50k-molecules-now-available-for-seesar/>
- (193) ZINC <https://zinc15.docking.org/substances/having/trials+patterns/subsets/trials.current+patterns.pains/>

- (194) Jones, G.; Willett, P.; Glen, R. C. Molecular recognition of receptor sites using a genetic algorithm with a description of desolvation. *J. Mol. Biol.* **1995**, *245* (1), 43–53.
- (195) HADDOCK Web Server <https://wenmr.science.uu.nl/haddock2.4/> (accessed Jul 23, 2022).
- (196) Altmann, E.; Cowan-Jacob, S. W.; Missbach, M. Novel purine nitrile derived inhibitors of the cysteine protease cathepsin K. *J. Med. Chem.* **2004**, *47* (24), 5833–5836.
- (197) Świderek, K.; Moliner, V. Revealing the molecular mechanisms of proteolysis of SARS-CoV-2 Mpro by QM/MM computational methods. *Chem. Sci.* **2020**, *11* (39), 10626–10630.
- (198) Arafet, K.; Ferrer, S.; Moliner, V. Computational study of the catalytic mechanism of the cruzain cysteine protease. *ACS Catal.* **2017**, *7* (2), 1207–1215.
- (199) Arafet, K.; González, F. V.; Moliner, V. Elucidating the dual mode of action of dipeptidyl enoates in the inhibition of rhodesain cysteine proteases. *Chem. Eur. J* **2021**, *27* (39), 10142–10150.
- (200) Kóna, J.; Brinck, T. A combined molecular dynamics simulation and quantum chemical study on the mechanism for activation of the OxyR transcription factor by hydrogen peroxide. *Org. Biomol. Chem.* **2006**, *4* (18), 3468–3478.
- (201) Chen, H.; Xu, G.; Zhao, Y.; Tian, B.; Lu, H.; Yu, X.; Xu, Z.; Ying, N.; Hu, S.; Hua, Y. A novel OxyR sensor and regulator of hydrogen peroxide stress with one cysteine residue in *Deinococcus radiodurans*. *PLoS One* **2008**, *3* (2), e1602.
- (202) Teramoto, H.; Inui, M.; Yukawa, H. OxyR acts as a transcriptional repressor of hydrogen peroxide-inducible antioxidant genes in *Corynebacterium glutamicum* R. *FEBS J.* **2013**, *280* (14), 3298–3312.
- (203) Kim, J.-S.; Holmes, R. K. Characterization of OxyR as a negative transcriptional regulator that represses catalase production in *Corynebacterium diphtheriae*. *PLoS One* **2012**, *7* (3), e31709.
- (204) Kumar, D.; Sastry, G. N.; de Visser, S. P. Effect of the axial ligand on substrate sulfoxidation mediated by iron(IV)-oxo porphyrin cation radical oxidants. *Chem. Eur. J* **2011**, *17* (22), 6196–6205.
- (205) Quesne, M. G.; Ward, R. A.; de Visser, S. P. Cysteine protease inhibition by nitrile-based inhibitors: a computational study. *Front. Chem.* **2013**, *1*, 39.
- (206) Ferreira, J. C.; Fadl, S.; Villanueva, A. J.; Rabeh, W. M. Catalytic Dyad Residues His41 and Cys145 Impact the Catalytic Activity and Overall Conformational Fold of the

- 
- Main SARS-CoV-2 Protease 3-Chymotrypsin-Like Protease. *Front. Chem.* **2021**, *9*, 692168.
- (207) Terenin, A.; Kariakin, A. Proton transfer between organic molecules caused by light. *Nature* **1947**, *159* (4052), 881.
- (208) Reece, S. Y.; Nocera, D. G. Proton-coupled electron transfer in biology: results from synergistic studies in natural and model systems. *Annu. Rev. Biochem.* **2009**, *78*, 673–699.
- (209) Chansen, W.; Kungwan, N. Theoretical Insights into Excited-State Intermolecular Proton Transfers of 2,7-Diazaindole in Water Using a Microsolvation Approach. *J. Phys. Chem. A* **2021**, *125* (24), 5314–5325.
- (210) Srivastava, R. The role of proton transfer on mutations. *Front. Chem.* **2019**, *7*, 536.
- (211) Beceiro, A.; Tomás, M.; Bou, G. Antimicrobial resistance and virulence: a successful or deleterious association in the bacterial world? *Clin. Microbiol. Rev.* **2013**, *26* (2), 185–230.
- (212) Miller, M. B.; Bassler, B. L. Quorum sensing in bacteria. *Annu. Rev. Microbiol.* **2001**, *55*, 165–199.
- (213) Tang, H.; Zhang, Y.; Ma, Y.; Tang, M.; Shen, D.; Wang, M. Regulation of Nicotine Tolerance by Quorum Sensing and High Efficiency of Quorum Quenching Under Nicotine Stress in *Pseudomonas aeruginosa* PAO1. *Front. Cell Infect. Microbiol.* **2018**, *8*, 88.
- (214) Hentzer, M.; Wu, H.; Andersen, J. B.; Riedel, K.; Rasmussen, T. B.; Bagge, N.; Kumar, N.; Schembri, M. A.; Song, Z.; Kristoffersen, P.; et al. Attenuation of *Pseudomonas aeruginosa* virulence by quorum sensing inhibitors. *EMBO J.* **2003**, *22* (15), 3803–3815.
- (215) Hall-Stoodley, L.; Costerton, J. W.; Stoodley, P. Bacterial biofilms: from the natural environment to infectious diseases. *Nat. Rev. Microbiol.* **2004**, *2* (2), 95–108.
- (216) Huedo, P.; Coves, X.; Daura, X.; Gibert, I.; Yero, D. Quorum Sensing Signaling and Quenching in the Multidrug-Resistant Pathogen *Stenotrophomonas maltophilia*. *Front. Cell Infect. Microbiol.* **2018**, *8*, 122.
- (217) Ryan, R. P.; An, S.; Allan, J. H.; McCarthy, Y.; Dow, J. M. The DSF Family of Cell-Cell Signals: An Expanding Class of Bacterial Virulence Regulators. *PLoS Pathog.* **2015**, *11* (7), e1004986.
- (218) Davies, D. G.; Marques, C. N. H. A fatty acid messenger is responsible for inducing dispersion in microbial biofilms. *J. Bacteriol.* **2009**, *191* (5), 1393–1403.

- (219) Amari, D. T.; Marques, C. N. H.; Davies, D. G. The putative enoyl-coenzyme A hydratase DspI is required for production of the *Pseudomonas aeruginosa* biofilm dispersion autoinducer cis-2-decenoic acid. *J. Bacteriol.* **2013**, *195* (20), 4600–4610.
- (220) Hamed, R. B.; Batchelar, E. T.; Clifton, I. J.; Schofield, C. J. Mechanisms and structures of crotonase superfamily enzymes--how nature controls enolate and oxyanion reactivity. *Cell Mol. Life Sci.* **2008**, *65* (16), 2507–2527.
- (221) Holden, H. M.; Benning, M. M.; Haller, T.; Gerlt, J. A. The crotonase superfamily: divergently related enzymes that catalyze different reactions involving acyl coenzyme a thioesters. *Acc. Chem. Res.* **2001**, *34* (2), 145–157.
- (222) Modis, Y.; Filppula, S. A.; Novikov, D. K.; Norledge, B.; Hiltunen, J. K.; Wierenga, R. K. The crystal structure of dienoyl-CoA isomerase at 1.5 Å resolution reveals the importance of aspartate and glutamate sidechains for catalysis. *Structure* **1998**, *6* (8), 957–970.
- (223) Liu, L.; Li, T.; Cheng, X.-J.; Peng, C.-T.; Li, C.-C.; He, L.-H.; Ju, S.-M.; Wang, N.-Y.; Ye, T.-H.; Lian, M.; et al. Structural and functional studies on *Pseudomonas aeruginosa* DspI: implications for its role in DSF biosynthesis. *Sci. Rep.* **2018**, *8* (1), 3928.
- (224) Roca, C.; Requena, C.; Sebastián-Pérez, V.; Malhotra, S.; Radoux, C.; Pérez, C.; Martínez, A.; Antonio Páez, J.; Blundell, T. L.; Campillo, N. E. Identification of new allosteric sites and modulators of AChE through computational and experimental tools. *J Enzyme Inhib Med Chem* **2018**, *33* (1), 1034–1047.
- (225) Lu, S.; Huang, W.; Zhang, J. Recent computational advances in the identification of allosteric sites in proteins. *Drug Discov. Today* **2014**, *19* (10), 1595–1600.
- (226) Parvaiz, N.; Abbasi, S. W.; Uddin, R.; Azam, S. S. Targeting isoprenoid biosynthesis pathway in *Staphylococcus lugdunensis*: Comparative docking and simulation studies of conventional and allosteric sites. *J Mol Liq* **2018**, *269*, 426–440.
- (227) Meisel, J. E.; Fisher, J. F.; Chang, M.; Mobashery, S. Allosteric inhibition of bacterial targets: an opportunity for discovery of novel antibacterial classes. In *Antibacterials*; Fisher, J. F., Mobashery, S., Miller, M. J., eds.; Topics in medicinal chemistry; Springer International Publishing: Cham, 2018; Vol. 25, pp 119–147.
- (228) Baseer, S.; Ahmad, S.; Ranaghan, K. E.; Azam, S. S. Towards a peptide-based vaccine against *Shigella sonnei*: A subtractive reverse vaccinology based approach. *Biologicals* **2017**, *50*, 87–99.
- (229) Ahmad, S.; Navid, A.; Akhtar, A. S.; Azam, S. S.; Wadood, A.; Pérez-Sánchez, H. Subtractive Genomics, Molecular Docking and Molecular Dynamics Simulation Revealed LpxC as a Potential Drug Target Against Multi-Drug Resistant *Klebsiella pneumoniae*. *Interdiscip Sci* **2018**.

- (230) Groom, C. R.; Bruno, I. J.; Lightfoot, M. P.; Ward, S. C. The cambridge structural database. *Acta Crystallogr. B, Struct. Sci. Cryst. Eng. Mater.* **2016**, *72* (Pt 2), 171–179.
- (231) Lipinski, C. A. Lead- and drug-like compounds: the rule-of-five revolution. *Drug Discov. Today. Technol.* **2004**, *1* (4), 337–341.
- (232) Daina, A.; Michielin, O.; Zoete, V. SwissADME: a free web tool to evaluate pharmacokinetics, drug-likeness and medicinal chemistry friendliness of small molecules. *Sci. Rep.* **2017**, *7*, 42717.
- (233) Halgren, T. A. Merck molecular force field. III. Molecular geometries and vibrational frequencies for MMFF94. *J. Comput. Chem.* **1996**, *17* (5-6), 553–586.
- (234) Humphrey, W.; Dalke, A.; Schulten, K. VMD: visual molecular dynamics. *J Mol Graph* **1996**, *14* (1), , 27.
- (235) Wallace, A. C.; Laskowski, R. A.; Thornton, J. M. LIGPLOT: a program to generate schematic diagrams of protein-ligand interactions. *Protein Eng Des Sel* **1995**, *8* (2), 127–134.
- (236) Pettersen, E. F.; Goddard, T. D.; Huang, C. C.; Couch, G. S.; Greenblatt, D. M.; Meng, E. C.; Ferrin, T. E. UCSF Chimera—a visualization system for exploratory research and analysis. *J. Comput. Chem.* **2004**, *25* (13), 1605–1612.
- (237) Le Guilloux, V.; Schmidtke, P.; Tuffery, P. Fpocket: an open source platform for ligand pocket detection. *BMC Bioinformatics* **2009**, *10*, 168.
- (238) Xu, Y.; Wang, S.; Hu, Q.; Gao, S.; Ma, X.; Zhang, W.; Shen, Y.; Chen, F.; Lai, L.; Pei, J. CavityPlus: a web server for protein cavity detection with pharmacophore modelling, allosteric site identification and covalent ligand binding ability prediction. *Nucleic Acids Res.* **2018**, *46* (W1), W374–W379.
- (239) Pearlman, D. A.; Case, D. A.; Caldwell, J. W.; Ross, W. S.; Cheatham, T. E.; DeBolt, S.; Ferguson, D.; Seibel, G.; Kollman, P. AMBER, a package of computer programs for applying molecular mechanics, normal mode analysis, molecular dynamics and free energy calculations to simulate the structural and energetic properties of molecules. *Comput Phys Commun* **1995**, *91* (1-3), 1–41.
- (240) Salomon-Ferrer, R.; Case, D. A.; Walker, R. C. An overview of the Amber biomolecular simulation package. *WIREs Comput Mol Sci* **2013**, *3* (2), 198–210.
- (241) Pastor, R. W.; Brooks, B. R.; Szabo, A. An analysis of the accuracy of Langevin and molecular dynamics algorithms. *Mol. Phys.* **1988**, *65* (6), 1409–1419.

- (242) Kräutler, V.; van Gunsteren, W. F.; Hünenberger, P. H. A fast SHAKE algorithm to solve distance constraint equations for small molecules in molecular dynamics simulations - Semantic Scholar. *undefined* **2001**.
- (243) Andersen, H. C. Molecular dynamics simulations at constant pressure and/or temperature. *J. Chem. Phys.* **1980**, *72* (4), 2384.
- (244) Roe, D. R.; Cheatham, T. E. PTRAJ and CPPTRAJ: software for processing and analysis of molecular dynamics trajectory data. *J. Chem. Theory Comput.* **2013**, *9* (7), 3084–3095.
- (245) Kokh, D. B.; Richter, S.; Henrich, S.; Czodrowski, P.; Rippmann, F.; Wade, R. C. TRAPP: a tool for analysis of transient binding pockets in proteins. *J. Chem. Inf. Model.* **2013**, *53* (5), 1235–1252.
- (246) Liu, H.-Y.; Zou, X. Electrostatics of ligand binding: parameterization of the generalized Born model and comparison with the Poisson-Boltzmann approach. *J. Phys. Chem. B* **2006**, *110* (18), 9304–9313.
- (247) Kitao, T.; Lepine, F.; Babloui, S.; Walte, F.; Steinbacher, S.; Maskos, K.; Blaesse, M.; Negri, M.; Pucci, M.; Zahler, B.; et al. Molecular Insights into Function and Competitive Inhibition of *Pseudomonas aeruginosa* Multiple Virulence Factor Regulator. *MBio* **2018**, *9* (1).
- (248) Srivastava, S.; Chaudhary, S.; Thukral, L.; Shi, C.; Gupta, R. D.; Gupta, R.; Priyadarshan, K.; Vats, A.; Haque, A. S.; Sankaranarayanan, R.; et al. Unsaturated Lipid Assimilation by Mycobacteria Requires Auxiliary cis-trans Enoyl CoA Isomerase. *Chem. Biol.* **2015**, *22* (12), 1577–1587.
- (249) V, S.; K, R. Role of the Cation- $\pi$  Interaction in Therapeutic Proteins: A Comparative Study with Conventional Stabilizing Forces. *J Comput Sci Syst Biol* **2009**, *02* (01).
- (250) Dougherty, D. A. The cation- $\pi$  interaction. *Acc. Chem. Res.* **2013**, *46* (4), 885–893.
- (251) Gung, B. W.; Wekesa, F.; Barnes, C. L. Stacking interactions between nitrogen-containing six-membered heterocyclic aromatic rings and substituted benzene: studies in solution and in the solid state. *J. Org. Chem.* **2008**, *73* (5), 1803–1808.
- (252) Alberts, B.; Johnson, A.; Lewis, J.; Raff, M.; Roberts, K.; Walter, P. Protein Function. **2002**.
- (253) Yuan, Y.; Pei, J.; Lai, L. Binding site detection and druggability prediction of protein targets for structure-based drug design. *Curr. Pharm. Des.* **2013**, *19* (12), 2326–2333.

- (254) Karplus, M.; Kuriyan, J. Molecular dynamics and protein function. *Proc. Natl. Acad. Sci. USA* **2005**, *102* (19), 6679–6685.
- (255) Suprun, A. D.; Shmeleva, L. V. Alpha-helical regions of the protein molecule as organic nanotubes. *Nanoscale Res. Lett.* **2014**, *9* (1), 200.
- (256) Alberts, B.; Johnson, A.; Lewis, J.; Raff, M.; Roberts, K.; Walter, P. The Shape and Structure of Proteins. **2002**.
- (257) Lobanov, M. Y.; Bogatyreva, N. S.; Galzitskaya, O. V. Radius of gyration as an indicator of protein structure compactness. *Mol. Biol. (N.Y.)* **2008**, *42* (4), 623–628.
- (258) Hou, T.; Wang, J.; Li, Y.; Wang, W. Assessing the performance of the MM/PBSA and MM/GBSA methods. 1. The accuracy of binding free energy calculations based on molecular dynamics simulations. *J. Chem. Inf. Model.* **2011**, *51* (1), 69–82.
- (259) Barth, A. The infrared absorption of amino acid side chains. *Prog. Biophys. Mol. Biol.* **2000**, *74* (3-5), 141–173.
- (260) Grifferty, G.; Shirley, H.; McGloin, J.; Kahn, J.; Orriols, A.; Wamai, R. Vulnerabilities to and the socioeconomic and psychosocial impacts of the leishmaniasis: A review. *Res. Rep. Trop. Med.* **2021**, *12*, 135–151.
- (261) Gedda, M. R.; Singh, B.; Kumar, D.; Singh, A. K.; Madhukar, P.; Upadhyay, S.; Singh, O. P.; Sundar, S. Post kala-azar dermal leishmaniasis: A threat to elimination program. *PLoS Negl. Trop. Dis.* **2020**, *14* (7), e0008221.
- (262) Sasidharan, S.; Saudagar, P. Leishmaniasis: where are we and where are we heading? *Parasitol. Res.* **2021**, *120* (5), 1541–1554.
- (263) Carter, N. S.; Kawasaki, Y.; Nahata, S. S.; Elikae, S.; Rajab, S.; Salam, L.; Alabdulal, M. Y.; Broessel, K. K.; Foroghi, F.; Abbas, A.; et al. Polyamine metabolism in leishmania parasites: A promising therapeutic target. *Med Sci (Basel)* **2022**, *10* (2).
- (264) Talevi, A.; Carrillo, C.; Comini, M. The Thiol-polyamine Metabolism of *Trypanosoma cruzi*: Molecular Targets and Drug Repurposing Strategies. *Curr. Med. Chem.* **2019**, *26* (36), 6614–6635.
- (265) Jain, S.; Sahu, U.; Kumar, A.; Khare, P. Metabolic pathways of leishmania parasite: source of pertinent drug targets and potent drug candidates. *Pharmaceutics* **2022**, *14* (8), 1590.
- (266) Leroux, A. E.; Krauth-Siegel, R. L. Thiol redox biology of trypanosomatids and potential targets for chemotherapy. *Mol. Biochem. Parasitol.* **2016**, *206* (1-2), 67–74.



- (267) Trypanosomatid Diseases: Molecular Routes to Drug Discovery | Wiley <https://www.wiley.com/enie/Trypanosomatid+Diseases:+Molecular+Routes+to+Drug+Discovery-p-9783527670406>
- (268) Flohé, L. The trypanothione system and the opportunities it offers to create drugs for the neglected kinetoplast diseases. *Biotechnol. Adv.* **2012**, *30* (1), 294–301.
- (269) Colotti, G.; Baiocco, P.; Fiorillo, A.; Boffi, A.; Poser, E.; Chiaro, F. D.; Ilari, A. Structural insights into the enzymes of the trypanothione pathway: targets for antileishmaniasis drugs. *Future Med. Chem.* **2013**, *5* (15), 1861–1875.
- (270) Berman, J. Amphotericin B formulations and other drugs for visceral leishmaniasis. *Am. J. Trop. Med. Hyg.* **2015**, *92* (3), 471–473.
- (271) Kumari, D.; Perveen, S.; Sharma, R.; Singh, K. Advancement in leishmaniasis diagnosis and therapeutics: An update. *Eur. J. Pharmacol.* **2021**, *910*, 174436.
- (272) Babokhov, P.; Sanyaolu, A. O.; Oyibo, W. A.; Fagbenro-Beyioku, A. F.; Iriemenam, N. C. A current analysis of chemotherapy strategies for the treatment of human African trypanosomiasis. *Pathog. Glob. Health* **2013**, *107* (5), 242–252.
- (273) Bisceglia, J. A.; Mollo, M. C.; Gruber, N.; Orelli, L. R. Polyamines and related nitrogen compounds in the chemotherapy of neglected diseases caused by kinetoplastids. *Curr. Top. Med. Chem.* **2018**, *18* (5), 321–368.
- (274) Decuypere, S.; Rijal, S.; Yardley, V.; De Doncker, S.; Laurent, T.; Khanal, B.; Chappuis, F.; Dujardin, J.-C. Gene expression analysis of the mechanism of natural Sb(V) resistance in *Leishmania donovani* isolates from Nepal. *Antimicrob. Agents Chemother.* **2005**, *49* (11), 4616–4621.
- (275) Jones, C. M.; Welburn, S. C.; Jones, J. D. Treatment failure of pentavalent antimonial therapy for human visceral leishmaniasis: a meta-analysis. *J. Glob. Health Rep.* **2019**, *3*.
- (276) Ponte-Sucre, A.; Gamarro, F.; Dujardin, J.-C.; Barrett, M. P.; López-Vélez, R.; García-Hernández, R.; Pountain, A. W.; Mwenechanya, R.; Papadopoulou, B. Drug resistance and treatment failure in leishmaniasis: A 21st century challenge. *PLoS Negl. Trop. Dis.* **2017**, *11* (12), e0006052.
- (277) Hendrickx, S.; Guerin, P. J.; Caljon, G.; Croft, S. L.; Maes, L. Evaluating drug resistance in visceral leishmaniasis: the challenges. *Parasitology* **2018**, *145* (4), 453–463.
- (278) Ong, Y. C.; Kedzierski, L.; Andrews, P. C. Do bismuth complexes hold promise as antileishmanial drugs? *Future Med. Chem.* **2018**, *10* (14), 1721–1733.

- (279) Salvador, J. A. R.; Figueiredo, S. A. C.; Pinto, R. M. A.; Silvestre, S. M. Bismuth compounds in medicinal chemistry. *Future Med. Chem.* **2012**, *4* (11), 1495–1523.
- (280) Mehmood, M.; Imtiaz-ud-Din; Abbas, S.; Azam, S. S.; Ihsan-ul-Haq; Tahir, M. N.; Parvaiz, N.; Tameez Ud Din, A. Bioactive heteroleptic Bismuth(V) carboxylates: Synthetic Stratagem, characterization and binding pattern validation. *J. Organomet. Chem* **2020**, *921*, 121357.
- (281) Basselin, M.; Lawrence, F.; Robert-Gero, M. Pentamidine uptake in *Leishmania donovani* and *Leishmania amazonensis* promastigotes and axenic amastigotes. *Biochem. J.* **1996**, *315* (Pt 2), 631–634.
- (282) Tiphine, M.; Letscher-Bru, V.; Herbrecht, R. Amphotericin B and its new formulations: pharmacologic characteristics, clinical efficacy, and tolerability. *Transpl Infect Dis* **1999**, *1* (4), 273–283.
- (283) Bang, C. S.; Lim, H.; Jeong, H. M.; Shin, W. G.; Choi, J. H.; Soh, J. S.; Kang, H. S.; Yang, Y. J.; Hong, J. T.; Shin, S. P.; et al. Amoxicillin or tetracycline in bismuth-containing quadruple therapy as first-line treatment for *Helicobacter pylori* infection. *Gut Microbes* **2020**, 1–10.
- (284) Alkim, H.; Koksall, A. R.; Boga, S.; Sen, I.; Alkim, C. Role of Bismuth in the Eradication of *Helicobacter pylori*. *Am J Ther* **2017**, *24* (6), e751–e757.
- (285) Andleeb, S.; Imtiaz-Ud-Din; Rauf, M. K.; Azam, S. S.; Haq, I.-U.; Tahir, M. N.; Zaman, N. Structural characterization and antileishmanial activity of newly synthesized organo-bismuth(V) carboxylates: experimental and molecular docking studies. *J. Biol. Inorg. Chem.* **2022**, *27* (1), 175–187.
- (286) Musyoka, T.; Tastan Bishop, Ö.; Lobb, K.; Moses, V. The determination of CHARMM force field parameters for the Mg<sup>2+</sup> containing HIV-1 integrase. *Chem. Phys. Lett.* **2018**, *711*, 1–7.
- (287) Carloni, P.; Rothlisberger, U.; Parrinello, M. The role and perspective of ab initio molecular dynamics in the study of biological systems. *Acc. Chem. Res.* **2002**, *35* (6), 455–464.
- (288) Li, P.; Merz, K. M. Metal ion modeling using classical mechanics. *Chem. Rev.* **2017**, *117* (3), 1564–1686.
- (289) Seminario, J. M. Calculation of intramolecular force fields from second-derivative tensors. *International Journal of Quantum Chemistry* **1996**.
- (290) Liebeschuetz, J. W.; Cole, J. C.; Korb, O. Pose prediction and virtual screening performance of GOLD scoring functions in a standardized test. *J. Comput. Aided Mol. Des.* **2012**, *26* (6), 737–748.

- (291) Metals Modeling with Avogadro Software - LAMMPS Tube <https://lammpstube.com/2022/01/19/metals-atomic-modeling-with-avogadro-software/> (accessed Aug 13, 2022).
- (292) Fracchia, F.; Del Frate, G.; Mancini, G.; Rocchia, W.; Barone, V. Force Field Parameterization of Metal Ions from Statistical Learning Techniques. *J. Chem. Theory Comput.* **2018**, *14* (1), 255–273.
- (293) Balogh, G.; Gyöngyösi, T.; Timári, I.; Herczeg, M.; Borbás, A.; Fehér, K.; Kövér, K. E. Comparison of Carbohydrate Force Fields Using Gaussian Accelerated Molecular Dynamics Simulations and Development of Force Field Parameters for Heparin-Analogue Pentasaccharides. *J. Chem. Inf. Model.* **2019**, *59* (11), 4855–4867.
- (294) Stevens, W. J.; Krauss, M.; Basch, H.; Jasien, P. G. Relativistic compact effective potentials and efficient, shared-exponent basis sets for the third-, fourth-, and fifth-row atoms. *Can J Chem* **1992**, *70* (2), 612–630.
- (295) Krauss, M.; Stevens, W. J. Effective core potentials and accurate energy curves for Cs<sub>2</sub> and other alkali diatomics. *J. Chem. Phys.* **1990**, *93* (6), 4236–4242.
- (296) Stevens, W. J.; Basch, H.; Krauss, M. Compact effective potentials and efficient shared-exponent basis sets for the first- and second-row atoms. *J. Chem. Phys.* **1984**, *81* (12), 6026–6033.
- (297) Seminario, J. [PDF] Calculation of intramolecular force fields from second-derivative tensors | Semantic Scholar. *undefined* **1996**.
- (298) Bayly, C. I.; Cieplak, P.; Cornell, W.; Kollman, P. A. A well-behaved electrostatic potential based method using charge restraints for deriving atomic charges: the RESP model. *J. Phys. Chem.* **1993**, *97* (40), 10269–10280.
- (299) Maier, J. A.; Martinez, C.; Kasavajhala, K.; Wickstrom, L.; Hauser, K. E.; Simmerling, C. ff14SB: Improving the Accuracy of Protein Side Chain and Backbone Parameters from ff99SB. *J. Chem. Theory Comput.* **2015**, *11* (8), 3696–3713.
- (300) Petersen, H. G. Accuracy and efficiency of the particle mesh Ewald method. *J. Chem. Phys.* **1995**, *103* (9), 3668–3679.
- (301) Miller, B. R.; McGee, T. D.; Swails, J. M.; Homeyer, N.; Gohlke, H.; Roitberg, A. E. MMPBSA.py: An Efficient Program for End-State Free Energy Calculations. *J. Chem. Theory Comput.* **2012**, *8* (9), 3314–3321.
- (302) Torrie, L. S.; Wyllie, S.; Spinks, D.; Oza, S. L.; Thompson, S.; Harrison, J. R.; Gilbert, I. H.; Wyatt, P. G.; Fairlamb, A. H.; Frearson, J. A. Chemical validation of trypanothione synthetase: a potential drug target for human trypanosomiasis. *J. Biol. Chem.* **2009**, *284* (52), 36137–36145.

- (303) Benítez, D.; Franco, J.; Sardi, F.; Leyva, A.; Durán, R.; Choi, G.; Yang, G.; Kim, T.; Kim, N.; Heo, J.; et al. Drug-like molecules with anti-trypanothione synthetase activity identified by high throughput screening. *J Enzyme Inhib Med Chem* **2022**, *37* (1), 912–929.
- (304) Koch, O.; Cappel, D.; Nocker, M.; Jäger, T.; Flohé, L.; Sotriffer, C. A.; Selzer, P. M. Molecular dynamics reveal binding mode of glutathionylspermidine by trypanothione synthetase. *PLoS One* **2013**, *8* (2), e56788.
- (305) Zaman, N.; Azam, S. S. From normal to competitive-allosteric regulation: Insights into the binding pattern dynamics of DSPI protein of *Pseudomonas aeruginosa*. *J Biomol Struct Dyn* **2020**, 1–32.
- (306) Fyfe, P. K.; Oza, S. L.; Fairlamb, A. H.; Hunter, W. N. Leishmania trypanothione synthetase-amidase structure reveals a basis for regulation of conflicting synthetic and hydrolytic activities. *J. Biol. Chem.* **2008**, *283* (25), 17672–17680.
- (307) Benítez, D.; Medeiros, A.; Fiestas, L.; Panozzo-Zenere, E. A.; Maiwald, F.; Prousis, K. C.; Roussaki, M.; Calogeropoulou, T.; Detsi, A.; Jaeger, T.; et al. Identification of Novel Chemical Scaffolds Inhibiting Trypanothione Synthetase from Pathogenic Trypanosomatids. *PLoS Negl. Trop. Dis.* **2016**, *10* (4), e0004617.
- (308) Baiocco, P.; Poce, G.; Alfonso, S.; Coccozza, M.; Porretta, G. C.; Colotti, G.; Biava, M.; Moraca, F.; Botta, M.; Yardley, V.; et al. Inhibition of *Leishmania infantum* trypanothione reductase byazole-based compounds: a comparative analysis with its physiological substrate by X-ray crystallography. *ChemMedChem* **2013**, *8* (7), 1175–1183.
- (309) Pujals, G.; Suñé-Negre, J. M.; Pérez, P.; García, E.; Portus, M.; Tico, J. R.; Miñarro, M.; Carrió, J. In vitro evaluation of the effectiveness and cytotoxicity of meglumine antimoniate microspheres produced by spray drying against *Leishmania infantum*. *Parasitol. Res.* **2008**, *102* (6), 1243–1247.
- (310) Baiocco, P.; Ilari, A.; Ceci, P.; Orsini, S.; Gramiccia, M.; Di Muccio, T.; Colotti, G. Inhibitory Effect of Silver Nanoparticles on Trypanothione Reductase Activity and *Leishmania infantum* Proliferation. *ACS Med. Chem. Lett.* **2011**, *2* (3), 230–233.
- (311) Kean, W. F.; Kean, I. R. L. Clinical pharmacology of gold. *Inflammopharmacology* **2008**, *16* (3), 112–125.
- (312) Ali, M. I.; Rauf, M. K.; Badshah, A.; Kumar, I.; Forsyth, C. M.; Junk, P. C.; Kedzierski, L.; Andrews, P. C. Anti-leishmanial activity of heteroleptic organometallic Sb(v) compounds. *Dalton Trans.* **2013**, *42* (48), 16733–16741.
- (313) Biological Chemistry of Arsenic, Antimony and Bismuth | Wiley  
<https://www.wiley.com/en-us/Biological+Chemistry+of+Arsenic%2C+Antimony+and+Bismuth-p-9780470713907>

- (314) WHO Coronavirus (COVID-19) Dashboard | WHO Coronavirus (COVID-19) Dashboard With Vaccination Data <https://covid19.who.int/>
- (315) Different COVID-19 Vaccines | CDC <https://www.cdc.gov/coronavirus/2019-ncov/vaccines/different-vaccines.html>
- (316) The coronavirus pandemic is far from over | Science| In-depth reporting on science and technology | DW | 11.06.2021 <https://www.dw.com/en/coronavirus-global-pandemic-trend/a-53954594>
- (317) Viana, J.; van Dorp, C. H.; Nunes, A.; Gomes, M. C.; van Boven, M.; Kretzschmar, M. E.; Veldhoen, M.; Rozhnova, G. Controlling the pandemic during the SARS-CoV-2 vaccination rollout. *Nat. Commun.* **2021**, *12* (1), 3674.
- (318) Wouters, O. J.; Shadlen, K. C.; Salcher-Konrad, M.; Pollard, A. J.; Larson, H. J.; Teerawattananon, Y.; Jit, M. Challenges in ensuring global access to COVID-19 vaccines: production, affordability, allocation, and deployment. *Lancet* **2021**, *397* (10278), 1023–1034.
- (319) Vandebroek, I.; Pieroni, A.; Stepp, J. R.; Hanazaki, N.; Ladio, A.; Alves, R. R. N.; Picking, D.; Delgoda, R.; Maroyi, A.; van Andel, T.; et al. Reshaping the future of ethnobiology research after the COVID-19 pandemic. *Nat. Plants* **2020**, *6* (7), 723–730.
- (320) Mohammadi, S.; Jafari, B.; Asgharian, P.; Martorell, M.; Sharifi-Rad, J. Medicinal plants used in the treatment of Malaria: A key emphasis to Artemisia, Cinchona, Cryptolepis, and Tabebuia genera. *Phytother Res* **2020**, *34* (7), 1556–1569.
- (321) Gao, D.; Niu, M.; Wei, S.-Z.; Zhang, C.-E.; Zhou, Y.-F.; Yang, Z.-W.; Li, L.; Wang, J.-B.; Zhang, H.-Z.; Zhang, L.; et al. Identification of a Pharmacological Biomarker for the Bioassay-Based Quality Control of a Thirteen-Component TCM Formula (Lianhua Qingwen) Used in Treating Influenza A Virus (H1N1) Infection. *Front. Pharmacol.* **2020**, *11*, 746.
- (322) Growing demand drives herb prices up <https://www.thenews.com.pk/print/669097-growing-demand-drives-herb-prices-up>
- (323) Kumar, S.; Naeem, R.; Radhawi, A. S. T.; Mahmood, S. U.; Batool, Z.; Naqi, S. R. A. Senna Makki and the COVID-19 pandemic: a reflection from Pakistan. *Int. J. Community Med. Public Health* **2020**, *7* (12), 5194.
- (324) Zhao, Y.; Zhao, K.; Jiang, K.; Tao, S.; Li, Y.; Chen, W.; Kou, S.; Gu, C.; Li, Z.; Guo, L.; et al. A Review of Flavonoids from Cassia Species and their Biological Activity. *Curr. Pharm. Biotechnol.* **2016**, *17* (13), 1134–1146.

- (325) Elansary, H. O.; Szopa, A.; Kubica, P.; Ekiert, H.; Ali, H. M.; Elshikh, M. S.; Abdel-Salam, E. M.; El-Esawi, M.; El-Ansary, D. O. Bioactivities of traditional medicinal plants in alexandria. *Evid. Based Complement. Alternat. Med.* **2018**, *2018*, 1463579.
- (326) Beuers, U.; Spengler, U.; Pape, G. R. Hepatitis after chronic abuse of senna. *Lancet* **1991**, *337* (8737), 372–373.
- (327) Sindh governor claims herbs helped him recover from coronavirus - Pakistan - DAWN.COM <https://www.dawn.com/news/1557883>
- (328) Bashir, A.; Sizar, O. Laxatives. In *StatPearls*; StatPearls Publishing: Treasure Island (FL), 2022.
- (329) Senna: Health Benefits, Side Effects, Uses, Dose & Precautions <https://www.rxlist.com/senna/supplements.htm>
- (330) European Association for the Study of the Liver. Electronic address: [easloffice@easloffice.eu](mailto:easloffice@easloffice.eu); Clinical Practice Guideline Panel: Chair;; Panel members; EASL Governing Board representative: EASL Clinical Practice Guidelines: Drug-induced liver injury. *J. Hepatol.* **2019**, *70* (6), 1222–1261.
- (331) Zhou, P.; Yang, X.-L.; Wang, X.-G.; Hu, B.; Zhang, L.; Zhang, W.; Si, H.-R.; Zhu, Y.; Li, B.; Huang, C.-L.; et al. A pneumonia outbreak associated with a new coronavirus of probable bat origin. *Nature* **2020**, *579* (7798), 270–273.
- (332) Ahmad, S.; Navid, A.; Farid, R.; Abbas, G.; Ahmad, F.; Zaman, N.; Parvaiz, N.; Azam, S. S. Design of a Novel Multi Epitope-Based Vaccine for Pandemic Coronavirus Disease (COVID-19) by Vaccinomics and Probable Prevention Strategy against Avenging Zoonotics. *Eur J Pharm Sci* **2020**, *151*, 105387.
- (333) Ryu, Y. B.; Jeong, H. J.; Kim, J. H.; Kim, Y. M.; Park, J.-Y.; Kim, D.; Nguyen, T. T. H.; Park, S.-J.; Chang, J. S.; Park, K. H.; et al. Biflavonoids from *Torreya nucifera* displaying SARS-CoV 3CL(pro) inhibition. *Bioorg. Med. Chem.* **2010**, *18* (22), 7940–7947.
- (334) Park, J.-Y.; Kim, J. H.; Kwon, J. M.; Kwon, H.-J.; Jeong, H. J.; Kim, Y. M.; Kim, D.; Lee, W. S.; Ryu, Y. B. Dieckol, a SARS-CoV 3CL(pro) inhibitor, isolated from the edible brown algae *Ecklonia cava*. *Bioorg. Med. Chem.* **2013**, *21* (13), 3730–3737.
- (335) Jo, S.; Kim, S.; Shin, D. H.; Kim, M.-S. Inhibition of SARS-CoV 3CL protease by flavonoids. *J Enzyme Inhib Med Chem* **2020**, *35* (1), 145–151.
- (336) Smit, C.; Peeters, M. Y. M.; van den Anker, J. N.; Knibbe, C. A. J. Chloroquine for SARS-CoV-2: Implications of Its Unique Pharmacokinetic and Safety Properties. *Clin Pharmacokinet* **2020**, *59* (6), 659–669.

- (337) Kc, G. B.; Bocci, G.; Verma, S.; Hassan, M. M.; Holmes, J.; Yang, J. J.; Sirimulla, S.; Oprea, T. I. A machine learning platform to estimate anti-SARS-CoV-2 activities. *Nat. Mach. Intell.* **2021**.
- (338) Benarba, B.; Pandiella, A. Medicinal Plants as Sources of Active Molecules Against COVID-19. *Front. Pharmacol.* **2020**, *11*, 1189.
- (339) Davies, M.; Nowotka, M.; Papadatos, G.; Dedman, N.; Gaulton, A.; Atkinson, F.; Bellis, L.; Overington, J. P. ChEMBL web services: streamlining access to drug discovery data and utilities. *Nucleic Acids Res.* **2015**, *43* (W1), W612–20.
- (340) Grottesi, A.; Bešker, N.; Emerson, A.; Manelfi, C.; Beccari, A. R.; Frigerio, F.; Lindahl, E.; Cerchia, C.; Talarico, C. Computational Studies of SARS-CoV-2 3CLpro: Insights from MD Simulations. *Int. J. Mol. Sci.* **2020**, *21* (15).
- (341) Pfizer's Vizimpro is among 3 FDA-approved drugs that combat COVID-19 in lung cells: report | FierceBiotech <https://www.fiercebiotech.com/research/pfizer-s-vizimpro-among-three-fda-approved-drugs-combat-covid-lung-cells-report> (accessed Jun 17, 2021).
- (342) The Amber Molecular Dynamics Package <https://ambermd.org/> (accessed Jun 16, 2021).
- (343) Parks, J. M.; Smith, J. C. How to discover antiviral drugs quickly. *N. Engl. J. Med.* **2020**, *382* (23), 2261–2264.
- (344) Park, J.-Y.; Ko, J.-A.; Kim, D. W.; Kim, Y. M.; Kwon, H.-J.; Jeong, H. J.; Kim, C. Y.; Park, K. H.; Lee, W. S.; Ryu, Y. B. Chalcones isolated from *Angelica keiskei* inhibit cysteine proteases of SARS-CoV. *J. Enzyme Inhib Med Chem* **2016**, *31* (1), 23–30.
- (345) Lin, C.-W.; Tsai, F.-J.; Tsai, C.-H.; Lai, C.-C.; Wan, L.; Ho, T.-Y.; Hsieh, C.-C.; Chao, P.-D. L. Anti-SARS coronavirus 3C-like protease effects of *Isatis indigotica* root and plant-derived phenolic compounds. *Antiviral Res.* **2005**, *68* (1), 36–42.
- (346) Aziz, N.; Kim, M.-Y.; Cho, J. Y. Anti-inflammatory effects of luteolin: A review of in vitro, in vivo, and in silico studies. *J. Ethnopharmacol.* **2018**, *225*, 342–358.
- (347) Ribas, J.; Cubero, E.; Luque, F. J.; Orozco, M. Theoretical study of alkyl- $\pi$  and aryl- $\pi$  interactions. Reconciling theory and experiment. *J. Org. Chem.* **2002**, *67* (20), 7057–7065.
- (348) Ramos-Guzmán, C. A.; Ruiz-Pernía, J. J.; Tuñón, I. Unraveling the SARS-CoV-2 Main Protease Mechanism Using Multiscale Methods. *ACS Catal.* **2020**, *10*, 12544–12554.
- (349) Yang, J.; Petitjean, S. J. L.; Koehler, M.; Zhang, Q.; Dumitru, A. C.; Chen, W.; Derclaye, S.; Vincent, S. P.; Soumillion, P.; Alsteens, D. Molecular interaction and

- inhibition of SARS-CoV-2 binding to the ACE2 receptor. *Nat. Commun.* **2020**, *11* (1), 4541.
- (350) Goc, A.; Sumera, W.; Rath, M.; Niedzwiecki, A. Phenolic compounds disrupt spike-mediated receptor-binding and entry of SARS-CoV-2 pseudo-virions. *PLoS One* **2021**, *16* (6), e0253489.
- (351) Wang, Y.; Liu, M.; Gao, J. Enhanced receptor binding of SARS-CoV-2 through networks of hydrogen-bonding and hydrophobic interactions. *Proc. Natl. Acad. Sci. USA* **2020**, *117* (25), 13967–13974.
- (352) Huang, Y.; Yang, C.; Xu, X.-F.; Xu, W.; Liu, S.-W. Structural and functional properties of SARS-CoV-2 spike protein: potential antiviral drug development for COVID-19. *Acta Pharmacol Sin* **2020**, *41* (9), 1141–1149.
- (353) Bassendine, M. F.; Bridge, S. H.; McCaughan, G. W.; Gorrell, M. D. COVID-19 and comorbidities: A role for dipeptidyl peptidase 4 (DPP4) in disease severity? *J. Diabetes* **2020**, *12* (9), 649–658.
- (354) Khezri, M. R. PI3K/AKT signaling pathway: a possible target for adjuvant therapy in COVID-19. *Hum Cell* **2021**, *34* (2), 700–701.
- (355) Solerte, S. B.; Di Sabatino, A.; Galli, M.; Fiorina, P. Dipeptidyl peptidase-4 (DPP4) inhibition in COVID-19. *Acta Diabetol.* **2020**, *57* (7), 779–783.
- (356) Begum, J.; Mir, N. A.; Dev, K.; Buyamayum, B.; Wani, M. Y.; Raza, M. Challenges and prospects of COVID-19 vaccine development based on the progress made in SARS and MERS vaccine development. *Transbound Emerg Dis* **2021**, *68* (3), 1111–1124.
- (357) Li, H.; Wang, Y. M.; Xu, J. Y.; Cao, B. [Potential antiviral therapeutics for 2019 Novel Coronavirus]. *Zhonghua Jie He He Hu Xi Za Zhi* **2020**, *43* (3), 170–172.
- (358) Khan, Z.; Karataş, Y.; Ceylan, A. F.; Rahman, H. COVID-19 and therapeutic drugs repurposing in hand: The need for collaborative efforts. *Le Pharmacien Hospitalier et Clinicien* **2020**.
- (359) Su, H.; Xu, Y.; Jiang, H. Drug discovery and development targeting the life cycle of SARS-CoV-2. *Fundamental Research* **2021**, *1* (2), 151–165.
- (360) Du, H.-Z.; Hou, X.-Y.; Miao, Y.-H.; Huang, B.-S.; Liu, D.-H. Traditional Chinese Medicine: an effective treatment for 2019 novel coronavirus pneumonia (NCP). *Chin. J. Nat. Med.* **2020**, *18* (3), 206–210.



- (361) Mohebbi, N.; Talebi, A.; Moghadamnia, M.; Nazari Taloki, Z.; Shakiba, A. Drug Interactions of Psychiatric and COVID-19 Medications. *Basic Clin. Neurosci.* **2020**, *11* (2), 185–200.
- (362) Spina, E.; Pisani, F.; de Leon, J. Clinically significant pharmacokinetic drug interactions of antiepileptic drugs with new antidepressants and new antipsychotics. *Pharmacol. Res.* **2016**, *106*, 72–86.
- (363) Ghasemiyeh, P.; Mortazavi, N.; Karimzadeh, I.; Vazin, A.; Mahmoudi, L.; Moghimi-Sarani, E.; MohammadSadeghi, A.; Shahisavandi, M.; Kheradmand, A.; Mohammadi-Samani, S. Psychiatric Adverse Drug Reactions and Potential Anti-COVID-19 Drug Interactions with Psychotropic Medications. *Iran J Pharm Res* **2021**, *20* (3), 66–77.
- (364) Raymonda, M. H.; Ciesla, J. H.; Monaghan, M.; Leach, J.; Asantewaa, G.; Smorodintsev-Schiller, L. A.; Lutz, M. M.; Schafer, X. L.; Takimoto, T.; Dewhurst, S.; et al. Pharmacologic profiling reveals lapatinib as a novel antiviral against SARS-CoV-2 in vitro. *BioRxiv* **2020**.
- (365) He's a Nobel laureate. Critics say he was misleading on Covid - STAT <https://www.statnews.com/2021/05/24/stanford-professor-and-nobel-laureate-critics-say-he-was-dangerously-misleading-on-covid/>
- (366) Khandia, R.; Singhal, S.; Alqahtani, T.; Kamal, M. A.; El-Shall, N. A.; Nainu, F.; Desingu, P. A.; Dhama, K. Emergence of SARS-CoV-2 Omicron (B.1.1.529) variant, salient features, high global health concerns and strategies to counter it amid ongoing COVID-19 pandemic. *Environ. Res.* **2022**, *209*, 112816.
- (367) Chekol Abebe, E.; Tiruneh G/Medhin, M.; Behaile T/Mariam, A.; Asmamaw Dejenie, T.; Mengie Ayele, T.; Tadele Admasu, F.; Tilahun Muche, Z.; Asmare Adela, G. Mutational Pattern, Impacts and Potential Preventive Strategies of Omicron SARS-CoV-2 Variant Infection. *Infect. Drug Resist.* **2022**, *15*, 1871–1887.
- (368) Laffeber, C.; de Koning, K.; Kanaar, R.; Lebbink, J. H. G. Experimental Evidence for Enhanced Receptor Binding by Rapidly Spreading SARS-CoV-2 Variants. *J. Mol. Biol.* **2021**, *433* (15), 167058.
- (369) Cameroni, E.; Bowen, J. E.; Rosen, L. E.; Saliba, C.; Zepeda, S. K.; Culap, K.; Pinto, D.; VanBlargan, L. A.; De Marco, A.; di Iulio, J.; et al. Broadly neutralizing antibodies overcome SARS-CoV-2 Omicron antigenic shift. *Nature* **2022**, *602* (7898), 664–670.
- (370) Starr, T. N.; Greaney, A. J.; Hilton, S. K.; Ellis, D.; Crawford, K. H. D.; Dingens, A. S.; Navarro, M. J.; Bowen, J. E.; Tortorici, M. A.; Walls, A. C.; et al. Deep Mutational Scanning of SARS-CoV-2 Receptor Binding Domain Reveals Constraints on Folding and ACE2 Binding. *Cell* **2020**, *182* (5), 1295–1310.e20.

- (371) Yurkovetskiy, L.; Wang, X.; Pascal, K. E.; Tomkins-Tinch, C.; Nyalile, T. P.; Wang, Y.; Baum, A.; Diehl, W. E.; Dauphin, A.; Carbone, C.; et al. Structural and Functional Analysis of the D614G SARS-CoV-2 Spike Protein Variant. *Cell* **2020**, *183* (3), 739–751.e8.
- (372) Mishra, T.; Dalavi, R.; Joshi, G.; Kumar, A.; Pandey, P.; Shukla, S.; Mishra, R. K.; Chande, A. SARS-CoV-2 spike E156G/Δ157-158 mutations contribute to increased infectivity and immune escape. *Life Sci. Alliance* **2022**, *5* (7).
- (373) Zhu, L.; Deng, Y.-Q.; Zhang, R.-R.; Cui, Z.; Sun, C.-Y.; Fan, C.-F.; Xing, X.; Huang, W.; Chen, Q.; Zhang, N.-N.; et al. Double lock of a potent human therapeutic monoclonal antibody against SARS-CoV-2. *Natl Sci Rev* **2021**, *8* (3), nwa297.
- (374) Hoffmann, M.; Kleine-Weber, H.; Schroeder, S.; Krüger, N.; Herrler, T.; Erichsen, S.; Schiergens, T. S.; Herrler, G.; Wu, N.-H.; Nitsche, A.; et al. SARS-CoV-2 Cell Entry Depends on ACE2 and TMPRSS2 and Is Blocked by a Clinically Proven Protease Inhibitor. *Cell* **2020**, *181* (2), 271–280.e8.
- (375) Rodrigues, C. H.; Pires, D. E.; Ascher, D. B. DynaMut: predicting the impact of mutations on protein conformation, flexibility and stability. *Nucleic Acids Res.* **2018**, *46* (W1), W350–W355.
- (376) Upadhyay, V.; Patrick, C.; Lucas, A.; Mallela, K. M. G. Convergent Evolution of Multiple Mutations Improves the Viral Fitness of SARS-CoV-2 Variants by Balancing Positive and Negative Selection. *Biochemistry* **2022**.
- (377) Cao, Y. R.; Wang, J.; Jian, F.; Xiao, T.; Song, W.; Yisimayi, A.; Huang, W.; Li, Q.; Wang, P.; An, R.; et al. B.1.1.529 escapes the majority of SARS-CoV-2 neutralizing antibodies of diverse epitopes. *BioRxiv* **2021**.
- (378) Mlcochova, P.; Kemp, S. A.; Dhar, M. S.; Papa, G.; Meng, B.; Ferreira, I. A. T. M.; Datir, R.; Collier, D. A.; Albecka, A.; Singh, S.; et al. SARS-CoV-2 B.1.617.2 Delta variant replication and immune evasion. *Nature* **2021**, *599* (7883), 114–119.
- (379) Sun, C.; Kang, Y.-F.; Liu, Y.-T.; Kong, X.-W.; Xu, H.-Q.; Xiong, D.; Xie, C.; Liu, Y.-H.; Peng, S.; Feng, G.-K.; et al. Parallel profiling of antigenicity alteration and immune escape of SARS-CoV-2 Omicron and other variants. *Signal Transduct. Target. Ther.* **2022**, *7* (1), 42.
- (380) Starr, T. N.; Greaney, A. J.; Dingens, A. S.; Bloom, J. D. Complete map of SARS-CoV-2 RBD mutations that escape the monoclonal antibody LY-CoV555 and its cocktail with LY-CoV016. *Cell Rep. Med.* **2021**, *2* (4), 100255.
- (381) Cui, Z.; Liu, P.; Wang, N.; Wang, L.; Fan, K.; Zhu, Q.; Wang, K.; Chen, R.; Feng, R.; Jia, Z.; et al. Structural and functional characterizations of infectivity and immune evasion of SARS-CoV-2 Omicron. *Cell* **2022**, *185* (5), 860–871.e13.

- (382) Mannar, D.; Saville, J. W.; Zhu, X.; Srivastava, S. S.; Berezuk, A. M.; Tuttle, K. S.; Marquez, A. C.; Sekirov, I.; Subramaniam, S. SARS-CoV-2 Omicron variant: Antibody evasion and cryo-EM structure of spike protein-ACE2 complex. *Science* **2022**, *375* (6582), 760–764.
- (383) Saito, A.; Irie, T.; Suzuki, R.; Maemura, T.; Nasser, H.; Uriu, K.; Kosugi, Y.; Shirakawa, K.; Sadamasu, K.; Kimura, I.; et al. Enhanced fusogenicity and pathogenicity of SARS-CoV-2 Delta P681R mutation. *Nature* **2022**, *602* (7896), 300–306.
- (384) Meng, B.; Abdullahi, A.; Ferreira, I. A. T. M.; Goonawardane, N.; Saito, A.; Kimura, I.; Yamasoba, D.; Gerber, P. P.; Fatihi, S.; Rathore, S.; et al. Altered TMPRSS2 usage by SARS-CoV-2 Omicron impacts infectivity and fusogenicity. *Nature* **2022**, *603* (7902), 706–714.
- (385) Zhao, H.; Lu, L.; Peng, Z.; Chen, L.-L.; Meng, X.; Zhang, C.; Ip, J. D.; Chan, W.-M.; Chu, A. W.-H.; Chan, K.-H.; et al. SARS-CoV-2 Omicron variant shows less efficient replication and fusion activity when compared with Delta variant in TMPRSS2-expressed cells. *Emerg. Microbes Infect.* **2022**, *11* (1), 277–283.
- (386) Meng, B.; Ferreira, I.; Abdullahi, A.; Kemp, S. A.; Goonawardane, N.; Papa, G.; Fatihi, S.; Charles, O.; Collier, D.; CITIID-NIHR BioResource COVID-19 Collaboration; et al. SARS-CoV-2 Omicron spike mediated immune escape, infectivity and cell-cell fusion. *BioRxiv* **2021**.
- (387) Walls, A. C.; Xiong, X.; Park, Y.-J.; Tortorici, M. A.; Snijder, J.; Quispe, J.; Cameroni, E.; Gopal, R.; Dai, M.; Lanzavecchia, A.; et al. Unexpected receptor functional mimicry elucidates activation of coronavirus fusion. *Cell* **2019**, *176* (5), 1026–1039.e15.
- (388) Kumar, S.; Thambiraja, T. S.; Karuppanan, K.; Subramaniam, G. Omicron and Delta variant of SARS-CoV-2: A comparative computational study of spike protein. *J. Med. Virol.* **2022**, *94* (4), 1641–1649.
- (389) Jiang, H.; Blouin, C. Insertions and the emergence of novel protein structure: a structure-based phylogenetic study of insertions. *BMC Bioinformatics* **2007**, *8*, 444.
- (390) Levy, Y.; Onuchic, J. N. Water and proteins: a love-hate relationship. *Proc. Natl. Acad. Sci. USA* **2004**, *101* (10), 3325–3326.
- (391) Covalt, J. C.; Roy, M.; Jennings, P. A. Core and surface mutations affect folding kinetics, stability and cooperativity in IL-1 beta: does alteration in buried water play a role? *J. Mol. Biol.* **2001**, *307* (2), 657–669.
- (392) Papoian, G. A.; Ulander, J.; Eastwood, M. P.; Luthey-Schulten, Z.; Wolynes, P. G. Water in protein structure prediction. *Proc. Natl. Acad. Sci. USA* **2004**, *101* (10), 3352–3357.

- 
- (393) Cheng, M. H.; Krieger, J. M.; Banerjee, A.; Xiang, Y.; Kaynak, B.; Shi, Y.; Arditi, M.; Bahar, I. Impact of new variants on SARS-CoV-2 infectivity and neutralization: A molecular assessment of the alterations in the spike-host protein interactions. *iScience* **2022**, *25* (3), 103939.
- (394) Sun, Y.; Lin, W.; Dong, W.; Xu, J. Origin and evolutionary analysis of the SARS-CoV-2 Omicron variant. *Journal of Biosafety and Biosecurity* **2022**, *4* (1), 33–37.
- (395) Berkhout, B.; Herrera-Carrillo, E. SARS-CoV-2 Evolution: On the Sudden Appearance of the Omicron Variant. *J. Virol.* **2022**, *96* (7), e0009022.
- (396) Nie, C.; Sahoo, A. K.; Netz, R. R.; Herrmann, A.; Ballauff, M.; Haag, R. Charge matters: mutations in omicron variant favor binding to cells. *Chembiochem* **2022**, *23* (6), e202100681.
- (397) Maher, M. C.; Bartha, I.; Weaver, S.; di Iulio, J.; Ferri, E.; Soriaga, L.; Lempp, F. A.; Hie, B. L.; Bryson, B.; Berger, B.; et al. Predicting the mutational drivers of future SARS-CoV-2 variants of concern. *Sci. Transl. Med.* **2022**, *14* (633), eabk3445.
- (398) Cheng, M. H.; Zhang, S.; Porritt, R. A.; Noval Rivas, M.; Paschold, L.; Willscher, E.; Binder, M.; Arditi, M.; Bahar, I. Superantigenic character of an insert unique to SARS-CoV-2 spike supported by skewed TCR repertoire in patients with hyperinflammation. *Proc. Natl. Acad. Sci. USA* **2020**, *117* (41), 25254–2526

## Discrete Dynamics of Warhead Modulation on Covalent Inhibition of OxyR: A QM/MM Study

Naila Zaman and Syed Sikander Azam\*



Cite This: *J. Phys. Chem. B* 2023, 127, 5993–6005



Read Online

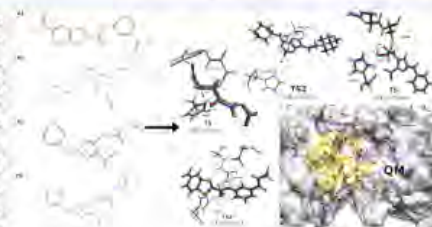
ACCESS |

Metrics & More

Article Recommendations

Supporting Information

**ABSTRACT:** The bacterial transcriptional factor OxyR, a peroxide sensor conserved in bacterial virulence pathways, has the capability to exhibit exceptional reactivity toward hydrogen peroxide ( $H_2O_2$ ).  $H_2O_2$  is essential for oxidizing cysteine thiolates to maintain cellular redox homeostasis and is dispensable for bacterial growth that can potentially mitigate drug resistance, thus underlining OxyR as a valuable target. We employ quantum mechanics/molecular mechanics (QM/MM) umbrella sampling (US) simulations at the DFTB3/MM level of theory and propose a reaction mechanism with four potential covalent inhibitors. The potential of mean force reveals the direct role of intrinsic reactivity of inhibitors, for instance, benzothioophenes and modified experimental inhibitors with methyl oxo-enoate warhead-activated carbonyl samples in the first step of reaction, which shed light on the significance of proton transfer indispensable for full inhibition, whereas the nitrile inhibitor undergoes a stepwise mechanism with a small proton-transfer energy barrier and lower imaginary frequencies that materialize instantly after nucleophilic attack. To unveil the molecular determinants of respective binding affinities, transition states along the reaction path are optimized and characterized with B3LYP 6-31+G(d,p). Furthermore, the post-simulation analysis indicates the catalytic triad (His130/Cys199/Thr129), thermodynamically favored for inhibition, which restricts water molecules from acting as the potential source of protonation/deprotonation. This study thus serves as a preamble to add variation in the proposed structures and unveils the impact of functional groups lying in warheads that modulate the kinetics of proton transfer, which will certainly aid to design more selective and efficient irreversible inhibitors of OxyR.



### INTRODUCTION

Rapid evolution and dissemination of antimicrobial resistance drastically undermine the effectiveness of antimicrobial agents, thus posing a serious threat to public health globally that prompts uncontrolled resistance in microorganisms.<sup>1–4</sup> According to the World Health Organization (WHO), antimicrobial treatment is inconceivable in the absence of effective antimicrobial agents that could lead to more than 10 million deaths annually by 2050 if left unaddressed.<sup>5–9</sup> In that respect, concerted efforts in the design and development of effective drugs are required to overcome the emergence of multi-drug resistance that has outpaced drug discovery due to limitations of investment in research and pharmaceutical industries.<sup>10–11</sup> Generally, the convergent approach to classify antipathogenic compounds is to target virulent pathways that interfere with regular defense mechanisms of organisms, thus limiting the possibility of acquired resistance due to milder evolutionary pressure.<sup>12–16</sup>

In this context, Gram-negative bacteria exhibit a reactive oxidative specie,  $H_2O_2$ , that is produced in response to higher stress levels, which in turn triggers the expression of multiple genes involved in the maintenance of homeostasis, or repair, especially transcription factors that regulate bacterial defense mechanisms.<sup>17</sup>  $H_2O_2$  mainly targets protein thiol groups or

metal centers present in transcription factors, especially those that have relatively higher reactivity toward oxygen/nitrogen species.<sup>16,19</sup> One such transcription sensor, OxyR, that responds to enhanced levels of  $H_2O_2$  is necessary for full virulence of *Pseudomonas aeruginosa*<sup>20–23</sup> and is thus the protein of interest in this study. OxyR is a highly sensitive and selective transcription factor sensor of  $H_2O_2$ , which is reduced by cysteine comprising an active site, leading to increased transcription of antioxidant genes such as KatA, and is responsible for acute intrinsic resistance in *P. aeruginosa*.<sup>23</sup> To date, multiple crystal structures of the OxyR regulatory domain (RD) have been solved using *Escherichia coli*, *P. aeruginosa*, *Vibrio vulnificus*, *Neisseria meningitidis*, and *Porphyromonas gingivalis*, but the molecular evidence of involvement of  $H_2O_2$  in catalysis and binding at the catalytic triad of OxyR is published in biochemical studies of full-length *P. aeruginosa*

Received: October 20, 2022

Revised: June 11, 2023

Published: June 28, 2023



# Quantum Dynamics and Bi Metal Force Field Parameterization Yielding Significant Antileishmanial Targets

Naila Zaman and Syed Sikander Azam\*

Cite This: <https://doi.org/10.1021/acs.jcim.2c01100>

Read Online

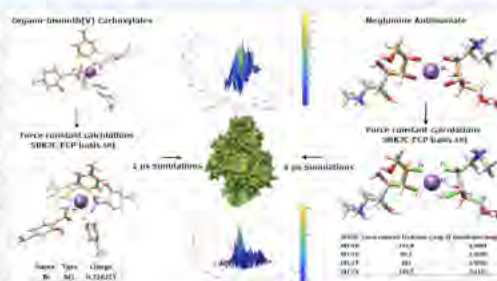
ACCESS

Metrics & More

Article Recommendations

Supporting Information

**ABSTRACT:** Amid emerging drug resistance to metal inhibitors, high toxicity, and onerous drug delivery procedures, the computational design of alternate formulations encompassing functional metal-containing compounds greatly relies on large-scale atomistic simulations. Simulations particularly with Au(I), Ag, Bi(V), and Sb(V) pose a major challenge to elucidate their molecular mechanism due to the absence of force field parameters. This study thus quantum mechanically derives force field parameters of Bi(V) as an extension of the previous experimental study conducted on heteroleptic triorganobismuth(V) biscalboxylates of type  $[\text{BiR}_3(\text{O}_2\text{CR}')_2]$ . We have modeled two organo-bismuth(V) carboxylates, which are optimized and parameterized along with the famous pentavalent antimonial drug: meglumine antimoniate using quantum mechanics original Seminario methods with the SBKJ/C effective core potential (ECP) basis set. Furthermore, molecular dynamics (MD) simulations of bismuth- and antimony-containing compounds in complex with two enzymes, trypanothione synthetase-amidase (TSA) and trypanothione reductase, are performed to target the  $(\text{T}(\text{SH})_2)$  pathway at multiple points. MD simulations provide novel insights into the binding mechanism of TSA and highlight the role of a single residue Arg569 in modulating the ligand dynamics. Moreover, the presence of an ortho group in a ligand is emphasized to facilitate interactions between Arg569 and the active site residue Arg313 for higher inhibitory activity of TSA. This preliminary generation of parameters specific to bismuth validated by simulations in replica will become a preamble of future computational and experimental research work to open avenues for newer and suitable drug targets.



## INTRODUCTION

According to the World Health Organization (WHO), protozoan parasitic diseases from the genera *Trypanosoma* and *Leishmania*, particularly visceral leishmaniasis, have reportedly caused more than 90% new cases in 2020.<sup>1</sup> Due to a limited number of treatment options and rapidly evolving drug resistance to available drugs, it has resulted in more than 500 000 cases annually with greater than 50,000 mortality instances globally, which includes 69 different countries namely Europe, Middle East, and South America.<sup>2,3</sup> More precisely, the WHO has categorized it as one of the top mortality outbreaks that has recently occurred in 10 countries, namely, Brazil, China, Ethiopia, Eritrea, India, Kenya, Somalia, South Sudan, Sudan, and Yemen.<sup>4,5</sup> Commonly used drugs in the treatment of leishmaniasis include the famous pentavalent antimonial, amphotericin B, miltefosine, and paromomycin, each with its own efficacy and toxicity limitations.<sup>5,14,15</sup> Apart from the difficult administration regimen of these drugs, their continuous and long-term use has resulted in parasitic resistance in multiple strains, causing a dramatic decrease in their efficacy. These drugs most commonly target thiol-based redox systems of parasites. The most common and critical pathway, trypanothione metabolic pathway  $(\text{T}(\text{SH})_2)$ , however serves as a suitable

target carrying a unique thiol-based metabolic system different from humans.<sup>6–8</sup> The substantial role of this pathway in a myriad of reactions comprises defense against oxidative damage, redox, homeostasis, and replication,<sup>9–12</sup> presenting itself as suitable for the design of antitrypanosomatid agents. Two widely circulated drug targets, namely, trypanothione synthetase-amidase (TSA) and trypanothione reductase (TR), play a central role in the  $(\text{T}(\text{SH})_2)$  pathway.  $(\text{T}(\text{SH})_2)$  is synthesized from two processes: one is from the reaction of GSH and Spd catalyzed by TSA while the other is the TR-catalyzed TS2 reduction reaction.<sup>8,13</sup> Amid continuous efforts after genetic and chemical validation in the design of effective and less toxic inhibitors, multiple studies have proposed chemotherapy with metal-containing compounds. Pentavalent antimonial including sodium stibogluconate and meglumine antimoniate is the most

Received: August 31, 2022



## Modulating structural dynamics of dual drugs for CDK4 complex addressing prostate cancer

Naïla Zaman<sup>1</sup>, Rimsha Yousaf<sup>1</sup>, Zahra Akhtar, Syed Sikander Azam<sup>\*</sup>

Computational Biology Lab, National Center for Bioinformatics (NCB), Quaid-i-Azam University, Islamabad, Pakistan



### ARTICLE INFO

#### Article history:

Received 20 October 2022

Revised 8 February 2023

Accepted 9 February 2023

Available online 11 February 2023

#### Keywords:

Drug combination

Molecular dynamics simulations

Palbociclib

Abemaciclib

Ribociclib

p27-CDK4/cyclin D

### ABSTRACT

Multiple drug therapies have been proposed to inhibit dysregulated activation of cyclin-dependent kinases (CDK) 4/6, resulting in primary or secondary resistance or partial deactivation. Owing to the presence of drug repurposing and drug combination therapies, the current study targeted p27-CDK4/cyclin D1 complex to investigate nine different experimentally verified drug combinations targeting the central binding groove (CBG) and ATP binding site. Our findings reveal top drug combinations that impart stability to dimer in active conformation are: ShetA2-Palbociclib, ShetA2-Abemaciclib (IC<sub>50</sub>, 2 nM), and Letrozole-Ribociclib (IC<sub>50</sub>, 11 nM). Impact of dual inhibition on structure dynamics categorically demonstrates the role of catalytic amino acids (Asp341 and Ala166) that forges interactions with aromatic rings and chemical scaffolds particularly pyrido-pyrimidine substructures efficaciously uphold an active conformation. Furthermore, the role of p27 linker is emphasized and validated that modulates compact domain organization and confers enhanced structure stability thus acting as molecular effectors of dual drugs binding in solution. Additionally, local conformational changes, hydrophobic microenvironment around CBG, and polar ATP site underpin the significance of aromatic rings in ligands that serve as targets for prostate cancer. Conclusively, the ADMET properties of combination drugs, the structural dynamics of each inhibitor in its respective binding site, and molecular determinants for enhanced binding affinities provide summarized data on dual inhibition therapy that can significantly aid in designing accurate dual inhibitors.

© 2023 Elsevier B.V. All rights reserved.

### 1. Introduction

Prostate cancer is the third most commonly occurring cancer in men [1] reaching over 1,414,259 cases in 2020 surfacing globally with specifically high prevalence in developed countries [2]. Initially, prostate cancer may be asymptomatic; however, in severe cases, men suffer various symptoms such as disturbance in urine flow, pain and burning during urination, blood in urine, and the need for frequent urination. In advanced cases, prostate cancer affects other body parts such as ribs, the spine, hips, and other parts [3]. Androgen deprivation therapy (ADT) has been employed to treat metastatic prostate cancer; however, men develop resistance to ADT leading to a condition called Metastatic castration-resistance prostate cancer (mCRPC) [4]. To overcome resistance, the primary objective of cancer research has always been to

identify the most effective anticancer agents with low toxicity. In this context, multiple studies have been conducted on serine/threonine kinases (CDK) that play a significant role in cell cycle regulation [5]. In the early cell cycle, catalytic subunits of CDK4 are activated by cyclin D1 for their kinase activity [6]. It requires phosphorylation of the activation loop to become a fully active CDK4/cyclin D1 complex. Concomitantly, it reacts in a two-step procedure of early recognition by cyclin D1, followed by the phosphorylation by kinase subunit [7]. This is the reason certain kinases act as potential targets of inhibition in proliferating cancerous cells. Like other kinases, CDK4 has a bilobal structure containing 5-stranded beta-sheets, an N-terminal domain, and a helical C-terminal domain. Between C and N-terminal domains, the ATP binding site is located. Whereas cyclin D1 comprises cyclin box domain that contains 11 helices. The binding site of cyclin D1 is referred to as the central binding groove (CBG) and is shaped by the hydrophobic cleft [8]. The CDK4/cyclin D1 complex is established by binding cyclin D1 with an alpha-C helix of CDK4 [9]. CDK4/cyclin D1 complexes are inhibited by a variety of mechanisms such as (1) binding of inhibitors from INK and Cip/Kip families of protein on the ATP binding site of CDKs, (2) inhibition

\* Corresponding author at: Syed Sikander Azam, National Centre for Bioinformatics, Quaid-i-Azam University, Islamabad 45320, Pakistan.

E-mail addresses: [syediazam2008@gmail.com](mailto:syediazam2008@gmail.com), [ssiazam@quai.edu.pk](mailto:ssiazam@quai.edu.pk) (S. Sikander Azam).

<sup>1</sup> Authors contributed equally to this work.



## From normal to competo-allosteric regulation: insights into the binding pattern dynamics of DSPI protein of *Pseudomonas aeruginosa*

Naila Zaman and Syed Sikander Azam

Computational Biology Lab, National Center for Bioinformatics, Quaid-i-Azam University, Islamabad, Pakistan

Communicated by Ramaswamy H. Sarma

### ABSTRACT

DSPI, a putative enoyl-coenzyme A (CoA) hydratase/isomerase, is anticipated to be involved in the synthesis of *cis*-2-decenoic acid (CDA), a quorum sensing (QS) signal molecule present in the superbug *Pseudomonas aeruginosa*. The current study not only adapts a broad-spectrum strategy for the lucid design of small molecule modulators but also provides novel allosteric inhibitors for DSPI, to investigate its function and potential as a therapeutic target. Docking analysis revealed that the compound 10252273, bound to the specific allosteric site, interacted with Glu118, unique amino acid residue of the active binding pocket, hence indicates the presence of a competitive allosteric site. The current study thus identifies and characterizes inhibitors by targeting the normal binding site and also reports the presence of the competo-allosteric site in the same binding tunnel as the normal site. Molecular docking studies proposed two chemical compounds that share a benzamide-benzimidazole (BB) backbone as potent inhibitors that can obstruct the mechanism of DSPI by targeting both the normal and proposed allosteric binding sites. MD simulations further revealed the disruption of the normal binding site due to the displacement of critical residues Cys146 and Glu118. The rearrangement of H-bond pattern, pi-pi interactions, and strong hydrophobic interactions were observed at both the binding sites. The allosteric pocket inhibitor exhibited improved binding energy than the normal site inhibitor based on MMGBSA and MMPBSA analysis. With subsequent characterization, the current study reveals the allosteric binding site and provides insights into the drug binding mechanism of DSPI.

### ARTICLE HISTORY

Received 19 March 2019  
Accepted 30 December 2019

### KEYWORDS

Allosteric inhibition;  
benzamide-benzimidazole;  
quorum sensing; biofilm  
dispersion; putative  
enoyl-coenzyme A  
hydratase DSPI;  
*Pseudomonas aeruginosa*

### 1. Introduction

Bacterial virulence mechanisms have emerged as new potential targets for the progression of antibacterial mediators. These mechanisms include pervasive signaling pathways that are of vital importance in many of these processes, such as the quorum-sensing (QS) signaling system (Beceiro, Tomás, & Bou, 2013). In many pathogenic bacteria, quorum-sensing (QS) signaling is a significant controlling factor that contributes to bacterial virulence and persistence (Miller & Bassler, 2001). *Pseudomonas aeruginosa*, one of the foremost causes of nosocomial infections, is primarily controlled by QS (Tang et al., 2018). Therefore, inhibiting these signaling pathways represents attractive strategies for developing novel therapeutics against *P. aeruginosa* infection (Hall-Stoodley, Costerton, & Stoodley, 2004; Hentzer et al., 2003). So far, the frequently studied QS system in *P. aeruginosa* is the one established on the DSF fatty acid (FA) signal *cis*-11-methyl-2-dodecenoic acid (CDA), formerly justified in *Xanthomonas campestris* (*Xcc*) (Huedo, Coves, Daura, Gibert, & Yero, 2018). The diffusible signaling factor (DSF)-based quorum sensing (QS) system has been recognized as an extensively preserved cell-cell communication mechanism in Gram-negative bacteria (Ryan, An, Allan, McCarthy, & Dow, 2015). Lately, a small messenger fatty

acid molecule *cis*-2-decenoic acid (CDA), produced by *P. aeruginosa*, is reported to work as the autoinducer of biofilm dispersion. The role of this molecule has also been observed in multiple Gram-negative and Gram-positive bacteria to enhance the biofilm dispersal (Davies & Marques, 2009).

Recently reported protein DSPI has been identified as a significant virulence factor in *P. aeruginosa* and further characterized as an essential enzyme for CDA biosynthesis (Amari, Marques, & Davies, 2013). Significant homology to Rpff in *Xanthomonas campestris* has been observed in the gene sequence for this protein. DSPI is a member of the crotonase superfamily (CS), demonstrating a common crotonase motif and assembles as a homotrimer (Hamed, Batchelar, Clifton, & Schofield, 2008). The structural representation of DSPI in biological assembly and as a monomer is depicted in Figure S1 (Supplementary material). CS members catalyze diverse metabolic reactions with CoA-ester substrates. Approximately 20 CS reactions, including alkene hydration/isomerization, aryl-halide dehalogenation, carboxylation, CoA ester, and peptide hydrolysis, have been classified in previous studies (Holden, Benning, Haller, & Gerlt, 2001). As a critical enzyme responsible for the 2,3 double bond formation during CDA biosynthesis, DSPI has been predicted as an

**CONTACT** Syed Sikander Azam  syedazam2008@gmail.com  ssazam@qu.edu.pk  Computational Biology Lab, National Center for Bioinformatics, Quaid-i-Azam University, Islamabad 45320, Pakistan

 Supplemental data for this article is available online at <https://doi.org/10.1080/07391102.2020.1711805>.

© 2020 Informa UK Limited, trading as Taylor & Francis Group





Contents lists available at ScienceDirect

## Journal of Molecular Graphics and Modelling

journal homepage: [www.elsevier.com/locate/jmglm](http://www.elsevier.com/locate/jmglm)

## Roxadustat and its failure: A comparative dynamic study

Kainat Gul, Naila Zaman, Syed Sikander Azam\*

Computational Biology Lab, National Centre for Bioinformatics (NCB), Quaid-i-Azam University, Islamabad, Pakistan

## ARTICLE INFO

## Keywords:

Roxadustat  
3D-QSAR Pharmacophore  
Molecular docking  
MMGB/PBSA  
Molecular dynamics simulation

## ABSTRACT

Roxadustat, a small-molecule inhibitor of hypoxia-inducible factor prolyl hydroxylase domain 2 (HIF-PHD2) has been recently overruled by the American Food and Drug Administration (FDA) in Phase 3 clinical trials. This study provides insights into the dynamics of Roxadustat with PHD2 and proposes two FDA-approved drugs; Pemetrexed and Valrubicin to treat chronic kidney disease (CKD). Role of chemical scaffolds such as synthetic pyrimidine-based antifolate is found critical for PHD2 inhibitory activity, which is concurrent with the experimental findings for stimulating Endogenous erythropoietin (EPO) gene expression. Furthermore,  $Fe^{+2}$  and  $Mn^{+2}$  in solution are essential for imparting structural stability to the screened carboxylic and non-carboxylic acid drugs. Comparative analysis of FDA-approved drugs namely, Roxadustat, two-hit carboxylic, and non-carboxylic-acid type compounds (Pemetrexed and Valrubicin), as well as the control ligands (KU1 and 4JR), unveil structural dynamics of Roxadustat and its failure. However, the proposed FDA compounds, Pemetrexed and Valrubicin, used to treat mesothelioma, non-small cell lung cancer, and bladder cancer should be subjected to *in vitro* analysis for renal anemia.

## 1. Introduction

According to the World Health Organization (WHO), anemia occurs when the amount of circulating red blood cells (RBCs) cannot meet the body requirements [1]. Anemia can be caused by chronic kidney disease (CKD), cancer, inflammatory issues, nutrient inadequacies, hereditary problems, and some medicines [2,3]. In CKD patients, anemia is caused by decreased erythropoietin production in the kidney (a mirror of decreased renal mass) where erythropoietin is a hormone that influences differentiation and maturation of RBC precursors [4]. Over the last several years, researchers have discovered that renal anemia can be caused by increased levels of hepcidin, inflammation, reduced iron availability for erythropoiesis, and a shorter RBC half-life [5]. This disease affects a third of the world's population and causes severe illness and death [6]. Erythropoiesis-stimulating agents (ESAs) and iron supplements are two extremely effective treatments for renal anemia. Conversely, erythropoietin (EPO) resistance affects approximately 5%–10% of individuals with renal anemia [7], leading to greater dosages of EPO that are required to attain basic hemoglobin levels; thus, resulting in increased cardiovascular events, mortality, and other adverse effects [8–10].

In this context, identification of prolyl hydroxylase domain 2 (PHD) enzyme as HIF-dependent erythropoiesis regulators has resulted in the creation of innovative renal anemia treatments. Most PHD2 inhibitors are derivatives of the endogenous cofactor 2OG, and they all have similar pharmacophores, which are compatible with the binding mechanism of the PHD2 enzyme and 2OG cofactor [11]. Many of these inhibitors have a bidentate chelating moiety as well as a carboxylic acid group. PHD2 inhibitors that lack the carboxylic acid group in their structures however differ considerably from 2OG in terms of structure [2]. As a hypoxia-inducible factor (HIF)-prolyl hydroxylase inhibitor, Roxadustat, which was in clinical phase 3 developed by FibroGen for the treatment of renal anemia has recently been precluded [6]. It was reported as a therapeutic potential target for HIF-related diseases such as anemia, as well as a novel target for modulating the response to hypoxia [12]. The Prolyl hydroxylase domain-containing enzymes are found active at normal oxygen concentrations (normoxia), which are hydroxylated by active PHD2. When HIF- $\alpha$  is hydroxylated, the Hippel Lindau tumor suppressor protein (pVHL) recognizes it, which enables its proteasomal destruction through E3 ubiquitin ligase. As a result, E3 ubiquitin ligase ligates rather than degrading HIF, labelling it with a signal that allows it to be carried to the proteasome for disintegration.

**Abbreviations:** RMSF, Root mean square fluctuation;  $\beta$ -factor, Beta factor; RMSD, Root mean square deviation; EPO, Endogenous erythropoietin; NCB, National center for biotechnology information; MD, Molecular dynamics; FDA, Food and drug administration.

\* Corresponding author. Computational Biology Lab, National Centre for Bioinformatics, Quaid-i-Azam University, Islamabad-45320, Pakistan.

E-mail addresses: [kainatgul702@gmail.com](mailto:kainatgul702@gmail.com) (K. Gul), [nyla.zaman87@gmail.com](mailto:nyla.zaman87@gmail.com) (N. Zaman), [syedazam2008@gmail.com](mailto:syedazam2008@gmail.com), [ssazam@quau.edu.pk](mailto:ssazam@quau.edu.pk) (S.S. Azam).

<https://doi.org/10.1016/j.jmglm.2023.108422>

Received 24 November 2022; Received in revised form 19 January 2023; Accepted 20 January 2023

Available online 21 January 2023

1093-3263/© 2023 Elsevier Inc. All rights reserved.



## Deciphering the role of sulfonamides and molecular basis of thioredoxin domain dynamics through comparative simulations

Azka Ahmed <sup>1</sup>, Naila Zaman <sup>1</sup>, Syed Sikander Azam <sup>\*</sup>

Computational Biology Lab, National Center for Bioinformatics (NCB), Quaid-i-Azam University, Islamabad, Pakistan

### ARTICLE INFO

#### Article history:

Received 20 March 2020

Received in revised form 24 September 2020

Accepted 13 November 2020

Available online 19 November 2020

#### Keywords:

DsbA

Thioredoxin domain

Sulfonamides

Molecular dynamics simulations

Binding energy

Axial frequency distribution

### ABSTRACT

DsbA, a thioredoxin periplasmic protein was prioritized based on subtractive proteomics and immunoinformatics in-depth investigation of *Providencia rettgeri* proteome. It is an important member of the protein family thioredoxins that catalyzes disulfide bond formation and acts as a folding catalyst for multiple categories of virulence factors. Herein, we performed the molecular dynamics (MD) simulation analysis of synthetic analogues of ubiquinone (dimedone derivatives) that inhibit disulfide bond formation (IC<sub>50</sub> ~ 1 μM) catalyzed by *E. coli* DsbA: DsbB and in comparison propose a sulfonamide comprising compound from the Chembridge library. Both the structures were confined to crystal water molecules and placed in a 5-Å shell of water. The enzyme in solution underwent ligand-induced conformational changes, which appeared to correspond to position shifts in the equilibrium in the crystallographically defined thioredoxin domains. Dimedone derivative eventually drifted away from the thioredoxin domain and shifted to the conserved hydrophobic patch exposing itself to interact preferably with the solvent or the membrane protein DsbB. Comparatively, a Chembridge compound 10,005,560 exhibited strong hydrogen bonding and π-π stacking with the residues ASN155 and PHE56 while moving towards the thioredoxin domain and revealing stability till 250 ns. This positional shift relative to the thioredoxin domain was further analyzed through advanced Radial distribution function (RDF) and Axial frequency distribution (AFD) analyses to confirm the substantial collaboration of sulfonamide core like structures, which could be a starting point into the development of potential DsbA: DsbB inhibitors.

© 2020 Elsevier B.V. All rights reserved.

### 1. Introduction

*Providencia rettgeri* is an anaerobic Gram-negative bacterium that proved to be resilient against many recent antibiotics [1]. It plays a crucial role in causing infections in the urinary tract, gastrointestinal tract, wounds, skin, eye, and bacteremia [1]. It mainly targets immunocompromised patients as they are extremely susceptible to the nosocomial infections that can be caused while using different invasive therapeutic techniques namely colposcopy, bronchoscopy, catheterization, and surgical biopsies [1]. Traveller's diarrhea, neonatal sepsis, and other serious infections in humans like meningitis caused by *P. rettgeri* have also been recently reported [1,2]. Its strains are resilient to many antimicrobials that include ampicillin, first-generation cephalosporins, polymyxins, and tigecycline. This pathogen has become progressively significant due to the emergence of carbapenemases; enzymes that can hydrolyse almost all types of β-lactams [3]. According to recent studies, it also possesses resistance against cefepime, imipenem, and

piperacillin-tazobactam with a mortality rate of 29% [4]. Consequently, the catastrophe of antibiotic resistance is raising a substantial economic and scientific burden on the healthcare structure worldwide [5], prompting the need to hunt the innovative potential therapeutic targets in pathogens.

Many computational techniques in this regard are playing a critical role in preventing drug-resistant pathogens while cutting down on the cost and time involved in the conventional drug discovery process [6,7]. Subtractive proteomics is one of the significant *in silico* techniques that aid in screening the probable drug targets based on their fundamental role in the pathogen and absence in the host [8–10]. *In silico* subtractive proteomics methodology identifies the species-specific dynamic proteins responsible for the unique phenotype along with the virulent factors of the pathogen [11]. Thus, in the current study, the former approach was employed to screen the whole proteome of *P. rettgeri* to scrutinize and identify the potential novel candidates for antibacterial drug discovery, which lead to the identification of a drug target DsbA (PrDsbA).

DsbA is an important member of the protein family thioredoxins, comprising a disulfide bond and possesses the solubilizing capability, a molecular weight of 22.91-kDa, and a thioredoxin domain. Dsb enzymes are a core of virulence assembly in bacterial cells that behave as

<sup>\*</sup> Corresponding author at: National Center for Bioinformatics, Quaid-i-Azam University, Islamabad 45320, Pakistan.

E-mail address: [ssazam@qu.edu.pk](mailto:ssazam@qu.edu.pk) (S.S. Azam).

<sup>1</sup> Both authors contributed equally.



Contents lists available at ScienceDirect

European Journal of Pharmaceutical Sciences

journal homepage: [www.elsevier.com/locate/ejps](http://www.elsevier.com/locate/ejps)

## Design of a Novel Multi Epitope-Based Vaccine for Pandemic Coronavirus Disease (COVID-19) by Vaccinomics and Probable Prevention Strategy against Avenging Zoonotics



Sajjad Ahmad, Afifa Navid, Rabia Farid, Ghulam Abbas, Faisal Ahmad, Naila Zaman, Nousheen Parvaiz, Syed Sikander Azam\*

Computational Biology Lab, National Center for Bioinformatics (NCB), Quaid-i-Azam University, Islamabad, 45320, Pakistan.

### ARTICLE INFO

#### Keywords:

Coronavirus disease (COVID-19)  
Vaccinomics  
Non-structural protein 8  
3C-like proteinase  
Spike glycoprotein

### ABSTRACT

The emergence and rapid expansion of the coronavirus disease (COVID-19) require the development of effective countermeasures especially a vaccine to provide active acquired immunity against the virus. This study presented a comprehensive vaccinomics approach applied to the complete protein data published so far in the National Center for Biotechnological Information (NCBI) coronavirus data hub. We identified non-structural protein 8 (Nsp8), 3C-like proteinase, and spike glycoprotein as potential targets for immune responses to COVID-19. Epitopes prediction illustrated both B-cell and T-cell epitopes associated with the mentioned proteins. The shared B and T-cell epitopes: DRDAAMQRK and QARSEDKRA of Nsp8, EDMLNPNYEDL and EFTPFDVVR of 3C-like proteinase, and VNNSYECDIPI of the spike glycoprotein are regions of high potential interest and have a high likelihood of being recognized by the human immune system. The vaccine construct of the epitopes shows stimulation of robust primary immune responses and high level of interferon gamma. Also, the construct has the best conformation with respect to the tested innate immune receptors involving vigorous molecular mechanics and solvation energy. Designing of vaccination strategies that target immune response focusing on these conserved epitopes could generate immunity that not only provide cross protection across Betacoronaviruses but additionally resistant to virus evolution.

### 1. Introduction

A recent outbreak of pneumonia in Wuhan, China, is associated with Betacoronavirus of group 2B from family Coronaviridae and the order Nidovirales [1] [2]. The viruses are positive-sense RNA, enveloped and non-segmented [2]. This coronavirus disease (COVID-19) is known as a third human zoonosis of the 21<sup>st</sup> century and is caused by a new strain not previously identified in humans [1]. The coronaviruses causing minor infections of the respiratory tract in humans are NL63, OC43, hCoV-229E, and HKU1 while, the lethal coronavirus infections that emerged in this century are the Middle East respiratory syndrome coronavirus (MERS-CoV), severe acute respiratory syndrome coronavirus (SARS-CoV) and the recent SARS-CoV 2 or COVID-19 [2]. The source of the COVID-19 is still not confirmed but some evidence suggests that the source may be in the seafood market of Huanan in Wuhan, China [3] [4]. The Center for Disease Control and Prevention (CDC) reported that the recent COVID-19 is caused by Betacoronavirus just like the previous two outbreaks of coronaviruses; MERS and SARS,

the source of which is camels and bats, respectively [5]. The first transmission of CoV from animals to humans was notified in 2002 causing SARS-CoV with a 10% mortality rate [6]. It was suggested that the virus needs some intermediate reservoir to infect humans efficiently as confirmed later by a thorough investigation revealing palm civets and raccoon dogs of the wet market carried SARS-CoV viral RNA and might act like intermediate reservoirs [3].

The COVID-19 RNA virus carries a high mutation rate and ability to transfer from person to person as compared to other coronaviruses. According to the World Health Organization (WHO), till 23rd February 2020, the COVID-19 affected a total of 78,811 individuals across globally of which, 77,042 were reported in China while 1769 were reported in other countries. The death toll in China is 2445 and 17 deaths have been reported in the rest of the world. According to the reports till 2nd January 2020, 41 patients have been admitted to the hospital of which most of the patients were men and 66% of them had exposure to the Huanan seafood market and the median age of patients was 49 years [2]. The health-care workers are also diagnosed with the

\* Corresponding author: National Center for Bioinformatics, Quaid-i-Azam University, Islamabad 45320, Pakistan  
E-mail address: [syedazam2008@gmail.com](mailto:syedazam2008@gmail.com) (S.S. Azam).

<https://doi.org/10.1016/j.ejps.2020.105387>


Received 14 March 2020; Received in revised form 22 April 2020; Accepted 19 May 2020

Available online 23 May 2020

0928-0987/ © 2020 Elsevier B.V. All rights reserved.



## Structural characterization and antileishmanial activity of newly synthesized organo-bismuth(V) carboxylates: experimental and molecular docking studies

Sohaila Andleeb<sup>1</sup> · Imtiaz-ud-Din<sup>2</sup> · Muhammad Khawar Rauf<sup>2,3</sup>  · Syed Sikander Azam<sup>4</sup> · Ihsan-ul Haq<sup>5</sup> · Muhammad Nawaz Tahir<sup>6</sup> · Naila Zaman<sup>4</sup>

Received: 25 April 2021 / Accepted: 18 November 2021 / Published online: 4 January 2022  
© The Author(s), under exclusive licence to Society for Biological Inorganic Chemistry (SBIC) 2021

### Abstract

In a quest to discover new formulations for the treatment of various parasitic diseases, a series of heteroleptic triorganobismuth(V) biscarboxylates of type  $[\text{BiR}_3(\text{O}_2\text{CR}')_2]$ , where  $\text{R}=\text{C}_6\text{H}_5$  for **1–4** and  $p\text{-CH}_3\text{C}_6\text{H}_4$  for **5–8**, were synthesized, characterized and evaluated for their biological potential against *L. tropica*. All the synthesized complexes were fully characterized by elemental analysis, FT-IR, multinuclear ( $^1\text{H}$  and  $^{13}\text{C}$ ) NMR spectroscopy and X-ray crystallography. The crystal structures for  $[\text{BiPh}_3(\text{O}_2\text{CC}_6\text{H}_4(o\text{-Br}))_2]$  (**1**),  $[\text{BiPh}_3(\text{O}_2\text{CC}_2\text{H}_2\text{C}_6\text{H}_4)_2]$  (**2**),  $[\text{BiPh}_3(\text{O}_2\text{CC}_6\text{H}_4(m\text{-NO}_2))_2]$  (**3**) and  $[\text{BiPh}_3(\text{O}_2\text{CC}_6\text{H}_4(2\text{-OH},3\text{-CH}_3))_2]$  (**4**) were determined and found to have a distorted pentagonal bipyramidal molecular geometry with seven coordinated bismuth center for **1–3** and for **4** distorted octahedral geometry, respectively. All the synthesized complexes demonstrated a moderate to significant activity against leishmania parasites. A broad analytical approach was followed to testify the stability for (**1–8**) in solid state as well as in solution and in leishmanial culture M199, ensuring them to be stable enough to exert a significant antileishmanial effect with promising results. Cytotoxicity profile suggests that tris(tolyl) derivatives show lower toxicity against isolated lymphocytes with higher antileishmanial potential. Molecular docking studies were carried out to reveal the binding modes for (**1–8**) targeting the active site of *trypanothione reductase* (TR) (PDB ID: 4APN) and *Trypanothione Synthetase-Amidase* structure (PDB ID 2vob).

**Graphical abstract**

Turnitin Originality Report

Characterization and Dynamic Studies of Drugs for Combating Multi-Drug Resistance  
by Naila Zaman .



From CL QAU (DRSML)

- Processed on 12-Sep-2022 14:56 PKT
- ID: 1897846893
- Word Count: 51752

Similarity Index

11%

Similarity by Source

Internet Sources:

6%

Publications:

9%

Student Papers:

1%

**sources:**

- 1 1% match (publications)  
[Nousheen Parvaiz, Sumra Wajid Abbasi, Reaz Uddin, Syed Sikander Azam. "Targeting isoprenoid biosynthesis pathway in Staphylococcus lugdunensis : Comparative docking and simulation studies of conventional and allosteric sites", Journal of Molecular Liquids, 2018](#)
- 2 < 1% match ()  
[Li Liu, Tao Li, Xing-Jun Cheng, Cui-Ting Peng et al. "Structural and functional studies on Dspl: implications for its role in DSF biosynthesis", Scientific Reports](#)
- 3 < 1% match ()  
[Yu Wu, Liangyu Kang, Zirui Guo, Jue Liu, Min Liu, Wannian Liang. "Incubation Period of COVID-19 Caused by Unique SARS-CoV-2 Strains", JAMA Network Open](#)
- 4 < 1% match (Internet from 15-Aug-2022)  
<https://www.ncbi.nlm.nih.gov/books/NBK570580/>
- 5 < 1% match (Internet from 02-May-2020)  
<https://www.ncbi.nlm.nih.gov/pubmed?Cmd=ShowDetailView&Db=pubmed&TermToSearch=27979499>